THE INTEGRATION OF MULTI-SOURCE DATA TO IMPROVE THE CLASSIFICATION OF REMOTELY SENSED IMAGES

Mohamad Ala Shalan
Doctor of Philosophy

Aston University
October 2005

Aston University

THE INTEGRATION OF MULTI-SOURCE DATA TO IMPROVE THE CLASSIFICATION OF REMOTELY SENSED IMAGES

Mohamad Ala Shalan
Doctor of Philosophy, 2005

Abstract

The number of remote sensing platforms and sensors rises almost every year, yet much work on the interpretation of land cover is still carried out using either single images or images from the same source taken at different dates. Two questions could be asked of this proliferation of images: can the information contained in different scenes be used to improve the classification accuracy and, what is the best way to combine the different imagery?

Two of these multiple image sources are MODIS on the Terra platform and ETM+ on board Landsat7, which are suitably complementary. Daily MODIS images with 36 spectral bands in 250-1000 m spatial resolution and seven spectral bands of ETM+ with 30m and 16 days spatial and temporal resolution respectively are available. In the UK, cloud cover may mean that only a few ETM+ scenes may be available for any particular year and these may not be at the time of year of most interest. The MODIS data may provide information on land cover over the growing season, such as harvest dates, that is not present in the ETM+ data. Therefore, the primary objective of this work is to develop a methodology for the integration of medium spatial resolution Landsat ETM+ image, with multi-temporal, multi-spectral, low-resolution MODIS\Terra images, with the aim of improving the classification of agricultural land. Additionally other data may also be incorporated such as field boundaries from existing maps.

When classifying agricultural land cover of the type seen in the UK, where crops are largely sown in homogeneous fields with clear and often mapped boundaries, the classification is greatly improved using the mapped polygons and utilising the classification of the polygon as a whole as an *apriori* probability in classifying each individual pixel using a Bayesian approach.

When dealing with multiple images from different platforms and dates it is highly unlikely that the pixels will be exactly co-registered and these pixels will contain a mixture of different real world land covers. Similarly the different atmospheric conditions prevailing during the different days will mean that the same emission from the ground will give rise to different sensor reception. Therefore, a method is presented with a model of the instantaneous field of view and atmospheric effects to enable different remote sensed data sources to be integrated.

Multi temporal MODIS imagery can give an insight into the different growth patterns of vegetated land cover, especially the date of harvest. A method based upon Dempster-Shafer weight of evidence modelling is presented that integrates this multi temporal data with single scene ETM+ data to give an improved agricultural land cover classification.

Keywords: Data fusion, Bayes multisource classification, Dempster-Shafer, per-parcel classification, Linear Mixture Modelling.

Acknowledgements and Dedication

There are a number of people without whom this thesis might not have been written, and to whom I am greatly indebted. Although a few words do not do justice to their contribution I would like to thank all the anonymous people for their help in completing this thesis in its final shape. Their careful reading of my original manuscript and their detailed, perceptive comments contributed in many ways to the shape and clarity of the finished thesis.

To my parents who have raised me to be the person I am today. They helped me to succeed and boosted my confidence that I am capable of doing anything I put my mind to. Thanks for their guidance, support, love and enthusiasm,

To my wife Lina who has patiently allowed me to study at the expense of household chores, holidays and countless other little things. Thanks for her sacrifices, support and patience during my long years as a student,

To my energetic, bright, boundless son you kept my spirit alive!,

To my brother and sisters for their great support,

To all my friends,

I dedicate this work.

Table of Contents

List of figures

List of Tables

Chapter 1

Introduction

1.1. Overview

The work presented in this thesis is the result of nearly three years of research at Aston University under the supervision of Dr John Elgy. The main broad objective of this research was triggered by the ambition to improve the accuracy of land cover classification using remotely sensed images. The main problem with mapping land cover from satellite images is that none of the existing classification techniques provide a complete and unique solution. For example, each technique has its merits and demerits, thus the resulting classification is always subject to the selection of appropriate training areas and the parameters of the classifier. Therefore, it is unlikely that identical classifications will be obtained for the same image using different classifiers or even using the same classifier but with different parameters. Accuracy indicators may help in the selection of the optimal classifier. However, the accuracy assessment depends on the availability of ground truth data and its quality, which may not be available in real situations.

These problems with the performance of existing classification techniques are addressed in this work as part of the search for factors that might improve the classification of remotely sensed images.

When this work was started three years ago, the research was aimed toward improving the geo-referencing of the satellite images. This was because the geometric errors may

influence the accuracy assessment of the classified images due to the misalignment between the classified image, and the data which has been used as ground truth.

However, discussions with the supervisor of this work revealed an alternative research area, which would exploit the idea of multi-source data fusion to improve the land cover classification. Both of these areas of research are linked together, because the success of any fusion technique from multi-source data is highly dependent on the accuracy of the co-registration of the data and the quality of each data source itself. Thus, a provisional title for this thesis was selected: "The Integration of Hyper-Spectral Low Spatial Resolution with Multi-spectral Medium Spatial Resolution Satellite Images to improve the classification of agricultural land cover".

For this, a multi-spectral medium resolution Landsat Enhanced Thematic Mapper plus (ETM+) image acquired on 17th June 2000 was obtained as the primary image to be classified. The intention was then to improve a basic classification by incorporating the information extractable from a hyper-spectral coarse resolution image. Subsequently, the main problem encountered was to obtain suitable hyper-spectral low spatial resolution data.

Hyper-spectral means collecting remotely sensed data in hundreds of narrow spectral bands. It is difficult to record the amount of the energy reflected in a very narrow bandwidth and therefore such data is acquired using low spatial resolution sensors. With increased pixel size more energy can be collected from a large area which enables the activation of the sensor. Unfortunately the requisite hyper-spectral data was not available to pursue this project. Therefore, the MODerate resolution Imaging Spectroradiometre (MODIS) sensor on the Terra platform was used instead. This provides daily images in

36 spectral bands, of which 20 bands are in the visible and near-infrared regions of the spectrum. These bands have three distinctive nominal spatial resolutions. The red and near-infrared bands are at 250m resolution, another five visible and near-infrared bands are at 500m, and the remaining bands are at 1000m nominal spatial resolution. The multi-resolution multi-temporal MODIS data would therefore be integrated with the classification derived from the medium resolution Landsat ETM+ image.

The proposed procedure is that the Landsat ETM+ imagery will be initially classified to provide a per pixel classified image. Field boundaries from the Ordnance Survey (OS) 1:2500 digital map will subsequently be used to improve this classification and create a per parcel classification. Finally information from multi temporal MODIS data will be used to further improve these classifications.

As a consequence of the research project evolution the final title for the thesis has become as: "The Integration of Multi-Source Data to Improver the Classification of Remotely Sensed Images", with the aim of developing a methodology for combining multi-temporal with multi-scale, multi-source data to improve land cover classification from remotely sensed images.

The next section presents brief details about remote sensing data platforms and sensors.

1.2. Remote sensing platforms and sensors

Remote sensing data is the observation of an object from a distance using sensors on board aircraft and satellites and can be described as a complete sample of the ground data where almost each point is represented (Richards, 1993). These data are often useful for improved understanding and management of natural resources (Vogelman, 1998). Thus it represents one of the fastest-growing sources for raster GIS data (Dowman, 1998). The

advances in sensor technology within the last decade have led to a dramatic increase in the types of remotely sensed imagery.

The benefits of space-borne imagery over airborne data include: the rapid acquisition of data covering large areas; continuous acquisition of data; regular revisit capabilities; the cost effectiveness; map-accurate data with more stable platforms; possibility of stereo viewing; large archive of historical data; ability to acquire data without any restriction by local air traffic constraints; and, accessibility to remote or restricted areas (Colwell, 1983). However, the main disadvantage of satellite imagery is that the spatial resolution is relatively low, with off-nadir viewing angle not acceptable, especially for wide-view-angle satellite such as MODIS, and a strong possibility of cloud cover. Though, some recently launched satellites provide images with high spatial resolution such as Ikonos and QuickBird images, but the data is very costly, and beyond the resources available for this project.

Current sensors offer a wide variety of image data with different characteristics in terms of temporal, geometric, radiometric and spectral resolution. Most sensors fall into one of two categories passive or active. The passive sensors rely on the naturally reflected or emitted energy of the imaged surface. By contrast, active remote sensing means that the sensors provide their own illumination and measure the energy reflected back from the target. Thus, active sensors offer a great potential for observing the physical nature of the environment irrespective of the weather, day or night (Colwell, 1983).

All sensors can be made sensitive to specific signals. Although the information content from a number of sensors together might be partially overlapping, the complementary

aspects represent a valuable source for reducing the ambiguity of the information obtainable from only one sensor. Therefore, the integration of multi-sensor data can be highly beneficial and may lead to a better understanding of the diversity in the real world. A representative selection of some satellite sensors and their characteristics are presented in Appendix 1.

1.3. Current Trends in Data Fusion

Land cover maps are important data source that influence decision making and defining strategy (Binaghi and Rampini, 1993). Many general circulation and carbon exchange models in the earth system processes require vegetative cover as input data (Sellers *et al.*, 1997). Obtaining accurate and relevant information on natural resources, land cover and crop production is a key factor for decision making (Serrano, *et al.*, 2000). Quantifying the types and extent of vegetation is important to resource management and issues regarding land cover change (Townshend, 1999). These examples demonstrate the importance of, and need for land cover maps.

Land cover maps can be derived by classifying remote sensing images. Many image classification techniques are proposed in the literature (see section 2.5), and several studies have proven the superiority of the per-parcel classification over the traditional per-pixel classifiers (Esch, *et al.* 2003; Sande, *et al.*, 2003). Parcel-based classification methods have been adopted by several researchers (Mason *et al.*, 1988; Janssen *et al.*, 1992; Aplin and Atkinson, 2001), and these are mainly based on a pre-segmented image. However, the segmentation needs powerful edge detection techniques, and therefore, for this work, the OS Land-Line.Plus digital map was used to overcome the potential problems of applying edge detection techniques to satellite imagery.

With the increasing number of operational remote sensing satellites, one current trend in remote sensing is to exploit the complementary nature of data provided at different spatial and temporal resolutions. It is believed that this will lead to significant advances in earth monitoring and continental land cover classifications (Le Hégarat-Mascle *et al.*, 2003).

Much work have been done on multi-scale data fusion with many analytical or numerical data fusion techniques developed in order to obtain multispectral images at the highest possible spatial resolution (Shettigara, 1992; Pellemans *et al.*, 1993; Pohl and Van Genderen, 1998). These techniques have been largely employed to visually enhance the multi-spectral lower resolution imagery. One example being the fusing of Landsat Thematic (TM) and SPOT (Satellite Pour l'Observation de la Terre) panchromatic data (Chavez *et al.* 1991). However, it is rare to find studies in the literature that deal with the integration of multi-scale images that possess a large difference in the spatial resolution. This is a clear limitation in the currently available multi-scale fusion techniques.

Multi-temporal data fusion has been addressed in many publications (Coppin and Bauer, 1994; Pax Lenney *et al.*, 1996; Wagtenonk and Ralph, 2000). More recently, Latifovic and Pouliot (2005) proposed a new methodology for mapping land cover classification using advanced very high-resolution radiometer (AVHRR) data. In their approach time series AVHRR data were used to update an existing classification through minimizing the inconsistency in the observation from the National Oceanic and Atmospheric Administration (NOAA) satellite data. However, most of the work on multi-temporal data fusion was undertaken using single resolution satellite data. This research will

therefore address the problem of integrating multi-temporal with multi-scale, multi-source data.

1.4. Methodology and Research Objectives

After reviewing the other related works from the literature some objectives were set up for this research with the aim of developing a methodology for the integration of multi-temporal with multi-scale, multi-source data.

Therefore, in this work, following the current trend in the classification using per-parcel classification, the OS 1:2500 digital map will be used to extract the boundary information around each agricultural field. Then information from all pixels in the Landsat ETM+ image within each field will be used to assign the appropriate class to each field, polygon or land parcel.

The information extractable from the multi-temporal MODIS image will be used to update the per-parcel classification. This needs suitable multi-scale fusion techniques. For this a methodology will be proposed based on the Linear Mixture Model (LMM). All radiances from all pixels within the instantaneous field of view (IFOV) of each individual coarse resolution MODIS pixel will be aggregated through the LMM to calculate the expected reflectance in the coarse resolution multi-temporal MODIS image. Therefore, it is very important to obtain the multi-temporal reflectance for each class. This will be derived for each day of MODIS images using the LMM where the proportions for the classes are assumed to be known from the classified Landsat ETM+ image, and the unknowns will be the reflectance of each class on that day of MODIS image. Thus, the combination of these different data sources emerges as a new challenge in the remote sensing community and requires very careful integration techniques to account for the

inconsistency in the data and the huge differences in pixel resolutions between these sensors. Therefore, the main objectives of this research are:

1. To develop a methodology for classifying the medium resolution satellite images if there is no reliable ground truth.
2. To develop a methodology to integrate the OS Land-Line.Plus with the medium resolution Landsat ETM+ image to perform a per-parcel classification of the land cover.
3. To develop a methodology to integrate the multi-scale multi-temporal data from the MODIS images to improve the per-parcel classification of Landsat ETM+ image.

The flowchart in figure 1.1 outlines the methodology of the integration process of the data sources available.

1.5. Introduction to the software used

In order to process the data available for this project some commercial and free software packages were used. As an acknowledgment the packages used and a brief description are presented in the following subsections.

1.5.1. Commercial packages:

- Idrisi32 package for windows system Release Two, version 132.22, Clark Labs. Idrisi Source Code copyright© 1987-2002, J. Ronald Eastman. All modules used in this work from this package are listed in Appendix 2.

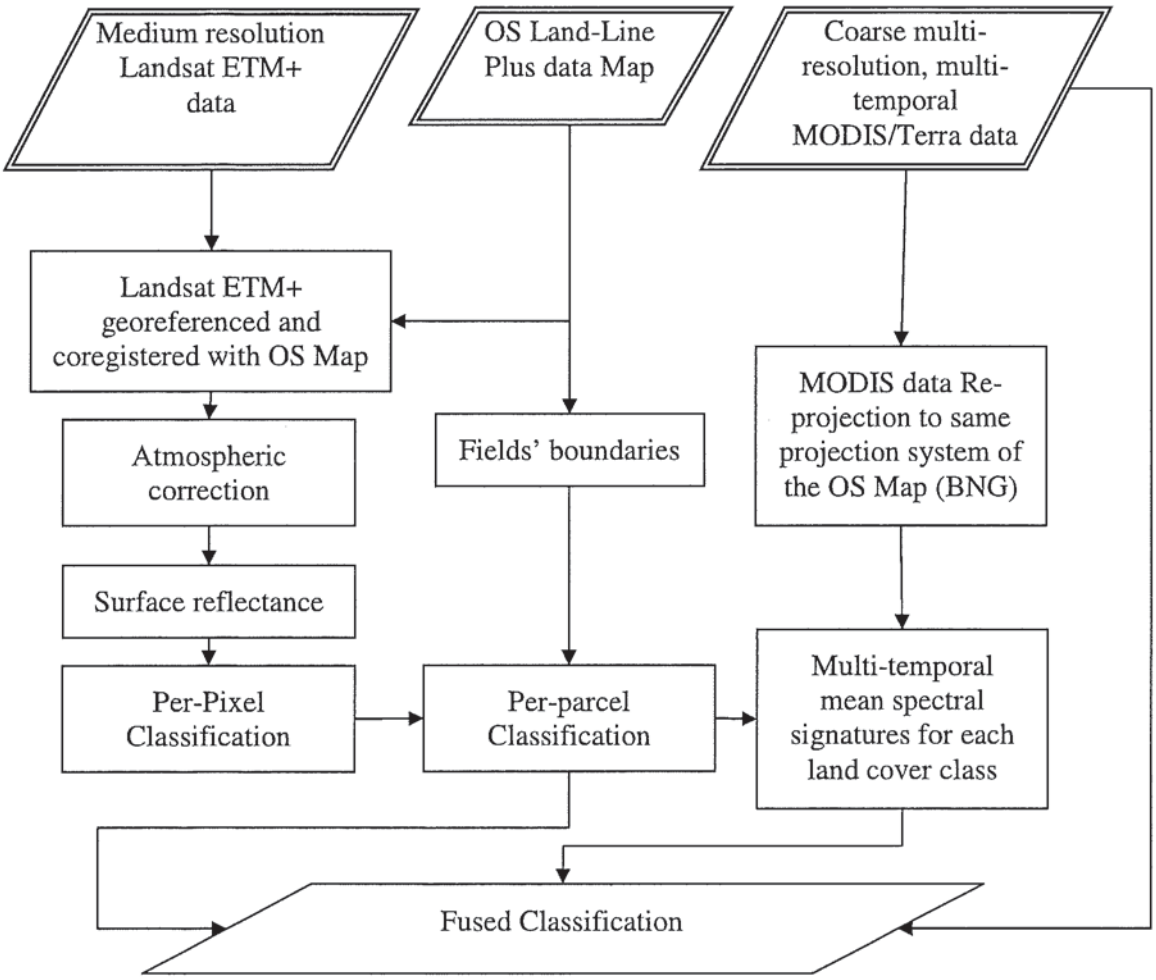

Figure 1.1: The flowchart of the proposed integration methodology

- MATLAB: The Language of Technical Computing, Version 6, Release 12, from The MathWorks, Inc. (http://www.mathworks.com/). MATLAB is a matrix programming system with many mathematical methods implemented. It also has many toolboxes. The MathWorks web site has useful information including books describing the basic system and toolboxes. The major functions used from

MATLAB are listed in Appendix 3, together with the code developed for this work is included on a CD-ROM.

- AutoCAD® which is a computer aided drafting (CAD) software package that allows the user to model, analyze, and express physical systems digitally in 2 dimensions and 3 dimensions, created by Autodesk, Inc. An overview of AutoCAD® and a detailed discussion of features and specifications can be found at (http://www.autodesk.com, No Date).
- ESRI (UK) Map Manager V6.2 (http://www.esriuk.com, No Date)

1.5.2. Free packages:

- HDFView, version 2.1 for Windows XP, University of Illinois. The HDFView is a graphic utility designed for viewing and editing the contents of HDF4 and HDF5 files. Details of the HDF object model are available from http://hdf.ncsa.uiuc.edu/hdf-java-html/hdf-object/ (No Date).
- MSPHINX (Satellite Process Handling Images uNder XWindows) available from ftp://loa.univ-lille1.fr/MSPHINX/ (No Date). Authors: Gonzalez L. and Deroo C., Laboratoire d'Optique Atmosphérique, Université des Sciences et Technologies de Lille, U.F.R. de Physique Fondamentale, 59655 Villeneuve d'Ascq Cedex, France.

1.6. Thesis Outline

The work in this thesis has been divided into seven chapters:

Chapter 1 is the introduction for the thesis. It puts the context of this work among other related research, and gives the main objectives of this research and proposed outline of the methodology.

Chapter 2 is the literature review chapter. It contains brief introduction to remote sensing and the classification procedure for the multi-spectral images. Since it has been decided to use multi source data for the classification, it is anticipated that the pre-processing step is very important to minimize the potential inconsistency between the data sources. Therefore, in order to minimize the atmospheric effects on the Landsat ETM+ image a more in depth literature review on the atmospheric correction is conducted and presented in this chapter. The classification techniques are discussed in detail after that to emphasize the problems encountered in supervised and unsupervised classifications. The most popular classification techniques are described and their merits and demerits are highlighted. A combination of the most suitable methods presented in this chapter will be used for developing the methodology proposed in this work in the light of the data available.

Chapter 3 describes in detail all the data sources available including the satellite imagery, the aerial photography, the landlines and the agricultural census data. The problems in each data set were highlighted especially the inconsistent pixels location and size in the multi-temporal MODIS images. In this chapter all the data sources available have been geo-referenced to the same projection system, the British National Grid (BNG) coordinated system. The accuracy of this co-registration is vital to the success of data fusion techniques.

Chapter 4 presents the detailed analyses of the Landsat ETM+ data. This includes the atmospheric correction and the semi-supervised classification method that has been proposed to overcome the problem of insufficient ground truth and to fulfil the first objective in this work (section 1.5) about developing a methodology for classifying the Landsat image in the case of insufficient ground truth. The second objective is also achieved in this chapter by integrating the Land-Line.Plus data with the Landsat ETM+ image to obtain a per-parcel classification.

Chapter 5 includes the data fusion techniques for multi-temporal and multi-resolution satellite images. In this chapter a multi-temporal spectral signature for the land cover classes were derived using the multi-temporal MODIS images and the classification of the Landsat ETM+ image. This chapter is considered as the corner stone for the next chapter.

Chapter 6 the methodology for the integration of multi-temporal with multi-scale multi-source data has been developed. In this chapter the per-parcel classification of the medium spatial resolution Landsat ETM+ image obtained in the fourth chapter, the multi-temporal signature of each land cover class derived in the fifth chapter and the multi-temporal coarse resolution MODIS images are used altogether to improve the per-parcel classification of ETM+ image. To this end the main third objective of this research will be achieved.

Chapter 7 summarise the results obtained from each chapter and bring forward the recommendations and future research works.

Chapter 2

Review of Image Processing Techniques for Land Cover Classification

2.1. Introduction

Thematic maps are a representation of the real world that contain both a spatial and attribute components. They are an important scientific tool in natural resource science, and are mainly produced by means of field surveying, aerial photography, and remote sensing data in photographic form. They are made for a specific purpose and portray information using some system of classification for the landscape (soil taxonomy, vegetation classes, land use, etc.). Analyses and models based on such maps often influence policy and management decisions.

Remote sensing data in digital form have been used widely to generate thematic maps. These can be presented as either digital raster data derived from image classification, or simply as cartographical images.

Classification is a mapping process from a discrete or continuous feature space X to a discrete set of labels Y. In remotely sensed data classification involves a set of generalisation processes. In essence, reality is simplified or reduced to a limited set of classes, relevant for the application being considered, and having a spatial representation in a map or in a digital spatial data structure. The class can be either spectral class which includes pixels with similar grey level vectors in feature space, or information class that is specified by image analyst based on a classification scheme. Thus, image classification can be defined as a process of assigning an individual pixel or a group of pixels (object)

in an image, to one of a number of classes. As a result of image classification, a thematic map can be generated.

Many studies indicate the lack of high quality land cover maps (Elgy *et al.*, 1993). The classification of remotely sensed images offers an excellent opportunity of obtaining such maps, yet its quality is often questionable. This research concerns the possible improvement of the classification of remotely sensed data. The hypothesis being tested is that it is possible to increase the information content of the classified image by using a variety of data sources.

This chapter is mainly concerned with the background literature about image classification procedures. After a brief introduction to the principal of remote sensing, a general procedure for classification is presented. This is followed by an extended discussion on the most popular classification algorithms and evaluates their performance.

2.2. Introduction to remote sensing

In physics each material interacts with electromagnetic energy by reflecting, absorbing or transmitting it. The exact nature of that interaction varies from one wavelength to the other. This is usually referred to as the Spectral Response Pattern (SRP). In the early days of remote sensing, it was hoped that the earth surface material could be detected and identified from its distinctive spectral response patterns. Thus, the fundamental concept of remote sensing is to find some area of the electromagnetic spectrum in which the nature of that interaction is distinctively different from that of other materials.

Therefore, remote sensing can be defined as a process in which the interactions between earth surface materials and electromagnetic energy emitted by the sun is measured without being in contact with the surface. However, other energy sources are also available, such as sonar. For some wavelengths the energy emitted directly from the surface is measured, such as thermal infrared, rather than relying on the interaction with energy from an independent source (Eastman, 2001).

The energy can be measured by sensors which in turn can be divided into two broad groups passive and active. Passive system generally consists of an array of small sensors or detectors which record the amount of electro-magnetic radiation reflected and/or emitted from the Earth's surface. A multi-spectral scanner is an example of a passive system. An active system propagates its own electro-magnetic radiation and measures the intensity of the return signal. Synthetic Aperture Radar (SAR) is an example of an active system. The majority of satellite remote sensing is done with passive sensors, for which the sun is the major energy source.

Photography is an excellent example of satellite remote sensing image. However, there are two major differences between satellite multi-spectral images and panchromatic or colour photography. First, the former covers a wider range of the electromagnetic spectrum. It can measure energy at wavelengths invisible to the eye such as near-infrared, thermal infrared and radio wavelengths. Second, most remote sensing instruments record these different wavelengths at the same time, yielding not one (or three from colour photography) but numerous images of the same location on the ground, each corresponding to a different range of wavelengths called a band. For example, the

Enhanced Thematic Mapper Plus instrument (ETM+) on board the Landsat7 satellite has seven bands in the visible, near-infrared, mid-infrared and thermal-infrared wavelengths, as well as a fine-resolution panchromatic band that record the energy reflected over the green to near-infrared wavelengths. Therefore, a single ETM+ image does in fact consist of eight separate images or bands, each corresponding to a different part of the electromagnetic spectrum.

Even though the imaging system records the reflected and/or emitted energy in tens or even hundreds of very narrow bands (hyperspectral sensors), there is still a common problem of identifying all the materials that may exist in the image. Eastman (2001) has pointed out four main reasons that hinder the process of identifying the earth surface materials from remotely sensed images as follow:

- It is difficult to determine a consistent distinctive spectral response pattern. For example, due to the chronological changes throughout the growing season, most of the vegetation types can have highly variable responses.
- Changes in illumination (because of slope or the time of the year) and moisture variations can lead to significantly different spectral response patterns.
- Most land cover consists of mixtures of elementary features that are sensed as single pixels. For example, a row crop such as maize actually contains a mixture of plant and soil as sensed by a satellite. Likewise, a pixel may contain a mixture of conifers and deciduous species in a forest area.
- For a given sensor, there is no guarantee that the wavelengths in which it senses, will be the same as those in which a material is most distinctive.

Consequently, it is common practice to extract the spectral response for the land cover materials from the image itself rather than relying on the spectral libraries for different land cover types. The main reason for this is that the spectral libraries have been created under laboratory conditions, which may differ from the environmental condition. Further, the natural variations in land cover materials make it difficult to match the spectral signatures from the image with the spectral libraries. As a consequence, field work still represents the main way of enabling the interpretation of remotely sensed images.

2.3. General classification procedure

Deriving land cover from satellite images requires at first the right choice of image data. The most widely used type of imagery is multispectral data with a resolution between 20 and 30m, such as SPOT and Landsat ETM+ images. Multispectral data are a prerequisite for the differentiation of the required land cover types based on their different spectral reflections, but it may not guarantee the success of classifying the land cover accurately.

There is an increasing use of panchromatic data with a spatial resolution between 5 and 15m (such as IRS-1C/D PAN or Landsat7 ETM+ PAN), or even finer spatial resolution, such as Ikonos. These data can be combined with the multispectral data to improve their spatial resolution. The final scale of any derived map will depend on the image data used. According to Dekker (2003), the satellite images give a physical description of the earth's surface (materials, surface roughness and structure), while most maps give a functional (socio-economic) description. These descriptions are referred to as land cover and land use respectively and are often mixed up (Barnsley *et al.* 2001, Fisher *et al.* 2005). Examples of land cover are grass, trees, building and asphalt. Examples of land use are

agricultural, residential, commercial and industrial. Most land use classes are composed of several land cover types, and often possessing a wide range relationship between these cover types (Gong and Howarth 1990; Cihlar and Jansen 2001; Fisher *et al.* 2005).

The general procedure for image classification is shown in (Figure 1.1). Each of these steps will be discussed in some detail in the following subsections.

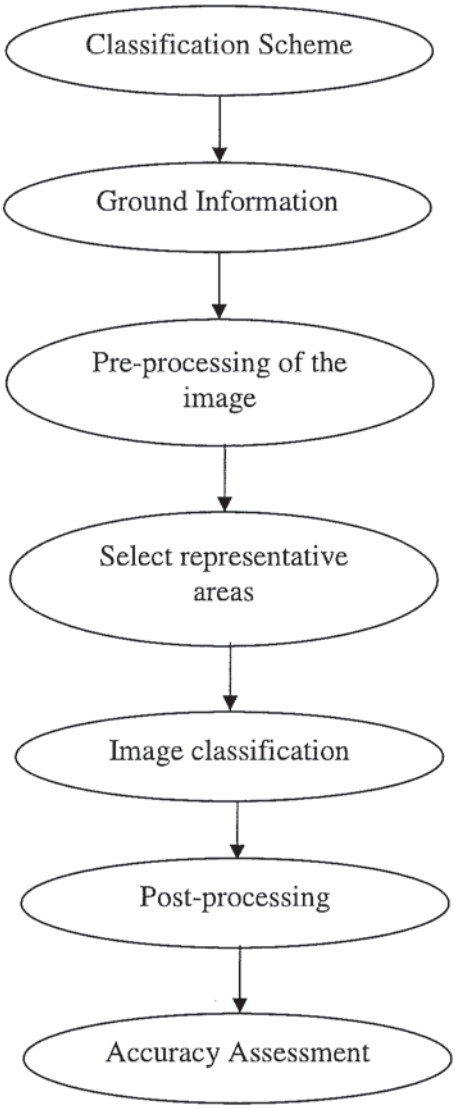

Figure 2. 1: General procedure for image classification

2.3.1. Classification Scheme

A classification scheme is usually a set of related information classes, such as urban, agriculture, forest areas, etc. A number of classification schemes have been set up for use with remote sensing imagery, usually providing a hierarchical structure, where the degree of detail increases with the level of the hierarchy. Well-known nomenclatures are the one from the USGS (United States Geological Survey) (Anderson, *et al.*, 1976) and the CORINE land cover nomenclature from the EC (Table 1.1, source: EC, 1993). Vegetation cover can be classified in a number of ways depending on the application. A classification system aims to separate types of vegetation into groups according to certain characteristics of the plants. For example, the cover types used by the Meteorological Office Surface Exchange Scheme (MOSES) in the Unified Model (UM) is: broadleaf tree, needle leaf tree, C3 grass, C4 grass, shrub, bare soil, urban, water, and ice.

The hierarchical structure of the CORINE land cover system is very useful and may help in the classification procedure. Thus, in this work, a hierarchy system will be followed to separate land cover discernible in the satellite imagery. However, it may not be possible to define the land cover classes to the third level in the hierarchy since the spectral signature for the classes at this level may not distinguishable from the satellite imagery.

Table 2.1: CORINE Land Cover Nomenclatures (source: EC, 1993)

Level 1	Level 2	Level 3
1. Artificial surfaces	1.1. Urban fabric	1.1.1. Continuous Urban Fabric
		1.1.2. Discontinuous urban fabric
	1.2. Industrial commercial and transport units	1.2.1. industrial or commercial units
		1.2.2. Road and rail networks and associated land
		1.2.3. Port areas
		1.2.4. Airports
	1.3. Mine, dump and construction	1.3.1. Mineral extraction Sites
		1.3.2. Dump sites
		1.3.3. Construction Sites
	1.4. Artificial non-agricultural vegetated areas	1.4.1. Green urban areas
		1.4.2. Sport and leisure facilities
2. Agricultural areas	2.1 Arable land	2.1.1. Non-irrigated arable land
		2.1.2. Permanently irrigated land
		2.1.3. Rice fields
	2.2. Permanent crops	2.2.1. Vineyards
		2.2.2. Fruit trees and berry plantations
		2.2.3. Olive groves
	2.3. Pastures	2.3.1. Pastures
	2.4. Heterogeneous agricultural areas	2.4.1. Annual crops associated with permanent crops
		2.4.2. Complex cultivation patterns
		2.4.3. Land principally occupied by agriculture with significant areas of natural vegetation
		2.4.4 Agro-forestry areas
3. Forests and semi natural areas	3.1. Forest	3.1.1. Broad leaved forest
		3.1.2. Coniferous forest
		3.1.3. Mixed forest
	3.2. Shrub and/or herbaceous vegetation associations	3.2.1. Natural grassland
		3.2.2. Moors and heathland
		3.2.3. Sclerophyllous vegetation
		3.2.4. Transitional woodland shrub
	3.3. Open spaces with little or no vegetation	3.3.1. Beaches, dunes and sand planes
		3.3.2. Bare rock
		3.3.3. Sparsely vegetated areas
		3.3.4. Burnt areas
		3.3.5. Glaciers and perpetual snow
4. Wetlands	4.1. Inland wetlands	4.1.1. Inland marshes
		4.1.2. Peat bogs
	4.2. Coastal wetlands	4.2.1. Salt marshes
		4.2.2. Salines
		4.2.3. Intertidal flats
5. Water bodies	5.1 Inland Waters	5.1.1. Water courses
		5.1.2. Water bodies
	5.2. Marine waters	5.2.1. Coastal lagoons
		5.2.2. Estuaries
		5.2.3. Sea and ocean

2.3.2. Field Work

The second step in the classification procedure is to conduct field studies in order to collect ground information and other ancillary data for the study area. Though this is the most important step in the classification procedure, yet it is the most costly, laborious and time consuming. In this stage ground truth data are obtained for use in the training stage of a supervised classification. Ideally, the ground truth for the agricultural areas must be collected on the same day as the imagery. However, this may not be possible for a large area. Therefore, at least the ground truth should be collected before any major changes can happen in the status of the land cover captured, relative to the time of the imagery. Unfortunately, in many situations only the archived images are available with no related ground truth data. In this case it is very hard to conduct a supervised classification or to interpret the results of an unsupervised classification.

2.3.3. Pre-Processing of Remotely Sensed Data

The pre-processing of the image (see Figure 2.1) includes image enhancement, radiometric, atmospheric, geometric and topographic corrections. However, these processes may alter the information content in the original image and thus may affect the resulting classification. However, in some cases it is necessary to perform this step. For example if one wants to classify an image using training data from another image captured on a different date, then radiometric and atmospheric corrections are essential to bring both images to a similar scale of DN values. The atmospheric correction is one of the most important steps in the pre-processing stage. Therefore, section 2.4 is dedicated

to a literature review of atmospheric correction, to highlight its necessity and how it can be applied to remotely sensed images.

2.3.4. Training Stage

In order to define the idealised representation of the classes, some appropriate areas on the image must be selected. This helps in defining some key discriminating features of the existing classes. The analyst may use the extracted training data at the classification stage to perform a supervised classification.

2.3.5. Classification Stage

After the determination of the discernable classes from the imagery, an image classification algorithm is used. Depending on the availability of the training data, classification algorithms are divided into supervised and unsupervised classifiers. Since the classification stage is the most important part in the body of the classification procedure, and the selection of the classification algorithm may influence the results of the output classification map, a detailed discussion on image classification will be presented in section 2.5.

2.3.6. Post-processing Stage

The post-processing can improve classification results considerably. Isolated pixels with other class assignment within a large homogenous area are assigned to this class or mixed pixels at the border between classes are assigned to the dominant class using simple filters.

2.3.7. Accuracy Assessment

Accuracy assessment comes as the final stage in the classification procedure (Figure 2.1), where a comparison between the classification results and ground truth is performed. This step is important for evaluating the utility of any map produced. Conducting a proper accuracy assessment of a land cover map derived from remotely sensed data can be time consuming and costly. Typically, the accuracy assessment provides an overall accuracy and the accuracy of each class. This is because some classes can be mapped more accurately than other classes: for example, water bodies can be classified more accurately than a vegetation class. More detailed discussion on accuracy assessment can be found in Arora *et al.* (2005).

2.4. Atmospheric correction

Two of the most common uses of remotely sensed images are the mapping of the land cover by means of image classification and the study of land cover changes through change detection. These remotely sensed data are usually not ready for direct use, but require to go through a series of pre-processing steps in which atmospheric correction is often a primary concern. This is mainly because, for multi-temporal or multi-spatial classification the variation in the spectral signature for the same land cover must be minimized.

Many methods for atmospheric correction were found in the literature. Thus, the main objective of this section is to understand the concepts behind the atmospheric correction process and to identify an appropriate correction algorithm from the literature.

2.4.1 The necessity of atmospheric correction

The radiance measured by optical remote sensing systems over a given ground feature is influenced by changes in illumination, atmospheric conditions, viewing geometry, and instrument response characteristics. These affect the ability to accurately estimate physical properties of the surface (e.g., soil moisture and biomass) from remotely sensed imagery. In many cases this can reduce the accuracy of land cover classifications and change detection algorithms (Kufman, 1985; Carlotto, 1999). Furthermore, a very large percentage of the imagery recorded by optical instruments is severely contaminated by haze, aerosols, clouds, and cloud shadows. As the processing applied to these images become more quantitative, the precise retrieval of surface reflectance becomes more and more vital. The procedure for retrieving surface reflectance is usually called atmospheric correction. This allows for improved evaluation of satellite imagery, especially for multi-temporal datasets, for different applications such as change detection, classification, crop yield estimation and environmental monitoring (Richter, 1996a).

The objective of the atmospheric correction is to retrieve the surface reflectance from remotely sensed imagery by removing the atmospheric effects. It has been demonstrated (Fraser *et al.*, 1977; Fraser and Kaufman, 1985; Richter, 1996b) that atmospheric correction can significantly improve the data analysis and image classification. For studying the changes in the reflectance of ground objects at different times or locations, it is usually necessary to apply a sun elevation correction and an earth-sun distance correction. Both of these corrections ignore topographic and atmospheric effects (Lillesand and Kiefer, 2000). The multi-temporal scenes recorded under diverse atmospheric conditions can better be compared after atmospheric correction; changes

observed will be due to changes on the earth's surface and not due to different atmospheric conditions (Richter, 1996b). Similar spectral bands from different sensors (e.g. Landsat ETM+: band 4, MODIS\Terra: band 2) can be compared if the images are corrected for atmospheric effects. This is a particular advantage for multitemporal monitoring, as the probability of getting data with low cloud coverage will increase with the number of sensors. The results of classification and change detection algorithms can also be improved if careful consideration of the sensor calibration aspects is taken into account (Fraser and Kaufman, 1985). The surface reflectance data retrieved from satellite imagery may be compared with ground measurements, thus providing an opportunity to verify the results.

Atmospheric correction has received substantial attention from researchers in remote sensing, who have devised a number of atmospheric correction approaches. The more complicated approaches are computationally demanding and have only been validated on a very small scale (Fallah-Adl *et al.*, 1995), furthermore they may not necessarily lead to an improved performance in classification and change detection. For certain applications it may not be necessary to derive the surface reflectance. The top of atmosphere (TOA) radiance may be acceptable provided the atmospheric condition over the whole image is uniform (Liang *et al.*, 2001) or a simple dark object subtraction may be all that is required (this may be applied with or without a Rayleigh atmosphere correction due to the molecular scattering (Schroeder and Fischer, 2003)), or relative atmospheric correction (Song *et al.*, 2001). Under the assumption of a horizontally homogeneous atmosphere the classification is not affected by atmosphere correction. A number of studies (Potter, 1974; Fraser et al., 1977; Kawata *et al.*, 1990) showed that the atmospheric correction has little

effect on classification accuracy of a single date image as long as the training data and the data to be classified are in the same relative scale.

For Landsat ETM+ data, the dominant atmospheric effect is scattering, which has an additive effect on the remotely sensed signals. Multiplicative effects from absorption are often neglected because the Landsat ETM+ bands were selected to avoid these effects (Song *et al.*, 2001).

Thus atmospheric correction for a single date image is often equivalent to subtracting a constant from all pixels in a spectral band. The unnecessary nature of atmospheric correction on classification with single date image can be extended to post-classification change detection (Singh, 1989) where multiple images are classified individually and the resulting maps are compared to identify changes (Foody *et al.*, 1996). In essence, if the spectral signatures characterizing the desired classes are derived from the image to be classified, atmospheric correction is unnecessary (Song *et al.*, 2001).

However, it is necessary to correct atmospheric effects before classification and change detection in many other situations, for example, if one wants to use the normalized difference vegetation index (NDVI) in the classification procedure. This is because different bands may interact differently with the atmosphere. The NDVI is often used to monitor vegetation dynamics (Sader, 1987; Pax Lenney *et al.*, 1996; Michener and Houhoulis, 1997) and can be calculated using Equation 2.1:

$$NDVI = \frac{\rho_{IR}^{Surf} - \rho_{R}^{Surf}}{\rho_{IR}^{Surf} - \rho_{R}^{Surf}} \qquad \textbf{Equation 2. 1}$$

where ρ_R^{Surf} and ρ_{IR}^{Surf} are the land surface reflectance in the red and infrared spectral bands, respectively. Considering the atmospheric effects, Equation (2.1) using TOA reflectance value should be written as:

$$NDVI = \frac{(TOA_{IR} - TOA_R) - (A_{IR} - A_R)}{(TOA_{IR} + TOA_R) - (A_{IR} + A_R)} \qquad \textbf{Equation 2. 2}$$

where A_R and A_{IR} are the additive atmospheric effects for the red and infrared, respectively. Equation (2.2) indicates that the atmospheric effects contaminate NDVI value and that the modification is non-linear. For satellite observations of a vegetated area reflectance in the red band at the top of the atmosphere will be larger than its surface counterpart, due to the effects of multiple scattered radiation occurring within the atmosphere. In the infrared, however, the TOA reflectance is generally similar in value to its surface counterpart. Thus, the NDVI computed using the TOA radiances can be considerably smaller for a densely vegetated area than the corresponding NDVI computed using the surface reflectance. Myneni and Asrar (1994) found that the NDVI at the top of the atmosphere is always smaller than that at the top of the canopy from simulations using a vegetation/atmosphere radiative transfer model. Contributions from the atmosphere to NDVI are significant (McDonald *et al.*, 1998) and can amount to 50% or more over thin or broken vegetation cover (Verstraete, 1994). Similarly, the simple ratio (SR) vegetation index ($\rho_{IR}^{Surf} / \rho_R^{Surf}$) is contaminated by the atmosphere.

In general, whether atmospheric correction is needed or not, depends on the information to be extracted from the image and the analytical methods used to extract the information. For applications where a common radiometric scale is assumed among the multitemporal

or multisensor images, atmospheric correction should be taken into consideration in pre-processing. The effect of the atmosphere can prevent the proper interpretation of the images if it is not taken into account (Verstraete, 1994), while choosing the most suitable correction approach one should also consider the remote sensing and atmospheric data available (Song *et al.* 2001).

2.4.2. Theory of atmospheric correction

At this point it is worth clarifying some of the terminology used in the literatures for atmospheric correction. The term radiance refers to any radiation leaving the earth (i.e. upwelling, toward the sensor). A different term, irradiance, is used to describe downwelling radiation reaching the earth from the sun.

The images from the optical sensors on board the satellites mapping the land surface are strongly depend on the atmospheric conditions and the solar zenith angle. Digital sensors record the intensity of the electromagnetic radiation (ER) from each spot viewed on the Earth's surface, as a digital number (DN) for each spectral band. The exact range of DN that a sensor utilises depends on its radiometric resolution. For example, a sensor such as Landsat MSS (Multi-Spectral Scanner) measures the radiation in a 6-bit DN scale, whilst Landsat ETM+ measures it on an 8-bit scale, even though the actual radiometric resolution of the sensor is often less than 8-bit. For example if the actual DN range has only 128 levels then one may consider the data to have a 7-bit range.

The DN values recorded by a sensor are proportional to the upwelling ER, and contains information about solar radiance reflected at the ground and scattered by the atmosphere. To infer the spectral properties (reflectance) of the earth's surface, the atmospheric

influence has to be eliminated. The radiation is affected by two processes: absorption which reduces its intensity, and scattering which alters its direction.

Scattering and absorption create an overall effect of "haziness" which reduces the contrast of the image. Scattering and absorption by aerosols are difficult to characterize due to their variation in time and space (Kaufman, 1993), and they therefore constitute the most severe limitation to the radiometric normalization of satellite data (Coppin and Bauer, 1994; Liang *et al.*, 1997). Absorption occurs when electromagnetic radiation interacts with gases, such as water vapour, carbon dioxide and ozone. Scattering results from interactions between ER and both gas molecules and airborne particulate matter (aerosols), which may range in size from the raindrop ($>100\,\mu m$) to the microscopic ($<1\,\mu m$). These aerosols will redirect incident electromagnetic radiation from its path. Further, the reflected energy from the earth surface may also be affected by the scattering problem, with the consequence that dark areas surrounded by bright areas appear brighter to the remote observer than to the near observer (adjacency effect). Hence, the radiance recorded for a given pixel partially incorporates the scattered radiance from neighbouring pixels. Therefore, the atmospheric influence modifies the spectral information of the earth's surface and also degrades the spatial resolution of the sensors (Richter, 1996a).

The majority of image processing has been based on raw DN values (Fraser *et al.*, 1977) in which actual spectral radiances are not of interest (e.g. when classifying a single satellite image). However, the spectral signature of a land cover is not transferable if measured in digital numbers. The values are image specific (i.e. they are dependent on the viewing geometry of the satellite at the moment the image was taken) and are a

function of the location of the sun, the specific weather conditions pertaining, and so on. It is generally far more useful to convert the DN values to spectral radiance units, as it has two great advantages. Firstly, a spectral signature with meaningful units can be compared from multi-temporal / multi-sensors images. Second, the libraries of spectral signatures, which contain lists of land cover and their reflectance, can be used more effectively to analyse remotely sensed images.

The spectral radiance unit is $wm^{-2}ster^{-1}\mu m^{-1}$. That is, the rate of transfer of energy (Watt, w) recorded at a sensor, per square metre on the ground, for one steradian (the three dimensional angle from a point on Earth's surface to the sensor), per unit wavelength measured in microns μm ($1\times10^{-6} meter$).

The spectral radiance of features on the ground is usually converted to reflectance, which is the ratio of upwelling to downwelling radiation. This is because spectral radiance will depend on the degree of illumination of the object (i.e. the irradiance). Thus spectral radiances will depend on such factors as time of day, season, latitude, etc. Since reflectance represents the ratio of radiance to irradiance, it does not have units and provides a common measure which is directly comparable between images independent of space and time.

2.4.3. The concept of atmospheric correction

The sensor receives radiance reflected directly from the target, together with radiant energy scattered by the atmosphere. The relationship between the at-satellite spectral

radiance and the surface reflectance for a uniform flat lambertian surface and a cloudless atmosphere can be expressed by the formula (Liou, 1980; Kaufman and Sendra, 1988):

$$L_{sat} = \frac{\rho}{\pi(1-s\rho)} F_d T_v + L_p \qquad \textbf{Equation 2. 3}$$

where

L_{sat} is spectral radiance at sensor aperture in $wm^{-2}ster^{-1}\mu m^{-1}$.

L_p path radiance in $wm^{-2}ster^{-1}\mu m^{-1}$.

ρ surface reflectance.

s spherical albedo of the atmosphere (that is the fraction of the upward radiation back scattered by the atmosphere to the surface).

F_d is the incoming irradiance received at the surface in ($wm^{-2}ster^{-1}\mu m^{-1}$). The irradiance from the sun decrease as the square of the earth-sun distance, and the combined influence of solar zenith angle and earth-sun distance F_d can be expressed as $F_d = \frac{E_0 \cos(\theta_z) T_z}{d^2} + E_{down}$. Here E_{down} is the downwelling diffuse irradiance; and E_0 is the exoatmospheric solar irradiance at mean earth-sun distance; T_z the atmospheric transmittance in the illumination direction; θ_z the solar zenith angle, and is calculated by subtracting the sun elevation from 90^0 ($\pi/2$); and d is the earth-sun distance in astronomical units*.

T_v is the atmospheric transmittance from the target toward the sensor.

All quantities depend on wavelength. Since the field of view of the satellite sensor is small, it is assumed that the atmospheric conditions within each individual scene are constant. Thus, the correction factor is a constant for each channel of the dataset. Only the first term in equation 2.3 contains valid information about ground reflectance. The second term represents the scattered path radiance, which introduces haze in the imagery and reduces image contrast (Lillesand and Kiefer, 2000). Since s is small in Equation 2.3, it can be neglected, and subsequently solving for ρ we get:

* Astronomical Unite (AU) is a unit of distance approximately equal to the mean distance between earth and sun. The currently accepted value of the (AU) is 149 597 870 691 ± 30 meters (about 150 million kilometers or 93 million miles. (Wikipedia, the free encyclopedia).

$$\rho = \frac{\pi(L_{sat} - L_p)}{F_d T_v}$$ **Equation 2. 4**

In order to calculate ρ from equation 2.4, it is easier to split the calculation into three steps: first, convert DN to spectral radiance L_{sat}; second, convert spectral radiance to apparent reflectance; third, eliminate the atmospheric effects due to absorption and scattering.

2.4.4. Conversion of DN to spectral radiance

The at-satellite spectral radiance L_{sat} can be obtained by converting the digital number (DN) in the image to spectral radiance. Prior to the launch of a sensor, the relationship between measured spectral radiance and DN is determined. This is known as the sensor calibration. Most simple approaches assume that detectors and data systems are designed to produce a linear response to incident spectral radiance resulting in a linear radiometric response function (Forster, 1984; Köpke, 1989; Richter, 1990). Each spectral band and detector of the sensor has its own response function, and its characteristics are monitored using onboard calibration lamps. The absolute spectral radiance output of the calibration sources is known from pre-launch calibration and is assumed to be stable over the life of the sensor. Thus, the onboard calibration sources form the basis for constructing the radiometric response function by relating known radiance values incident on the detectors to the resulting DNs. A linear fit to the calibration data results in the following relationship (Lillesand and Kiefer, 2000):

$$L_{sat(\lambda)} = Bias_{\lambda} + (Gain_{\lambda} * DN)$$ **Equation 2. 5**

where:

DN : digital number value.

$Gain_\lambda$: slope of response function (channel gain at wavelength λ).

$L_{sat(\lambda)}$: spectral radiance measured over the spectral bandwidth of the channel of wavelenght λ.

$Bias_\lambda$: intercept of response function (channel offset).

The header or calibration file contained in the Fast Format of a Landsat image stores the gains/biases for each spectral band in the form of L_{max} (minimum radiance required to generate the maximum DN, i.e. the radiance at which the channel saturates), and L_{min} (the spectral radiance corresponding to the minimum DN response). The minimum and maximum DN depend on the radiometric resolution of the sensor. For 8-bits resolution there are 256 levels, so DN_{min} can be 0 or 1 and DN_{max} is 255 or 256 respectively. In the case of DN_{max}=255, the gain and bias are:

$$Gain = \frac{L_{max} - L_{min}}{255} \qquad \textbf{Equation 2. 6}$$
$$Bias = L_{min}$$

Equation (2.5) can be used to convert any DN in a particular band to absolute units of spectral radiance in that band if L_{max} and L_{min} are known from the sensor calibration.

2.4.5. Conversion of spectral radiance to apparent reflectance

The apparent reflectance, which for satellite images is called the exoatmospheric reflectance ρ^*, relates the measured radiance, L_{sat}, to the solar irradiance incident at the top of the atmosphere, and is expressed as a value between 0 and 1 (Markham and Baker, 1985):

$$\rho^* = \frac{\pi L_{sat(\lambda_i)} d^2}{E_{0(\lambda_i)} \cos\theta_z}$$ **Equation 2. 7**

where ρ^*, $L_{sat(\lambda_i)}$ and $E_{0(\lambda_i)}$ are unit-less planetary reflectance at the satellite, spectral radiance at sensor aperture, and extraterrestrial solar irradiance respectively (Slater *et al.* 1987; Price, 1989; Richter, 1996a), λ_i is the centre wavelength of the considered band, θ_z is the solar zenith angle which is normally part of the ancillary data supplied with the digital data (Lillesand and Kiefer, 2000), and d^2 is the square of the Earth-Sun distance in astronomical units, and is calculated as (Cracknell and Hayes, 1993):

$$d^2 = \left(1 - 0.01674\cos[(2\pi/365.25)(JD-3)]\right)^2$$ **Equation 2. 8**

where JD is the Julian Day (day's number of the year) of the image acquisition.

2.4.6. Removal of atmospheric effects

Atmospheric correction algorithms basically consist of two major steps: parameter estimation and surface reflectance retrieval. In the first step, the optical characteristics of the atmosphere are estimated either by using special features of the ground surface, or by direct measurements of the atmospheric constituents (Kaufman, *et al.*, 1994), or by using theoretical models, such as Radiative Transfer Codes (RTCs) (Fallah-Adl *et al.*, 1995; Richter, 1996a; Vermote *et al.*, 1997). In the latter various quantities relating to the atmospheric correction can be computed, given the atmospheric optical properties.

All methods reported in the literature to minimise atmospheric effects can be roughly classified into the following three groups: atmospheric modelling, regression-based method and dark pixel subtraction. The first two methods require numerous

measurements to be made at the time of the overpass, while method three may be affected by noise in the dataset and may lack suitable dark pixels in the image. Each approach will not be reviewed comprehensively, but understanding the advantages and limitations of the representative algorithms may be helpful.

2.4.6.1. Atmospheric modelling

Atmospheric modelling is perhaps the most sophisticated method used to compensate for atmospheric absorption and scattering. A number of radiative transfer codes (RTCs) based on radiative transfer theory have been developed to correct for atmospheric effects in satellite images (Kneizys *et al.*, 1988; Haan *et al.*, 1991), e.g. Second Simulation of the Sensor Signal in the Solar Spectrum (6s) radiative transfer code (Vermote *et al.*, 1997). The model predicts the apparent (exoatmospheric) reflectance at the top of the atmosphere ($\overline{\rho^*}$) using information about the surface reflectance and atmospheric conditions. Since the true apparent reflectance (ρ^*) can be calculated from the sensor calibration and exoatmospheric irradiance ($E_{0(\lambda_i)}$), the model can be inverted to predict the true surface reflectance (ρ).

Studies have shown that these RTCs can accurately convert the satellite measurements to surface reflectance (Holm *et al.*, 1989; Moran *et al.*, 1992). However, some pixels, primarily those over deep water areas, may have values which are very small negative numbers. This can be quite a common occurrence in radiometric correction and shows that the atmospheric correction is not necessarily precise, particularly when inputs to the radiative transfer code are limited. Ideally, modelling approaches are best used when

accurate measurements of ground condition and actual atmospheric properties in effect at the time of the satellite overpass are available. However, the required measurements are numerous and must be done for each spectral band. It is unlikely therefore, that there will be a ground network providing these daily measurements, which makes routine atmospheric correction of images difficult with RTCs. Many applications of remote sensing have to rely on algorithms that utilize information derived from the image itself to correct for atmospheric effects.

There is no way to correct the gaseous absorption (water vapour, ozone and aerosols) directly from Landsat ETM+ imagery itself unless certain ancillary information is available (Liang *et al.*, 2001). However, with the recent launch of MODIS on Terra platforms, a daily data measurement of atmospheric optical properties can be provided (MOD04_L2, MOD05_L2, and MOD07_L2), from which several atmospheric parameters are obtained, such as the optical depth, water vapour and ozone content.

2.4.6.2. Regression intersection method

Crippen (1987) developed an atmospheric correction method using a regression technique. In this method, known reflectance values for some surface materials of contrasting spectral properties are compared with the sensor recorded radiance values. A regression line is then calculated for these different surface materials. Since two spectrally different materials can only be equal at zero, the intersection of the lines represents the point of zero ground reflectance. Atmospheric scattering however will offset this intersection point. The correction factor therefore is the "measured displacement of the hypothetical zero ground radiance pixels from the zero data number

position on the graph" (Crippen, 1987). To determine the correction factor, training sets representing homogenous land cover types should yield regression lines that intersect in two-dimensional space.

2.4.6.3. Dark pixel subtraction

The Dark Object Subtraction (DOS) is perhaps the simplest and most widely used image-based absolute atmospheric correction approach for classification and change detection applications (Spanner *et al.*, 1990; Ekstrand, 1994; Jakubauskas, 1996; Huguenin *et al.*, 1997). This approach assumes the existence of dark objects, with zero or small surface reflectance, within the image scene and a horizontally homogeneous atmosphere. Due to the atmospheric scattering effects, a dark object is not absolutely dark (Chavez, 1988). The minimum DN value in the histogram from the entire scene is thus attributed to the effect of the atmosphere that needs to be factored out of the data set (Chavez, 1989). The accuracy of this method is compromised by noise within the data set and requires suitable dark pixels to exist somewhere in the image. Assuming 1% surface reflectance for the dark objects (Chavez, 1989, 1996; Moran *et al.*, 1992, Song *et al.* 2001), the path radiance is estimated as:

$$L_p = Gain * DN_{\min} + Bias - 0.01[E_0 \cos(\theta_z)T_z + E_{down}]T_v / \pi \quad \textbf{Equation 2. 9}$$

More sophisticated algorithms derive atmospheric optical properties from dark objects in the image, and then correct the images using the derived information. Ahern *et al.*, (1977) and Gordon (1978) used clear water as the dark object to derive atmospheric optical information for radiometric normalization.

Kaufman *et al.* (1997) proposed a new approach using dense dark vegetation (DDV). The DDV approach assumes the existence of dense dark vegetation in the scene, which can be used as a dark object for the blue (TM 1) and red (TM 3) channels. The Landsat TM 7 ($2.2\,\mu m$) is transparent to most aerosol types (Kaufman *et al.*, 1997). Thus, as an approximation, TM 7 surface reflectance is assumed to be equal to the apparent reflectance at the top of the atmosphere. Kaufman *et al.* (1997) found the following relationships exist between the DDV surface reflectance for channel TM 7 and those of channels TM 1 and 3:

$$\rho_1^{DDV} = \rho_7^{DDV} / 4$$
$$\rho_3^{DDV} = \rho_7^{DDV} / 2 \qquad \textbf{Equation 2. 10}$$

where ρ stands for surface reflectance and the subscripts for the relevant TM channels. Thus, any differences between the apparent reflectance in TM 1 and 3 and the predicted DDV surface reflectance from Equation 2.10 can be attributed to atmospheric path radiance, from which the atmospheric optical depth is estimated. This information can be used by atmosphere radiative transfer codes to retrieve the atmospheric optical depth, which is in turn used to correct the image. Liang *et al.* (1997) implemented this algorithm to correct Landsat TM imagery with a "smart moving window", in which each pixel in the image was corrected according to the dense dark vegetation surface reflectance within the window or neighbouring windows. The dense dark vegetation can be identified where $\rho_7^* \le 0.05$ and $NDVI > 0.1$ (Song *et al.*, 2001).

More recently, Wen *et al.* (1999) used the Path Radiance (PARA) technique that evolved from DDV. This is based on the relationship that the apparent reflectance of visible and

mid-IR bands at the top of the atmosphere, are linearly correlated if the surface reflectance is linearly correlated at the ground level for a horizontally homogeneous atmosphere. For Landsat TM imagery, the following relationships exist:

$$\rho_1 = \rho_1^* + \beta_1\rho_7$$
$$\rho_3 = \rho_3^* + \beta_3\rho_7 \qquad \textbf{Equation 2. 11}$$

where β_1 and β_3 are the slopes of the linear relationships, and ρ_1^* and ρ_3^* are the apparent reflectance due to path radiance from which the aerosol optical depth is retrieved. To reduce the uncertainty in estimating ρ_1^* and ρ_3^*, Wen *et al.* (1999) used the mean apparent reflectance of what appear homogeneous clusters of vegetation identified from TM 7. A homogeneous cluster of vegetation is defined as a 10×10 window whose standard deviation of TM 7 apparent reflectance is less than 0.02. On a scatter plot graph of TM 1 or 3 versus TM 7 for homogenous clusters, only the lower 20% of the lower DN value of the homogeneous clusters were used to determine the linear relationships (Wen *et al.*, 1999).

2.4.7. Conclusion on atmospheric correction

From the previous sections, which reviewed the literature atmospheric correction, it may be concluded that it is necessary to correct the satellite images for atmospheric effects especially if multi-sensor data fusion is to be conducted. Therefore, it was decided to correct the satellite images for the atmospheric effects before pursuing the classification procedure.

Since the atmospheric correction will alter the information content in the satellite images, the literature search for the appropriate correction methods was important in understanding the limitations of each method.

However, because there are no accurate atmospheric data available, it is hard to decide at this stage which correction method of these reviewed, will be most suitable for this study. Therefore, a small experiment was conducted using the available correction methods, to find the one which would minimize the atmospheric effect between the data sources available for this study. This is reported in section 4.2.1.

2.5. Image classification

Depending upon the form of data in hand, classification or interpretation of remote sensing images may be performed either visually or digitally. Visual interpretation is based on human vision and pattern recognition capacities. Human identification of terrain features is based on some interpretation keys such as tone, texture, shadow, site, shape, size, and association (Richards, 1993). This approach is laborious, time consuming and may not produce an accurate classification.

With the advancement in computer technology and the increased used of digital remote sensing data for a variety of applications, digital image processing has gained enormous importance. Most image processing software offer a range of classification algorithms that aim to convert each pixel in the image into one of the representative classes of interest, such as urban, agriculture, forest etc. These algorithms will divide data uniquely, and can have differing results. In the literature, this type of pixel allocation is generally referred to as hard or crisp classification. Recently, however, there has been a trend to

relax this traditional classification into what is called soft or fuzzy classification (Wang, 1990a and 1990b; Maselli, *et al.*, 1996).

2.5.1. Hard classification

In hard classification, each pixel is assumed to possess a homogenous content and is classified to a particular class. In reality, not all pixels may be pure, but consist of a number of land cover classes. Furthermore, the differences in growth stage, soil background and the presence of intercropping make it difficult to create a definitive decision about the classification. Therefore, this technique tends to cause a loss in the pixel's information content (Foody, 1996a) and the output result obtained from a hard classification may not be accurate. All conventional classification algorithms produce crisp classification outputs. It is also important to note that in all probability classifiers, such as the maximum likelihood classifier, the pixel homogeneity is assumed. These classifiers determine the probability that a homogenous pixel belongs to a particular class, and they do not assume that a pixel is made up of a number of cover classes.

2.5.2. Soft classification

In contrast to hard classifiers, soft or fuzzy classifiers produce a soft decision about the identity of each pixel. The output will be in a form of a membership grade to each of the classes being considered. These membership values or grades may be used to determine the mixture of land cover classes. For example, if the membership grade for a pixel is 0.43 deciduous and 0.57 coniferous, then if one could assume that these two classes were the only ones present, it might be reasonable to conclude that the pixel contains 43%

deciduous cover and 57% coniferous (Eastman 2001). Such a conclusion is known as sub-pixel classification.

Other uses of a soft classifier might be to determine the strength of evidence in support of the best conclusion that can be made, or to combine the lines of evidence made to produce a stronger statement of the probability of finding a particular class. For example, one might extract a mapping of the probability that each pixel belongs to an agricultural field land cover class from the spectral data. Subsequently DTM data might be used to develop a map of slopes, from which the probability of not being agricultural fields might be deduced (areas on greater slopes are highly unlikely to be agricultural due to cultivation and soil erosion problems). These two lines of evidence can then be combined to produce a stronger statement of the probability that a particular class exists.

2.6. Supervised classification

Supervised classification involves three distinct stages: training, allocation and testing (Foody, 1995). The first step in undertaking a supervised classification is to define training sites. These are groups of pixels in the input image that correspond to a certain class. The training sites should be homogeneous areas with known class types, for example, bare ground. The DN value of these pixels provide a statistical description of land cover based on a class structure and enable the range of values for each class to be determined. The training samples are usually obtained by fieldwork, from aerial photography or maps, and from expert knowledge.

Once identified, the training area will be delineated on the image using on-screen digitization. To do this the user should choose a band with strong contrast (such as a

near-infrared band) or a colour composite, so that the classes of interest can be seen more clearly to facilitate the digitizing. Good training site locations are generally those with as typical a sample of the information class as possible. For example, if a deciduous forest were to be defined, it would be important to choose an area that was not mixed with conifers, and that had little soil background or understory vegetation visible.

When digitizing training sites it is also important to avoid including any pixels belonging to adjacent land cover. In general, the number of training pixels should be representative and sound if a statistical classification approach will be used. The Idrisi32 Manual (Online: http://www.earth.wvu.edu/earth1/wvu/wvulabs.pdf [2004, April]) suggest that users should aim to delineate enough pixels so that there are at least 10 times as many pixels for each training class as there are bands in the image to be classified. Thus, for a Landsat TM image with six bands, the user should aim to have at least 60 pixels per training class.

If the training areas are selected manually, there is a natural tendency only to choose those areas that are clear and well defined. For example, when delineating wheat fields one may choose only those areas that are in the centre of the field, or healthy growing wheat because there is no doubt about their class. The boundary areas and poorly growing wheat are likely to be ignored. This will give a bias in the statistics since the near infra red bands reflectance may be higher than the average for wheat. To get a truly random and representative sample one must choose the points to be classified before knowing what class they belong to. This way contentious pixels also get included into the training statistics. One solution is to generate random locations in the image, and then

classify those pixels to be used subsequently as training pixels. This approach may reduce the bias in the statistics of training data.

In some instances, it may make sense to define the training data locations by direct reference to ground locations (such as by means of point locations gathered with a GPS). However, this requires very exact prior geo-referencing of the image, and a confidence that positional errors will not include unwanted pixels in the training sites. Under these circumstances, the classification results are limited to the user's ability to identify suitable training areas in the image. This interaction with the analyst makes the supervised classification more subjective than objective. Furthermore, mono-temporal satellite images will only offer information on the status of land-cover at the moment of data capture, and in some cases it will be impossible to obtaining training areas on the same day of image capture.

The classification process followed once suitable training areas have been identified, involves the assignment of these pixels to their appropriate classes. The most commonly used classification method evaluates the likelihood that each pixel belongs to each class based on their spectral and statistical characteristics. Thus, according to the decision rules used, the classifier may be categorized as a parametric or a non-parametric classifier. Parametric rules assign the pixels to the classes based on assumption that the training samples belong to a statistical distribution. Nonparametric decision rules, by contrast, have no assumptions about the distribution of the data in the spectral space (known as feature space). For example, a nonparametric classifier will assign the pixels based on their location in the spectral space either inside or outside a region generated from the

training samples. The following sections present some examples of the more commonly used classification techniques.

2.6.1. Parametric classifiers

The statistically-based classifiers are called parametric because they employ the statistical parameters, mean and covariance, of the training samples. These statistics are the basis of the decision rule used in assigning every pixel in the image to a class (Kloer, 1994).

2.6.1.1. Minimum Distance to Means

For each identified class the mean of the reflectance in each band under consideration is calculated from the relevant training area data. To classify an unknown pixel, the minimum distance classifier examines the distance in the spectral space from that pixel to the mean of each class, and assigns it the nearest class. The distance measure between an unknown pixel and the centroid of each class can be an Euclidean, City-block, or Mahalanobis distance.

Euclidean distance:

$$d_i = \left\| \vec{X} - \vec{\mu}_i \right\|_{L2} = \sqrt{\sum_{j=1}^{b} (x_j - \mu_{ij})^2} \qquad ,i = 1,\ldots,C \qquad \textbf{Equation 2. 12}$$

where: $\vec{X} = (x_1, x_2, \ldots, x_b)$ is the DN value vector in the considered bands of the pixel under examination

$\vec{\mu}_i = (\mu_{i1}, \mu_{i2}, \ldots, \mu_{ib})$ the vector of the mean DN value of the training sample for class (i) in each band (1, 2... b).

b is the total number of bands under consideration.

City Block Distance:

$$d_i = \left\| \vec{X} - \vec{\mu}_i \right\|_{L1} = \sum_{j=1}^{b} \left| x_j - \mu_{ij} \right| \qquad ,i = 1,\ldots,C \qquad \textbf{Equation 2. 13}$$

Mahalanobis distance:

$$d_i = (\vec{X} - \vec{\mu}_i)^T \boldsymbol{Cov}_i^{-1} (\vec{X} - \vec{\mu}_i) \qquad \textbf{Equation 2. 14}$$

where: $\boldsymbol{Cov}_i^{-1}$ is the inverse of the covariance matrix for class (i).

The Euclidian and city block metrics suffer from problems related to signature variability. To overcome this problem the concept of standardized distance may be employed using the following equation (Eastman, 2001):

standardized distance = (original distance - mean) / standard deviation

The mean in this equation refers to the mean of the distances for all samples within a particular class to its centroid. When using the standardised distance this classifier can perform very well, and often outperforms a maximum likelihood procedure whenever training areas have high variability (Eastman, 2001).

Another alternative to account for the variability in the classes is to use the Mahalanobis distance. However, the Mahalanobis distance algorithm assumes that the histograms of the bands in the training samples have normal distributions, which is not always true. Therefore, in this case, the standardized distance may give better classification results.

Finally, the minimum distance classifier is traditionally used to produce a hard classification. It is mathematically simple and computationally efficient. It can employ a maximum distance threshold which allows for any pixels that are unlike any of the given classes, to be left unclassified. However, this classifier is limited by its assumptions and restrictions, and as a consequence, is not widely used.

2.6.1.2. Maximum Likelihood

Maximum Likelihood Classification is the most common supervised classification method (Zenzo, *et al.*, 1987). This classifier relies heavily on the assumption that each spectral class can be described by a probability distribution in multispectral space (Mather, 1999). Such a distribution is usually called the probability density function (pdf) and is also known as the likelihood function. The probability density function describes the chance of finding a pixel belonging to a particular class at any given location in multispectral space (Andrews, 1972). Using the parameters of the pdf, the probability of a pixel belonging to each class is calculated, and the pixel is then assigned to the class for which the probability is the highest.

The distribution found to be of most value is the normal or Gaussian distribution (Williamson, 1996). In a multivariate case, it assumes that each observation consists of a set of measurements in each spectral band. Under the Gaussian distribution assumption, a class can be described by a vector of means and a variance-covariance matrix (Appendix 4). These statistics describe the interrelationships among the measurement variables of the class and are usually determined from a training set of pure pixels (Abkar, 1999).

During the classification with a maximum likelihood decision rule, the unknown pixel is assigned to the class from whose distribution the vector $\vec{X}$ is most likely to be drawn. These probabilities are calculated by evaluating the probability density function (pdf) for each class (c). For a one-dimensional normal distribution (one band) the equation is given by (Weisstein, No date):

$$p(x \mid c) = \frac{1}{\sqrt{2\pi\sigma_c^2}} \exp\left\{-\frac{(x-\mu_c)^2}{2\sigma_c^2}\right\} \qquad \textbf{Equation 2. 15}$$

and for multivariate normal distributions (n bands) it is given by (Azzalini and Capitanio, 1999):

$$p(\vec{X} \mid c) = \frac{1}{(2\pi)^{n/2}\sqrt{|\boldsymbol{Cov}_c|}} \exp\left\{-\tfrac{1}{2}(\vec{X}-\vec{\mu}_c)^T \boldsymbol{Cov}_c^{-1}(\vec{X}-\vec{\mu}_c)\right\} \qquad \textbf{Equation 2. 16}$$

where: $\sigma_c^2, |\boldsymbol{Cov}_c|$ are the variance and the determinant of the variance-covariance matrix of the training sample for class (c) respectively.

In practical applications, Equation (2.16) can be further reduced to following expression by taking the natural logarithm (Tso and Mather, 2001):

$$ln\left[p(\vec{X} \mid c)\right] = \frac{-n}{2} * ln(2\pi) * \frac{-1}{2} ln(|\boldsymbol{Cov}_c|) - \frac{1}{2}(\vec{X}-\vec{\mu}_c)^T \boldsymbol{Cov}_c^{-1}(\vec{X}-\vec{\mu}_c) \qquad \textbf{Equation 2. 17}$$

This equation can be further reduced by dropping the constant term $\frac{-n}{2} * ln(2\pi)$ from the equation and multiplying it by the constant (-2) to become:

$$-ln\left[p(\vec{X} \mid c)\right] = ln(|\boldsymbol{Cov}_c|) + (\vec{X}-\vec{\mu}_c)^T \boldsymbol{Cov}_c^{-1}(\vec{X}-\vec{\mu}_c) \qquad \textbf{Equation 2. 18}$$

It is clear that maximizing the conditional probability in Equation (2.16) is equivalent to minimizing Equation (2.18).

This classifier accounts for the highest variability in classes. Despite the complex equation, which takes a long time to compute and a computation time that increases significantly with the number of input bands, this classifier is widely used. However, the main drawback of this classifier is that it relies heavily on the assumption that the data is normally distributed in each spectral band.

The Maximum Likelihood classifier has generally been used as a technique for providing a crisp classification output. However, the output of a Maximum Likelihood may also be softened to obtain the partial and multiple class membership for each pixel (Wang, 1990a). Here, the measures of strength of class membership, rather than the code of the most likely class of membership, may be the output (Foody, 1996b). Thus, for instance, the a-posterior probabilities from a maximum likelihood classification may reflect to some extent the class composition of a mixed pixel (Foody *et al.*, 1992). The important term here is "may"; there is no reason to suppose that the probabilities give us any insight to the percentages of land cover in a mixed pixel and they may, in fact, be entirely misleading. Indeed, the probabilistic approach of maximum likelihood has already assumed a homogeneous pixel content and is then calculating the probabilities of that content. This is well illustrated if we consider the following example: figure 2.2 shows the hypothetical spectral signatures for 3 land cover classes: bare earth, pine forest and pasture derived from training data. If we now had a pixel consisting of 50% bare earth and 50% pasture then the DN value of that would be about 120. The maximum likelihood

classifier would give probabilities for each land cover of about 0.1% bare earth, 70% pine forest and 0.05% pasture. If we then assumed that these probabilities represented proportions of land cover in the pixel we would have 99.9% pine forest and some tiny proportions of pasture and bare earth. This is clearly false.

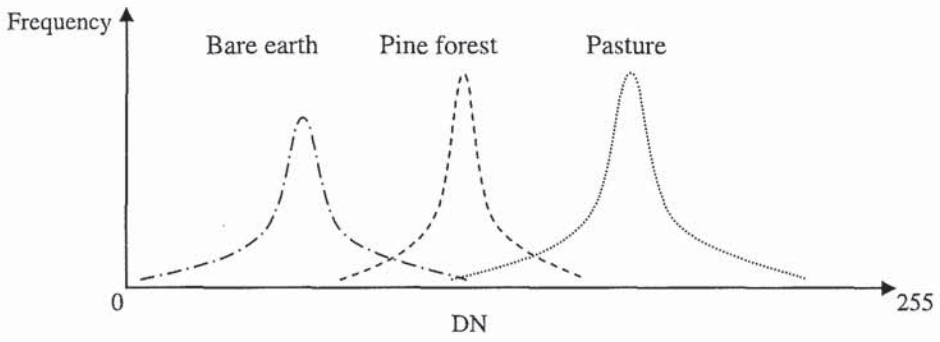

Figure 2.2: An example of three land cover classes

2.6.1.3. Bayesian classifier

The Bayesian classifier is an extension to the maximum likelihood classifier. Bayesian Probability theory allows us to combine new evidence about a hypothesis along with prior knowledge to arrive at an estimate of the likelihood that the hypothesis is true. In other words, Bayes' theorem provides a method for adjusting the degrees of belief in the light of new information. This is known as the law of conditional probabilities and can be expressed in the notation of probability theory as:

$$P(c \mid \vec{X}) = \frac{P(\vec{X} \mid c) \cdot P(c)}{P(\vec{X})} \qquad \textbf{Equation 2. 19}$$

This can be read as: the probability of class c given observation $(\vec{X})$ equals the probability of $(\vec{X})$ given it belong to class c times the probability of class c, divided by the

probability of $(\vec{X})$. Here $\vec{X} = (x_1, x_2, \ldots, x_b)$ denotes the observation of a specific pixel in each band.

For our purposes, the class c can be taken to be a hypothesis which may have been induced from some preceding set of observations before any information about the evidence $(\vec{X})$. Thus, $P(c)$ is conventionally known as prior probability. Practically, one can assume the prior probabilities are equal for all classes, or can be estimated from the number of training sample in each class.

The term $P(\vec{X} \mid c)$ is the conditional probability of seeing the observation $(\vec{X})$ given that the hypothesis c is true. This term can be estimated from the likelihood function of class c, which can be expressed for a normal distribution as in Equations (2.15 and 2.16).

The term $P(\vec{X})$ is called the marginal probability of the observation $(\vec{X})$ which means the probability of $(\vec{X})$ given no other information. It is a normalizing constant to assure the resulting posterior probability $P(c \mid \vec{X})$ will not exceed (1), and can be calculated as the sum of all mutually exclusive hypotheses $\sum_{i=1}^{k} P(\vec{X} \mid c_i) P(c_i)$. This normalization is important in that it makes the assumption that the classes considered are the only classes that are possible as interpretations for the pixel under consideration (Eastman, 2001).

Finally, the term $P(c \mid \vec{X})$ is called the posterior probability of c given the observation $(\vec{X})$. This may interpreted as multiplying the prior probability $P(c)$ of a class c, by a scaling factor to obtain a measure of the posterior probability of the hypothesis

being true given the observation. The scaling factor is known as standardized likelihood. Thus, Equation (2.19) can be rewritten to obtain the Bayesian classifier equation:

$$P(c \mid \vec{X}) = \frac{P(\vec{X} \mid c)}{\sum_{i=1}^{k} P(\vec{X} \mid c_i) P(c_i)} \cdot P(c) \qquad \textbf{Equation 2. 20}$$

The decision rule in Bayesian classifier assigns the class (c) to a pixel ($\vec{X}$) if the posterior probability $P(c \mid \vec{X})$ is the highest among all $P(c_i \mid \vec{X}), i = 1,\ldots,k)$. This decision rule is known also as Maximum a *Posteriori* (MAP). In the case of no prior knowledge of the prior probabilities, then one may assume the prior probabilities are equal and the decision rule is then simplified to assign the pixel ($\vec{X}$) to the class (c) if the conditional probability (likelihood) $P(\vec{X} \mid c)$ is the highest among all $P(\vec{X} \mid c), i = 1,\ldots,K)$ which is basically the same as the Maximum Likelihood classification.

The prime motivation of using Bayesian classification is to determine the probability that a pixel belongs to each possible class. Some authors have interpreted this directly as proportional representation if the classes were exhaustive (i.e., there are no other possible interpretations for that pixel), and as if the conditional probability $P(\vec{X} \mid c)$ do not overlap as in the case of pure pixels, which are practically difficult to meet (Eastman, 2001).

Finally, the Bayesian classifier is restricted by the assumption of the existence of complete knowledge of the evidence, and does not recognize the possibility of incomplete knowledge or ignorance. Thus, Dempster-Shafer theory comes as an extension to Bayesian probability theory, which allows for the expression of ignorance

(Gordon and Shortliffe, 1985; Lee *et al.*, 1987). This will be discussed in more details in the multisource classification in (section 2.8).

2.6.1.4. Discriminant Analysis (Fisher classifier)

Discriminant analysis involves deriving the linear combination of the independent variables (bands) that will discriminate best between the a priori defined classes (Fisher, 1936). In other words, the classes can be distinguished by a linear combination of bands that describe the class. This is achieved by the statistical decision rule of maximizing the between-class variance relative to the within-class variance.

Linear Discriminant Analysis (LDA) makes several restrictive assumptions such as normally distributed classes, homogeneity of variance-covariance matrices of bands across classes, and the bands are independent with no collinearity.

In this classifier linear functions will be derived to maximize the differences among classes while minimizing variation within classes. These linear functions express the degree of support for each class, and have a form similar to that of a multivariate linear regression equation, where the independent variables are the image bands, and the dependent variable is the measure of support to each class. Thus, there are as many classification functions as there are classes. In fact, the equations are calculated such that they maximize the variance between classes and minimize the variance within classes to ensure maximal separability similar to principal component analysis (PCA) which aims at reducing the data dimensionality (Richards, 1993). The prime difference between LDA and PCA is that the location of the original data sets in the spectral space changes to a different space when using the PCA transformation, whereas LDA does not change the

location but only tries to provide more class separability and draw a decision region between the given classes.

The number of discriminant equations will be equal to the number of classes, each describing a hyperplane of support. The assigned class for each pixel is then that class which receives the highest support after evaluation of all functions.

2.6.1.5. Linear Spectral Unmixing

This approach - also known as Linear Mixture Modelling – is the most widely used method for extracting the proportion of land cover in mixed pixels (Gebbinck, 1998). However, this technique assumes that a pixel value is a combination of the signatures of all the classes present in the pixel. It assumes no error. In other words, a pure pixel should have exactly the signature for that class, while a pixel that is made up of half one class and half another class should have a value that is the average of the two class signatures. This assumption implies no interaction between materials. Thus, the multiple scattering between different land cover types should be at its lowest level to satisfy the linearity of the model (Settle and Drake, 1993). This means the majority of photons have interacted with one land cover type before arriving to the sensor. This situation may arise if the land cover surface clustered in large patches relative to the sensor's resolution (Campbell, 1996). In most cases, many surface materials mix in non-linear mode with a second order effect. However, linear unmixing techniques appear to work well in many circumstances (Boardman and Kruse, 1994).

Horwitz *et al.* (1971) used the linear mixture model to increase the crop area estimation accuracy achieved by standard processing techniques. They assumed that the

instantaneous field of view (IFOV) consist of many small elements belonging to c different classes. The spectral signature of each class i is taken to be an b-dimensional Gaussian distribution with mean μ_i and variance-covariance matrix $\boldsymbol{Cov}_i$, where b represents the number of spectral bands. Now if the fractions of the classes present in the IFOV defined by $f = (f_1, f_2, \cdots, f_c)$, and if the variables were statistically independent, then the composite signature of the IFOV will be given by (Gebbinck, 1998):

$$\mu = \sum_{i=1}^{c} f_i \cdot \mu_i$$
$$\boldsymbol{Cov} = \sum_{i=1}^{c} f_i \cdot \boldsymbol{Cov}_i \qquad \textbf{Equation 2. 21}$$

Therefore, the classification of mixed pixel can be performed by inverting this statistical model which is usually written in matrix notation as:

$$\boldsymbol{X} = \boldsymbol{Mf} + \boldsymbol{e} \qquad \textbf{Equation 2. 22}$$

where:

$\boldsymbol{X}$ represents a one column vector of the multispectral observation for a pixel.

$\boldsymbol{M}$ is a matrix contains the representative spectrum of each class – also known as the end members – each column is for one end member. Thus, the number of columns will be equal to the total number of classes, and the number of rows will be equal to the total number of bands under consideration.

$\boldsymbol{f}$ is one column vector, each row represent the fraction of the considered class in the pixel.

$\boldsymbol{e}$ is the error vector used to model the statistical fluctuations around the mean value μ in Equation 2.21.

The representative spectrum of the class of interest should be known before the classification process can take place. This is usually represents the typical reflectance in the IFOV that contains nothing but the class of interest. Several methods to determine the end member spectrum can be found in Gebbinck (1998). For example, the end member spectrum can be obtained from spectral libraries, principal component analysis, linear regression of known mixtures, or the mean of pure pixels.

Two important constraints usually accompany Equation (2.22). The first constraint is the sum to one that is the proportions should add up to unity and the second constraint is the positivity constraint which implies no component in the mixed pixel can make a negative contribution:

$$\sum_{i=1}^{c} f_i = 1 \quad \text{and } f_i \geq 0, \qquad \forall i = 1,2,\cdots,c \qquad \textbf{Equation 2. 23}$$

Both Equations (2.22 and 2.23) describe the linear mixture model which can be used to determine the compositional classes that exist in the mixed pixels. If the number of spectral bands considered is n, then the total number of linear equations that can be obtained from the model will be n+1. These are: one equation for each band plus one equation to satisfy the sum to one constraint. If the error vector $\boldsymbol{e}$ in Equation (2.22) is disregarded, then the number of unknown variables (the fraction f_i of each class) in the system of these linear equations will be equal to the number of the classes c that exist in the mixed pixel. Therefore, according to the number of unknowns and the number of

equation three cases can be recognised. First, if the number of unknown fraction was greater than the number of equations ($c>n+1$) then the system of linear equation will be underdetermined and the system will have infinitely many solutions. Second, if ($c=n+1$) then the system has only one solution. Third, if ($c<n+1$) then the system of linear equations is over determined and there is at most one solution. However, to provide a general solution in the last two cases an error vector ($\boldsymbol{e}$) unequal to zero may be considered so that an optimal solution can be identified based on minimizing the error vector. An elaborated discussion on solving the linear mixture model can be found in Gebbinck (1998). However, the primary limitation of solving the linear mixture model is that the number of end member's classes cannot exceed the number of bands. This can be a severe limitation in the case of multispectral imagery, but of little consequence with hyperspectral imagery. Eastman (2001) proposed a probabilistic guided approach for this case of insufficient bands exist. This approach uses a probability model as first step to determine the most likely constituents up to the number of available bands, and then in a second step a linear mixture model is used to determine the fraction of these most likely constituents. However, as it has been discussed earlier in section (2.6.1.2), the probability measures may falsely indicate a higher probability for a class that may not exist in the mixed pixel simply because the composite signature may simulate the signature of other classes as shown in Figure (2.2). Another approach called exhaustive search is described by (Eastman, 2001). This approach works by testing all the possible combinations of the end members up to the number of available bands and reports the fractions of that combination with the lowest sum of squared residuals. However, (Eastman, 2001) reports

that the result of this approach is inferior to the probability guided approach if the end member signature is drawn from training areas.

As a conclusion, the linear mixture model techniques is most effective if the signatures of all the target cover types in the scene are few and distinct and must be spectrally identified. Even though, in best conditions, the variable illumination due to topography and object's shadow will modify the mixed signal received at the sensor, thus, limiting the application of this model. However, for areas mainly made up of agricultural fields with relatively flat topography the linear mixing model can be assumed to be a good abstraction of the mixing process.

2.6.2. Non-Parametric classifiers

A common problem with parametric classifiers is that they assume the pixel DNs within the features to be normally distributed. Although other classifiers can be designed, there can still be the problem of features having different probability distributions. Another solution is to apply nonparametric techniques.

The nonparametric classifiers are not based on statistical assumption, but on discrete objects (region polygons or rectangles) in the spectral space. These spectral space objects are used to define the boundaries for the classes. A nonparametric classifier may use a set of nonparametric signatures to assign pixels to a class based on their location either inside or outside the class' region in the spectral space (Pouncey, *et al.*, 1999). It is important to notice that it is possible for a pixel to fall outside all regions or inside overlapped regions. Therefore, it is necessary to add some rules to leave those pixels unclassified or to classify them to one or multiple classes.

Since the decisions rules in the nonparametric classifier have no dependency on the statistics of the training samples, then for specific non-normal classes, such as urban and exposed rock, this classifier may improve the classification accuracies (Faust, 1989). Some examples of a non-parametric classifier are discussed in the next sub-sections.

2.6.2.1. Parallelepiped classifier

The parallelepiped classification is implemented by defining a parallelepiped-like subspace in the spectral space for each class. The boundaries of the parallelepiped are defined by the minimum and maximum pixel values in the given class in each band. Alternatively, the boundaries can be defined by the mean of the training data for the given class in each band plus and minus a number of standard deviations, or any limits specified by the analyst based on the knowledge of the data and signatures. The decision rule is simply to check whether the point representing the candidate pixel in the spectral space lies inside any of the parallelepiped. This is achieved by checking that the pixel' DN values fall between the limits for every band in the class' signature. However, in the case of pixels outside all or in the overlapping parallelepipeds, a decision rule should be defined to leave those pixels unclassified or to classify them using any of the parametric classifiers, for example, minimum distance decision rule.

The parallelepiped classifier is fast and simple and it is not dependent on any assumption for the probability distribution. However, it is hard to provide a robust classification using this classifier considering the problems in the outside and overlapping parallelepiped regions (Richards, 1993).

2.6.2.2. K-nearest neighbour classifier

This classification method is similar to the minimum distance, however, the difference lies in the fact that rather than assigning a classification based upon the classification of the nearest class' mean, the algorithm selects a set of training observations which contains the k nearest neighbours and assigns the class label to the candidate pixel based upon the most numerous class with the set. The nearest neighbour is normally calculated using any spectral distance measure such as Mahalanobis distance (Fukunaga, 1990):

$$d_i^2 = (\vec{X} - \vec{X}_{i,NN})^T \Sigma_i^{-1} (\vec{X} - \vec{X}_{i,NN}) \qquad \textbf{Equation 2. 24}$$

Here $\vec{X}_{i,NN}$ is the nearest neighbour of class (i) to feature vector $\vec{X}$ under test and Σ_i^{-1} the inverse of the covariance matrix of class (i). The smallest distance determines the class. This procedure is also referred to as the volumetric k_{NN} procedure. For computational reasons Equation (2.24) can be simplified to:

$$d_i^2 = \sum_{j=1}^{b} \frac{(x_j - x_{ij,NN})^2}{\sigma_{ij}^2} \qquad \textbf{Equation 2. 25}$$

Here x_j is the j^{th} element of feature vector $\vec{X}$ with dimension b. $x_{ij,NN}$ is the j^{th} element of the nearest neighbour $x_{i,NN}$ and σ_{ij} is the standard deviation of all j^{th} elements of all sample feature vectors of class (i). The user will determine the parameter the number of nearest neighbour k, and then calculate the spectral distance between the candidate pixel and all the training samples. The candidate pixel will be assigned a class based on the majority of the class in the set of k nearest samples. For example, Figure (2.3) shows the feature space of the training pixels for three classes with only two bands under

consideration. The candidate pixel shown in this figure at the centre of the circle will be classified as class (3) if only four nearest pixels were considered (k=4). The same candidate pixel will classified as class (1) if fifteen nearest neighbour were considered (k=15). The classification is made with the highest confidence only if all of the nearest neighbours are of the same class.

The disadvantages of the k-nearest neighbour method are the need to determine a value for (k number of nearest neighbours), and it is not clear which features (bands) to use to produce the best results. Further, it is computationally exhaustive because we need to compute distance for each pixel to all training samples. This algorithm is sensitive to the size of training samples for each class, thus classes with fewer samples may be underdetermined. However, one may overcome this by using a proportion number of training samples

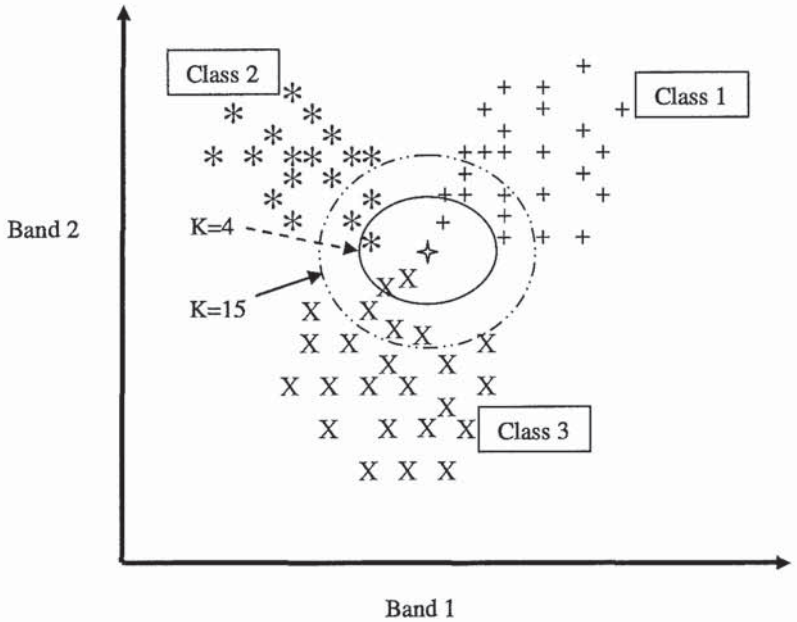

Figure 2.3: K-nearest neighbour example

2.6.2.3. Artificial neural networks

Recently the use of artificial neural networks (ANN) has been significantly increased for the classification of remotely sensed data. This is because ANN is believed to provide improved accuracy (Foody, 1995). Artificial neural networks are generally described as nonparametric as it does not require any assumptions about the statistical distribution of the data.

There are several kinds of ANN architecture. For example, multilayer perceptron with back-error propagation, the self-organised feature map (SOM), counter-propagation networks, Hopfield networks, and ART system. A comprehensive review of ANN classification can be found in Tso and Mather (2001).

A typical ANN consists of a series of layers (Figure 2.4), each containing a number of processing units or neurones. All neurones on a given layer are linked to all neurones on the previous and subsequent layers. There are no interconnections between neurones in the same layer. These interconnections have associated numerical weights. The value held by each neurone is called its activity. The neural activities and the interconnection weights are adjusted during the learning phase.

In Figure 2.4 the input layer contains the set of neurones that receive external inputs (pixel DN values in different bands or other feature values). The input layer performs no computations, unlike the elements of the other layers. The central layer is the hidden layer (there may be multiple hidden layers). The rightmost layer of neurones is the output layer, which produces the results of the classification.

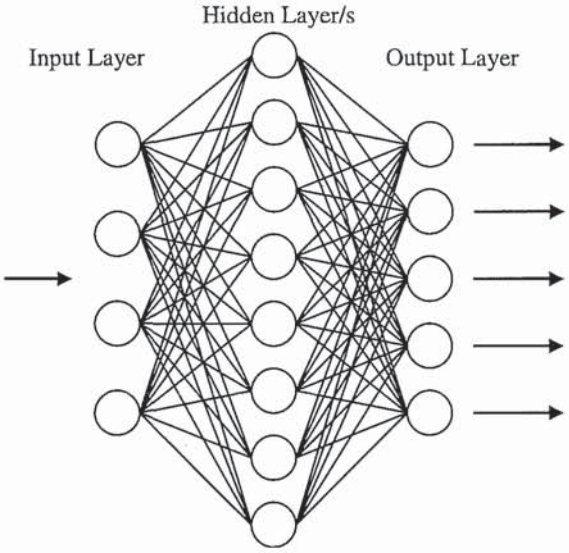

Figure 2.4: A typical multilayer perceptron ANN composed of three layers

The architecture of the network is determined by the analyst who also must define parameters such as the learning rate. There are no clear rules to assist with the design of the network, and only rules of thumb exist to guide users in their choice of network parameters. Therefore, ANN is perceived to be difficult to apply successfully.

2.6.2.4. Knowledge-based classifiers

Another example of a non-parametric classifier is the knowledge-based or rule-based classifier (Gong and Howarth, 1990; Richards, 1993). Knowledge can be heuristic, i.e. based on experience and reasoning, and may not necessarily involve a statistical model. The most common rule in such classification is the if-then rule: if condition then inference. Fuzzy rule-based systems follow the same rules, except that conditions are determined by a membership function which describes the degree of membership to a

fuzzy set (Benz *et al.*, 2004). Because land cover and land use have many-to-many relationships, knowledge-based or rule-based classification systems are ideal to convert one to another (Gong and Howarth, 1990; Cihlar and Jansen, 2001).

2.7. Unsupervised classification

In contrast to supervised classification, unsupervised classification requires only a minimal amount of initial inputs from the analyst (Robinove, 1981). Thus all class separation is accomplished numerically by the algorithm in an attempt to uncover the land cover classes that exist in the image (Martínez-Casasnovas, 2000). The multispectral image is classified into a number of spectral classes, without prior knowledge of what they might be. The analyst provides the number of the output spectral classes and indicates the clustering algorithm. After the clustering process, the analyst also needs to assign information labels to the spectral clusters by means of ground sampling procedures, and to determine which clusters need to be merged or to be further defined to achieve a legend according to the purposes of the user.

Unsupervised classification usually produces a wider range of spectral classes than supervised classification. An appropriate sampling strategy is required for cluster definition. A particular land cover class may be represented in more than one spectral class, and conversely, one spectral class may represent more than one land cover class. Thus, the analyst may merge clusters according to their composition in terms of informational classes and class similarity, or may try to further split clusters when they include more than one land cover class, always depending on the target legend. The following subsections present some of the most popular unsupervised classifiers.

2.7.1. K-means

The k-means algorithm assigns each point to the cluster whose centre (or centroid) is nearest. The centroid is the point generated by computing the arithmetic mean for each dimension separately for all the points in the cluster. The user has at first to choose the number of clusters (k) and mean change tolerance ε.

The basic structure of the algorithm (MacQueen, 1967) is as follow:

1. Randomly generate k clusters and determine the cluster centers or directly generate k seed points as cluster centres in the multispectral space, these points may denoted as $m_i^0; i = 1,2...,k$ where the superscript (0) denote the initial iteration.
2. Assign each point in the spectral space to the nearest cluster centre m. The nearest is defined either by the Euclidean or Mahalanobis distance measure.
3. Re-compute the new cluster centres based on the result in step 2.

$m_i^n = \frac{1}{N_i} \sum_{x \in C_i} x$ where: i=1,2,…,k; N_i is the total number of points labelled as C_i.

4. If $\left| m_i^n - m_i^{n-1} \right| < \varepsilon$ the procedure is terminated. Otherwise return to step 2 until the convergence criterion is met.

In the K-means algorithm, clustering may not be realized, i.e., the clustering is not converging. Therefore, we might have to specify the number of iterations to terminate a clustering process.

The main advantages of this algorithm are its simplicity and speed, which allows it to run on large datasets. However, the resulting clusters depend on the initial assignments. Therefore, the result of each run of the algorithm may be different. The k-means algorithm maximizes the variance between clusters, but it does not necessarily minimize the local variance within cluster.

2.7.2. ISODATA

This is an Iterative Self Organizing Data Analysis Technique, which is based on the K-means algorithm. The user of ISODATA defines additional criteria to optimize the clustering process. For example, one may set a tolerance for minimal distance, d_{min}, between clusters, and also maximal standard deviation, σ_{max}, of a cluster so that:

- If two clusters are too close, e.g. the distance between cluster centres is less than d_{min}, they are merged into one cluster.
- If the standard deviation of a cluster is larger than σ_{max}, that cluster is split into two clusters.

The choice of split and merge parameters σ_{max} and d_{min} is difficult. A trial and error process can be used. These additional parameters increase the adaptivety of the algorithm but also increase the time and complexity of the computation.

2.7.3. Fuzzy clustering

The main difference between fuzzy clustering and the ISODATA is that the resulting clusters generated by fuzzy clustering are no longer hard or crisp, but soft or fuzzy. In

other words, points on the edge of the cluster or near another cluster may not be as much in the cluster as point in the center of cluster. Thus, each pixel assigned a membership value for each cluster.

Most analytic fuzzy clustering algorithms are derived from the Bezdek (1981) fuzzy c-mean (fcm) algorithm. The fcm algorithm uses the probabilistic constraint that the membership probabilities of a data point across classes must sum to one. Thus, for each point n - from the total number of pixels to be clusterd (N) - we have a coefficient giving the degree of being in the k^{th} cluster (probability of belonging to a certain cluster). The coefficient $u_{k,n}$ should satisfy the following constraints:

$$u_{k,n} \in [0,1] \quad and \quad \sum_{k=1}^{C} u_{k,n} = 1 \qquad \textbf{Equation 2. 26}$$

where C is the total number of clusters; and $n \in [1,2....,N]$.

The fcm algorithm structure is as follow (Tso and Mather, 2001):

1. The user will choose the number of clusters C, the weighting exponent m, and the false tolerance ε.
2. Initialize randomley C centers. Compute the distance for each point from the initialized centers. Assign the clustering membership matrix **U** with C rows and N columns, where each entry of U is the membership value $u_{k,n}$ computed from:

$$u_{k,n} = \frac{1}{\sum_{j=1}^{C} \left(\frac{|x_n - \mu_k|}{|x_n - \mu_j|} \right)^{2/(m-1)}} \qquad \textbf{Equation 2. 27}$$

It is possible to assign the centers by the user instead of randomley initialize the centers. This approach may refered to as supervised fcm

3. Compute the new cluster mean for all clusters using:

$$\mu_k = \frac{\sum_n (u_{k,n})^m \cdot x_n}{\sum_n (u_{k,n})^m} \qquad \textbf{Equation 2. 28}$$

4. Update matrix **U** using Equation 2.26
5. Repeat steps 3 and 4 until $\left\|\mathbf{U}^{new} - \mathbf{U}^{old}\right\| < \varepsilon$.

The fuzzy *c*-means algorithm minimizes intra-cluster variance, but has the same problems as *k*-means, the minimum is local minimum, and the results depend on the initial choice of membership values. Further it is not easy to choose the number of clusters, especially, when there is no idea about the number of information classes.

Krishnapuram and Keller (1993, 1996) proposed the possibilistic c-means algorithm as an alternative for fcm, as it provides a means of estimating the absolute membership grade of each class independently of all other classes.

2.8. Multi-source image classification

Recently, greater attention is given to the use of multisource data in remote sensing image classification. For example, Richards *et al.* (1982) combine ETM+ images with topographic information and spatial context to iteratively adjust the label assigned to each pixel until between-source class consistancy is achieved. The general steps for multisource classification is shown in figure 2.5.

The feature extraction aim to determine what kind of input features should be used. The selection of suitable input features can enhance classification accuracy. For example, to classify crop types in an agricultural area, textural and tonal information may make no significant difference because of the scale and size of the object being classified. Where radar images are used, textural features may be more useful than image tonal information (Ulaby *et al.*, 1986).

The probability or evidence generation stage involves the definition of a p.d.f. or some alternative methodology (ANN) to compute the class-associated probabilities or evidence.

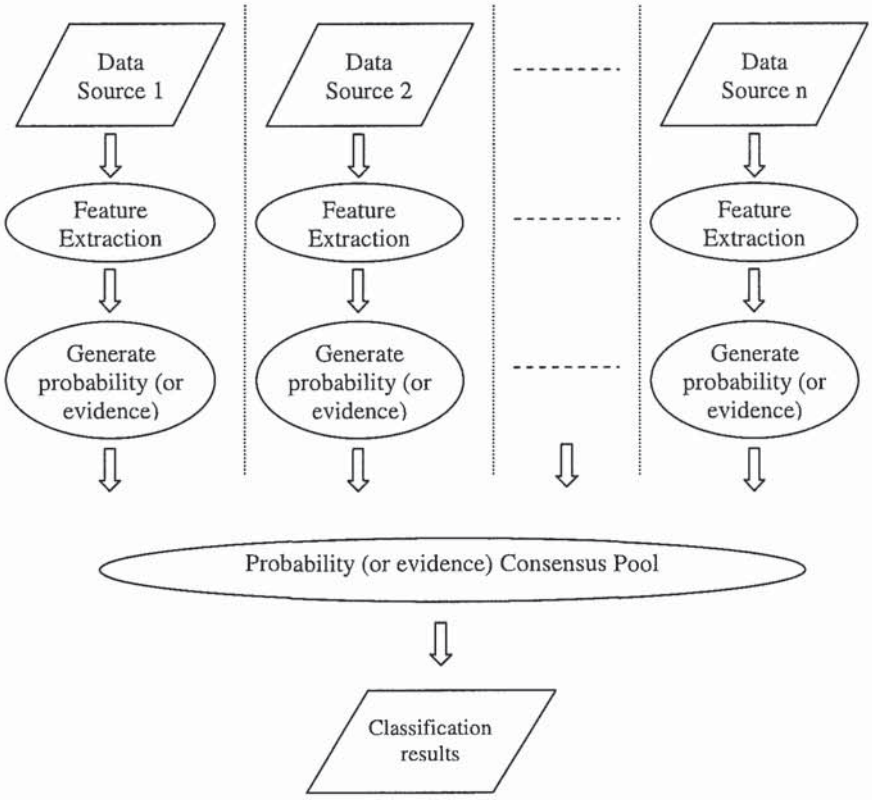

Figure 2.5: General steps in multi-source classification (source: Tso and Mather, 2001)

Finally, the classified image is obtained by combining all probability (or evidence) measures together. Two ways can be followed for combining the evidence, namely the Baysian inference and the Evidential reasoning:

2.8.1. Bayesian Inference

This is an extension of Bayesian theory to classify multi-source remotely sensed data. It assumes each data source as fully independent. Hence, probability measures (line of evidence) for each information class (hypothesis) should be generated from each source separately, and then these lines of evidence combined to obtain the classification result. Let $x_i, i \in [1,n]$, denote the probability measure of a specific pixel from data source, i. The prior probability of class c is denoted by $P(c)$. The aim is to derive the probability of the pixel belonging to each of the information classes c.

The Bayesian probability theory, the law of conditional probabilities states that (Tso and Mather, 2001):

$$P(c \mid \vec{X}) = P(c \mid x_1,\ldots,x_n) = \frac{P(c)\cdot P(x_1,\ldots,x_n \mid c)}{P(x_1,\ldots,x_n)} \qquad \textbf{Equation 2. 29}$$

where $P(c \mid x_1,\ldots,x_n)$ is known as the posterior probability that (c) is the correct class, given the evidence from the n data sources. $P(x_1,\ldots,x_n \mid c)$ is the probability density function p.d.f. associated with the probability measurements $(\vec{X})$ given that $(x_1,\ldots,x_n)$ belong to class (c). $P(x_1,\ldots,x_n)$ is the p.d.f. of data $(x_1,\ldots,x_n)$.

Assuming class conditional independence among the measurements, one obtains: $P(x_1,\ldots,x_n \mid c) = P(x_1 \mid c)\cdot P(x_2 \mid c)\cdot\ldots\cdot P(x_n \mid c)$, thus Equation 2.29 becomes:

$$P(c \mid x_1,\ldots,x_n) = \frac{P(x_1 \mid c)\cdot\ldots\cdot P(x_n)\cdot P(c)}{P(x_1,\ldots,x_n)} \qquad \textbf{Equation 2. 30}$$

Again, following the law of conditional probabilities:

$$P(x_i \mid c)\cdot P(c)_i = P(c \mid x_i)\cdot P(x_i) \Rightarrow P(x_i \mid c) = \frac{P(c \mid x_i)\cdot P(x_i)}{P(c)_i} \qquad \textbf{Equation 2. 31}$$

where $P(c)_i$ is the prior probability associated with data source (i). If Equation (2.30) is substituted into Equation (2.29), one obtains:

$$P(c \mid x_1,\ldots,x_n) = \frac{P(c \mid x_1)}{P(c)_1}\cdot\ldots\cdot\frac{P(c \mid x_n)}{P(c)_n}\cdot P(c)\cdot\frac{P(x_1)\cdot\ldots\cdot P(x_n)}{P(x_1,\ldots,x_n)} \qquad \textbf{Equation 2. 32}$$

If the intersource independence assumption has been made so that the joint probability distributions function $P(x_1,\ldots,x_n)$ can be expressed as the product of each class-conditional probability function $\left(P(x_1)\cdot\ldots\cdot p(x_n)\right)$ then Equation (2.32) becomes:

$$P(c \mid x_1,\ldots,x_n) \propto \frac{P(c \mid x_1)}{P(c)_1}\cdot\ldots\cdot\frac{P(c \mid x_n)}{P(c)_n}\cdot P(c) \qquad \textbf{Equation 2. 33}$$

Equation (2.33) is only valid under the assumption that the data sources are mutually independent. However, the validity of the assumption is hard to determine. Therefore, if there is no reliable information concerning the relationship between the data sources, one may ignore any intersource relationships and consider the data sources as independent variables (Tso and Mather, 2001).

It is natural that not all data sources are of the same reliability. Therefore, different weights for reliability measure to each data source can be appended as exponents to the contribution from each data source (Lee *et al.*, 1987; Benediktsson and Swain, 1992). Thus, Equation (2.33) can be written as:

$$P(c \mid x_1,\ldots,x_n) \propto \left[\frac{P(c \mid x_1)}{P(c)_1}\right]^{\alpha_1} \cdot \ldots \cdot \left[\frac{P(c \mid x_n)}{P(c)_n}\right]^{\alpha_n} \cdot P(c) \qquad \textbf{Equation 2. 34}$$

where $\alpha_i \in [0,1]$ is the source-specific weighting parameter which allows one to adjust the contribution from the i^{th} source. If $\alpha_i = 1$ then the data source i is fully reliable, and as $\alpha_i \to 0$ then the source i is considered to be less reliable (Tso and Mather, 2001).

2.8.2. Evidential reasoning (Dempster-Shafer theory of evidence)

This can be regarded as a more general approach to representing uncertainty than the Bayesian approach. In D-S theory, complete knowledge is represented as unity, i.e. the sum of all labelling possibilities is equal to one, which includes the case of uncertainty. The basic assumptions of D-S theory are that ignorance exists in the body of knowledge, and that belief for a hypothesis is not necessarily the complement of belief for its negation (Eastman, 2001).

Dempster-Shafer theory defines hypotheses in a hierarchical structure developed from a basic set of hypotheses. Thus, for example, if there are three classes in an image: A, B, and C, then the total number of hypotheses will be 2^3=8 hypotheses, which are a pixel may belong to class ([A], [B], [C], [A, B], [A, C], [B, C], [A, B, C], or [Φ]). Where Φ is the empty or null hypothesis which is included to express the lack of knowledge, for

example, a pixel may belong to some unknown class, for which a training site has not been provided. Further, including a hypothesis for all possible combination of classes makes it feasible to incorporate any line of evidence that may support any of these combinations. For example, if three classes exist in a scene ([deciduous], [coniferous] and [crops]), from satellite imagery one may derive a probability map for pixels belonging to each of these single classes. However, some pixels may have similar degree of support to be in any class: crops or forest (deciduous or coniferous). Therefore, using another data source (e.g. aerial photography) a probability map for pixels belonging to a combination class, [deciduous, coniferous], can be derived. This is because from aerial photography it is difficult to distinguish between deciduous and coniferous forest, but it is easy to distinguish forest from crops. Since Dempster-Shafer theory of evidence recognises this combination class ([deciduous, coniferous]), then incorporating this line of evidence in the classification process may reduce the ambiguity between crops and forest, thus improving the overall classification accuracy. However, this line of evidence may not help in distinguishing the deciduous from coniferous forest.

The degree of support (belief) to any particular hypothesis (Ψ) is represented by a function called the basic probability assignment (BPA) and denoted by $m(\Psi)$. This is also called mass of support to a hypothesis Ψ. Here Ψ can be any of the hypotheses in the structure (e.g. any of the eight hypotheses in the structure of three classes' case).

An important constraint in D-S theory that should be met is that, for all hypotheses supported from one line of evidence the sum ($m(\Psi)$) must be equal to 1. For example, if from a particular line of evidence we obtain a basic probability assignment for hypothesis

([A, C]) in the above example, and there was not any other assignment to support any of the other hypotheses in the structure, then if m([A, C])=q; (where q< 1), then a value of 1-q will be assigned to the set ([A, B, C]) for this particular line of evidence rather than to the opponents of ([A, C]), which in this example is ([B]). This is a key feature in D-S theory where a belief in a hypothesis does not imply the remaining belief (ignorance) gives evidence to its opponents, but it simply may represent one's inability to distinguish between any of the hypotheses considered.

The purpose of D-S theory is to extract a combined measure of support for each hypothesis by combining the BPA in each line of evidence using the orthogonal sum, or Dempster's rule of combination (Shafer, 1979). The evidence accumulation is performed in a sequential manner irrespective of the evidence order where the result of the accumulation will be the same if different order is used.

For example, if there are three lines of evidence (three data sources 1, 2, and 3) each has its own set of hypotheses to support. Let X denotes the set of hypotheses supported from the first line of evidence, and for each hypothesis $x \in X$ the following constraints are true: $0 < m_1(x) \leq 1; and \sum_{x \in X} m_1(x) = 1$), where $m_1(x)$ is the BPA (mass of support) assigned to the hypothesis $x \in X$ from the first line of evidence. Now let Y and Z denote the set of hypotheses supported from the second and third line of evidence respectively with similar constraints applied for their BPA.

The first step in D-S combination rule is to assign a new BPA value for each intersection between the set of hypotheses in the first and second line of evidence using the Dempster's orthogonal sum:

$$m_{1,2}(\psi) = m_1 \oplus m_2(x \cap y = \psi) = \frac{\sum_{x \cap y = \psi} m_1(x) \cdot m_2(y)}{K} \qquad \textbf{Equation 2. 35}$$

$$K = 1 - \sum_{x \cap y = \Phi} m_1(x) \cdot m_2(y)$$

where K is a normalising constant to ensure that no contribution is committed to the null set Φ. Thus, guarantee the resulting BPA for all non empty intersections to be subject to the required constraints which is $0 < m_{1,2}(\psi) \leq 1; and \sum_{\psi \in \Psi} m_{1,2}(\psi) = 1$.

The Equation (2.35) will be used to assign a new BPA value for each intersection between the resulting set of hypotheses Ψ from previous step with the hypotheses in the third line of evidence Z and so forth.

The final step in D-S evidence combination is to aggregate the final BPA obtained for each hypothesis using three concepts:

1. Belief: represent the total support for the hypothesis and denoted by *Bel*. It can be expressed as the sum of all BPA which is committed to the hypothesis considered and to its subsets if any. Thus:

$$Bel(\psi) = \sum_{\omega \subseteq \psi} m(\omega) \qquad \textbf{Equation 2. 36}$$

For example if $\psi = [A, B]$ then $Bel(\psi) = m([A, B]) + m([A]) + m([B])$

2. Plausibility: denoted by (*bl*) represents the degree to which a hypothesis cannot be disbelieved. In other words, it represents the degree of support for all hypotheses that do not intersect with that hypothesis. Thus:

$$Bl(\psi) = 1 - Bel(\sim \psi) = \sum_{\omega \cap \psi \neq \Phi} m(\omega) \qquad \textbf{Equation 2. 37}$$

3. Belief interval: is the range between belief and plausibility $[Bel(\psi), Bl(\psi)]$ which provides the lower bound and upper bound of the probability of the hypothesis under consideration.

Therefore, the decision rule in D-S evidence theory can be based on three possible choices (Shafer, 1979 cited by Tso and Mather, 2001):

1. Belief driven: Label is chosen on the basis of maximal belief.
2. Plausibility driven: Label is chosen on the basis of maximal plausibility.
3. Mean of the interval: Label is chosen on the basis of the maximal average of belief and plausibility values.

However, if the aim is to produce a single-class labelling then the three possible choices boil down to one choice as both belief-driven and plausibility driven can produce similar results (Tso and Mather, 2001).

2.9. Discussion and conclusions

This chapter the general procedure for the classification using remotely sensed data has been demonstrated. The atmospheric correction was anticipated to be an important step in the pre-processing stage if multi-temporal multi-source data are to be used. Therefore, the

appropriate atmospheric correction methods were researched from the literatures given the availability of the software and the parameters required for each model. This will be applied on the Landsat ETM+ image to minimize the effect of the atmosphere on the reflectance of the land cover, so that the integration technique can take place to integrate this data with the multi-temporal multi-resolution MODIS data to obtain a classified map for the study area.

In order to select the appropriate classification technique this chapter has examined, in depth, the principle and techniques behind existing classification methods. The discussed methods are listed in table 2.2, and the merits and demerits of each method have also been pointed out.

Table 2.2: Summary of Classification techniques discussed in this chapter

<table>
<tr><td rowspan="10">Supervised classifiers</td><td rowspan="5">Parametric</td><td rowspan="3">Minimum Distance to mean</td><td>Euclidian Distance</td></tr>
<tr><td>City-Block Distance</td></tr>
<tr><td>Mahalanobis Distance</td></tr>
<tr><td colspan="2">Maximum Likelihood</td></tr>
<tr><td colspan="2">Bayesian Classifier</td></tr>
<tr><td colspan="2">Discriminant Analysis</td></tr>
<tr><td colspan="2">Linear Mixture Unmixing</td></tr>
<tr><td rowspan="4">Non-parametric</td><td colspan="2">Parallelepiped</td></tr>
<tr><td colspan="2">K-nearest neighbour</td></tr>
<tr><td colspan="2">Artificial Neural Networks</td></tr>
<tr><td colspan="2">Knowledge-based classifiers</td></tr>
<tr><td rowspan="3">Unsupervised Classifiers</td><td colspan="3">K-means</td></tr>
<tr><td colspan="3">ISODATA</td></tr>
<tr><td colspan="3">Fuzzy clustering</td></tr>
<tr><td rowspan="2">Multi-source classifiers</td><td colspan="3">Bayesian Inference</td></tr>
<tr><td colspan="3">Evidential Reasoning (Dempster-Shafer)</td></tr>
</table>

Previous studies have shown the superiority of supervised classification over unsupervised (Shalan *et al.*, 2003). A supervised classification may give the user more control over resulting classes, but it requires *a priori* ground truth knowledge. It is,

however, more subjective since the analyst may force the discrimination of classes without a clear spectral meaning. Also, the supervised method is considered as restrictive, since some existing land cover classes may be unknown by the user prior to the classification process and, therefore, they are not considered in the training data set (Palacio and Luna, 1996). Sometimes, the existence of those non-sampled land cover classes may be known and it is a decision of the analyst either to consider them in the classification process or not. In other situations, those classes are mixtures of the known classes. This represents a loss of spectral information during the image classification process which some authors have tried to face through fuzzy supervised classification (Wang, 1990b, Foody, 1996a) or by In-Process Classification Assessment methods (Eastman, 2001).

Unsupervised classifications are sometimes difficult to interpret or to produce results that are related to the user needs. The unsupervised process, however, overcomes some problems related to the knowledge of the spectral response variability of terrain objects. In this respect, the combination of both classification procedures is often advised by using unsupervised classification as an alternative method for spectral signature definition (García and Álvarez, 1994).

Therefore, neither supervised nor unsupervised methods provide an immediate solution to the problems that a digital classification implies largely because they use only one of the key features human interpreters use. As a consequence, using a combination of supervised and unsupervised classification may yield optimum results. For example,

unsupervised classification may be useful for generating a basic set of classes, and then supervised classification can be used for further definition of the classes.

The classification techniques that were discussed can be applied to pixels or objects. From a land-cover point of view, an object is a region or segment in which the feature space is homogeneous to some degree, so that it fits one (physical) description. From a land-use point of view an object fits one function. In general, object-based classification is preferred to pixel based classification because it is more accurate (Janssen *et al.*, 1990). Objects can be extracted from the satellite image using segmentation techniques (Oliver, 1991, Benz *et al.*, 2004). In this thesis the object-based classification will be performed to classify each agricultural field to one of the identified classes, and this will be referred to in the remaining chapters as per-parcel or per-field classification.

Chapter 3

Study area and materials

3.1. Introduction

In this chapter the imagery and other data used in this project are introduced, and the classification schemes that can be applied using the available data sources are discussed.

3.2. The study area

The study area is situated south west of Birmingham, West Midlands, the UK. The study area is bounded by British National Grids (BNG) coordinates: East 360000 to 380000 and North 260000 to 270000. The site is located on OS pathfinder 973 (SO 66/76). The centre geographical coordinate is latitude 52:16:56N (52.2823°): longitude 2:26:28W (-2.4412°). The total area covered is 200 km^2. Figure 3.1 shows the site location within the map of Great Britain. Figure 3.2 is a detailed map of the study area obtained from Digimap (http://www.edina.ac.uk/digimap/ [2004, October]).

After acquiring a suitable Landsat ETM+ image that should be as cloud free as possible it was clear that the image covered too large an area and a smaller study area of about 200 km^2 was required. This area should meet the following criteria:

- It should be sufficiently close to Aston University for easy access for field work.
- It should contain minimal urban area with a variety of land cover types, including arable and pastoral farming, market gardening, tree crops, forest and woodland. All of which will be of interest in classifying agricultural land

- It should consist of gently sloping terrain so that differential illumination did not pose any serious problems.
- There should be little or no moor land.
- Ideally we should have aerial photography for the region.

After searching maps and records of the region and obtaining advice on the agriculture of the region, it was decided to use an area centred near the village of Stockton on Teme in the Teme valley of Worcestershire (see Figure 3.2).

Figure 3.1: The location site of the study area on the Great Britain map (source: http://www.uk.map24.com/ [2006, January])

Figure 3.2: The raster map for the study area (not to scale) (source: Digimap http://www.edina.ac.uk/digimap/)

3.3. Brief description of the site

The study area consists of relatively gentle rolling countryside, approximately 150m altitude above sea level (ASL) with the valley of the river Teme incised through it. The river meanders through the narrow valley floor at an altitude of approximately 40m ASL. The valley bottom is relatively flat and about half a kilometre wide. The valley sides are of moderate slope.

The valley bottom is sheltered and this gives rise to some market gardening and the growth of crops such as hops. Otherwise the valley floor contains the rearing of cattle and the growth of mixed cereal feedstock for them. Some potatoes and vining peas were growing when a field visit was conducted.

The southwest slopes of the valley have a band of woodland consisting of a mixture of deciduous and coniferous stands. Some of the woodland is semi natural and dates back to the Norman Conquest. There are some orchards on this side of the valley, but most of the fruit growing takes places on the southwest facing slopes on the other side of the river.

The hill tops are given over to a mixture of arable and pastoral farming. The average size of the fields is around one hectare.

3.4. Satellite imagery and its acquisition

With huge volume of remote sensing data from a wide range of available sensors (Appendix 1), the decision on what kind of data would be the most useful and efficient to accomplish the task, is very complex. The cost of the data may limit the choice of selecting the most appropriate images. However, other factors should also be considered,

such as the appropriate spatial resolution, spectral resolution, number of bands, coverage area, repeat time...etc, when selecting the imagery.

One may desire to acquire data for a given time. However, the cost of scheduled images may be very high. Sometimes pre-existing data is available, but the disadvantage of data from an archive is the lack of suitable ground truth data for use in classification.

Since the main objective of this work is to develop a methodology for integrating multi-scale multi-temporal image data, rather than to achieve a specific classification, the decision was taken to find suitable archived data. The medium spatial resolution Landsat data was deemed suitable for mapping the study area, since it has a spatial resolution of 30m and the average size of the agricultural fields to be mapped was approximately one hectare. The choice of multi-temporal coarse spatial resolution MODIS images from the Terra platform, was based on its free availability on a daily basis since February 2000. The following sections describe these data.

3.4.1. Landsat ETM+ satellite images

A Landsat Enhanced Thematic Mapper Plus (ETM+) imagery acquired on 17 June 2000 was downloaded from the landmap website (www.landmap.ac.uk , [2002, December]). The mid-June date of this image corresponds to the peak of the growing season within the study area. The image data was in raw format and georeferenced to the Universal Transverse Mercator (UTM 30) projection system. It was therefore reprojected to the British National Grid (BNG), and a window representing the study area was extracted.

Table 3.1: Landsat ETM+ bands details (source: http://www.infoterra-global.com/landsat.htm [2002, December])

Spectral Band		Band Number	Range (μm)	Resolution
Visible	Blue	1	0.450 to 0.515	30m
	Green	2	0.525 to 0.605	30m
	Red	3	0.630 to 0.690	30m
Infrared	near-infrared	4	0.750 to 0.900	30m
	short-wave infrared	5	1.550 to 1.750	30m
	mid infrared	7	2.350 to 3.090	30m
Panchromatic		8	0.520 to 0.900	15m
Thermal		6	10.40 - 12.50	60m

The Landsat ETM+ image obtained from landmap was already resampled to 25m spatial resolution. Therefore, this resolution was adopted for the subsequent analysis.

An important step in the integration of multi-source data is to achieve an accurate geometric rectification of all image data. The ETM+ provides 8 bands of data for each image (see Table 3.1). The panchromatic band was used to check the geometric registration with the OS 1:2500 digital map data (see section 3.6). Nine Ground Control points (GCP) were identified and the images were resampled using a linear mapping function and nearest neighbourhood resampling. The resulting Root Mean Square Error (RMSE) was less than one half of the image pixel resolution. This was judged to be quite acceptable for the subsequent analysis using per-parcel classification and mapping to 250m MODIS data.

A False Colour Composite for the ETM+ image acquired on 17th June 2000 was created using bands 2, 3, and 4 (FCC432) (see Table 3.1) and is displayed in figure 3.3. This composite shows the image was cloud free except in some parts of the scene, where the clouds appeared as white spots.

The Global Land Cover Facility (GLCF) at the University of Maryland hosts an archive for satellite images that are free to download (http://landcover.org/ [2003, January]). A further two ETM+ images were downloaded during October 2004 from GLCF. The acquisition date for these images was 4th April 2002 and 11th September 2002. The images were obtained for this study for sole the purpose of comparing the results of the atmospheric correction applied to the ETM+ images. These will not be considered in the classification study, because the main objective of this work is to develop a methodology to combine multi-temporal with multi-scale, multi-source data.

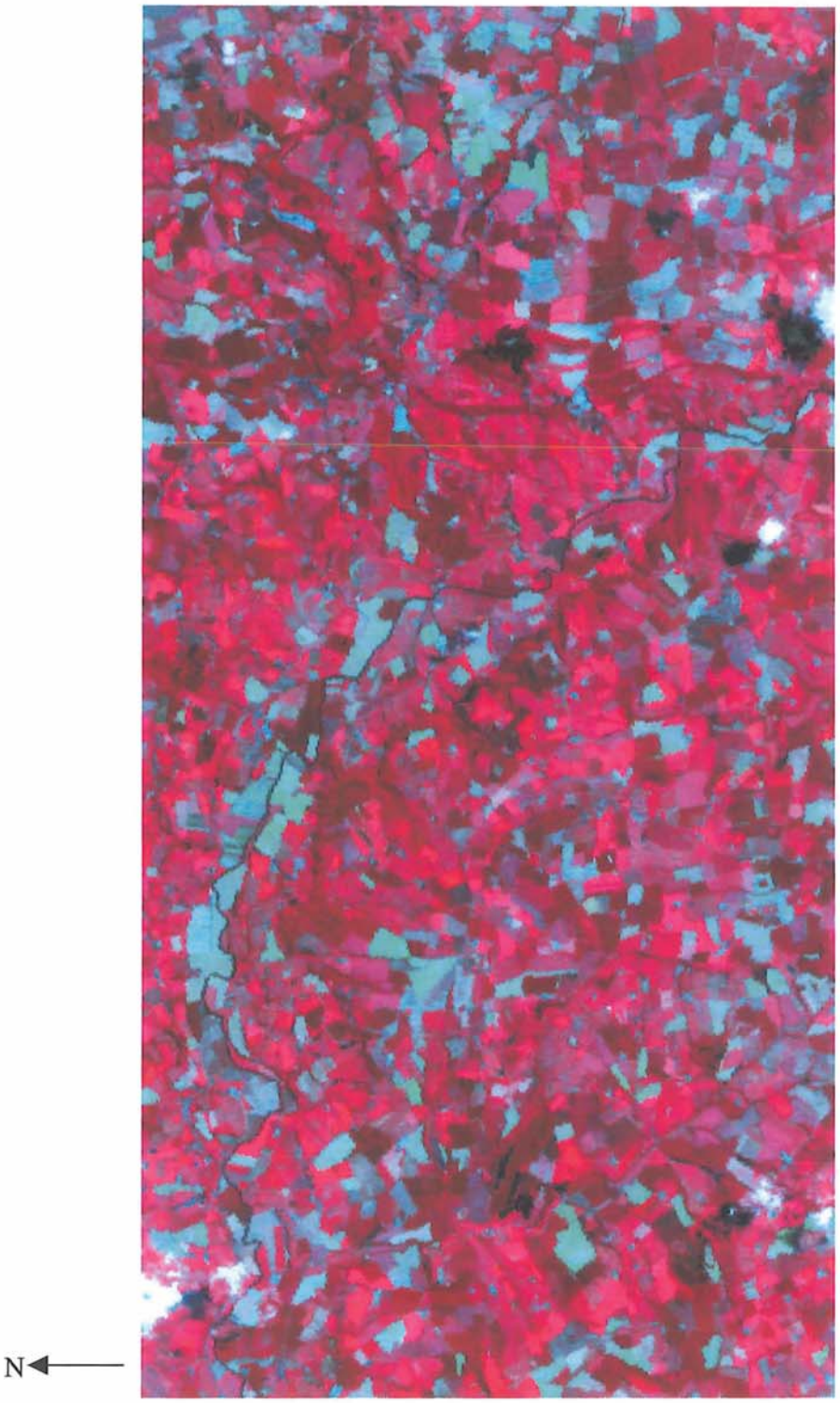

Figure 3.3: FCC for ETM+ image using Bands 2, 3, and 4 (17th June 2000)

3.4.2 MODIS\Terra Images

As the main objective of this study is to integrate suitable information from multi spatial resolution and/or multi-temporal satellite images for the purpose of developing a classification framework to improve the classification of remotely sensed data, it was decided to obtain images of coarser spatial resolution than the ETM+ image. The MODerate Resolution Imaging Spectroradiometer (MODIS) sensor on board the Terra satellite platform has a number of advantages over the alternatives, the Advanced Very High Resolution Radiometer (AVHRR) and the Sea-viewing Wide Field-of-view Sensor (SeaWiFS), in term of spectral resolution, number of channels and spatial resolution (Table 3.2)

Table 3.2: MODIS Bands Details

Nominal Spatial Resolution			
250 m	*500 m*	*1 km*	*1 km*
Reflected Solar Bands			**Emissive Bands**
Band 1 (620-670 nm)	Band 3 (459-479 nm)	Band 8 (405-420 nm)	Band 20 (3.660-3.840 μm)
Band 2 (841-876 nm)	Band 4 (545-565 nm)	Band 9 (438-448 nm)	Band 21 (3.929-3.989 μm)
	Band 5 (1230-1250 nm)	Band 10 (483-493 nm)	Band 22 (3.939-3.989 μm)
	Band 6 (1628-1652 nm)	Band 11 (526-536 nm)	Band 23 (4.020-4.080 μm)
	Band 7 (2105-2155 nm)	Band 12 (546-556 nm)	Band 24 (4.433-4.498 μm)
		Band 13L (662-672 nm)	Band 25 (4.482-4.549 μm)
		Band 13H (662-672 nm)	Band 27 (6.535-6.895 μm)
		Band 14L (673-683 nm)	Band 28 (7.175-7.475 μm)
		Band 14H (673-683 nm)	Band 29 (8.400-8.700 μm)
		Band 15 (743-753 nm)	Band 30 (9.580-9.880 μm)
		Band 16 (862-877 nm)	Band 31 (10.780-11.280 μm)
		Band 17 (890-920 nm)	Band 32 (11.770-12.270 μm)
		Band 18 (931-941 nm)	Band 33 (13.185-13.485 μm)
		Band 19 (915-965 nm)	Band 34 (13.485-13.785 μm)
		Band 26 (1.36-1.39 μm)	Band 35 (13.785-14.085 μm)
			Band 36 (14.085-14.385 μm)

Furthermore, there are a number of ready developed products produced for MODIS data by the National Aeronautics and Space Administration (NASA); for example, surface

reflectance, cloud cover, and vegetation indices. The difficulty with MODIS is that it is relatively new. This means that the data requires a bit more careful handling than would otherwise be the case. The MODIS instrument has detectors that are square or rectangular in shape and receive a signal at any particular instant of time from an area of the Earth's surface that is one of 1000, 500, or 250m nominal size for nadir pixels.

MODIS data comes in several levels. The raw data is what comes out of the ingest process. This is then converted to Level 0. Level 1A data set contains counts for 36 MODIS channels, along with raw instrument engineering and spacecraft ancillary data. The Level-1A data are used as input for geolocation, calibration, and processing. Level 1B (L1B) is a scene of MODIS data radiometrically calibrated and geolocated to the latitude and longitude centres of the 1 km resolution pixels. There are farther advanced levels that contain derived geophysical variables and model output or the results from analyses of lower level data.

As standard, MODIS data for each level comes in a Hierarchical Data Format (HDF) file. HDF is a file format developed by National Centre for Supercomputing Applications (NCSA) for storing multi type datasets. There is a separate geolocation product that contains useful ancillary products such as position, sensor and solar angles for each 1km pixel.

From the daily MODIS images, 31 images were selected. These images are spread over the year 2000, and are for days that visual inspection indicated had minimum cloud cover. These data (level 1B) were ordered through the GES Distributed Active Archive

Centre (DAAC, URL: http://daac.gsfc.nasa.gov/ [2004, May]). Each of these images contains the following data set:

- ❖ Calibrated and geolocated radiances at-aperture for MODIS spectral bands 1 through 7 at 500m resolution.
- ❖ Calibrated and geolocated radiances at-aperture for MODIS spectral bands 1 and 2 at 250m resolution.
- ❖ Calibrated and geolocated radiances at-aperture for all 36 MODIS spectral bands at 1km resolution.
- ❖ The products (MOD35_L2) that contain information about cloud cover.

The study area was extracted from the images using MsPhinx, free software available from the Web. However, the extracted image data were found to be of poor quality, and not of a sufficiently satisfactory geographic accuracy. In this software the user may specify the extent of the area of interest using minimum and maximum latitude and longitude, however, the actual output geo-location was not the same as the input minimum and maximum. A MATLAB program was therefore written to read the MODIS HDF files and extract the following data sets for the study area (Appendix 3):

- o Surface height above geoid, solar zenith and azimuth angles, satellite zenith and azimuth angles
- o All 36 bands at 1km resolution with the latitude/longitude geographic location for the center of each pixel
- o Bands 1 through 7 at 500m pixel resolution with their interpolated latitude/longitude geographical locations
- o Bands 1 and 2 at 250m pixels resolution with their interpolated latitude/longitude geographical locations
- o Cloud cover information

It was necessary for these data to be converted to the BNG projection. This was performed using the PROJECT module in IDRISI. Additional calculations were performed to find the coordinates of the corners of each pixel assuming that each pixel

has a rectangular shape, rather than the actual circular or elliptical shape. The purpose of this is to identify the area imaged simultaneously by each coarse MODIS pixel and Landsat ETM+ pixels.

All these information data sets were written again to HDF file format using MATLAB, so that it was easier to analyze than the huge files size downloaded from DAAC. Table 3.3 shows the contents of the new HDF file created for each date together with the source and the processing stage carried out.

Prior to any decision about how to use these multi-temporal MODIS images, the imagery must be displayed and examined so that any problems could be identified and resolved.

The most important aspect in incorporating data from different sources and / or multi-temporal data is the accurate registration between the images. The following section highlights the main problems with regard to these MODIS images.

Table 3.3: The SDS contained in each MODIS HDF file extracted for the study area

Data set name in the HDF file	Source	description
long_lat_1000	MOD03	Longitude and Latitude in degrees for each 1km pixel viewing the study area.
Height	MOD03	the average elevation in each pixel
SensorZenith	MOD03	Sensor Zenith angle for each pixel
SensorAzimuth	MOD03	Sensor Azimuth angle for each pixel
Range	MOD03	Distance between the sensor and the earth surface for each ground pixel
SolarZenith	MOD03	Sun zenith angle
SolarAzimuth	MOD03	Sun azimuth angle
Land/SeaMask	MOD03	Land sea mask
EV_250_Aggr1km_RefSB	MOD021KM	Aggregated reflectance band 1 and 2 to nominal spatial resolution 1 km
EV_500_Aggr1km_RefSB	MOD021KM	Aggregated reflectance band 3 through 7 to nominal spatial resolution 1 km
EV_1KM_RefSB	MOD021KM	bands 8 through 19 and band 26
EV_1KM_Emissive	MOD021KM	Earth view emissive bands 20-36 excluding band 26
long_lat_500	MOD02HKM	Longitude and Latitude for each 500m pixel viewing the study area.
EV_250_Aggr500_RefSB	MOD02HKM	Aggregated reflectance in band 1 and 2 to nominal spatial resolution 500 m
EV_500_RefSB	MOD02HKM	Earth View 500m Reflective Solar Bands 3-7
long_lat_250	Computed	Longitude and Latitude for each 250m pixel viewing the study area.
EV_250_RefSB	MOD02QKM	Earth View 250M Reflective Solar Bands 1 and 2
Cloud_Mask	MOD35_L2	MODIS Cloud Mask and Spectral Test Results from MOD35_L2
Quality_Assurance_cloudMask	MOD35_L2	Quality Assurance for Cloud Mask
bng_1000	Computed	Geo-location of each 1 km pixel re-projected to (BNG)
bng_500m	Computed	Geo-location of each 500m pixel re-projected to (BNG)
bng_250m	Computed	Geo-location of each 250m pixel re-projected to (BNG)
corner_bng1km	Computed	coordinate of the four corners of each 1km pixel assuming the footprint of the pixel is quadrilateral
corner_bng500	Computed	coordinate of the four corners of each 500m pixel
corner_bng250	Computed	coordinate of the four corners of each 250m pixel

3.4.2.1. Panoramic bowtie effect

Firstly, the data still has a 'bowtie' problem. This is a common problem with wide scan angle sensors, where the image seems distorted near the edges. This results from the fact that MODIS scans 10 lines at a time, and the footprint of a pixel increases with distance from the nadir. The distance to a pixel increases with scan angle and is further exaggerated due to the earth's curvature. This means that the pixels near the edge of an image are bigger than the ones in the middle.

The Terra satellite is configured to move forward 10km in the time that it takes MODIS to scan once. This is so that pixels in the middle of the scan line match up next to each other. However, at the edges the pixels are bigger; up to 6 times wider and 4 times longer. This results in over sampling, i.e. the same spot is imaged twice. Figures 3.4 and 3.5 show the bowtie effect on the MODIS images acquired on the 17 and 18 June 2000 for the study area. These figures show a plot of the MODIS pixels centres and the centre of each 1 km^2 ground pixels covering the study area. Figure 3.5 demonstrates the MODIS pixels' growth and the overlapping of scan lines due to the bowtie effects. This problem has nearly disappeared in Figure 3.4, because the study area is observed from near nadir. By contrast, in the second image, Figure 3.5, the study area was close to the edge of the MODIS scene with a large view angle.

The reason that bowtie effects are not obvious in ETM+ data, is that the earth curvature effect is smaller as the swath width of the instrument is smaller. Consequently reprojected image is free from the bowtie artefacts. However, it still suffers from the problem of the actual size of the footprints of the pixels.

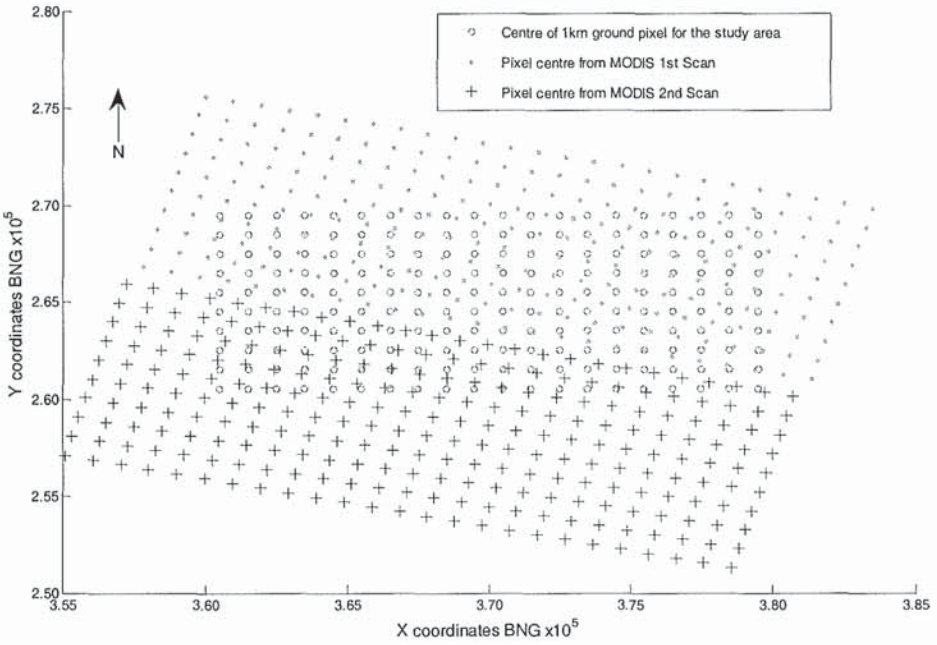

Figure 3.4: Overlapping due to bowtie effect over the study area from MODIS scene on 17th June 2000

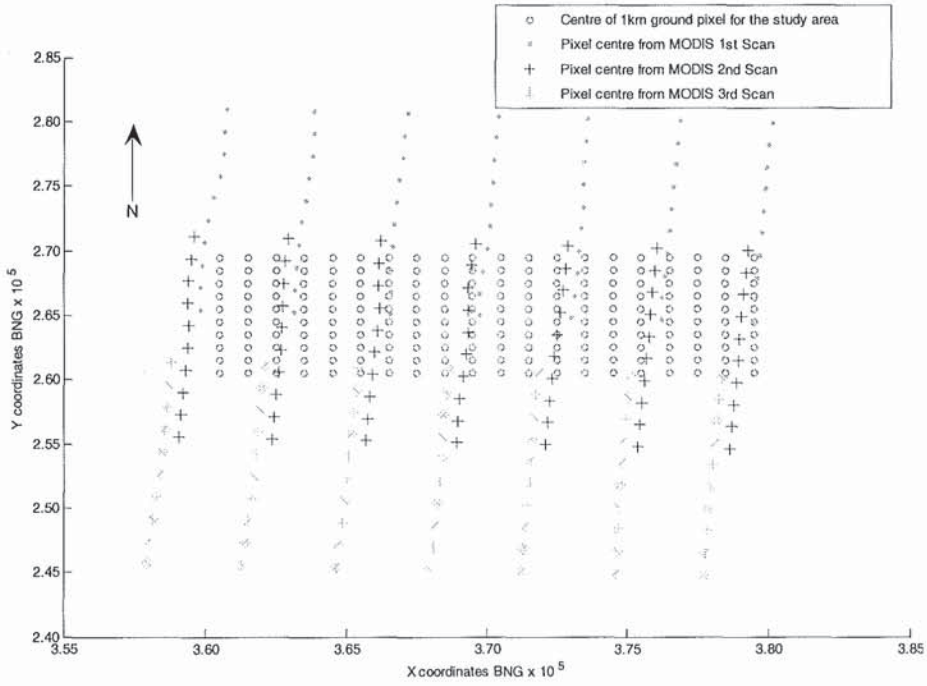

Figure 3.5: Overlapping due to bowtie effect over the study area from MODIS scene on 18th June 2000

For MODIS, 250m, 500m and 1000m are nominal resolutions, and unless an image is reprojected, the actual size of the pixel will vary with scan angle. If reprojection is undertaken, the DN values for each pixel should not be considered equivalent to what is actually within each reprojected pixel. For example, if the nearest neighbourhood resampling function were used to resample the MODIS image to 1 km^2 resolution image during reprojection, then the DN values of each 1 km^2 pixel will be equivalent to the measured values over an area covering more than 12 km^2. Thus, using a resampled MODIS image would not be suitable to infer the probability of finding a land-cover class, or the proportion of a class, within a 1 km^2 pixel. This error will become obvious if one tries to aggregate a high-resolution image to a coarse-resolution image.

This is a serious problem and it is therefore more appropriate to use the actual pixel's size, rather than the resampled pixel if multi-scale analysis is considered. Furthermore, in multi-temporal analysis we face another problem as discussed in the following section.

3.4.2.2. Problems with Inconsistent Pixels

Assuming perfect geo-referencing is obtained from the geo-location products for MODIS images, the problem of inconsistency of pixel location still exists. This means the actual area imaged by the sensor at a stated location is not the same for each revisit. Thus any change observed for a given location, between two different dates may not necessarily be due to an actual land cover change. The changes may be due to the different mixture of land cover imaged on these different dates.

Figure 3.6 shows the aerial photograph covering one MODIS ground pixel at 500m resolution centred at 369750, 265250 coordinate of the British National Grid system

(BNG). This photograph shows the expected types of land cover within the resampled 500m resolution MODIS pixel. However, the actual scene that has been imaged by the MODIS sensor at this resolution during each visit will vary. This effect is depicted in Figure 3.7 through to Figure 3.13, which show the footprint of the nearest IFOV MODIS pixel to this ground pixel, assuming for simplicity that the footprint of the area imaged by the MODIS sensor has a perfect rectangular shape.

According to Nishihama *et al.*, (1997), MODIS senses the earth surface using a scan mirror that rotates at a constant speed. A single sample consists of the integrated signal received at the detector during the entire sampling interval. This sampling interval is typically the amount of time it takes the projected image of the detector on the ground to move along-scan one sample, i.e. 333.333 μsec (dwell time) for the 1 km bands. The ground image effectively travels across the detector during the sampling period, and thus, each area is actually sensed for twice as long as the nominal detector pattern.

Furthermore, the accuracy of the MODIS geolocation is limited by the uncertainty in the spacecraft, instrument, and elevation data provided to the Earth location algorithm. It was estimated that the combined positional errors for 1 km pixel will vary with the scan angle, and may be approximately 303 to 1417m along-scan, and 303 to 588m along track (Nishihama *et al.*, 1997). This means that MODIS images should be handled cautiously when extracting information from a particular pixel.

From Figures 3.7 through to Figure 3.13, it is obvious that even if the pixels at the edge of a scan were excluded from the analysis, and only the pixels at nadir were considered,

the nearest pixel to the ground pixel of interest, they will contain different mixtures of classes.

If the bilinear resampling function were employed it would not achieve better results. This requires further research to address the effect of different resampling schemes on coarse mixed resolution pixels.

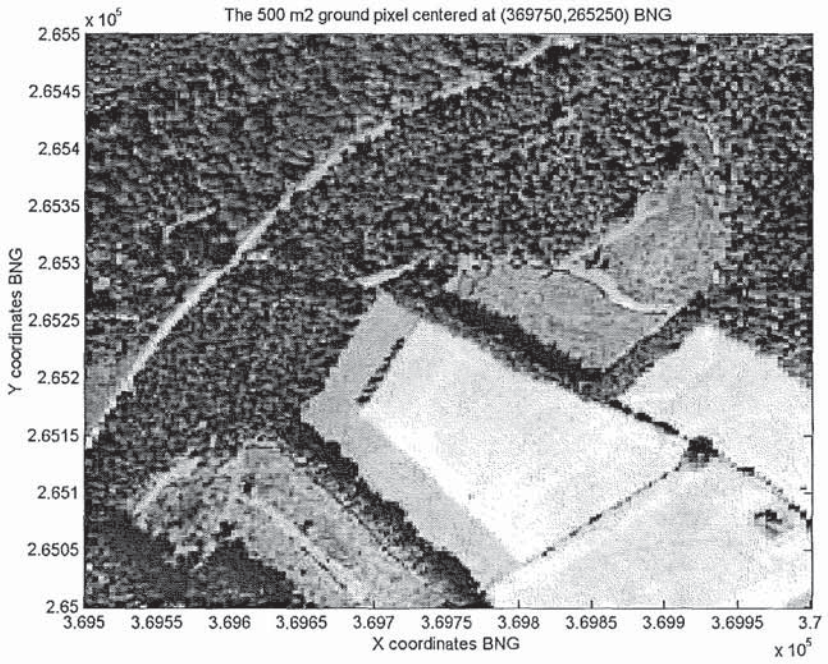

Figure 3.6: Miniature of what can view a typical 500 m resolution pixel on the ground centred at BNG coordinate 369750, 265250 (Not to scale)

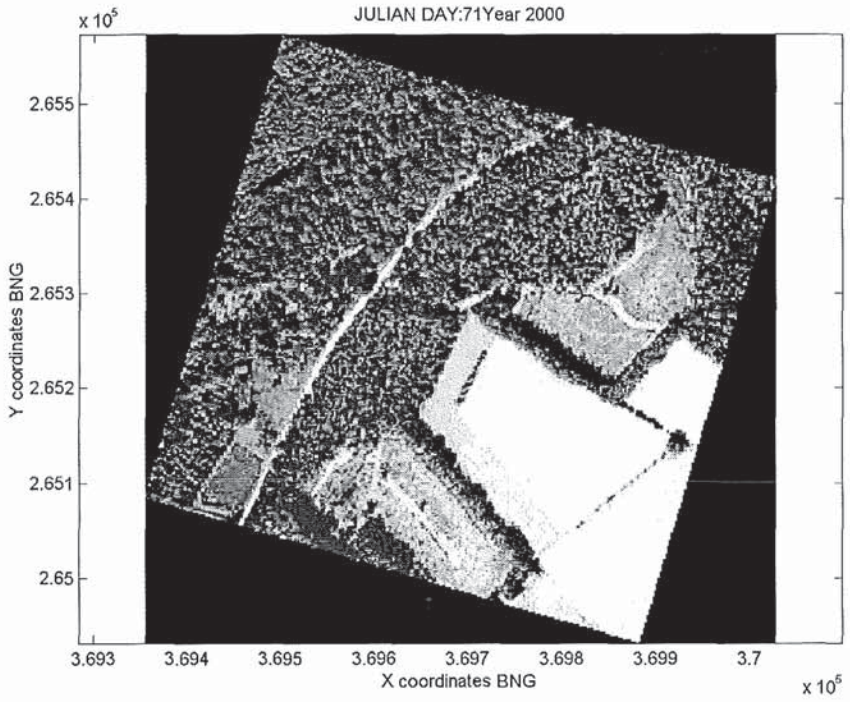

Figure 3.7: Miniatures of the closest footprint to the typical 500 m MODIS pixel (Fig 3.6) acquired on 11th March 2000 (Not to scale).

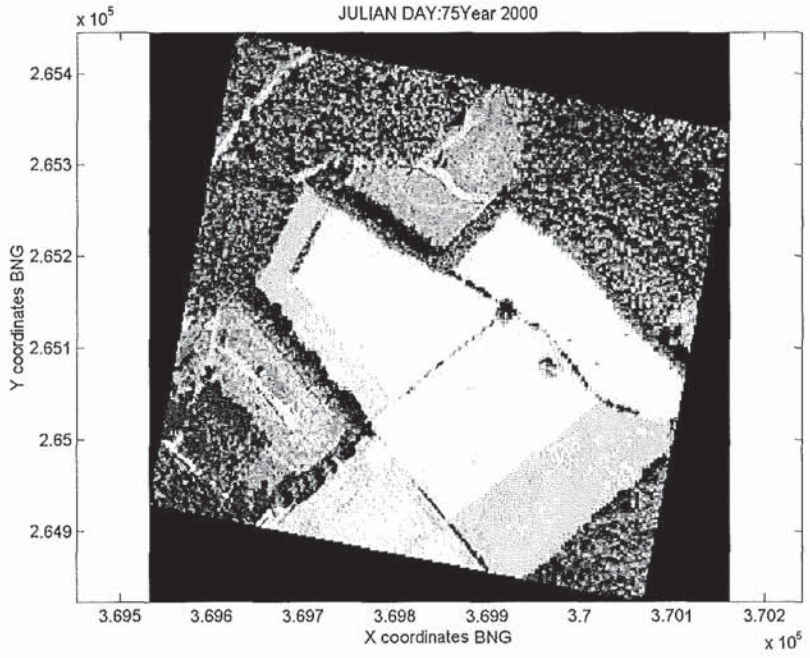

Figure 3.8: Miniatures of the closest footprint to the typical 500 m MODIS pixel (Fig 3.6) acquired on 15th March 2000 (Not to scale).

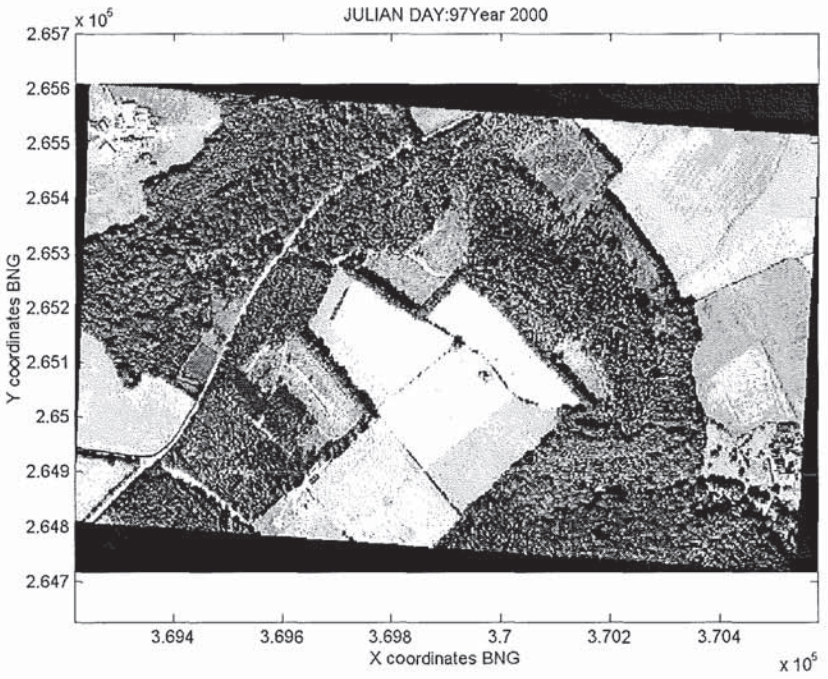

Figure 3.9: Miniatures of the closest footprint to the typical 500 m MODIS pixel (Fig 3.6) acquired on 6th April 2000 (Not to scale).

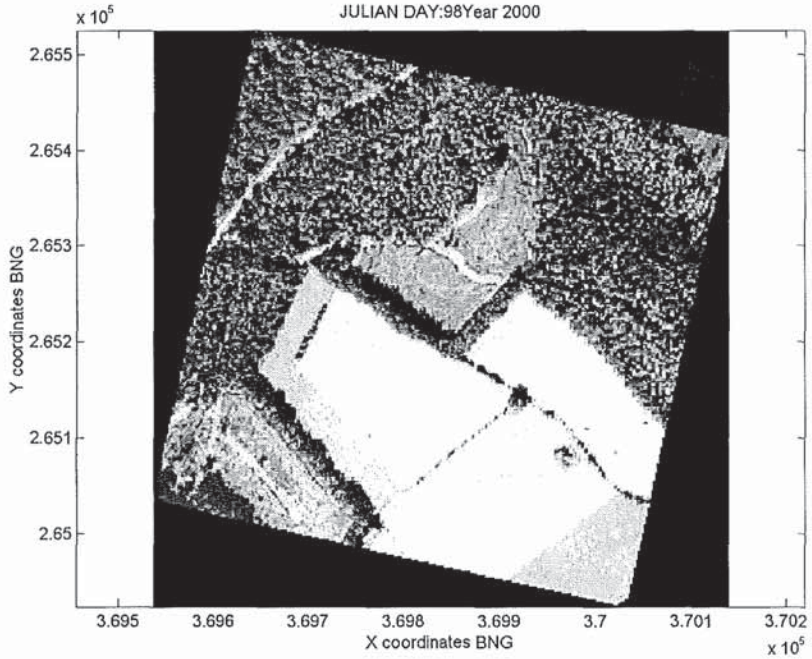

Figure 3.10: Miniatures of the closest footprint to the typical 500 m MODIS pixel (Fig 3.6) acquired on 7th April 2000 (Not to scale).

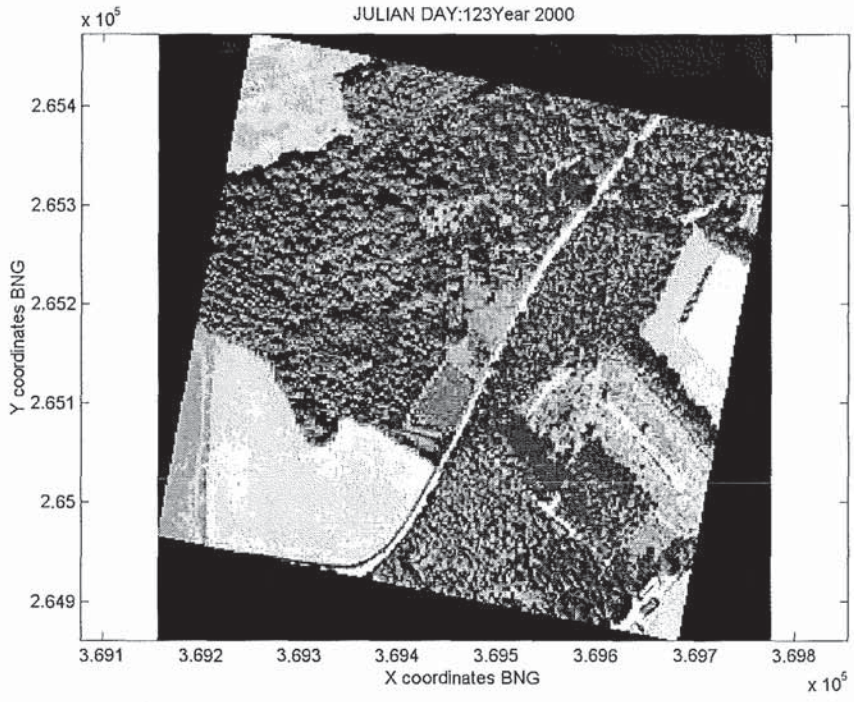

Figure 3.11: Miniatures of the closest footprint to the typical 500 m MODIS pixel (Fig 3.6) acquired on 2nd May 2000 (Not to scale).

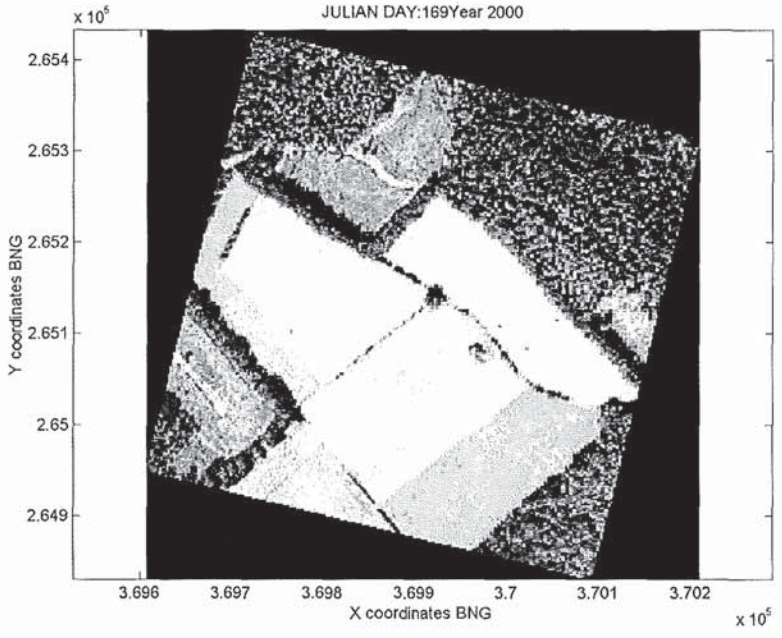

Figure 3.12: Miniatures of the closest footprint to the typical 500 m MODIS pixel (Fig 3.6) acquired on 17th June 2000 (Not to scale).

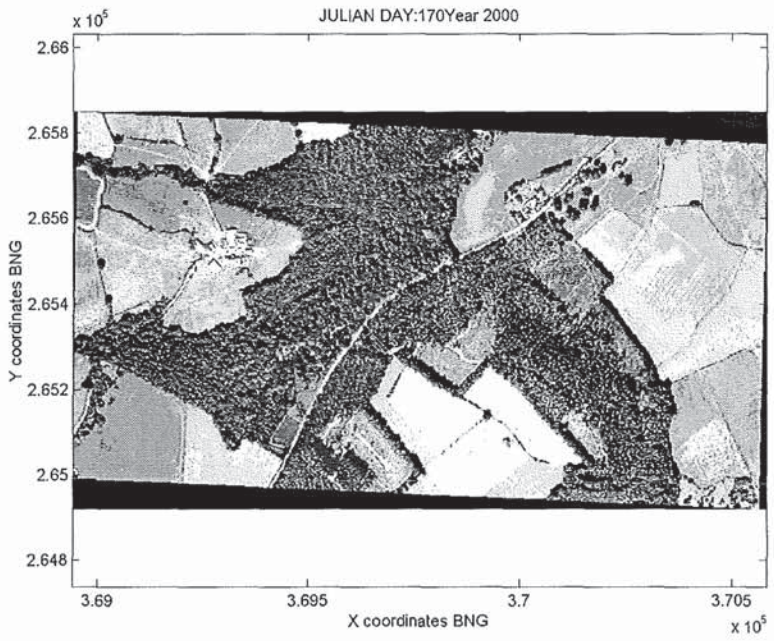

Figure 3.13: Miniatures of the closest footprint to the typical 500 m MODIS pixel (Fig 3.6) acquired on 18th June 2000 (Not to scale).

3.5. Aerial Photography

The primary use of aerial photography in this study is to get a closer look at the finer detail (resolution 2m) in order to identify the infrastructure of the study area. Thus the woodland and orchard areas can be identified and separated from the other agricultural lands, which are difficult to distinguish using satellite image at a resolution of 25m.

It is important to note that using photography will not help in identifying the crops growing in each field for two major reasons. Firstly, the aerial photographs were acquired during the spring of 1999, hence the crop distribution is not the same as in the ETM+ image captured on 17 June 2000. Secondly, the aerial photograph in JPG format is very

compressed in three visible bands only; therefore, it is not appropriate for classification purposes.

Furthermore, such aerial photographs are very costly and in many cases may not be available on or close to the date of the satellite images that are to be classified. Therefore, in this study, the aerial photograph will not be used to help in classification; however, it will help in the visual accuracy assessment of the classification procedure to be used.

The visual interpretation of the aerial photography for this project was preferred over computer-assisted interpretation, because firstly the image is highly compressed in RGB format with high spatial resolution and this would result in a noisy computer interpretation. Secondly, the use of context in the visual interpretation of the high resolution RGB image is efficient since it involves the relationships between the objects in the image and thus reduces the ambiguities in the classification.

The photograph data were obtained from www.multimap.com [2003, September] in the form of a series of photographs covering small areas with some overlap. These images were captured during spring 1999. After processing, the resulting photograph mosaic was geo-referenced and resampled to the BNG coordinate system using 11 ground control points selected from the Ordnance Survey OS 1:2500 digital map (see section 3.6). The resulting photograph has a good geo-registration with both satellite image and the OS 1:2500 digital map. Figure 3.14 displays the resulting photograph.

Figure 3.14: The constructed aerial photograph (Copyright: www.multimap.com, [2003, September])

3.6. OS 1:2500 digital map (Land-Line Plus®)

The OS 1:2500 digital map was downloaded on 19th October 2004 from Digimap (http://www.edina.ac.uk/digimap). The downloaded files were in NTF format. NTF is used by the Ordnance Survey in Britain and stands for Neutral Transfer Format (former National Transfer Format). Each file was for a tile covering 1x1 km created with a map scale of 1:2500. These files were amended on different dates during the year 2004. Therefore, insignificant changes can be expected between the field boundaries depicted in the OS 1:2500 digital map and the boundary of the fields discernible from the ETM+ image acquired on 17th June 2000.

It was anticipated that this data source would aid the segmentation of the Landsat ETM+ image, rather than using edge detection algorithms on the image itself. The purpose of the segmented image is to improve the classification results by per-parcel classification rather than per-pixel classification (see Chapter 4). Therefore, all downloaded files were converted from NTF format to Shape file format and mosaiced together using the ESRI (UK) Map Manager V6.2 software (http://www.esriuk.com, [December, 2005]). The shape file was then imported to Idrisi32 as a vector layer, to check its suitability as segmentation for the ETM+ image. However, close examination of this OS 1:2500 digital map confirmed that some modification to the original data was required, for example, to close the polygons surrounding the boundary of each field in the landsat image, and to add new lines where some fields have been changed or show different cultivation patterns.

The OS 1:2500 digital map, FCC432 and aerial photograph, were overlaid using AutoCAD (Figure 3.15) and the necessary modifications carried out manually - a process took several days to carry out for the entire study area. The purpose of this was to obtain an image of the boundaries of each field discernible in the ETM+ scene, to help in the field classification and to calculate the area of each crop more accurately. Figure (3.16) shows the resulting map of field boundaries.

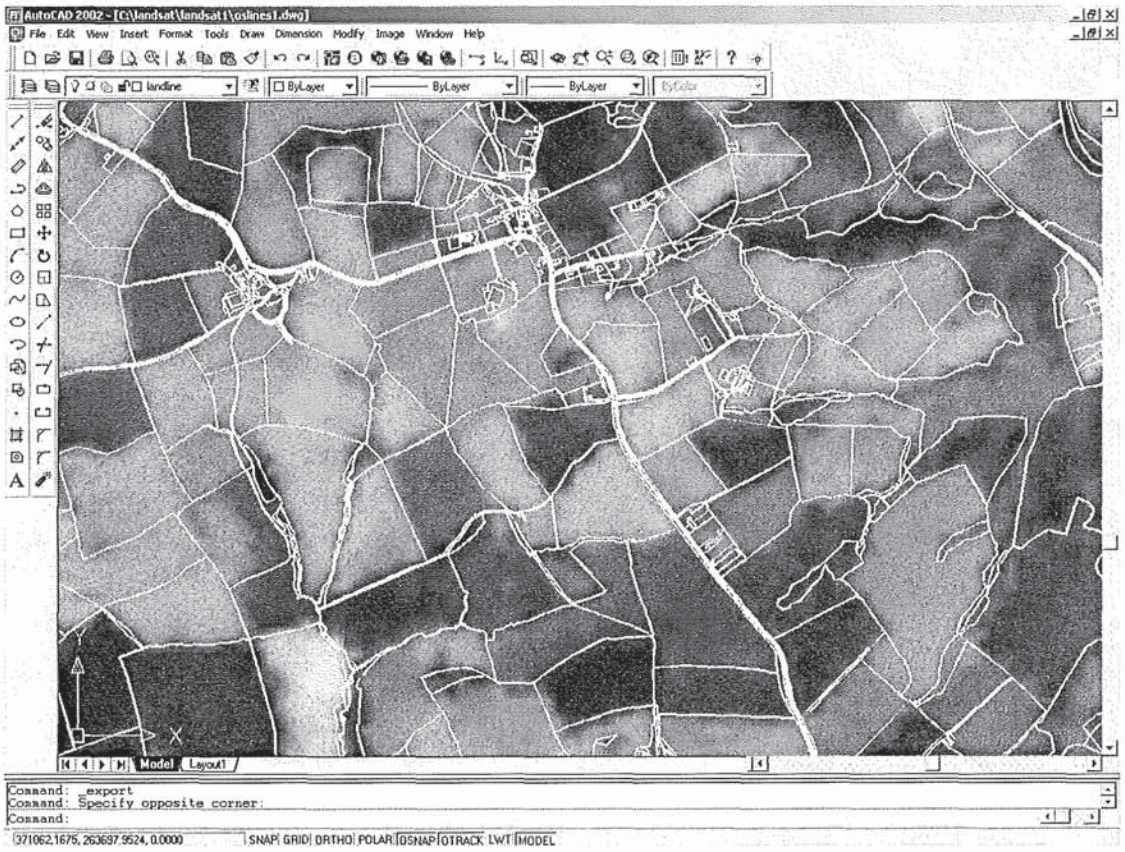

Figure 3.15: AutoCAD interface shows a small area of OS 1:2500 Digital map overlaid on the ETM+ FCC432 image

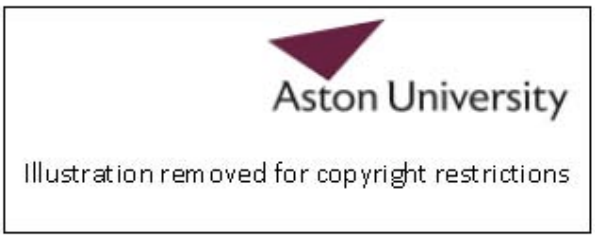

Figure 3.16: OS 1:2500 digital map (modified from original source: http://www.edina.ac.uk/digimap , [2004, October])

3.7. The agriculture census data

The Agricultural Census is conducted in June each year by the government departments dealing with Agriculture and Rural Affairs, and during the census information relating to land use, crops, livestock, labour, horticulture and glasshouse is collected. Each farmer declares the agricultural activity on their land via a postal questionnaire. The respective government departments collect the data and publish the results as aggregated information relating to the farm holdings in each parish.

The census data was obtained for year 2000 from the Edinburgh University Data Library (http://datalib.ed.ac.uk/ [2005, December]). Edinburgh University Data Library has developed algorithms, which convert the data from the parish level into grid square estimates (http://edina.ac.uk/agcensus [2004, April]). The key to transforming the raw data into grid square data is the definition of each parish in terms of 1km squares. This framework is used in conjunction with a 7-fold classification of the land-use of the same 1km grid squares. The resulting 1 km grid square data are aggregated to 2km, 5km, and 10km grid squares and are available in ASCII delimited format.

According to the data guide obtained along with the agricultural census data, this data provides a robust estimate of crop production at a broad national and regional level. However, for specific individual small areas, the level of usefulness diminishes. This is mainly because the survey is based on the aggregate data from registered farm holdings. Thus the unregistered farm holdings are excluded. Furthermore, farm holdings may have detached fields that may be separated by a very large distance. In addition a farmer is only required to return one census form, even if several holdings are owned. This can

lead to under- and over-reporting of agriculture in certain areas. If the farmer did not respond to the survey a crop distribution is estimated and input. These values can be extremely variable for individual holdings and for specific small areas. However, even if a response is received there is a possibility of a farmer either deliberately or accidentally makes a false return.

Furthermore, the location of the holding, as given on the register of holdings, is only an approximation to where any farming actually takes place. In general a central reference for each parish is known, or calculated. To produce small area figures it is assumed that all farming activity takes place at this point. Generally this approximation is good enough for practical purposes. However, it is likely to breakdown for a specific small area.

Therefore, in this work, the agriculture census data of 2km square grid was used as an approximation to what crops are likely to be grown in the study area. The primarily analysis of this data indicated that the areas (hectares) of the main agricultural classes that one would expect to find in this area are as shown in Table 3.4. From this Table the main classes that the research should be able to identify within the study area are: the grasslands (temporally and permanent), wheat, woodland (coniferous / deciduous), winter barley, field beans, oats, orchards, potatoes, sugar beet, and bare earth. Together these classes should account for more than 90% of the land cover within the study area.

Table 3.4: The total agriculture census data for the study area

Agriculture class	Total Area (hectares)	Proportions %
All Other Grassland, Excluding Rough Grazing - Permanent Grassland	5838.8	37.2
Wheat	2401.6	15.3
Woodland	1236.3	7.88
Grass Less Than 5 Years Old - Temporary Grassland	1184	7.54
Winter Barley	771	4.91
All Set-Aside	574.5	3.66
Field Beans	442.4	2.82
Oats	425.8	2.71
Total Orchards, Small Fruit and Grapes	397.4	2.53
All Other Land (Buildings, Ponds, Paths, Etc)	337.4	2.15
Oilseed Rape - Winter and Summer (Not On Set-Aside)	331.8	2.11
Orchards - Commercial and Non-Commercial	313.1	1.99
Potatoes	230.9	1.47
Sugar Beet	222.9	1.42
Spring Barley	206.2	1.31
Maize, Including For Stock Feeding	184.7	1.18
Other Arable - Hops, Flax and Others	151.6	0.97
Peas For Harvesting Dry	124.7	0.79
Fodder - Fodder Beet, Mangolds, All Other Crops Used For Stock Feeding	86.49	0.55
Linseed (Not On Set-Aside)	80.5	0.51
Other Cereals - Mixed Corn, Rye, Triticale	60.1	0.38
Bare Fallow (Not On Set-Aside)	34.8	0.22
Total Vegetables and Salad Grown In Open	31	0.2
Fodder - Turnips, Sweded, Kale, Cabbage, Savoy, Kohl Rabi and Rape	17.7	0.11
Small Fruit - Strawberries, Raspberries, Blackcurrants, Gooseberries, Blackberries, Wine Grapes and Other Small Fruit	10	0.06

3.8. Summary and conclusion

In this chapter all the data that were used in this thesis have been described. Some of the problems with these data have been highlighted, to emphasise potential problems of data analysis. This was of help in understanding the nature of each data source, and how it should be used efficiently during the remaining chapters of this thesis.

The study area covers 20x10 km in a typical rural area situated southwest of Birmingham, UK. It is mainly dominated by agricultural fields. An ETM+ image will be used as a primary image to be classified with the help of other data sources. This image was a subset image from the ETM+ scene acquired on 17th June 2000 obtained from (www.landmap.ac.uk , downloading date: 2002, December). The aerial photography will be used to visually check the quality of the resulting classification in this work rather than using it in the classification procedure. This is because the aerial photography is costly and may not exist in real world projects for larger areas.

The OS 1:2500 digital map was used because was considered a valuable data source for the segmentation of the ETM+ image, which was required in order to perform per-parcel classification instead of per-pixel classification. The advantages of the per-parcel classification will become more obvious in the following chapters. Despite the fact that this data source is expensive and field boundary delineation was laborious it was essential for this work. However, in cases where this source is not available, it can be substituted with a segmentation map derived from the image.

A number of images and other products from the MODIS sensor were downloaded free of charge from the Distributed Active Archive Centre (DAAC). This data source was

used as a secondary source of information to improve the classification of the Landsat ETM+ image. However, it was decided to exclude the MODIS images that fall near the edge of the swath, and to pay careful attention to the interpretation of the temporal reflectance or NDVI profile changes, in light of the misregistration and inconsistency of MODIS pixels.

The integration of MODIS images with the ETM+ image is a big challenge that will be addressed in chapter 5. Firstly, the bigger pixel size of MODIS images makes the majority of the pixels mixed and difficult to integrate with the relatively small ETM+ pixels. Secondly, the inconsistency in geo-referencing of multi-temporal MODIS images makes it difficult to study the potential changes in the land cover from these images. Therefore, each MODIS image should be integrated individually with the Landsat ETM+ image.

Finally, the agricultural census data obtained for this work was not as good as it was hoped. This data source gives an estimate of crops within 2 km grid square. Thus it can not be used to identify the crop growing in each individual agricultural field. However, it might be useful for an overall estimate of the crops in the study area and it may give an indication of the potential classes that can be mapped using remotely sensed images.

Chapter 4

Landsat ETM+ Data analysis and classification

4.1. Introduction

In this chapter the imagery and other data introduced in chapter 3 will be analysed. Several classification algorithms will be discussed in the light of the visual quality of these classifications to determine their effectiveness. For this a visual comparison of the classification results with both the Landsat ETM+ FCC and the aerial photograph is undertaken. This is, by nature, an inaccurate method for determine the accuracy of the resulting classification, but nevertheless is a useful exercise as a quick assessment can be achieved.

In this work, there was no training data apart from the aerial photography and the agriculture census data in 2 km grid square format. The date of the aerial photography was one year before the Landsat ETM+ image, thus inappropriate for annual cropping patterns. The agriculture census data provides an estimate of the crops grown within a 2km square, thus it is unsuitable for training purpose. Therefore, a site visit was organised in October 2003 to collect information about the agriculture activity within the study area. However, the data collected was insufficient to enable a supervised classification to be undertaken.

Consequently, unsupervised classification was employed to identify the agriculture crop classes with a view to matching them with the areas of crops given by the agriculture census obtained for same year.

When estimating the areas of crops one should be aware that mixed pixels will occur at the borderline between fields. One way to solve this is to use image fusion techniques that allow the increase of the spatial resolution of the multi-spectral images by combining them with higher resolution panchromatic images. The resulting sharpened multi-spectral image will have a reduced proportion of mixed pixels and an increase in the quality of the classification product. However, fusion techniques alter the spectral information in the original multi-spectral images, and increase the size of data to be analysed. Therefore, it was decided to calculate the areas of each land cover class (crops) using the polygons obtained from OS 1:2500 digital map.

As a first step the Landsat ETM+ image needs to go through the pre-processing stage so that it is ready for the subsequent stage of classification. The next section presents the pre-processing steps that were performed on the Landsat ETM+ image. In order to process the imagery some modules from commercial image processing software were used. The software and the modules used are introduced in section 1.6 and listed in Appendices 2 and 3.

4.2. The pre-processing of the ETM+ Image

In this section some pre-processing steps carried out on the ETM+ image will be described. The first steps were described in chapter 3 when the imagery was introduced. These were to select a window covering the study area from the original scene. The image was then reprojected to the BNG coordinate system. The misregistration with the OS 1:2500 digital map was minimized using nine Ground Control Points GCPs and resample to the nearest neighbourhood using the RESAMPLE module in Idrisi32

(Eastman, 2001). As discussed in Chapter 2, atmospheric correction is found to be necessary when a multi-source data is used. The following sub-sections demonstrate the application of the available methods reviewed in the literature, to correct the ETM+ image over the study area.

4.2.1. Atmospheric correction for Landsat ETM+

The main objective of this section is to perform the necessary atmospheric correction to the Landsat ETM+ image acquired on (17^{th} June 2000) for the study area. Several atmospheric correction methods are available. Some of these methods were demonstrated in the literature review (chapter 2). However, the software available for this study is Idrisi32 package (Eastman, 2001). In this package four methods are incorporated in the ATMOSC module. Since it was very likely that each method would produce different results, it was decided to conduct a small experiment to find which method gave a similar surface reflectance to the available surface reflectance MODIS/Terra product. To achieve this three Landsat ETM+ images were available for three different dates, along with three MODIS/Terra surface reflectance products on same dates as each of the Landsat ETM+ images. These dates are 17/ June /2000, 04/ April /2002, and 11/ September /2002. The study area was extracted from each image using the WINDOW module in Idrisi32. The window extracted from each scene was relatively cloud free.

The ATMOSC module in Idrisi32 offers the Dark Object Subtraction model with the added benefit that it compensates for variations in solar output, according to the time of year and the solar elevation angle. It requires the estimation of the DN of haze. This is accomplished using the minimum DN in the histogram of each band on each date.

However, as there are no deep lakes within the study area in the sub-image, the minimum DN for each band from the original whole image was used as the dark object. This can be justified by assuming that the atmosphere is horizontally homogenous over the whole image. To eliminate single erroneous pixels the minimum DN value was taken as that corresponding to a cumulative proportion of 0.0001 in the image histogram. This value was taken heuristically through examining the histogram and the image. Table 4.1 shows the selected DN values for representing the haze.

Table 4.1: DN values for haze in each band

Date	Band 1	Band 2	Band 3	Band 4	Band 5	Band 7	Band 8
17/06/2000	66	45	34	15	12	10	22
04/04/2002	64	44	33	24	10	7	22
11/09/2002	47	29	19	11	6	5	6

The other parameters required for the model are the date and time of the image, the central wavelength of the image band, the sun elevation, and radiance conversion parameters. These additional parameters were taken from the documentation of each image (the header files and calibration files).

The Cos(t) model was developed by Chavez (1996), as an approximation technique that works well if the data necessary for a full atmospheric correction are not available. It incorporates all of the elements of the Dark Object Subtraction model (for haze removal), plus a procedure for estimating the effects of absorption by atmospheric gases and Rayleigh scattering. It requires no additional parameters over the Dark Object Subtraction model and estimates these additional elements based on the cosine of the solar zenith angle (Eastman, 2001).

In addition to the parameters required for the Dark Object Subtraction and Cos(t) models, the full model requires an estimate of the optical thickness[†] of the atmosphere and the spectral diffuse sky irradiance[‡]. The optical thickness is extracted for each date from the scientific parameters contained within the MODIS/Terra product Level-2 (MOD04_L2) for same date of each ETM+ image. This product is in HDF format and has a data set called "corrected_optical_depth_land" produced at spatial resolution 10x10 km at nadir. Six values for corrected optical depth were found over the study area, some of which were the filling number, -999, which is used to fill the missing values in this product. Therefore, either an interpolated value or an average value for the optical depth can be used. For this study the average value over the study area was used for all bands. The average values of optical depth are 0.656, 0.6067, and 0.173 for the dates 17/6/2000, 4/4/2002, and 11/9/2002, respectively. The default value of (0) was selected for spectral diffuse sky irradiance, because there was no data source for this value.

The daily MODIS products Level-2 (MOD05_L2, MOD07_L2) were used to extract the total water vapour and ozone values required to run the 6S RTCs code. Unfortunately, the outputs were limited when using the 6S version available for the Windows operating system. Thus, the results from the 6S code were not as expected.

4.2.2. Results of atmospheric correction

The ideal way to evaluate the accuracy of an atmospheric correction algorithm would be to compare in situ measurements of atmospheric properties and surface reflectance at the

---

[†] Optical Thickness is a dimensionless distance over which a beam of radiation is attenuated by e^{-1} (GLOSSARY of Meteorological Remote Sensing).

[‡] Diffuse sky irradiance is solar irradiance that reaches the ground that has been scattered by an atmospheric constituent such as air molecules, dust, or clouds. (Online http://www.cmdl.noaa.gov/star/starmeas.html [2005, December 21)

time of image acquisition, with the estimates for these parameters resulting from the various forms of atmospheric correction (Holm *et al.*, 1989; Moran *et al.*, 1992; Ouaidrari and Vermote, 1999). Unfortunately, these measurements are not generally available, which was the case for the current dataset. However, classification and change detection do not necessarily need to be performed with absolute surface reflectance measurements, but can be performed with relative measurements as well. The key point is to maintain consistency in the measurement of surface reflectance among the multi-temporal datasets, whether it is absolute or relative.

In order to evaluate which the methods perform best for this study, the daily MODIS surface reflectance (MOD09) was compared with the atmospherically corrected Landsat ETM+, assuming that the best method for each image is the one that produces similar values to the MODIS surface reflectance products.

Figures 4.1 to 4.3 show the plot of variation in the mean value of surface reflectance over the study area for each spectral band of the MODIS and Landsat ETM+ on each of the dates under consideration. From these figures one can see that the full model produced the worst results. This may be attributed to the use of inappropriate parameters for optical depth and spectral diffuse sky irradiance. To find out whether the worst results were due to bugs in the full model or because of using inappropriate parameters, the optical depth was set to zero in the full model. This experiment produced identical results to the Dark Object Subtraction Model. The experiment goes same way to explaining the similar results obtained by the full model and the cos(t) method as for Figure 4.3 a very small value for optical depth was used for the Landsat ETM+ image on 11th September 2002.

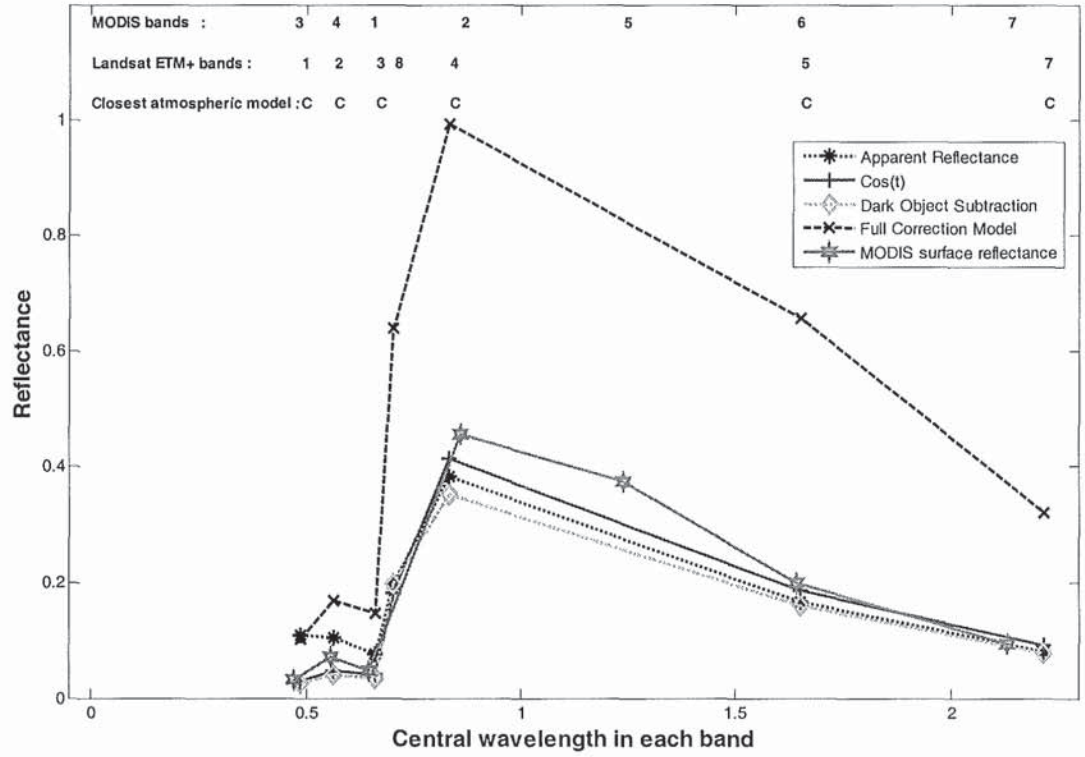

Figure 4.1: Mean surface reflectance for ETM+ and MODIS (17/06/2000)

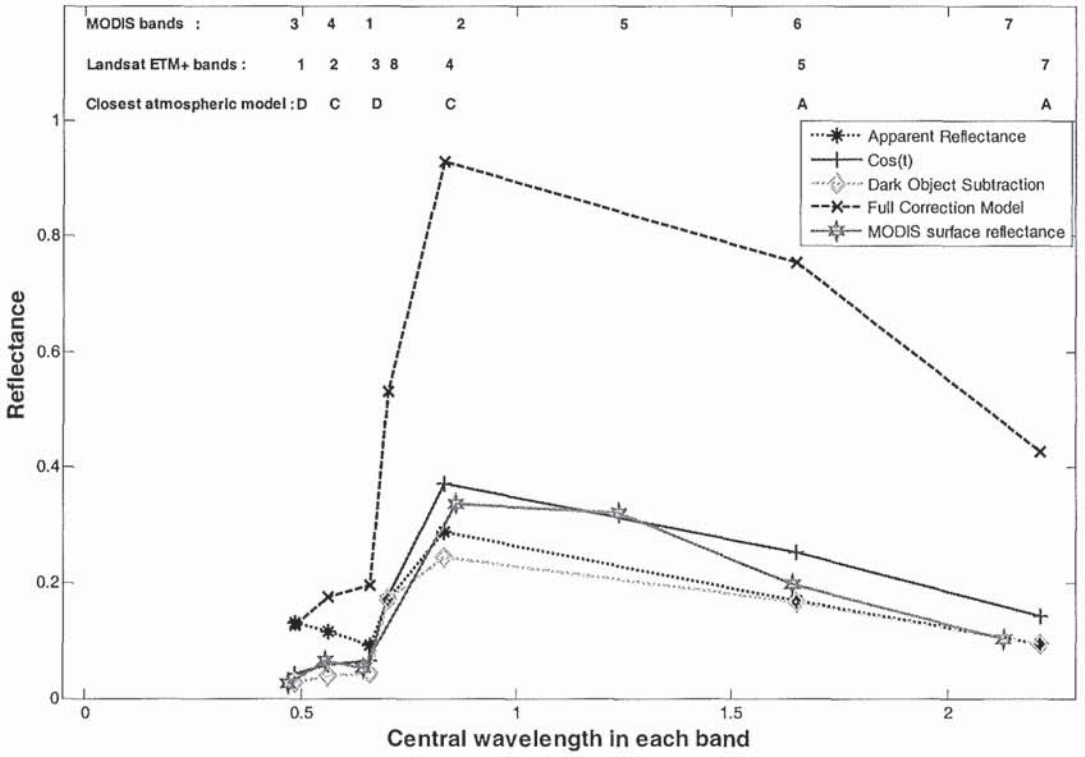

Figure 4.2: Mean surface reflectance for ETM+ and MODIS (04/04/2002)

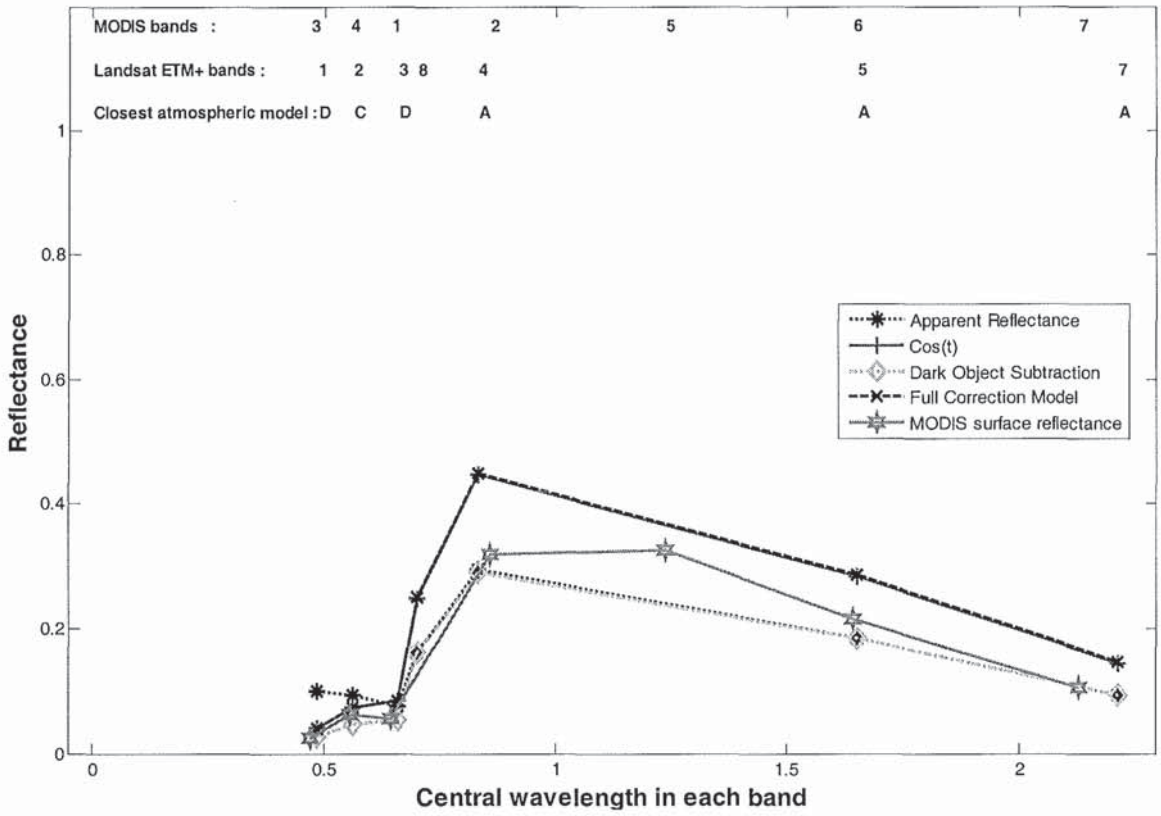

Figure 4.3: Mean surface reflectance for ETM+ and MODIS (11/09/2002)

Furthermore, from figure 4.3 it is clear that both dark object subtraction and apparent reflectance outperform the full and cos(t) models. Thus, if it is assumed that the MODIS surface reflectance is reasonable, then the parameters used for the full model are poor and the procedure incorporated in the cos(t) model overestimate the effects of atmospheric absorption and Rayleigh scattering.

The apparent model should not be used to correct the ETM+ visible bands (1, 2, and 3) as it clearly overestimates the surface reflectance. In general, the performance of both the Dark Object Subtraction and the cos(t) method are good and comparable with the MODIS products, though, it is clear that the cos(t) model always results in a surface reflectance higher than that of the Dark Object Subtraction method.

Figures 4.4 to 4.6 show the plot of the correlation coefficients between similar MODIS and ETM+ bands. Here the MODIS resolution is 250m for the comparison with the Landsat ETM+ bands 3, and 4, and 500m resolution for all other bands. For each band the average reflectance of all the Landsat ETM+ pixels falling within each MODIS pixel was used for this resampling process.

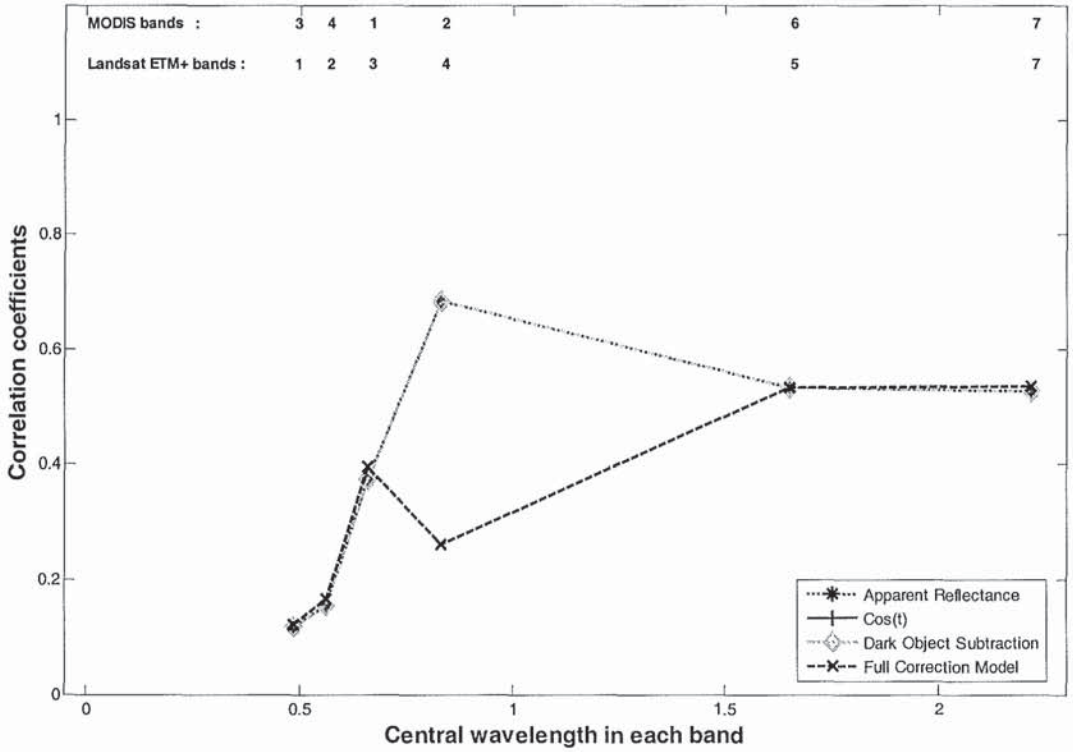

Figure 4.4: Correlation Coefficients of surface reflectance for ETM+ and MODIS (17/06/2000)

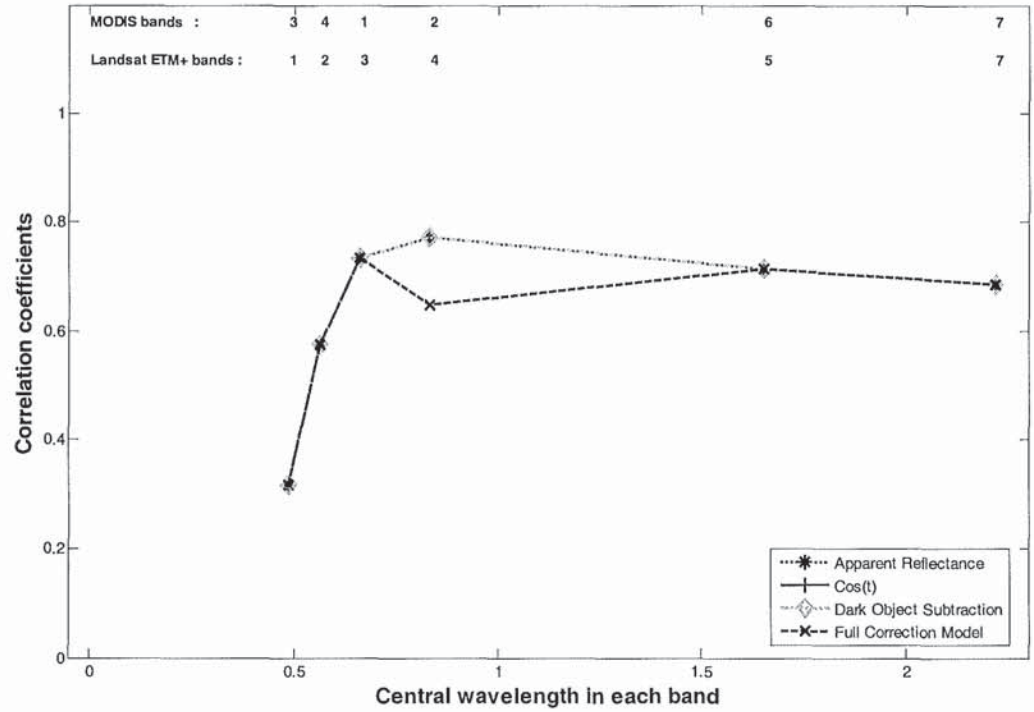

Figure 4.5: Correlation Coefficients of surface reflectance for ETM+ and MODIS (04/04/2002)

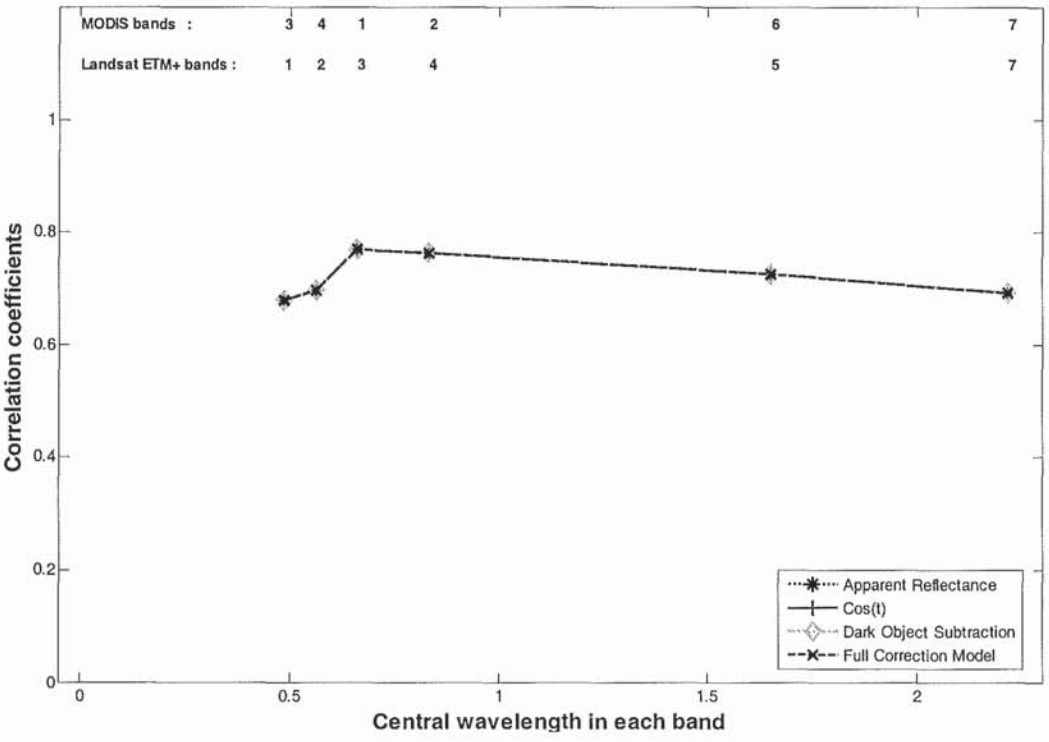

Figure 4.6: Correlation Coefficients of surface reflectance for ETM+ and MODIS (11/09/2002)

It was expected that the correlation coefficients for each band would be similar for all approaches, because the effect of various atmospheric corrections on each band is to increase or reduce all reflectance values in the image by a fixed value. This had no effect on the correlation coefficient, even though, in some cases the correlation is very low when using the full model for atmospheric correction. This as stated earlier is due to inappropriate parameters estimated for the model, and becomes more obvious in the identical curves which appear in figure 4.6, where both full model and cos(t) results are similar.

From these figures (4.4 to 4.6), one may notice that the highest correlation is observed for the NIR band, i.e. ETM+ band 4 and MODIS band 2. This may attributed to the smaller atmospheric interference in NIR band than in the other bands. In other words, the amount of the energy reflected in the NIR band is higher than in the other bands as can be seen in figures 4.1 to 4.3, and there is less absorption by the atmosphere at NIR wavelengths. This results in better quality images in the NIR band for both Landsat ETM+ and MODIS, thus resulting in a better correlation between the NIR images from both sensors.

4.2.3. Summary and conclusion for the atmospheric correction

The main objective of the comparison between the corrected reflectance in Landsat ETM+ imagery and the MODIS surface reflectance product is to find out the most suitable method for minimizing the atmospheric effect between these two data sources. This is so that the Landsat ETM+ imagery can be used for subsequent analysis with MODIS images to produce a land cover classification map for the study area.

All the atmospheric correction methods produced different results. Therefore, for the purpose of integrating the resulting ETM+ image with MODIS data, one may select corrected ETM+ bands that show the closest relationship with MODIS surface reflectance, regardless of the method used for the atmospheric corrections. For example from the image acquired on 11/09/2002, one may select the set of TM bands (1 to 7) which have been corrected using: apparent reflectance images for bands (4, 5, and 7), the dark object subtraction for bands (1, and 3), and the cos(t) for band 2. Selecting the corrected bands in this way may improve the integration process of ETM+ and MODIS as both corrected images will have similar spectral signatures for the same land cover.

However, only one ETM+ image (acquired on 17th June 2000) will be used for the remainder of this project. Therefore, since the cos(t) model shows the minimal differences with the MODIS surface reflectance in all bands for this ETM+ image, as shown in Figure 4.1, then the corrected bands using the cos(t) model alone will be used.

The main conclusion obtained from the atmospheric correction experiment, is that if the parameters required for atmospheric correction models are not available, or not reliable, then the cos(t) or the dark object subtraction give the best results. However, in some cases the apparent reflectance model may outperform these two models for the Landsat ETM+ NIR bands (4, 5 and 7), if the DN value for haze required for the cos(t) and dark object subtraction were not accurate.

4.3. Preliminary analysis of the Landsat ETM+ image

In order to obtain an insight about the imagery, and to see the distribution of the pixels, each band of the imagery was displayed and examined. Through the visual examination

of Landsat ETM+ band 1 image over the study area, it was found to be very hazy and noisy, which was attributed to Rayleigh scattering (Lillesand and Kiefer, 2000). The standard deviation of the DN reflectance values for this band was very small, 0.016, in comparison to the other bands. The remaining visible bands (green and red) were of relatively high quality, with standard deviations of 0.0219 and 0.0323 respectively, as were the three near-IR bands. As a consequences band 1 might contaminate the information content of the other bands, and therefore, the blue band was not be considered in the land cover classification algorithm. Band 6 is thermal IR and can help in detecting ground temperature variations due to the moisture content. However, band 6 will not be considered in this study since its spatial resolution is not compatible with the spatial resolution of the other ETM+ bands. The panchromatic band 8 will also not be used for the same reason of incompatibility with the other bands. However, this band was useful for selecting the GCPs for the geometric registration with the OS 1:2500 digital map as described in Chapter 3.

The histograms of the DN distributions for each band were plotted and compared to each other (Figure 4.7 to 4.9). Band 4 shows a better distribution than the other bands. The correlation coefficients obtained by comparing pairs of bands are shown in Table 4.2. This table shows a high correlation between the visible bands and between the near-IR bands 5 and 7. Band 4 has the lowest correlation with all other bands.

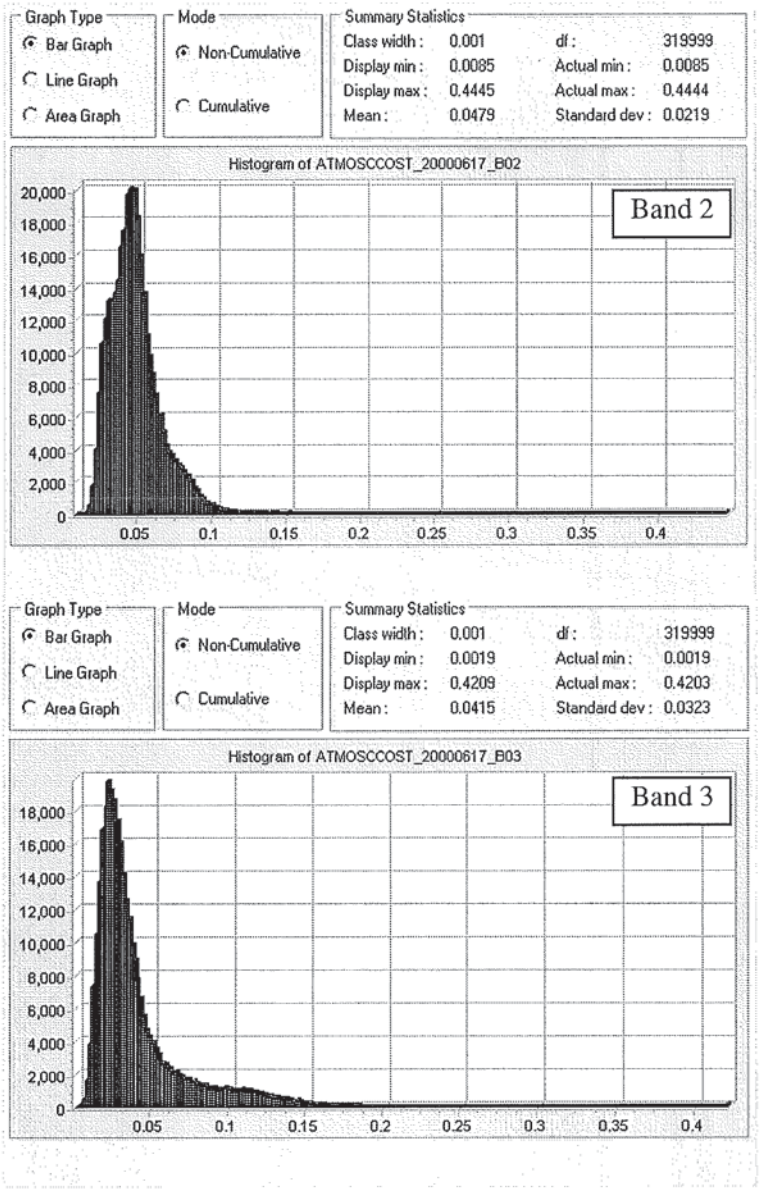

Figure 4.7: Histogram plot for bands (2 and 3) for the ETM+ image of the study area.

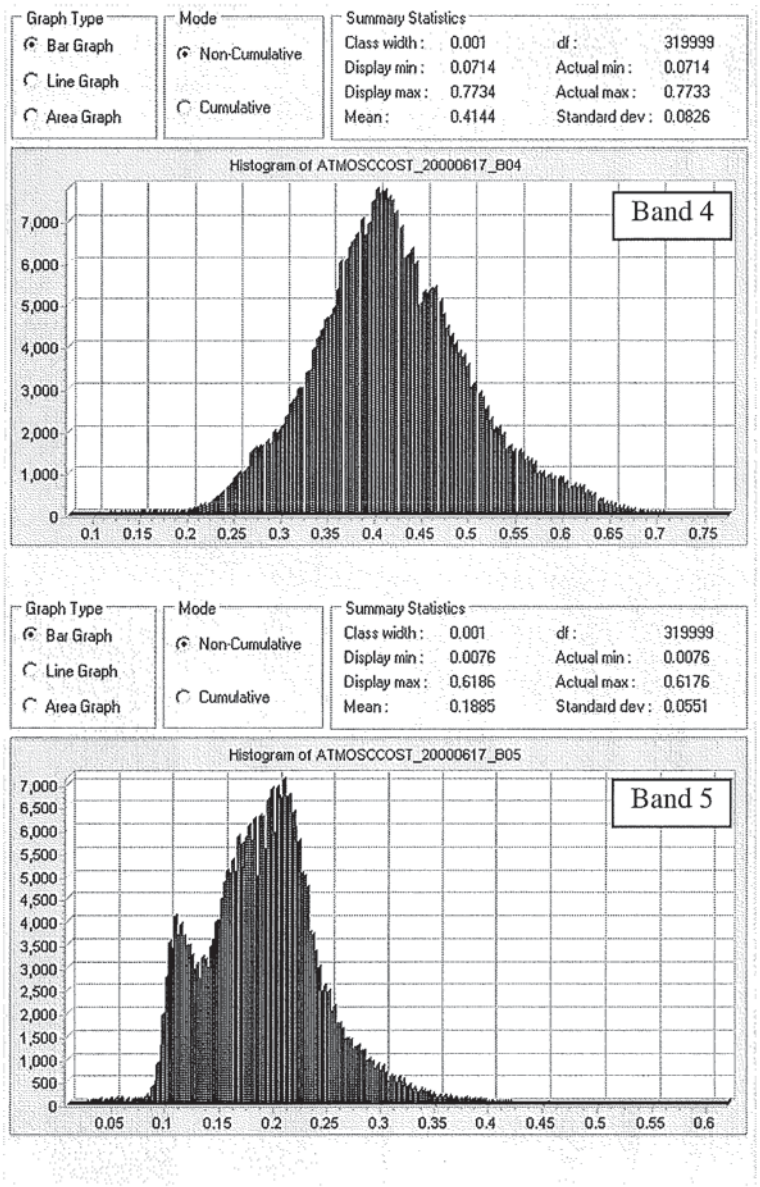

Figure 4.8: Histogram plot for bands (4 and 5) for the ETM+ image of the study area.

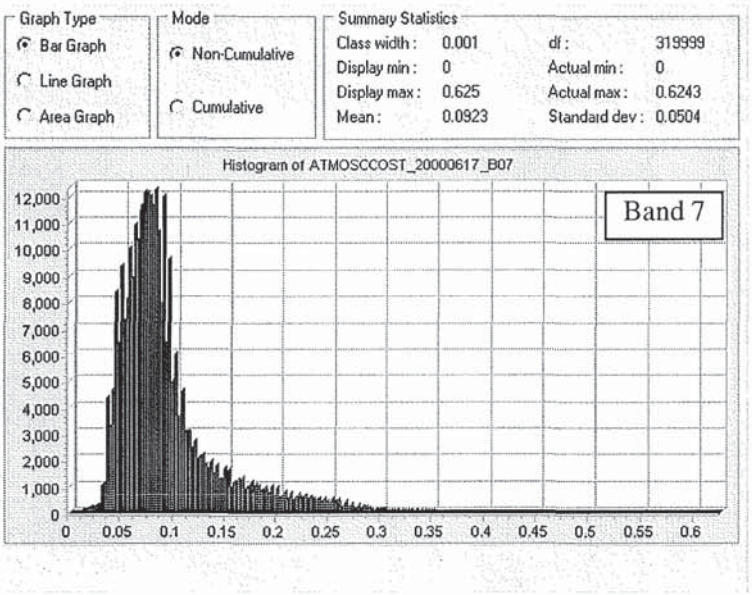

Figure 4.9: Histogram plot for band (7) for the ETM+ image of the study area

Table 4.2: Inter Band Correlation Coefficients for ETM+ image

	B2	B3	B4	B5	B7
B2	1.0000	0.9062	-0.0565	0.7197	0.7602
B3	0.9062	1.0000	-0.3502	0.7173	0.8865
B4	-0.0565	-0.3502	1.0000	0.0484	-0.3128
B5	0.7197	0.7173	0.0484	1.000	0.8617
B7	0.7602	0.8865	-0.3128	0.8617	1.0000

4.4. The unsupervised classification of the Landsat ETM+ image

In this section the two unsupervised classification methods which were used to classify the Landsat ETM+ scene of the study area are described. These methods are the Isoclust module implemented in the Idrisi32 for Windows package (Clark University) and the Fuzzy c-means function from the MATLAB software. The results of each classification were inspected visually and compared with the ETM+ false colour composite, and the aerial photography, to determine the ability of each method to classify this image.

The agricultural census data (section 3.7) gives a preliminary indication of the number of crop types in the study area. However, it is not possible at this stage to decide a definitive number of classes distinguishable from the available imagery. This is because no spectral data was available for each crop at this period of the growing cycle. Spectral libraries for some materials are available, for example, the United States Geological Survey (USGS) Spectroscopy Lab (http://speclab.cr.usgs.gov), but these spectral libraries are developed under laboratory conditions for pure materials. This means that there are likely to be some discrepancies between the spectral characteristics in the library and those of the crops in the field.

Taking all the accumulated knowledge of the study site into consideration it was decided to consider approximately 20 classes. Subsequently, the resulting classes would be matched with the agriculture census data.

4.4.1. Iterative self-organizing unsupervised classifier

An unsupervised classification was performed on the ETM+ imagery using the Isoclust algorithm, implemented in the Idrisi32 software. This algorithm is an iterative self-organising unsupervised classifier based on a concept similar to the ISODATA routine (Ball and Hall, 1965 cited by Eastman, 2001), that was introduced in section 2.7.2. This module requires an 8-bit colour composite image to seed the clusters, rather than determining the clusters' centres randomly, as in the ISODATA algorithm. Thus, the unsupervised classification process was seeded from a colour composite image, selected from the three-band combinations with the largest Optimum Index Factor OIF (Chavez *et al.* 1982).

This index is based on the variance and the correlation between the different bands. The three-band combination having the largest index value is usually selected for colour composition because it should display the most spectral information of the whole set of bands. Table 4.3 shows all the possible combinations of the Landsat ETM+ bands for the study area along with their respective OIF.

Table 4.3: Optimum Index Factor for ETM+ image over the study area

Band combination			OIF
4	5	7	0.0047
3	4	7	0.0039
3	4	5	0.0037
2	4	7	0.0034
1	4	7	0.0033
2	4	5	0.0032
1	4	5	0.0031
3	5	7	0.0031
2	3	4	0.0028
2	5	7	0.0027
1	3	4	0.0025
1	5	7	0.0025
1	2	4	0.0021
2	3	5	0.0019
2	3	7	0.0018
1	3	5	0.0018
1	3	7	0.0016
1	2	5	0.0014
1	2	7	0.0012
1	2	3	0.0008

From Table 4.3, bands 4, 5, and 7 have the highest OIF. However, the combination of bands 5, 4, and 3 is more sensitive to vegetation cover variability, and also covers the basic image spectral dimensions of greenness, brightness and moisture content (Eastman, 2001). Therefore, it might be more appropriate for use in seeding the clusters for the Isoclust unsupervised classification.

Principal component analyses (PCA) has the ability to reduce the image dimensionality. The first few components contain the major variability within the data set. Therefore, a combination from the first three principal components might also be used to create a composite image to seed the clusters. This would have the added advantage that this composite image might reveal the maximum differentiation between the clusters. The OIF for the first three components for this study is (0.0096) which is, as expected, higher than any other possible combination of the original bands.

Consequently, three composite images were tried for seeding the Isoclust classifier. These were the RGB 457, RGB 543, and RGB PCA123. Five bands were therefore selected for processing namely: 2, 3, 4, 5 and 7. The other bands, 1, 6 and 8, were not used in the classification algorithm for the reasons stated earlier. The number of clusters was fixed at 20, and the iterations to three, as suggested in the Idrisi32 manual in order to produce stable results. The following test was performed to find out whether the classification results using these three composite images were significantly different.

First, since the Isoclust algorithm was unsupervised, the clusters' identity numbers may differ from one classification from the others. In other words, the same class might be assigned a different identity number in each of the classifications obtained. Therefore, the clusters' identity numbers had to be changed in order to reduce the disagreement between these classifications. The classification using RGB457 was selected as a base classification, and the clusters' identity numbers for the remaining other two classification were changed to produce maximum agreement with this base classification. The way this was done was to use a cross-tabulation table. From this table one can find

the identity number for a cluster so that the best match between each pair of classifications is obtained.

After bringing all classification to a uniform clusters numbering system, the Kappa coefficient was used as a measure of the agreement between the classifications. If the classifications are in total agreement then the Kappa coefficient will be equal to one.

Table 4.4 shows the overall Kappa for the base classification using RGB457 with each of the following classifications:

- Isoclust classification using RGB543 for seeding and 3 iteration.
- Isoclust classification using RGB PCA 123 for seeding and 3 iteration.
- Isoclust classification using RGB457 for seeding. But the number of iterations was increased from 3 to 5, 7, and 9 iterations.

Table 4.4: Kappa Coefficient of agreement with the classification using RGB457 for seeding with 3 iterations

Seeding image	RGB543	RGB PCA123	RGB 457			
Iterations	3	3	3	5	7	9
Kappa (Ref: RGB457)	0.3299	0.3114	1	0.8287	0.7318	0.6664

It is important to note that the small value of Kappa in the first and second columns in this table is not because of different numbering system, as this problem had been minimized as explained above. These Kappa values are the maximum values that can be obtained by changing the clusters' identity number.

It is noticeable from Table 4.4, that using a different seeding image will yield a different classification result. The number of iterations has less effect on the classification results than the effect of the selected seeding image.

It was hard to judge which of these classifications was better than the others. Therefore, relating the results to the census data was not a straightforward exercise, given that the census data also contains some uncertainty. It is useful to note, however, that with different seeding images, the automatic classifications vary significantly and this indicates that the automatic classifications cannot be relied upon.

The main reason for the disagreement between these classification using different seeding images was because each seeding image was an 8-bit composite image having a maximum of 255 values. This will result in the pre-definition of the clusters' centres, which will segregate the multi-dimensional spectral space in different ways. Therefore, some of the pixels which are assigned to one cluster, will migrate to another cluster if any change occurs to the position of the centres. Consequently, in practical situations when adequate training data are available the supervised classification is more appropriate than an unsupervised classification, because the analyst has more control over the centres of desired classes.

One possible solution to this problem might be the use of the OS 1:2500 digital map that is available for this study (section 3.6). The object was to classify each parcel to one class, given that each field is more likely to hold a single class. This may reduce the uncertainty within each field. To do this the class of highest occurrence in a field, will be assigned as the likely class for that field. However, instead of using the crisp output of

Isoclust, it may be more appropriate to use the soft classification to calculate the likelihood of each parcel. The following section presents the fuzzy c-means classification used for this work.

4.4.2. Fuzzy c-means Classification

The fuzzy c-means classifier (fcm) is an iterative clustering algorithm that is used to partition a data set into a number of clusters. Each point in the data is assigned a degree of membership to each cluster. The membership grades indicate the degree of similarity, or strength of membership to the class considered. Maselli *et al.* (1996), used the membership grades associated with each pixel as the class-specific probabilities.

One attractive feature of the fcm classifier is that there is no need for a seeding image. The fcm algorithm starts by generating the cluster centres randomly. In order to see whether the final results will be the same for each run of this algorithm, an experiment was conducted to classify a number of data point. The result confirmed that the final centres for a given cluster number will be the same, and not subject to the initial centres selected by the algorithm during the first step.

To perform the fcm unsupervised classification, the (fcm) function from MATLAB toolbox was used. This required the determination of the number of clusters, together with some other optional parameters. Initially, 20 classes were selected for the number of clusters required to run the fcm function. The output from the maximum membership grades was compared with the aerial photography and the FCC457. This comparison showed that the bright pixels (bare earth) were confused with the clouds and the dark pixels were not classified correctly to their appropriate classes (water, vegetation, and

cloud shadows were highly confused). Increasing or decreasing the number of initial clusters did not prove useful in separating these confused classes. Hence, it was decided that a hierarchy system might be useful in achieving a step by step classification for the discernible features in the imagery.

The hierarchical classification scheme descried in section (2.3.1) inspired the idea of considering a systematic hierarchical classification technique. Several reasons led to this decision. Mainly because the fcm function in MATLAB can deal with subset pixels from the image. Whereas the Isoclust module in Idrisi32 does not allow the user to mask out some areas for exclusion from further processing (section 4.5.1). Furthermore, classifying the whole data at once might lead to inappropriate partitioning of the multidimensional spectral space if the number of clusters were badly chosen.

Therefore, instead of trying to classify the whole data set to N cluster at once, it was decided to follow a hierarchical classification technique, since the fcm function in MATLAB allows the user to select a subset of the pixels that are of interest for further classification.

The next task was then to mask out the known features in the image, that may influence the success of the classification. These features were those identified during the preliminary classification using fcm as mentioned above. The clouds were confused with bright surface classes and the water bodies were confused with dark vegetation and clouds' shadow. Thus, the decision was taken to mask out the clouds, remove the cloud shadows and then mask out the water bodies. All the other remaining pixels will be considered after that for further classification.

The following subsections describe the process employed in identifying the clouds, the cloud shadows and the water.

4.4.2.1. Delineation of the cloud cover

The majority of remotely sensed images are contaminated by clouds. Currently, the ground information below cloud regions cannot be retrieved with optical sensors. An experiment conducted during this research showed that cloud can get confused during classification with some bright objects, such as bare earth.

Liang *et al.* (2001) suggested a method of delineating the haze and thin clouds, that involved clustering the visible bands of Landsat ETM+ image (1, 2, and 3), and then separating the other bright surface objects through further clustering, since the brightness of hazes and thin clouds decreases with increasing wavelength, but bright surfaces usually have the reverse trend. In this work, a classification was performed on the true colour composite of the visible bands of the Landsat ETM+ image, by converting the RGB colour image into an indexed image. Since the clouds are very bright in the visible bands, then all pixels in the indexed image with DN values higher than a threshold were considered to be cloud. Figure 4.10 shows the indexed true colour composite image and Figure 4.11 shows the cloud cover mask.

Another straightforward way to delineate the clouds is to use the minimum composite of all bands. In this approach, the minimum reflectance for each pixel from all bands is selected and displayed. Subsequently all pixels higher than a selected threshold are classified as cloud. The results of this technique are shown in Figure 4.12, where a threshold of 0.13 was selected from consideration of the minimum composite reflectance

image. This technique was adopted in this thesis for masking the cloud in the ETM+ imagery because it was simple and much easier than using the indexed true colour image, and yet produced similar results.

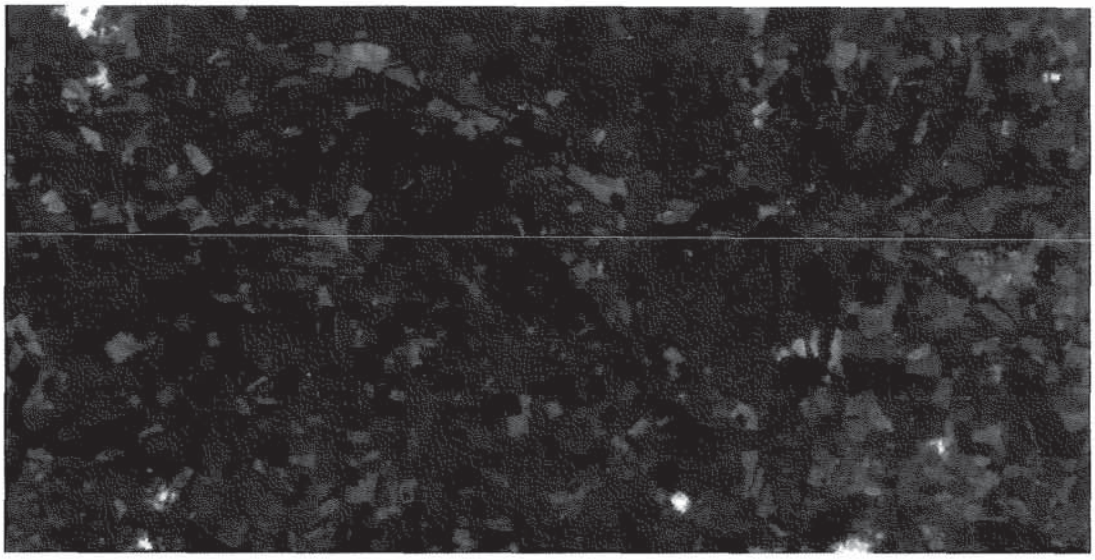

Figure 4.10: The true colour composite of the Landsat ETM+ bands 1, 2 and 3 (TCC123)

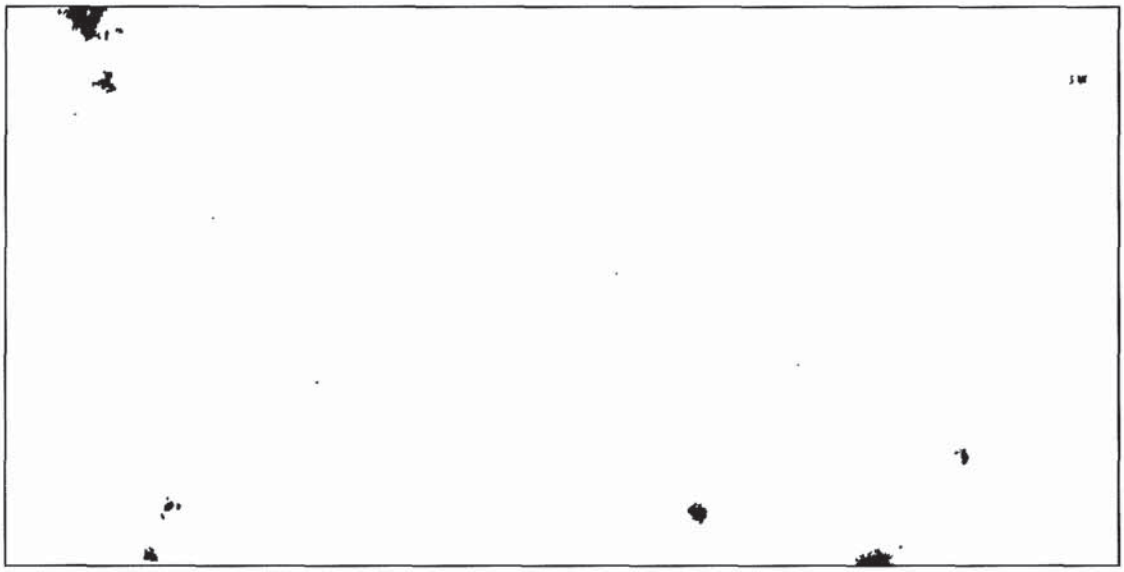

Figure 4.11: Cloud mask using threshold from the indexed TCC123 of the Landsat ETM+ image bands 1, 2 and 3

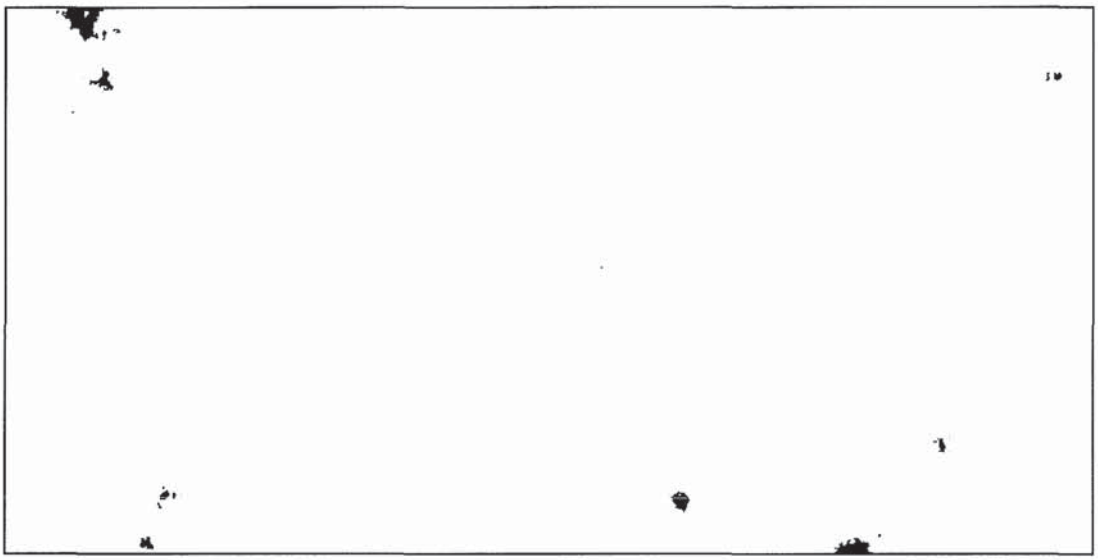

Figure 4.12: Cloud mask using a threshold (0.13) from the minimum composite of reflectance

4.4.2.2. Removing the cloud shadows

Clouds often cast shadows over the cloud-free areas. According to Liang *et al.* (2001), shadows are not evident in the visible bands. However, the near and mid-IR bands (4, 5, and 7) of the Landsat ETM+ image can be considerably contaminated as one can see in figure 4.13. In order to reduce the effects of these shadows in the near and mid-IR bands, the visible bands (1, 2, and 3) can be classified. Subsequently, the near and mid-IR reflectance of the cover types inside the shadows, are substituted by the reflectance in the near and mid-IR of the same cover types that are outside the shadows. For the study area, the true colour composite image using ETM+ bands 1, 2 and 3 was converted to an indexed image. Each index inside the shadow region was identified and their reflectances in bands 4, 5 and 7 were substituted by the mean value of bands 4, 5 and 7 for the same index outside the shadow. The results are shown in Figure 4.15, which clearly shows the large patches of shadow have been removed. This process is good for visual

enhancement, however, the compensated spectral values should not be considered as the true spectral values for the pixels in shadow.

The main objective of removing the shadow was to avoid any confusion that might occur during the classification stage with other features, such as water and dark vegetation. The importance of doing this will become more obvious when trying to classify water bodies which is discussed in section (4.4.2.3).

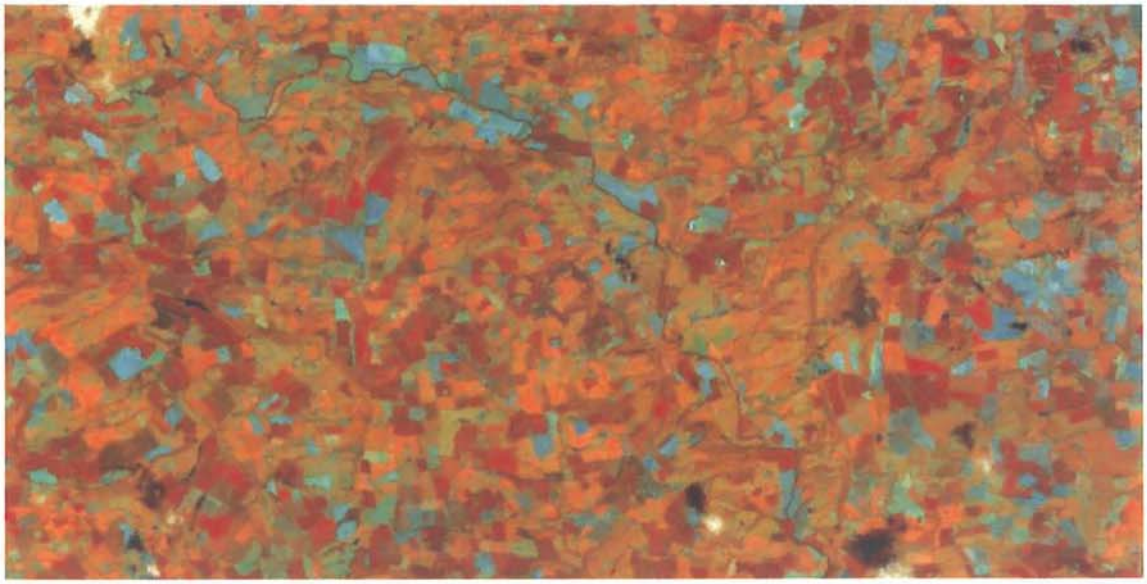

Figure 4.13: Landsat ETM+ false colour composite of band 4, 5 and 7 (FCC457) shows the contamination with cloud shadows

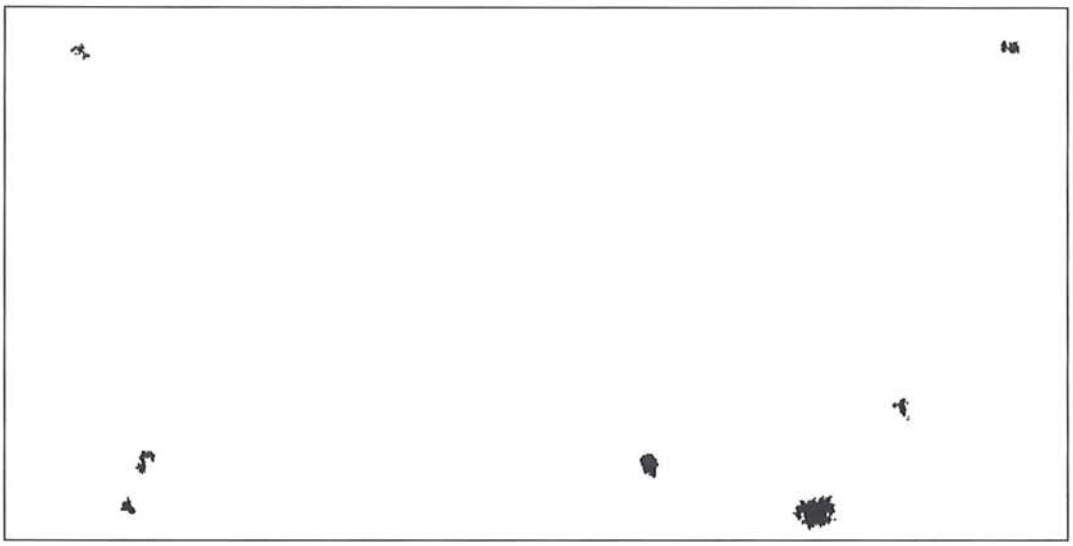

Figure 4.14: Cloud shadows mask

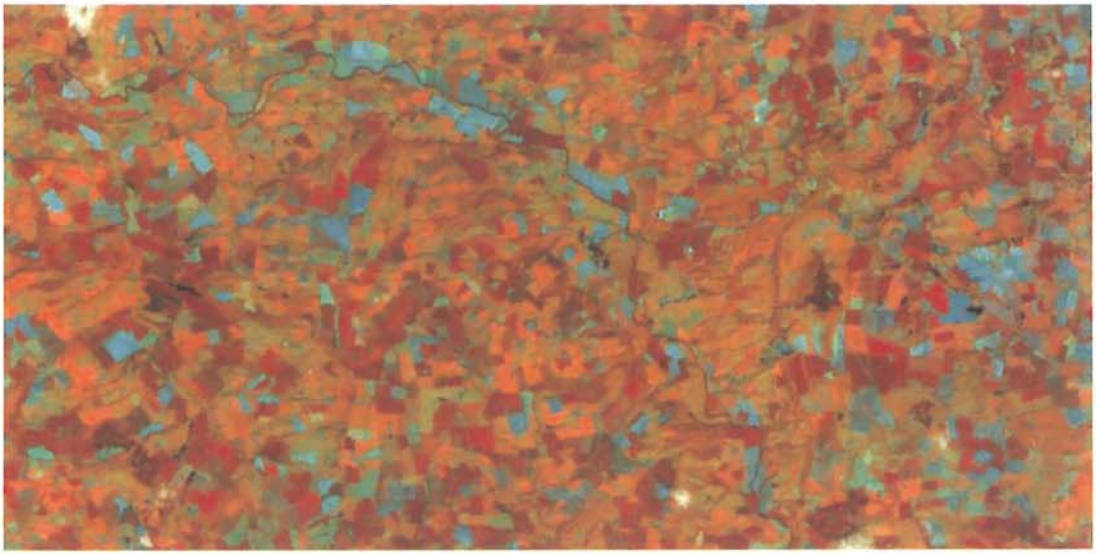

Figure 4.15: FCC457 after the removal of cloud shadows

4.4.2.3. Delineate the water bodies

In this section the water features in the ETM+ image are identified and masked. Since the water bodies have very low reflectance when compared to other features, then using a threshold for the pixels' spectral distance to zero reflectance may be useful in distinguishing water from dark vegetation. In other words, the square root of the sum of squares of the reflectance for the water feature will be smaller than for any other classes. Another way of masking the water feature, which was used for this image, is to use a maximum value composite (MVC) of all bands. The MVC image is shown in figure 4.16.

In figure 4.16 the water bodies show the lowest maximum reflectance values and can thus be distinguished from the forest stand shown in the middle-right of the image. There was a significant degree of confusion between this stand of trees and water in previous attempts to classify the image. Using a threshold for the maximum reflectance from this image, the water feature was masked. A value of 0.135 was used to mask the water, as shown in figure 4.17. These areas were checked with the aerial photography to confirm the existence of the water bodies. Unfortunately, the river can not be delineated using this method largely because it is a narrow linear feature surrounded by trees.

The aim of identifying the water and clouds before trying to use the fcm classifier to separate the vegetation from non-vegetation area was to avoid any confusion between these features and other features such as dark or bright objects in the scene.

The remaining image data can now be identified broadly as either vegetation or non-vegetation. This will be further classified next.

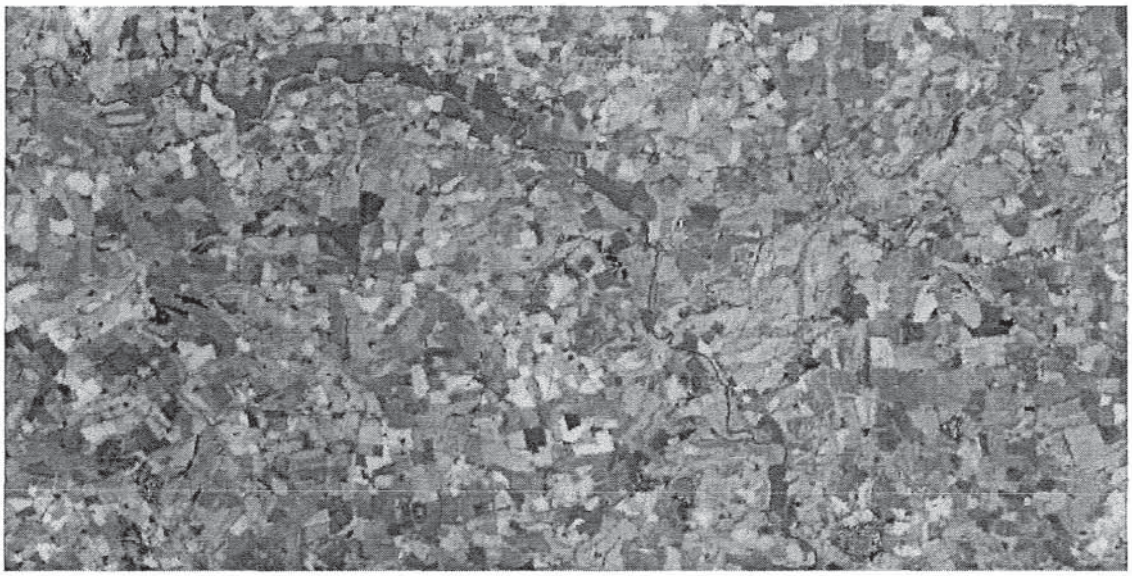

Figure 4.16: Maximum reflectance composite image

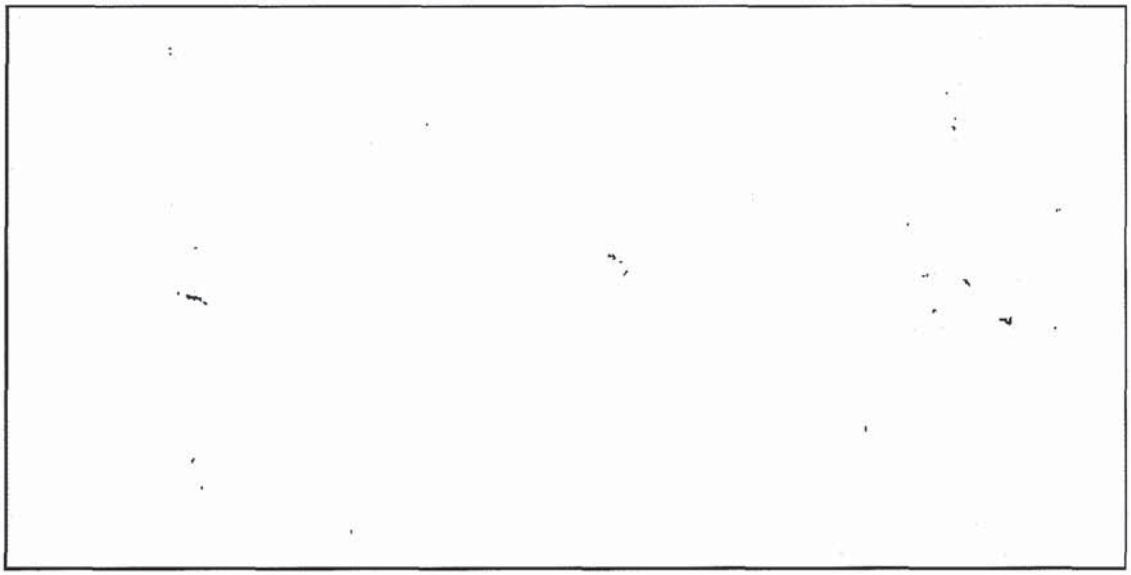

Figure 4.17: Water features delineation using a threshold from maximum reflectance composite image

4.4.2.4. Separation of the vegetation from non-vegetation classes

In the previous subsections the clouds were masked so they would not be confused with bare earth (bright features). In addition the cloud shadows were removed to minimize the confusion might happen with dark vegetation and water features. Similarly, the water features were masked to avoid any possible confusion with other dark features (such as dark vegetation) which had occurred when a preliminary fcm classification was conducted on the ETM+ image.

All remaining pixels in the ETM+ image can now be classified broadly as vegetation or non-vegetation. There are some small built-up areas, but these tended to be classified as bare earth. The fcm clustering algorithm was used for this task, and it was found, that for this data, the separation was better achieved if an NDVI image was used together with the spectral bands 2, 3, 4, 5, and 7, instead of using the spectral bands alone. This was because the NDVI value is a good discriminator between vegetation and non-vegetation classes. Thus, the fcm function was used to classify the remaining pixels into two classes using bands 2, 3, 4, 5, 7 and the NDVI. The resulting fuzzy classification was hardened using the class of maximum membership grade. This classification subsequently had four classes, namely: clouds, water, vegetation and non-vegetation, as shown in figure 4.18.

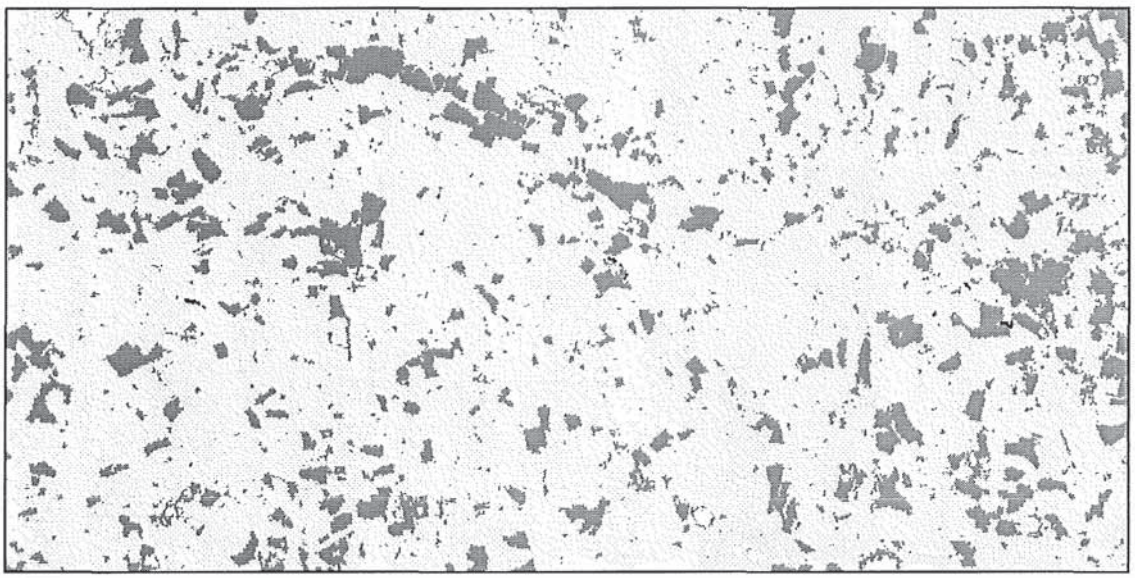

Figure 4.18: Crisp broad classification of ETM+ image

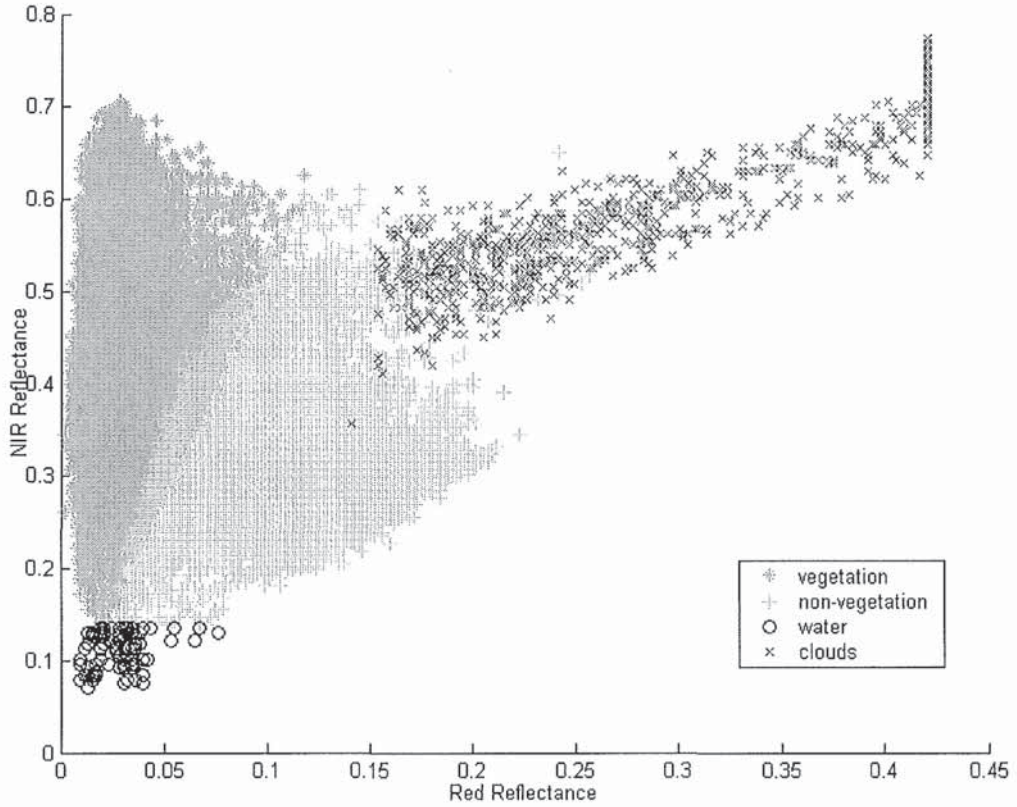

Figure 4.19: Pixels plot in Red/NIR spectral space showing the bare and vegetated area

A close inspection of this broadly classified image will reveal that some areas that appear in the FCC457 image as sparsely vegetated, or possibly recently harvested, are sometimes classified as vegetated and other times as non-vegetated areas. The reason for this is that this classification is the crisp output of fcm using the class of maximum membership grade. This problem might be rectified if the fuzzy outputs are used instead. In order to visualize the confusion between these classes in spectral space, the Red and NIR reflectances for all pixels in the scene were plotted in Red-NIR spectral space (figure 4.19). From this figure it was clear that there is no clear boundary for each of the features identified. Therefore if an attempt were made to classify the whole data set to four classes without any hierarchical system the result would be very disappointing. Furthermore, there is an apparent overlapping area between the vegetation and non-vegetation classes. This area is where the maximum confusion between these two classes occurs.

This low level classification in crisp format was used to further classify the vegetation pixels.

4.4.2.5. Classification of the vegetation area

In this section only those pixels classified as vegetation in the crisp output from the fcm classification conducted in the previous section (4.4.2.4) are considered for further classification into different vegetation classes.

An attempt was made to split the vegetation pixels to two classes using the fcm function and then each of these two classes to another two. A visual inspection of the results for the FCC457 revealed a great deal of misclassification. Increasing the number of clusters also did not prove satisfactory. Therefore, it was decided to determine the number of

vegetation classes to be used as input for the number of desired cluster in the fcm function, but now operating in a supervised mode. The supervised mode of fcm was used in a previous study and showed superiority over the unsupervised mode (Shalan *et al.*, 2003). This was because the unsatisfactory results obtained when the number of clusters increased, were largely due to the problem of inappropriate partitioning of the spectral space.

In order to do so, a false colour composite image was displayed and the total number of vegetation classes estimated, and the mean reflectance values of each vegetation class subsequently used in the supervised fcm function. There was need to decide which composite image best displayed the vegetation classes. The OIF was calculated for vegetation pixels to find the band combination with the highest variability. Table 4.5 shows that the band 4, 5, and 7 combination still has a higher OIF than bands 3, 4 and 5.

Table 4.5: Optimum Index Factor for vegetation pixels

Band combination			OIF
4	5	7	0.00380
3	4	5	0.00363
2	4	5	0.00370
3	4	7	0.00278
2	4	7	0.00276
2	3	4	0.00259
3	5	7	0.00202
2	5	7	0.00200
2	3	5	0.00068
2	3	7	0.00045

Therefore, the composite image RGB457 was used to estimate the number of vegetation classes discernible in the image as an input value for the number of clusters in the fcm algorithm. However, it was not easy to determine how many clusters there were. Therefore, the following methodology was adopted:

First the RGB457 image for the vegetation pixels was converted to an indexed image, and then the mean reflectance for each index was calculated and plotted in the Red-NIR spectral space. The aim was to identify some indices that portray different type of land cover classes so that their mean reflectance value could be used in a supervised mode. There were no specific criteria available to assist in deciding what indices should be kept and what should be discarded. As a rule of thumb, some indices with high frequency may seem of interest if they produce clusters at specific geographical locations in the image. However, this was not always a satisfactory rule for keeping an index, as several indices with a high frequency may represent the same class. In this case only one index with the highest frequency was considered as representing indices with similar characteristics. On the other hand, some indices will have a low frequency but if they represent distinct classes, they should be kept. Consequently, this becomes a process of trial and error, until eventually the indices that are used as the training areas for the fcm classification in the supervised mode are decided upon.

By following the methodology described above, for keeping or discarding the indices in the FCC457 indexed image, only 18 indices were found to provide a reasonable representation of the discernible classes in the image. Therefore, the mean reflectance for these 18 indices in each spectral band was considered as the cluster centres. Figure 4.20 shows the plot of the Red-NIR spectral space of pixels in the vegetated areas, along with the centres of the 18 indices selected for the clusters.

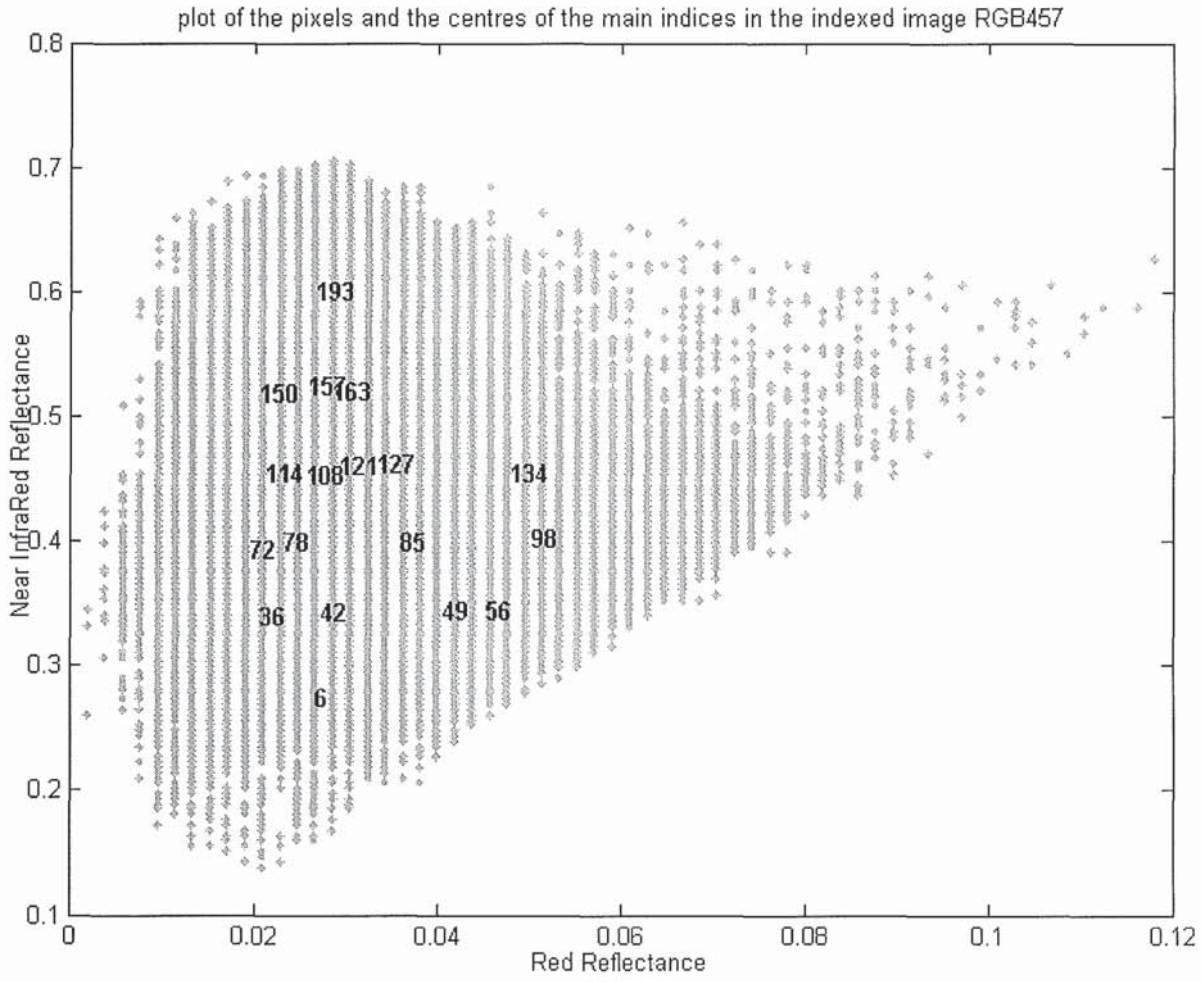

Figure 4.20: Plot of the vegetation pixels and the cluster centres

(Each axis is represented in a different scale emphasizing the distinct discrete values for the red reflectance)

After selecting the cluster centres as the mean reflectance value for each selected index, the fcm algorithm was run to assign a degree of membership for all vegetated pixels to each of these clusters. For this, only bands 2, 3, 4, 5, and 7 were used in the calculations because they produced, for this study, better results than using these bands together with the NDVI values as suggested in section 4.4.2.4. This decision was based on a visual inspection of the results obtained with and without the NDVI. The reason for the difference in the results was that the NDVI is a unit less value, and if used with this

metric classifier then it changed the results considerably. For example, the NDVI values were good for separating the vegetation from non-vegetation (section 4.4.2.4), as the NDVI values are very sensitive to the chlorophyll level of the vegetation. Thus, using the NDVI will shift the vegetation pixels away from the non-vegetation pixels in the spectral space. However, using the NDVI for classifying the vegetation may cause the opposite effects. For example, some of the agricultural fields with dense vegetation have been confused with the woodlands. Despite the difference in their spectral signatures, their NDVI values are close to one, which brings the values of these classes closer in spectral space, thereby increasing the confusion.

4.5. Context classification

The membership grades in the fuzzy c-means classification described in section 4.4.2 were based solely on the information about the reflectance of each individual pixel in each band. The spatial neighbourhood relationship between adjacent pixels provides potentially valuable information. Therefore, using Bayes' theorem, the membership grades of the centre pixel of a predefined window can be modified using the membership grades of the surrounding pixels in the window. This can be implemented as a contextual prior probability. The posterior probability according to Bayes' Theorem is given in Equation (4.1):

$$P(h \mid e) = \frac{P(e \mid h) * p(h)}{\sum_i P(e \mid h_i) * p(h_i)} \qquad \textbf{Equation 4. 1}$$

where:

$P(h|e)$: The probability of the hypothesis being true given the evidence (posterior probability)

$P(e|h)$: The probability of finding that evidence given the hypothesis being true

$P(h)$: The probability of the hypothesis being true regardless of the evidence (prior probability)

The evidence can be interpreted here as the membership grade to each class obtained from the surrounding pixels. Therefore, in Equation 4.1, the prior probability $P(h)$ of the centre pixel belonging to class (h) can be considered the same as the membership grade of the centre pixel of class (h). The $P(e|h)$ can be replaced by the averaged membership grade of class (h) for all pixels in the window. The multiplication is then normalized by the sum over all classes (h_i), to obtain the new membership grade of the centre pixel to class (h). The membership grade of the surrounding pixels can be adjusted using the weighted distance to the centre pixel. A numerical example of the application of this rule follows.

Suppose there are three classes A, B, and C, and the membership grades assigned to the central pixel of a 3x3 window were 0.4, 0.5, and 0.1 for class A, B, and C respectively. These are considered as $P(h)$ for each class. Figure 4.8 shows the membership grades for all surrounding pixels in the window.

0.2	0.3	0.5
0.6	0.4	0.4
0.5	0.4	0.5

Membership grades to Class A

0.4	0.3	0.4
0.3	0.5	0.4
0.1	0.2	0.2

Membership grades to Class B

0.4	0.4	0.1
0.1	0.1	0.2
0.4	0.4	0.3

Membership grades to Class C

Figure 4.21: Numerical Example of using Bayes rule to combine the evidence from surrounding pixels

Thus, the evidence of belonging to a particular class can be calculated as the average membership grades to this class in the surrounding pixels and the pixel itself:

$$P(context \mid \mathrm{A}) = \frac{0.4+0.3+0.6+0.4+0.4+\frac{1}{\sqrt{2}}(0.2+0.5+0.5+0.5)}{5+4\cdot\frac{1}{\sqrt{2}}} = 0.4218$$

where $1/\sqrt{2}$ is implemented to adjust the influence of diagonal pixels on the central pixel. Similarly,

$P(context \mid \mathrm{B}) = 0.3165$, and $P(context \mid \mathrm{C}) = 0.2617$

Now the posterior probabilities for the central pixel are:

$$P(\mathrm{A} \mid context) = \frac{0.4218 * 0.4}{0.4218 * 0.4 + 0.3165 * 0.5 + 0.2617 * 0.1} = 0.4778$$

$P(\mathrm{B} \mid context) = 0.4481$, and $P(\mathrm{C} \mid context) = 0.0741$

From this numerical example the prior probability suggests that the central pixel has a higher probability of belonging to class (B). However, the posterior probability suggest that the pixel may belong to class (A) instead. Furthermore, the degree of membership of

class (C) was considerably reduced in the posterior probability. As a consequence, the probable classes for the central pixel are confined to either A or B only.

Therefore, using the context to modify the membership grades is an effective means of reducing the classification uncertainty. This is because the pixels of the same class tend to be clustered close to each other within the image. Although, this method may not be applied successfully to linear features, for agricultural fields using the context can significantly improve the confidence of class membership. Therefore, to confirm this improvement, the classification uncertainty measure introduced by Eastman (2001) can be used to calculate the degree to which no class clearly stands out above the others in the assessment of class membership of a pixel.

The images of classification uncertainty before and after the context operation are shown in Figures 4.22 and 4.23 respectively. The average value of the classification uncertainty was 0.4951 before the context operation. This is reduced to 0.2957 after using the context to find the posterior probability. Figure 4.24 shows the difference between these two uncertainty images, from which it can be clearly seen that the maximum improvements were within the agricultural fields. This is further confirmed by displaying the percentage of the improvement expressed as the uncertainty difference divided by the original uncertainty, as shown in Figure 4.25.

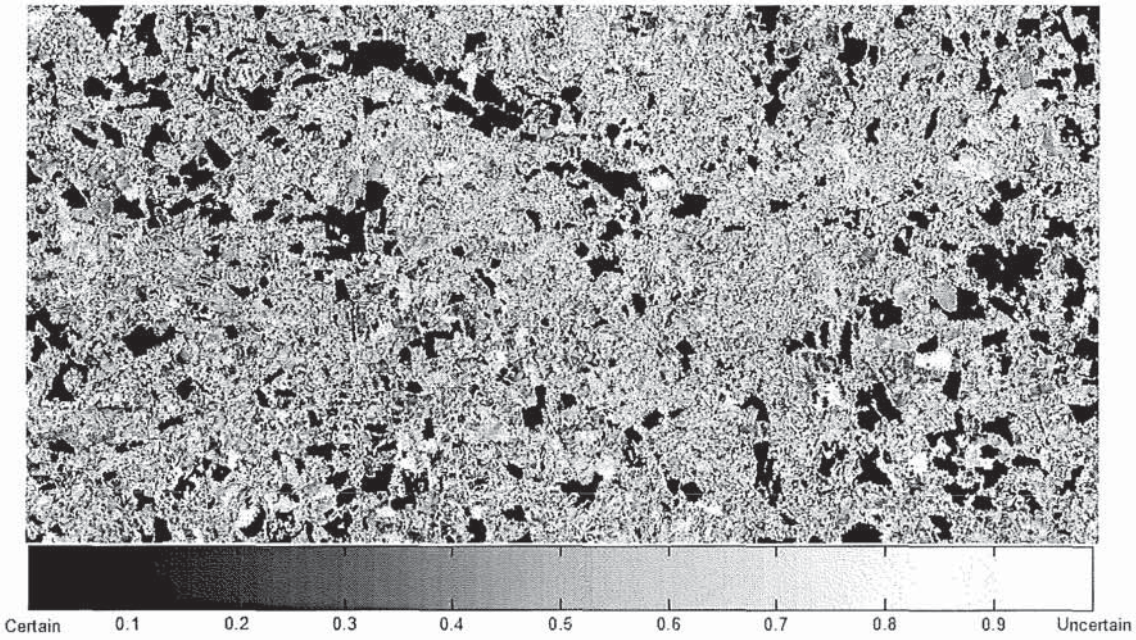

Figure 4.22: Classification uncertainty before the context operation

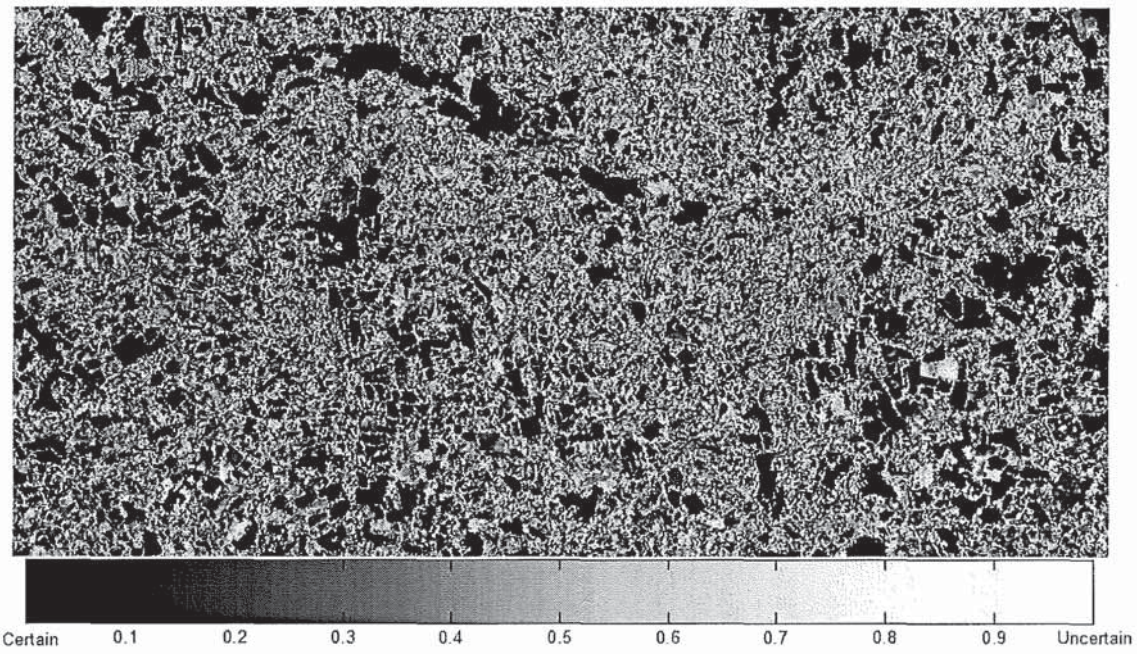

Figure 4.23: Classification uncertainty after the context operation

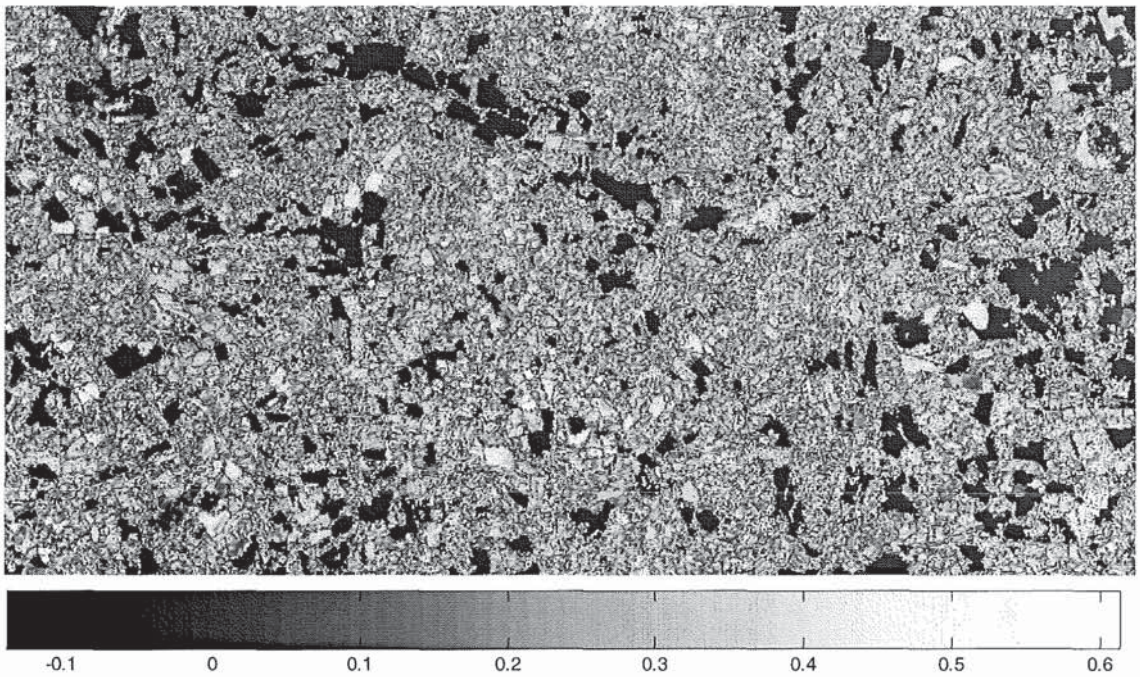

Figure 4.24: The uncertainty difference before and after the context operation

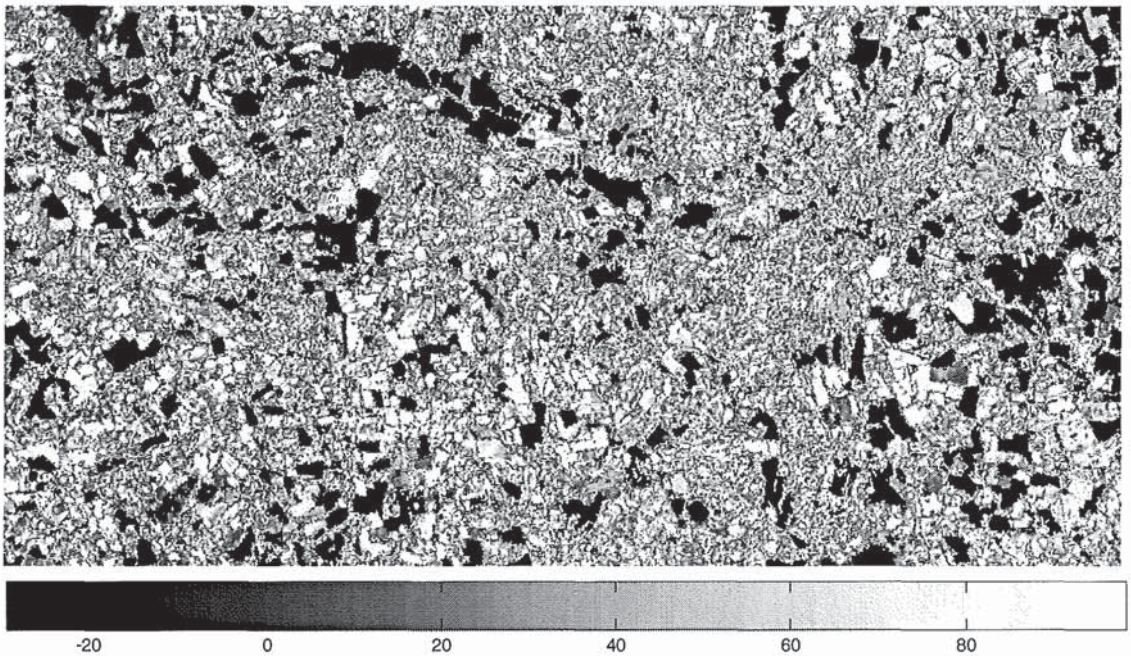

Figure 4.25: The percentage of uncertainty improvement before and after the context operation

4.6. Classification of the Fields

After reducing the classification uncertainty using the context of each pixel, the next step is to use this fuzzy classification output, together with the polygons obtained from the OS 1:2500 digital map, to find the most likely class for each agricultural field. It is possible to perform the per-field classification using the original probabilities without using the context of each pixel. There is some replication in modifying the posterior probability from fcm using these two spatial operations (i.e. pixel context and per-field). In this work both operations were used. However, further research may be required to compare the results of either applying each operation separately, or their combination together, to see how this will affect the classification results.

The estimate of the number of classes in the image was estimated as 18 for the vegetated area and 3 for water, cloud, and bare earth. Thus, the total number of classes considered was 21. Each pixel in the image has a degree of membership to each of these classes. The aim was now to derive for each agricultural field a probability measure of belonging to each class considered. This can be achieved by aggregating the membership grades of all pixels within each field in two ways:

- the average value of the membership grades for each class (h);
- Bayesian multi-source classification mechanism.

The second method was used here. If each pixel in the field is considered as an independent source of information for that agricultural field, then the Bayesian multi-

source classification mechanism can be used to derive the probabilities of it belonging to each class.

Assuming the membership grades are equivalent to the probability of a pixel belonging to each class, according to Bayesian probability theory (Tso and Mather, 2001):

$$P(h \mid e_1, e_2, \ldots, e_n) \propto \left[P(h \mid e_1)/P(h)\right]^{\alpha_1} * \left[P(h \mid e_2)/P(h)\right]^{\alpha_2} * \cdots * \left[P(h \mid e_n)/P(h)\right]^{\alpha_n} * P(h) \qquad \textbf{Equation 4. 2}$$

If equation 4.1 is substituted into equation 4.2, one obtains:

$$P(h \mid e_1, e_2, \ldots, e_n) \propto \left[\frac{P(e_1 \mid h)}{\sum_i P(e_1 \mid h_i) * p(h_i)}\right]^{\alpha_1} * \left[\frac{P(e_2 \mid h)}{\sum_i P(e_2 \mid h_i) * p(h_i)}\right]^{\alpha_2} * \cdots * \left[\frac{P(e_n \mid h)}{\sum_i P(e_n \mid h_i) * p(h_i)}\right]^{\alpha_n} * P(h) \qquad \textbf{Equation 4. 3}$$

In Equation 4.3, all the variable notations are the same as in Equation 4.1, and (n) is the total number of pixels in the field. The prior probability $P(h)$ of a field belonging to class (h) can be considered to be the same as the membership grade of each pixel to class (h). $P(e \mid h)$ is replaced by the averaged membership grade to class (h) for all pixels within the same field.

$\alpha_i \in [0,1]$ is the pixel-specific weighting parameter, which allows one to adjust the contribution for the i^{th} pixel (Lee *et al.*, 1987). The reason of appending the reliability measure is that the OS 1:2500 digital map is not perfectly geo-referenced with the ETM+ image, so some unwanted pixels from the neighbouring fields might be included in the field of interest, thus affecting its probability of belonging to its appropriate class. This

reliability measure might be estimated for each field using the normalized inverse spectral distance to the mean reflectance within the field.

The vector data for the polygons were converted to raster format with a 10m-pixel resolution, and were assigned the probabilities obtained by applying Equation 4.3. The fcm output after context operation was used as the probability measure of each pixel belonging to each class. All pixels inside each polygon were considered as n observations for that field, and their probabilities were aggregated using the Bayesian multisource classification mechanism. The results are discussed in the next section.

4.6.1. The results of the field classification

First of all the classification uncertainty is reduced significantly, as shown in Figure 4.26, with the overall value for the classification uncertainty is 0.2044. This means that each field has a high probability of belonging to a specific class rather than to many alternative classes. The first maximum probability and its corresponding classes are shown in Figures 4.27 and 4.28 respectively. The second rank maximum probability and its corresponding classes are shown in Figures 4.29 and 4.30 respectively. From consideration of these figures it is obvious that the second rank maximum probability is much lower than the first rank maximum probability, and thus the likelihood of the field belonging to second maximum class is much less plausible. Furthermore, some fields, which appears black in figure 4.30, have no alternatives probable class because the second rank maximum probability of these fields is very close to zero. Some fields appear to have high probability associated with the 2^{nd} ranked class.

The class identity number of the classification needs to be converted to a land cover class or an information class. Since the classification was semi-supervised, some of these classes are known, and Table 4.6 present the classes' identity numbers and their associated land cover classes where this is the case. However, this is not the final classification; there is a need to distinguish different types of crops, but before doing this there is a need to ascertain whether or not the classification quality is good enough for useful information about the planted areas to be extracted. This is done by visual inspection alongside the false colour composite (FCC457) and the aerial photography. A closer look at the first rank maximum likely classification (Figure 4.28) reveals imperfections, and therefore, a further step to improve this classification was undertaken. This is presented in the next section.

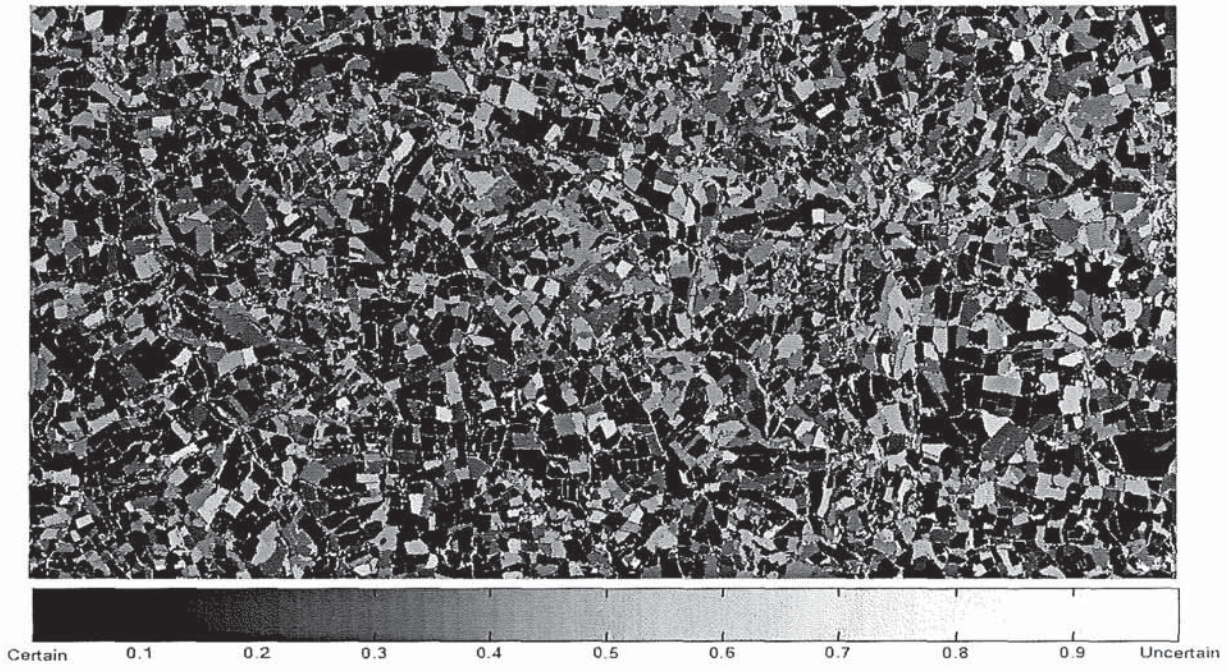

Figure 4.26: Classification uncertainty for Field Classification Using Bayesian model

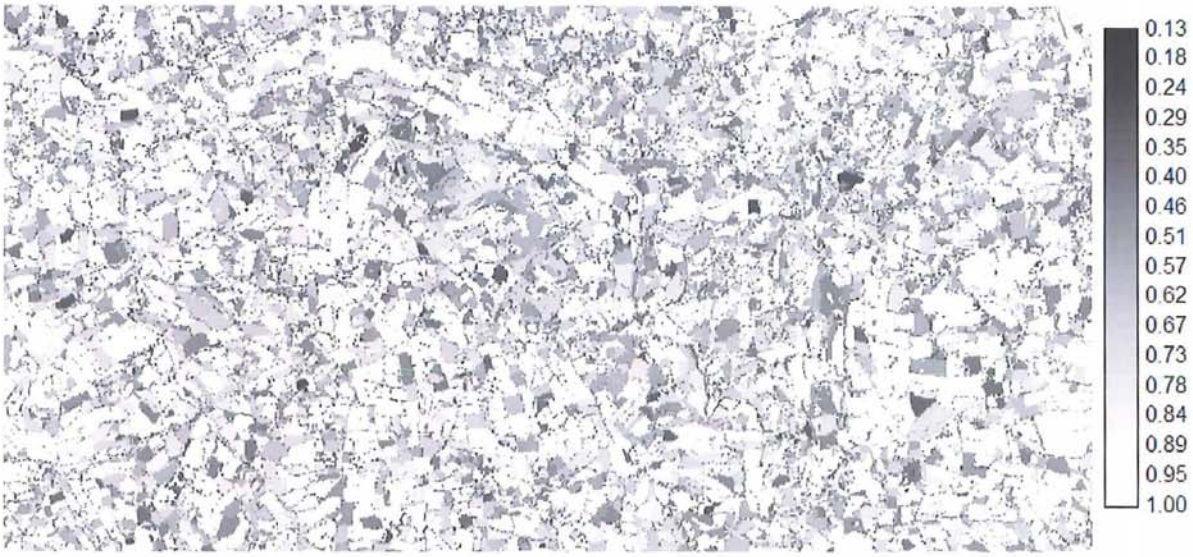

Figure 4.27: The probability for each field of belonging to the first rank maximum likely class in (Fig 4.28)

Figure 4.28: First rank maximum likely class for each field

Figure 4.29: The probability for each field of belonging to the second rank maximum likely class in (Fig 4.30)

Figure 4.30: Second rank maximum likely class for each field

Table 4.6: Classes identity numbers and their corresponding land covers name

Class 1,5,18	Woodland
Class 2-4,6-17	Crop or Grass
Class 19	Bare earth
Class 20	Water
Class 21	Cloud

4.7. Improving the semi-supervised classification of the Landsat ETM+ image

The vegetation cluster centres were determined from the indexed FCC457 image using the methodology presented in section 4.4.2.5. These centres were then used to calculate the membership grades of each vegetation pixel within each of the classes considered using fcm in supervised mode. The selection method from the indexed image may cause some bias in the centre of each class. This might explain to a certain degree the misclassification of some fields as discussed in section 4.6.1. Therefore, it was considered that adjusting the cluster centres would improve the results.

The field classification obtained in section 4.6 was used to determine the new centres. In this classification each agricultural field was assigned a membership grade for each of the 18 classes. The first rank maximum likely class was assigned to each agricultural field to produce a crisp classification. In this crisp classification all the fields are assigned to a particular class, but in reality the probability of their belonging to this class will vary. Thus, for a particular class, the probability of some fields will be higher than for other fields. Therefore, in this section, only half of the fields that have been assigned to a class will be considered as representing this class. For this exercise all fields of the same class were sorted into descending order, according to their probabilities, and only the top half

were used as representative of that class. Their mean reflectance was then used as the new cluster centres.

The new centres were then used in the supervised fcm to obtain the pixels' membership grades with respect to these new cluster centres. The context classification was then performed as described in section 4.5, and subsequently the field classification was performed as described in section 4.6.

The results of this new field classification show a good enhancement over the original classification in terms of both classification uncertainty and quality. Table 4.7 presents the classification uncertainty for both the original classification and the enhanced one.

Table 4.7: Classification Uncertainty after modifying the cluster centres

	Before context	After context	Field classification
Original classification	0.4951	0.2957	0.2044
Enhanced classification	0.4940	0.2941	0.2087

From Table 4.7 it can be seen that the uncertainty in field classification after adjusting the cluster centres, was greater than for the original classification of estimated centres. However, this does not imply that the original classification is of a higher quality. The classification uncertainty has nothing to do with the classification quality, as it merely indicates whether one class stands clearly above all other alternative classes in the fuzzy classification.

Therefore, to prove whether the adjustment in the cluster centres has indeed improved the classification quality or not, the variance of the reflectance for each class in each band

was calculated and the results are presented in Table 4.8. This table shows the average improvement is positive for all bands. It can be seen that some vegetation classes have negative values, which indicates that there has been no improvement in the within class variance. Therefore, to visually see if the overall within class variance improvement is positive the bar graph figure 4.31 was plotted, which confirms a good overall positive improvement.

The vegetation class number 18 shows the highest improvement. The reason for this may be attributed to the large number of pixels (8487) migrated from other classes into class 18. By contrast, only a few pixels (133) originally classified as class 18, moved to other classes in the second classification.

Table 4.8: Percentage of variance improvement in each band for each vegetation class

	Band 2	Band 3	Band 4	Band 5	Band 7	Average
Class 1	-1.68%	-0.72%	3.76%	3.99%	-0.51%	0.97%
Class 2	-11.46%	-8.42%	-10.31%	-7.39%	-2.90%	-8.10%
Class 3	8.18%	8.42%	2.19%	0.09%	3.51%	4.48%
Class 4	2.40%	0.24%	1.31%	11.06%	7.60%	4.52%
Class 5	-8.74%	-8.32%	4.23%	-3.53%	-3.21%	-3.91%
Class 6	8.63%	8.00%	1.14%	1.08%	2.24%	4.22%
Class 7	3.87%	2.78%	9.60%	-0.73%	0.18%	3.14%
Class 8	-5.74%	-0.32%	4.58%	-6.11%	0.09%	-1.50%
Class 9	-0.08%	-2.03%	0.57%	-1.10%	-2.13%	-0.96%
Class 10	9.14%	8.50%	-2.68%	1.06%	1.08%	3.42%
Class 11	16.66%	14.86%	9.49%	0.83%	3.30%	9.03%
Class 12	6.29%	12.34%	13.85%	3.03%	3.12%	7.73%
Class 13	-8.36%	-7.85%	-2.55%	17.40%	-1.33%	-0.54%
Class 14	-10.61%	-3.33%	10.43%	2.27%	-5.38%	-1.32%
Class 15	2.28%	1.48%	3.88%	2.60%	-1.29%	1.79%
Class 16	4.02%	0.36%	9.42%	12.48%	7.61%	6.78%
Class 17	-5.29%	2.45%	7.30%	-8.47%	-6.36%	-2.08%
Class 18	13.64%	16.89%	13.66%	14.18%	16.45%	14.97%
Average	1.29%	2.52%	4.44%	2.37%	1.23%	

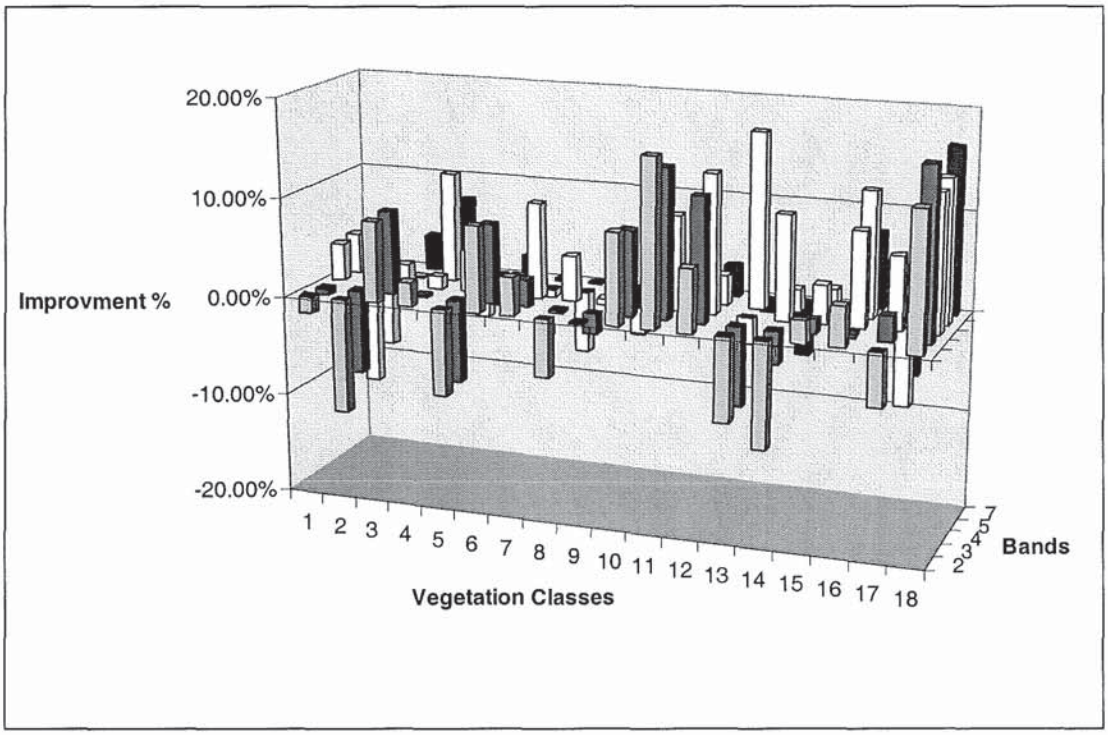

Figure 4.31 Visual inspection of the overall improvement

As this was not absolute proof of the enhancement, it was deemed that another visual inspection of the classification itself might reveal the quality of the adjusted classification. For this, both classifications were displayed using same colour palette, which was similar to the false colour composite FCC457, these are shown in Figures 4.32 and 4.33 for the classification before and after cluster centres adjustments respectively. Although these two classifications look similar to each other, the same field in the two images has different membership grades to each of the vegetation classes. Further, the second image is indeed better than the first one, as it is more similar to FCC457 (Figure 4.15). Examples of this are indicated with small dotted circles in the two images. Therefore, the second enhanced classification for area estimations will give better correspondence with the agriculture census data.

The next task was to attempt to relate the classes revealed by the semi-supervised classification to the information already obtained for the land cover classes. This is discussed in next section.

4.8. Identifying the crops from the semi-supervised classification

As discussed in section 3.7, the agriculture census data provides a robust estimation crops and vegetation cover for a large scale region. Further, it may not be possible differentiate between all crop types in the region using the classified image. Therefore, in this section, an attempt is made to identify some of these crops in the study area.

Table 4.10 shows the areas of each vegetation class in the classified image together with some of the agricultural census data. This table is for comparison only and does not indicate a definitive identification of the relevant classes' name. This mean, for example, class 2 does not necessarily have to be wheat, it simply shows that the areas are similar. However, class 2 is more likely to be wheat, because it has a large area that corresponds with the large area of wheat in the census data (Table 3.4). Clusters 1, 5 and 18 were recognised as woodland from the aerial photography, and they were therefore merged together. The resulting area is much higher than was reported by the census data. Although, Class 9 and 10 are very distinct in the image, it was not possible to determine their identity. To achieve this would require visiting the area and interviewing the farmers. However, although it was not possible to provide an identity to all the classes, this is not necessary in order to fulfil the main objective of the research - developing a methodology to improve the classification of the land cover by integrating multi-resolution multi-temporal imagery.

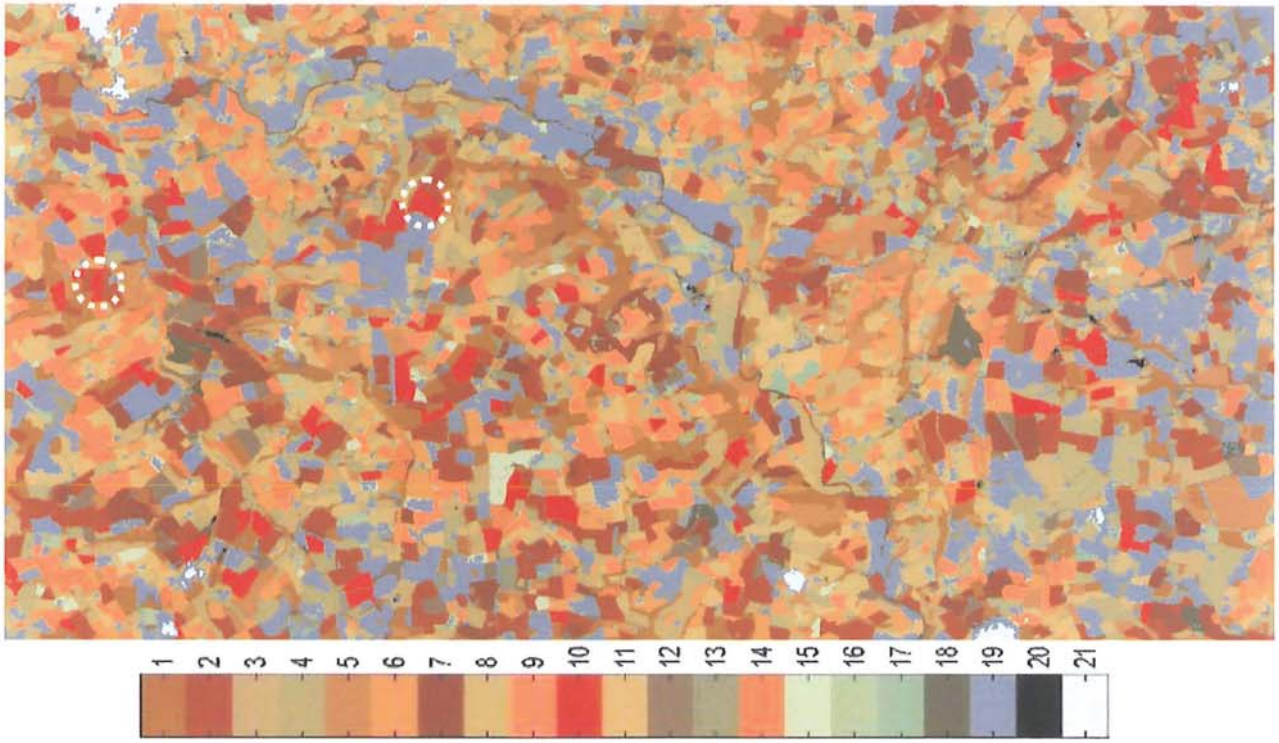

Figure 4.32: Hard fcm classification using estimated cluster centres

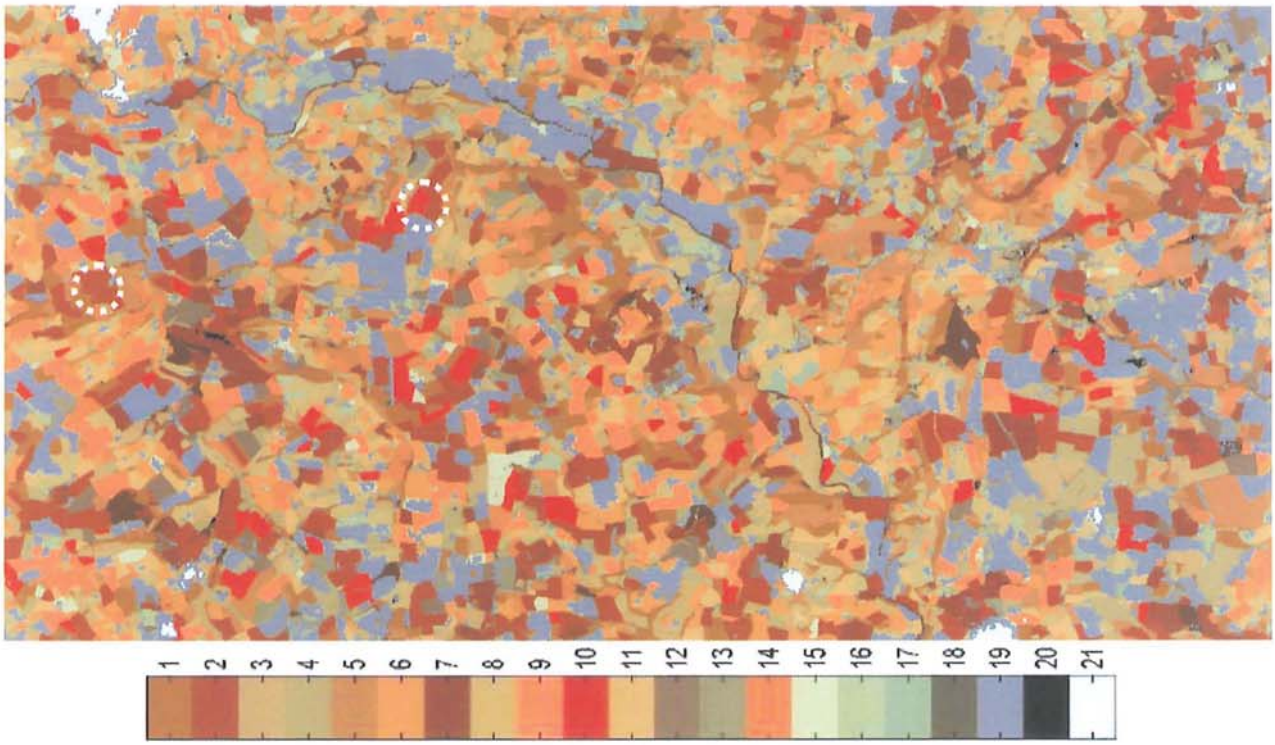

Figure 4.33: Hard fcm classification using adjusted cluster centres

Table 4.9: Area of each cluster from the classification and from the agricultural census data in hectares

Class		1, 5 and 18	2	3	4
Area	Classification	3494.27	1806.25	1325.14	1353.36
	Agricultural census data	Woodland* (1236.3)	Wheat* (2401.6)	-	-
Class		6	7	8	9
Area	Classification	1290.63	1091.57	1112.58	1049.65
	Agricultural census data	-	-	-	Temp. grass* (1184)
Class		10	11	12	13
Area	Classification	574.11	862.86	570.91	558.37
	Agricultural census data	-	-	-	-
Class		14	16	17	19
Area	Classification	681.25	458.74	244.01	3284.06
	Agricultural census data	-	-	Potatoes* (230.9)	-

(-) Unknown match between census data and the classification obtained
(*) Possible crop types

4.9. Summary and conclusions

In this chapter the per-parcel classification performed on the Landsat ETM+ image of the study area is described. The boundaries of the parcels were derived from OS 1:2500 digital maps. Each parcel is described by its membership grade to each class. The classification was unsupervised and based on the fuzzy c-means algorithm. However, the fcm classification was performed in a supervised mode, where the centre of each class was determined using the indexed image from the false colour composite of Landsat ETM+ bands 4, 5 and 7. The indexed image was used mainly for the identification of the

discernible classes in the study area. The identification process was performed by visual inspection of the spatial distribution of each index and matching each with the aerial photograph. As consequences, only 21 classes were defined including the cloud, water bodies and bare earth. Figure 4.34 outlines the steps performed during this classification process.

The resulting classification was of a very satisfying quality. The improvement in the classification was perceived through the reduction in the classification uncertainty, and has been achieved by two means. Firstly the membership grades were updated using the context information from the surrounding pixels. Secondly, the membership grades for each agricultural field were calculated from all the pixels within each parcel, assuming each pixel in the parcel is an independent data source. Therefore, using per-parcel classification rather than per-pixel classification is an effective means of improving the classification of agricultural fields. However, the land cover description could not be identified for all spectral classes. This is considered to be unimportant for this research, because the main objective was to investigate the improvement in classification that could be achieved through the integration of multi-resolution images from different data sources. The next chapter presents the method proposed for multi-resolution analysis.

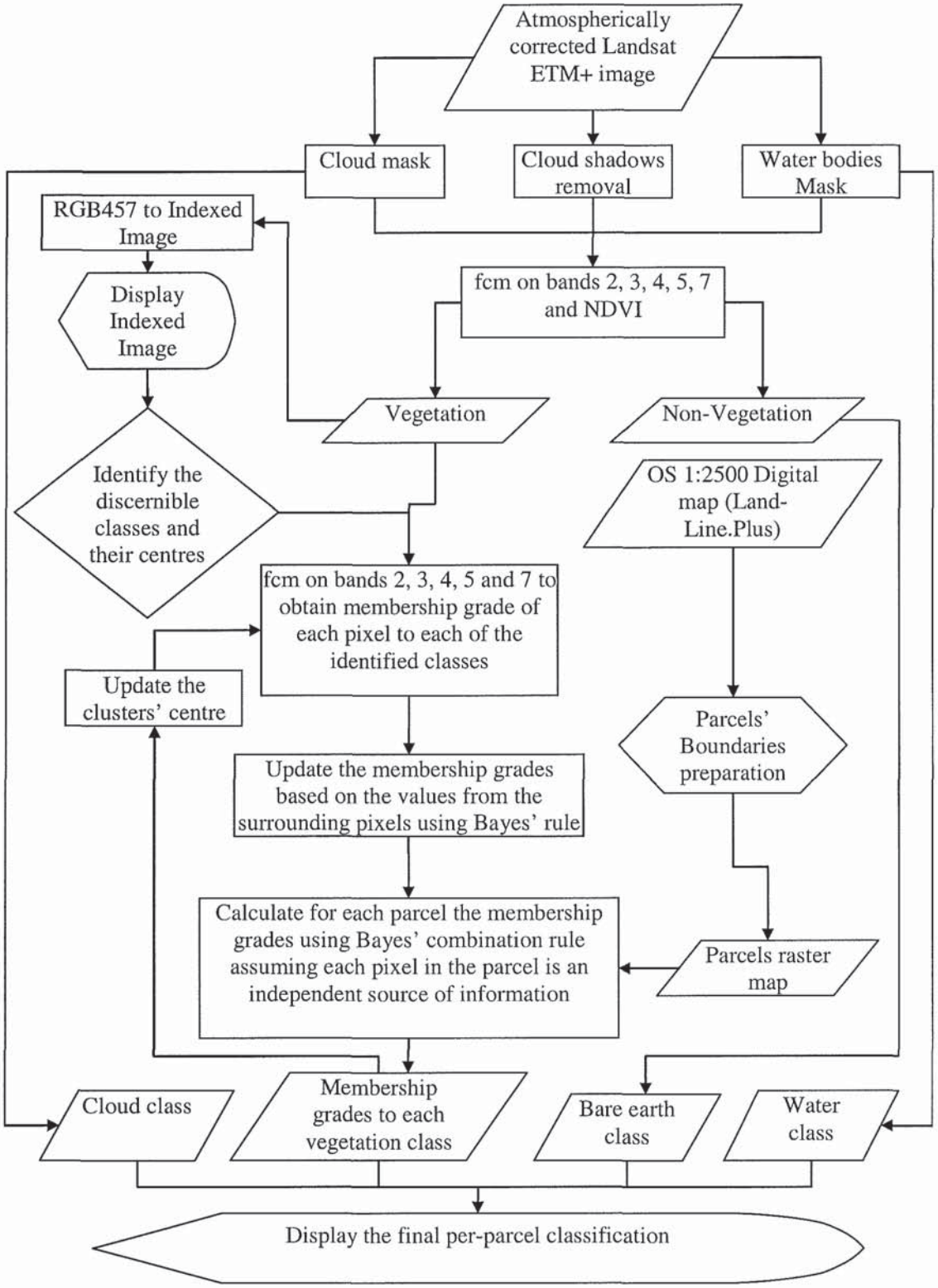

Figure 4.34: Approach for the per-parcel classification performed on the ETM+ image

Chapter 5

Multi-resolution Multi-temporal Analysis

5.1. Introduction

Earth observation satellites have provided us with huge volumes of remotely sensed data with a wide choice of multi-sensor, multi-resolution, multi-spectral and multi-temporal data. Recently, the cost of satellite data acquisition and processing has dropped dramatically, and satellite imagery has become more accessible to users, even free of any charge in some instances.

With the availability of multi-source data, data fusion has emerged as a new and promising research area that needs further investigation. The process of merging data from different sources of varying resolution, spectral values, and accuracy, requires a dedicated research effort. Many image fusion methods have been proposed for combining multi-spectral low-resolution remotely sensed images with higher resolution panchromatic images to obtain a result having the best characteristic of the original images (see section 5.2). The main constraint in remote sensing data is to preserve the spectral information that is used to distinguish land cover in image classification.

One of the objectives of this chapter is to explore the capability and the applicability of the existing fusion techniques to extract relevant information from the two data sources, Landsat ETM+ and MODIS\Terra imagery. The derived information will be used to improve the existing land cover classification of the study area derived using the semi-supervised classification (chapter 4).

This classification was compared visually with the aerial photography and FCC457, and some misclassified fields were identified where agriculture fields were wrongly classified as woodland and vice versa. The confusion between some agriculture fields and woodland is common problem for images acquired during the peak of the growing season. It may not be possible to resolve this confusion using a single date satellite image.

The single date image conveys the land cover status on the day of acquisition. The use of multi-temporal images has the advantage of adding chronological information during the growing period of each vegetation type. However, apart from the cost, it is highly unlikely that multi-temporal high resolution satellite images can be obtained on the desired days and with a clear sky, especially in countries where cloud cover is predominant. Therefore, using a combination of data from different satellites for vegetation classification is an effective means of exploiting the complementary nature of different data sources, and may improve the information content and the interpretability of the scene, which is not possible with a single data source (Ehlers, 1991).

There are two major benefit of integrating data from different sources of different spatial resolutions. Firstly, as mentioned earlier, the cloud free high spatial resolution images are not available very often, but multi-resolution analysis overcomes this problem by utilizing the data from high spatial and high temporal resolution. Secondly, the varying band widths of the sensors on board different satellite platforms capture different responses from different vegetation, thus offering an opportunity of enhancing a classification. However, the different radiometric resolution prevents the use of training

data obtained for higher spatial resolution images for low spatial resolution image. A crucial stage in integrating the multi-source multi-resolution images is, therefore, to define the pure training areas that are difficult to delineate from the coarse resolution image. A brief discussion on the existing multi-resolution fusion techniques is presented in the next section in order to explore its capability of extracting suitable information from different spatial resolution images. However, as will be discusses later, these fusion techniques exhibited many limitations. Section 5.3 describes the proposed algorithm developed to solve the problem of differing radiometric resolution of Landsat ETM+ and the low spatial resolution MODIS images.

5.2. Data Fusion Techniques

The multi-resolution optical image fusion techniques employed to derive multi-spectral images using the high spatial resolution panchromatic data from the same satellite, might be relatively straightforward. Multi-source image fusion of data originating from different satellites carrying similar sensors or even different sensors is probably the most difficult aspect in the integration of remote sensing image data products. A representative selection of studies on multi-sensor fusion approaches is given by Pohl and van Genderen (1998). This works tends to focus on the fusion of optical and SAR data (Harris *et al.* 1990; Schistad Solberg *et al.* 1994) and of optical image data with different spectral and spatial resolutions (Chavez *et al.* 1991; Pellemans *et al.* 1993; Shettigara 1992; Zhukov *et al.* 1995; Garguet-Duport *et al.* 1996; Yocky 1996; Vrabel 1996; Wald *et al.* 1997). These provide us with a wide range of image fusion techniques that can be used for multi-resolution analysis. However, the choice of the fusion method to be used is highly dependant on the application of the fused image.

Common fusion methods are arithmetic merging procedures or component substitution techniques, such as the Intensity-Hue-Saturation (IHS) or the Principal Component Substitution procedures (Carper *et al.*, 1990, Chavez *et al.*, 1991, Shettigara, 1992). These techniques can provide a valuable basis for visualisation products, as they strongly enhance textural features. On the other hand, they can lead to a significant distortion of the spectral characteristics of the merged images (Vrabel 1996). Thus they cannot be recommended for subsequent quantative processing, such as spectral classification.

Pellmans *et al.* (1993) presented a radiometric method, in which a linear combination of multispectral and panchromatic radiances was used to derive new multispectral bands. While this method preserves the radiometry of the spectral information, it is limited to bands that are spectrally located within the range of the panchromatic image. For example, the red, green and blue bands of MSS are used for fusion with the panchromatic band. An interesting approach was presented by Zhukov *et al.* (1995), which was based on the retrieval of spectral signatures, which correspond to constant grey levels in the panchromatic image. The result revealed sub-pixel variations in the multispectral bands, which were associated with grey level variations in the panchromatic image. However, most promising are methods that use wavelet transforms for the fusion of multiresolution images, as they largely preserve the spectral characteristics of the fused image (Ranchin and Wald 1993; Garguet-Duport *et al.* 1996; Yocky 1996; Wald *et al.* 1997).

A new approach, the Adaptive Image Fusion method, uses adaptive filters to extract edge information from the high resolution image, and transfers this information to the multispectral image. It was designed as a pre-segmentation tool for subsequent numerical

classification. Thus, the fusion product is a pre-segmented multispectral image, with low variance within spectral image objects and sharp borders between the objects. The inclusion of highly textured areas from the panchromatic image is not supported by the technique, but the spectral characteristics of the multispectral image are preserved to a large extent (Steinnocher 1999).

Usually, fusion is a relatively straightforward process when using different resolutions from sensors on the same platform. This is because the fused images are synchronised and have a very good registration but, using images from different satellites is a big challenge.

Most of the existing fusion techniques have been tested for the fusion of medium spatial resolution images with high spatial resolution panchromatic or SAR images. This means studies conducted for the fusion of coarse spatial resolution images, such as those of MODIS, with high spatial resolution are rare and their validity is questionable if the low resolution' pixel size is relatively large with no or few distinctive land cover types. The problem is that the fusion process works by injecting the DN values of each land cover from the medium resolution multispectral image into the corresponding large land cover pixels of a high resolution image. For the case where the land cover is distinctive in both of the fused images the problem of mixed pixel is moderate. However, for low spatial resolution images the majority of the pixels are mixed and for this, injecting the DN values of moderate resolution mixed land cover pixels directly into a coarse resolution image is not a valid course of action. Furthermore, the alignment between the pixels in high and low resolution images is a prerequisite for using any of the fusion techniques. In

this study, the misalignment and inconsistency of the pixels in multi-temporal MODIS images, as shown in Figure 3.10, is likely to seriously reduce the accuracy of the fused images.

Therefore, the application of the fusion techniques discussed so far, seems very limited for the data set in hand. Consequently, as a minimum another method is needed for deriving the spectral signature of the endmember' classes in the mixed pixels of the coarse resolution imagery.

5.3. Deriving land cover reflectance from a coarse resolution image

The problem with coarse resolution images is that the majority of its pixels are mixed. This means the derivation of the spectral characteristics of each land cover class is not easy or straightforward. A widely used method for determining spectrally pure pixels is the (PPI) pixel purity index (Jacobsen, *et al.* 1998, Wagtendonk, and Ralph, 2000). This method requires the identification of many pixels for the class of interest, which seems to work well for hyperspectral high resolution images. However, for coarse resolution images the success of PPI is limited because the majority of pixels are mixed, and it is hard or some times impossible to identify pure pixels in coarse resolution images.

When Takeuchi and Inanaga (2000) conducted a feasibility study for scaling-up the land cover information by combining Landsat-TM and NOAA-AVHRR satellite data they suggested the use of estimated mean vectors for land cover at the training stage. In their method they divided the land cover into major or minor categories according to the occupation ratio. The occupation ratio represents the proportion of the class of interest in a pixel. In their work, pure pixels were defined as those where the occupation ratio for the

category of interest exceeded 90%. Thus, the mean vector for this category was estimated as the mean value in each band of AVHRR data. For minor categories, the estimation of the mean vector was based on the regression line between the reflectance residual in each band, and the occupation ratio of the minor category when this ratio is extrapolated to 100%. They computed the occupation ratio for each category by counting the number of TM pixels classified to this category within the area corresponding to one pixel of the low resolution data (AVHRR). They used the linear mixture model for the spectral mixing of the multiple land cover categories within the coarse resolution AVHRR image.

For the data set of this research the linear mixture model (LMM) is assumed to be a good model for simulating the mixing process of the reflectance of multiple land cover in the coarse resolution MODIS pixels (see section 2.6.1.5). Therefore, the LMM was adopted for the derivation of the reflectance of the land cover classes from the MODIS pixels, assuming the proportions of the land cover is known from the classified ETM+ image.

There are two reasons for using the linear mixture model in this thesis. Firstly, to estimate the mean spectral reflectance of the land cover in each MODIS band, and this will be addressed in the following sections. Secondly, to use the extracted multi-temporal spectral signatures from the multi-temporal MODIS images for the purpose of improving the classification of the Landsat ETM+ image, and this will be discussed in next chapter. However, first several assumptions that were made in order to facilitate the task of integrating the MODIS and Landsat ETM+ data sources have to be justified.

First, and most important, it was assumed that the images were perfectly registered to each other. In reality this was difficult to achieve because locating sufficient Ground

Control Points GCPs in the coarse resolution images and in order to match it to the high resolution image is a laborious task. Nevertheless, this assumption can be justified since with increasing pixel size the potential misregistration is weakened. This is because the positional error for a fine resolution image is relatively higher than the positional error in a coarse resolution image. For peace of mind regarding the good association between the ETM+ and MODIS images acquired on 17th June 2000, false colour composites from similar bands were created for each of the sensors, and are displayed in Figures 5.1 and 5.2. The Landsat ETM+ is at 25m spatial resolution and created using bands 4, 5 and 3. This image was then rotated to match the orientation of the MODIS image. The MODIS image has nominal spatial resolutions of 250m for bands 1 and 2, but band 6 has 500m nominal spatial resolution. Therefore, band 6 was resampled using nearest neighbourhood to 250m nominal resolution. These bands were then used to create RGB image at nominal spatial resolution of 250m. However, the actual spatial resolution in this image is more than 250m because the original MODIS pixel size extracted from the HDF file was used. The areas outside the study area were masked to make the visual comparison easier. Visual comparison confirms a good correspondence between these two images in terms of the reflectance and the features visible, and therefore, a reasonable co-registration can be assumed.

The second assumption is that the per-field classification derived in chapter 4 for the Landsat ETM+ image is of good quality. Despite the fact that no quantitative accuracy assessment has been performed on the classification, it is believed to be the best that can be obtained given the limited data resources available for the study area. The acquisition of ground truth data would be vital at this stage particularly for enhancing this

classification and to support the findings from the study in general. However, the assumption of a good quality classification can be justified assuming the number of misclassified pixels is small and results in insignificant bias in the derived values of the mean reflectance for each class.

5.4. Estimating the mean reflectance of land cover in MODIS images

According to Nishihama *et al.* (1997), MODIS has detectors that are square or rectangular in shape and receive a signal at any particular instant of time from an area of the Earth's surface that is of 1000, 500, or 250m nominal size for nadir pixels. However, the area that is actually sensed along a scan is twice as long as the nominal detector pattern, and the effective time weighted response is triangular as shown in Figure 5.3 (Nishihama *et al.*, 1997).

Therefore, to simulate the MODIS pixel using Landsat ETM+ pixels, the radiances of each category from all ETM+ pixels within a two-MODIS-pixel wide rectangle must be weighted by the triangular weighting function and added together to get the expected MODIS pixel value. Figure 5.4 illustrates the actual area sensed by the MODIS detector at a nominal 250 m resolution.

According to the triangular weighting response function the land cover within the nominal MODIS pixel will contribute about 75% to the reflectance recorded by the sensor and the remaining 25% comes from the land cover outside the nominal pixel.

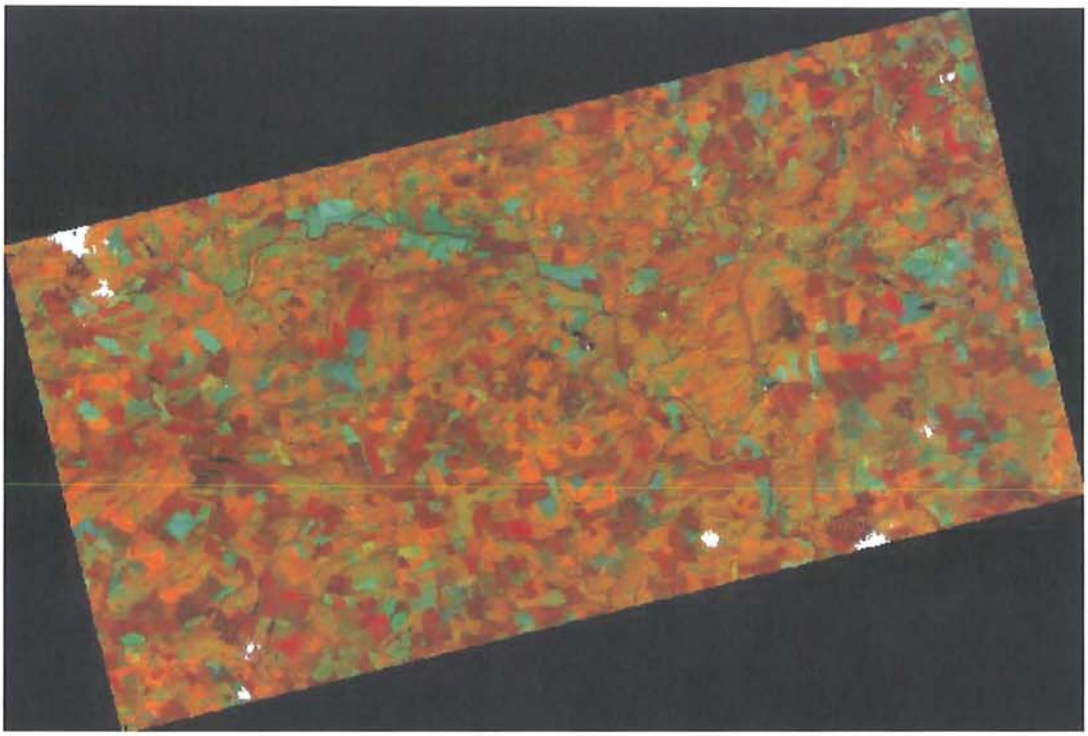

Figure 5.1: FCC453 (RGB) for ETM+ image at spatial resolution 25m (date: 17-June-2000)

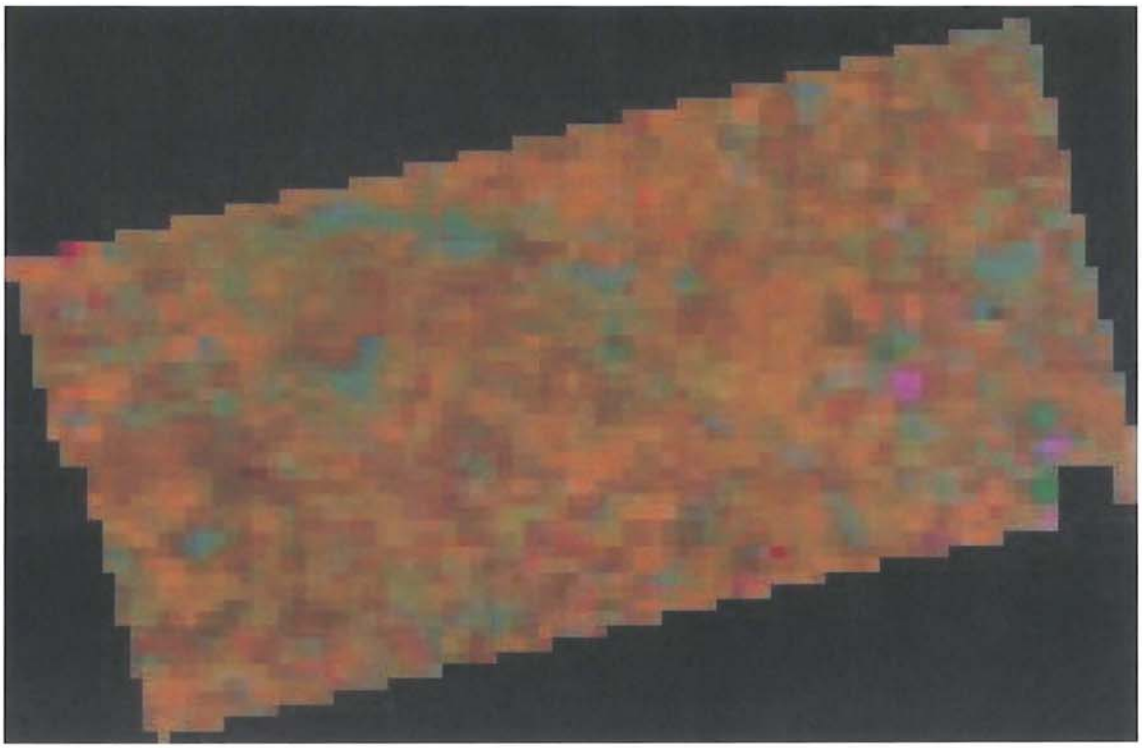

Figure 5.2: FCC261 (RGB) for MODIS image, 250m resolution (date: 17-June-2000)

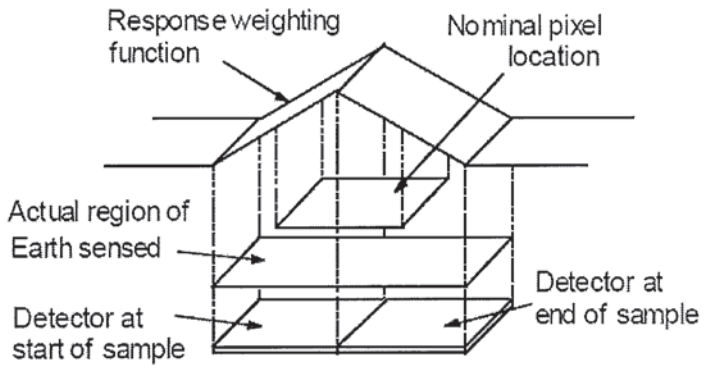

Figure 5.3: Triangular Response Function from the Effective Time Weighting (source: Nishihama *et al.*, 1997)

In order to implement the triangular weighting response into the equation of the linear mixture modelling, the normal proportions in the equation will be modified here and referred to as the triangular proportion. This triangular proportion is the sum of what will be called here the triangular weight.

The concept of triangular weight came from the fact that each point within the actual area sensed by MODIS detector, will contribute to the total radiance depending on the location of this point within the actual area sensed (see Figure 5.4) together with the reflectance of the land cover at this point. Each point will be given a weight depending on the location of the point within the actual area sensed. The points at the far ends of the actual area sensed along scan will therefore be assigned zero weight, and the points at the middle will have weight equal to one, all points in between will be assigned weights depending on their locations using interpolation between 0 and 1. Therefore, within the actual area sensed, all pixels assigned to a particular category must be found and their corresponding triangular weights will be added together. The total weight obtained for each category is

the triangular proportion for that category. Equation 5.1 expresses the linear mixture model as modified to account for the triangular weighting response:

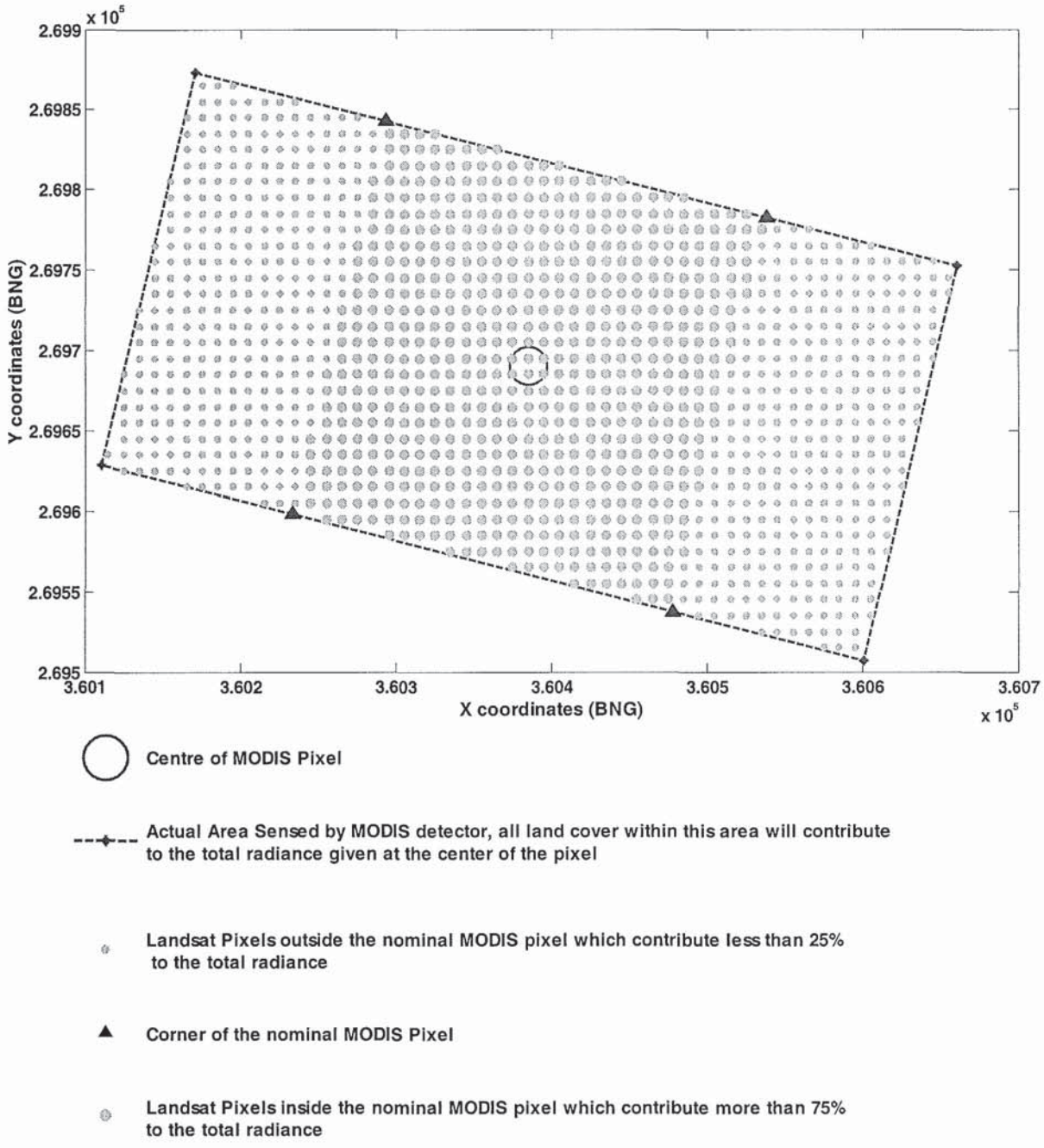

Figure 5.4: Simulated MODIS pixel from ETM+ Pixels (BNG Coordinate system)

$$\sum_{c=1}^{N}(a_c\rho_{ck}) = \overline{\rho_k}$$

$$a_c = \sum_{ic=1}^{m_c} w_{ic}$$

Equation 5. 1

where:

N: total number of classes (c) from the classified ETM+ image

a_c: The triangular proportion of the land class (c)

w_{ic}: The corresponding triangular weight for ETM+ pixel belonging to class (c) within the IFOV of MODIS pixel

ρ_{ck}: The Reflectance for class (c) in band k

$\overline{\rho_k}$: The observed reflectance in band k from MODIS mixed pixel

If the response was rectangular then the weights w_{ic} will be equal to the inverse of the total number of ETM+ pixels within the IFOV. Thus, summing them for a particular class will result in the rectangular proportion that is been used in the normal linear mixture model.

Using the modified linear mixture model for all MODIS pixel within the study area, the number of linear equations obtained will be equal to the number of MODIS pixels covering the area. However, since the MODIS images are sometimes contaminated with clouds, not all MODIS pixels are valid for use in the model. Therefore, The MODIS cloud mask product can be used to identify the contaminated MODIS pixels, and only

those pixels that are flagged as probably or confident clear are used in the model. All MODIS pixels that are flagged in the cloud mask as cloudy, uncertain clear or contain heavy aerosol contamination will be omitted.

This system of linear equations is over determined and the MODIS reflectance for each land cover class is unknown. Two approaches can be followed to estimate the mean vector of land cover, either method 1, by solving the simultaneous linear equations using a least square fit, or method 2 which is similar to that proposed by Takeuchi and Inanaga (2000). In the latter the land cover is divided into major and minor categories, where the reflectance for major categories is calculated as the mean reflectance of pure MODIS pixels, which are defined as pixels having a proportion of the land cover of interest greater than 90%. The reflectance for minor categories is then obtained from the regression line between the proportion and the residual of MODIS reflectance.

These two methods were used in this study to derive the reflectance of the various classes in the MODIS image acquired on the same day as the classified ETM+ image. Only two bands (Red: band1 and NIR: band2) are available from MODIS at 250m nominal spatial resolution for the derivation of the reflectance of land cover classes. In order to define the actual area sensed by the MODIS detector we can only use the un-resampled MODIS data.

The ready made product for MODIS surface reflectance (MOD09) was used in section 4.2.1 to compare the overall reflectance of the atmospherically corrected ETM+ image and the MODIS surface reflectance. This product was considered less useful for the work presented in this chapter, because it was already projected to sinusoidal projection system

(SIN) with a resampled 250 m ground pixel resolution. Therefore, it is deemed to be geometrically distorted, thus impeding the process of identifying the actual IFOV as discussed earlier in this section.

The resulting reflectance in the red and near infrared MODIS bands for all vegetation classes were compared with the mean reflectance of these classes from the ETM+ band 3 and 4 (red and NIR respectively). The result shows a very good association between the estimated value and the mean ETM+ value as shown in Figure 5.5.

Both methods produced good estimates of the reflectance of all vegetation classes. Method 2 is time consuming and more sensitive to the errors of the misclassification of ETM+ image. By comparison method 1 is straightforward, and the solution of the over determined linear simultaneous equations, in a least square sense, may have the advantage of reducing the bias in the estimation, if the class proportions in some MODIS pixel is incorrect due to the classification errors in the classified ETM+ image. Therefore, method 1 was adopted for the estimation of the mean reflectance vector of the land cover classes.

There are slight differences in the reflectance of each class calculated in the red and the NIR bands of the MODIS image and the reflectance of those classes found in the ETM+ image data, as shown in Figure 5.5. In fact, this was expected, apart from the different spectral characteristics of the MODIS sensor, another most likely source of difference was the atmospheric effects, path radiance, the different time of satellite overpass and the varying sun angle or view angle. While the ETM+ reflectance is for the surface reflectance, the MODIS reflectance is for the top of atmosphere. It can clearly seen from

Figure 5.5, that the red band reflectance for vegetation at the top of the atmosphere is always larger than its surface counterpart, due to additional components of multiple scattered radiation occurring within the atmosphere. Furthermore, the NIR reflectance at the top of atmosphere is always smaller than its surface counterpart, due to the absorbtion of NIR wavelength by the atmosphere. This produces an NDVI value that is always smaller than its surface counterpart (Myneni and Asrar, 1994).

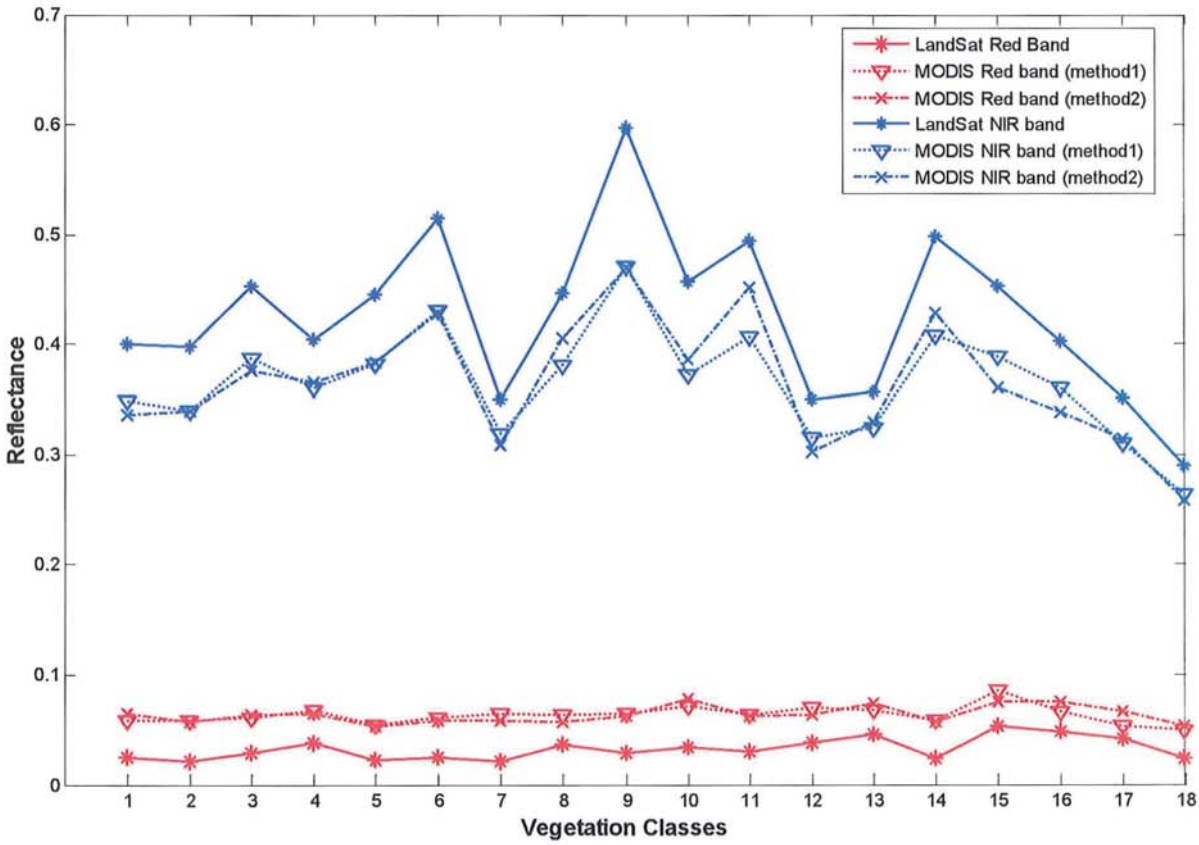

Figure 5.5: Comparison between the red, NIR reflectance of vegetation classes calculated from MODIS 250m resolution using method 1: solving the system of linear equation of modified linear mixture model, or method 2: mean value for major category and interpolated value for minor category.

However, for this work, using the top of atmosphere reflectance can be justified because the objective of this work is to develop a methodology for integrating the MODIS sensor data with the Landsat ETM+ data in order to improve the ETM+ classification. Furthermore, the intention is to use the multi-temporal spectral signatures derived from each individual MODIS image, and not a global spectral signature, to derive information from the multi-temporal MODIS images. Therefore, the atmospheric correction for MODIS image in this context might be considered as unnecessary step (Song *et al.* 2001).

Having derived the reflectance of each land cover in MODIS red and near infrared bands (band 1 and 2), for the 250m spatial resolution image, it is worth investigating whether the same method can be used to derive the reflectance in other MODIS bands (i.e. 3, 4, 5, 6 and 7), that are sensed with a nominal spatial resolution of 500m.

5.5. Using MODIS 500m resolution to derive the class reflectance

The modified linear mixture model presented in the previous section was used to construct a system of simultaneous equations for MODIS bands 4, 6 and 7 at 500m resolution. These equations were solved for the reflectance of all existing classes in the study area. The derived reflectance for all vegetation classes in MODIS bands 4, 6 and 7 were compared with their counterparts from ETM+ bands 2, 5 and 7, the results are shown in Figure 5.6.

Figure 5.6 shows that these derived class reflectances estimated from the MODIS 500 m resolution pixels are very well associated with the mean reflectance of these classes in the ETM+ bands, although there are some dissimilarities and a large deviation between the reflectance of the classes in the green bands (MODIS band 2 and ETM+ band 4). The

probable reason for these differences, beside the varying wavelengths, is the greater effect of the atmospheric interference in the visible bands.

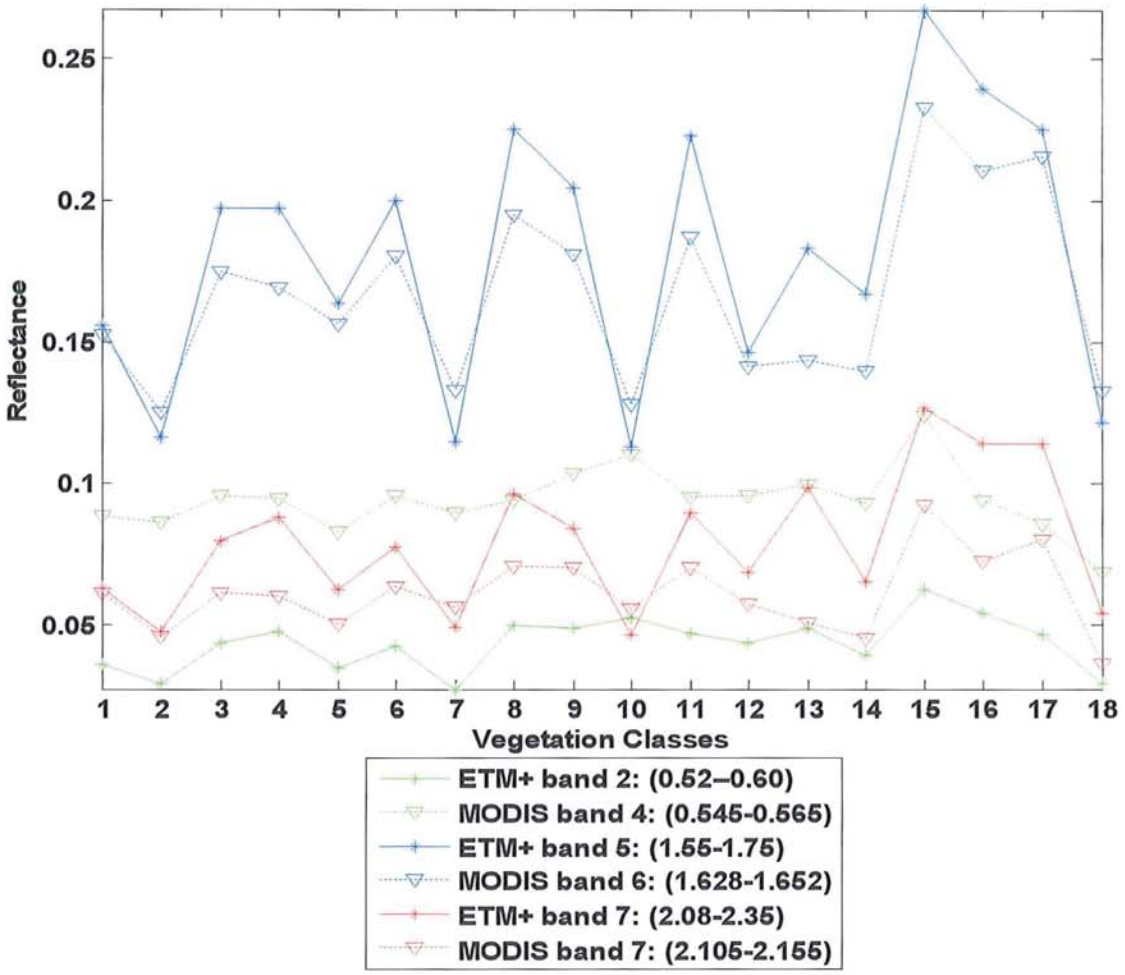

Figure 5.6: A comparison between the classes' reflectance derived from 500 spatial resolutions MODIS bands 4, 6, and 7 with the mean reflectance of these classes in ETM+ bands 2, 5 and 7.

The results of deriving the MODIS reflectance of the land cover classes using the classified ETM+ image were promising and could extended to derive the likely reflectance of each class in the multi-temporal MODIS image. It was assumed that the agricultural practice in the study area consist of a single crop per calendar year. The

importance of this assumption is that any changes in the reflectance for a particular land cover type will take place concurrently in all polygons (fields) assigned to that land cover. In other words, all fields growing the same crop had the same chronological growing profile. If this were not the case then a contradiction in the simultaneous equations would occur when calculating the percentage of each class in each MODIS pixel. The procedure followed to derive the multi-temporal reflectance of each class is presented in the next section.

5.6. Deriving the multi-temporal reflectance of each class from MODIS images

One of the merits of MODIS images is the availability of these images on a daily bases. However, for some parts of the world it can be difficult to obtain cloud-free images, for example over the UK. The archived MODIS images in the year 2000 were searched thoroughly to find images with minimum cloud cover over the study area in UK (section 3.2). 2000 was selected because the available Landsat ETM+ image was acquired during this year on 17th of June. From the daily MODIS record only 47 images were found satisfying the clear sky criteria for the study area. However, the problem of enlarged pixel size and bowtie effects (section 3.4.2.1) degrade the quality of the off nadir pixels with a view angle greater than 25 degree (Nishihama *et al.*, 1997). Therefore, both clear sky and view angle criteria were considered in the selection of a subset of the daily MODIS images, covering only the study area, which had been extracted from each full MODIS scene (section 3.4.2). As a consequence, only 18 images were selected, as shown in Table 5.1. The MODIS images cover the period from March till December were selected to enable the analysis of the change in land cover reflectance during this period. The percentage of clear sky was calculated using the data set (Cloud_Mask) in the HDF file

created for each daily image as described in section 3.4.2. A pixel was considered clear, when using the MODIS cloud mask, if it was flagged as confident clear or probably clear and not contaminated by heavy aerosols. However, as shown in Table 5.1 some of these images were selected even though they were contaminated by clouds over a large proportion of the study area (e.g. 50 %). The selection of these low percentage clear sky images was mainly based on the quality of these images, which were viewed at low zenith angle, thus, the pixels were near nadir for the MODIS sensor and therefore had a normal spatial resolution close to the nominal resolution. The sensor zenith angle was estimated as the mean zenith angle of the pixels that fell within the study area. Even though some images were viewed at an extreme angle they were not rejected as they possessed a high percentage of clear sky.

Each selected MODIS image was used in turn with the per-parcel classification of the ETM+ image (section 4.6) to estimate the likely class' reflectance on that date. This was performed by generating a system of simultaneous equations for each date, and solving the system for the unknown reflectance, as described in section 5.4.

The main concern about estimating the reflectance on a date where the image was partially covered by clouds, was the probable under representation of some classes. This could lead to a less reliable system of simultaneous equations, because only the clear pixels are used to construct the simultaneous equations using the modified linear mixture model. Thus, if 50% of the image were cloudy, then only half the number of MODIS pixels would be valid for use and the affected classes would be under represented in the system of the equations. Furthermore, this problem would become exacerbated and could

lead to a wrong estimation of the reflectance, if the proportions of the under represented classes were generated from misclassified ETM+ pixels.

Table 5.1: List of MODIS images selected from the archive
The highlighted row show the date of Landsat ETM+ image

Julian Day	Date of image acquisition	Percentage of Clear sky	Sensor Zenith Angle (Degree)
71	11-Mar-2000	82%	16.53
73	13-Mar-2000	37%	1.28
75	15-Mar-2000	75%	18.85
98	7-Apr-2000	97%	9.22
121	30-Apr-2000	68%	0.81
123	2-May-2000	69%	17.42
135	14-May-2000	100%	17.25
146	25-May-2000	52%	9.44
162	10-Jun-2000	49%	9.08
169	17-Jun-2000	98%	0.68
199	17-Jul-2000	75%	17.76
203	21-Jul-2000	100%	17.75
235	22-Aug-2000	56%	17.33
242	29-Aug-2000	62%	8.31
247	3-Sep-2000	100%	18.43
267	23-Sep-2000	62%	17.25
322	17-Nov-2000	83%	9.13
338	3-Dec-2000	41%	9.81

However, it is difficult to judge here how badly the aforementioned problem will affect the reflectance estimation on each day. Since the reflectance estimation was independent for each individual image it was decided to consider all the selected 18 MODIS images, bearing this problem in mind when further processing of these images was needed.

Another problem that could have the most effect on the resulting multi-temporal profile of the reflectance, is the atmospheric interference and the seasonal change in the solar illumination. Fortunately, the reflectance from MODIS level 1B was from the top of the

atmosphere and had already been adjusted for the Earth-Sun distance and the cosine of the solar incidence angle (Barbieri, 1997). Thus, the only factors affecting the temporal profile were the atmosphere and the clouds. However, different atmospheric conditions would affect an entire scene by adding a specific path radiance component that was constant for that day, but different from day to day. Assuming this, the amount of fluctuation in the profile for each land cover class would be similar over time. Therefore, for the purpose of classification the atmospheric effects can be ignored.

For each MODIS scene a system of linear equations was constructed using the modified linear mixture model. Only MODIS bands 1 and 2 at a nominal 250m spatial resolution were used to estimate the top of the atmosphere reflectance of the classes. The per-parcel classification of the ETM+ image was used to determine the percentage of each class in each MODIS pixel. The modified linear mixture model was then used to construct the equation for each MODIS pixel. All clear sky MODIS pixels were used to build the system of simultaneous equations for each date. This system of simultaneous equations was solved to obtain a single red and a single near infrared reflectance for each class on each date. For each class, the Red and NIR reflectance values were used to obtain an estimated NDVI value for that class on that date of MODIS image. These were then used to explore the multi-temporal NDVI values for each vegetation class (class ID: 1 through 18) and the bare earth (class ID: 19).

For the sake of clarity, Figure 5.7 shows the multi-temporal NDVI values estimated from multi-temporal MODIS images, for some of the vegetation classes and the bare earth class - these classes are as identified from the classification of ETM+ image, or from the

aerial photography. The displayed classes in Figure 5.7 are: class1 (WoodLand1), class2 (probably crop), Class5 (WoodLand2), class9 (probably crop), class10 (probably crop), and class19 (bare earth).

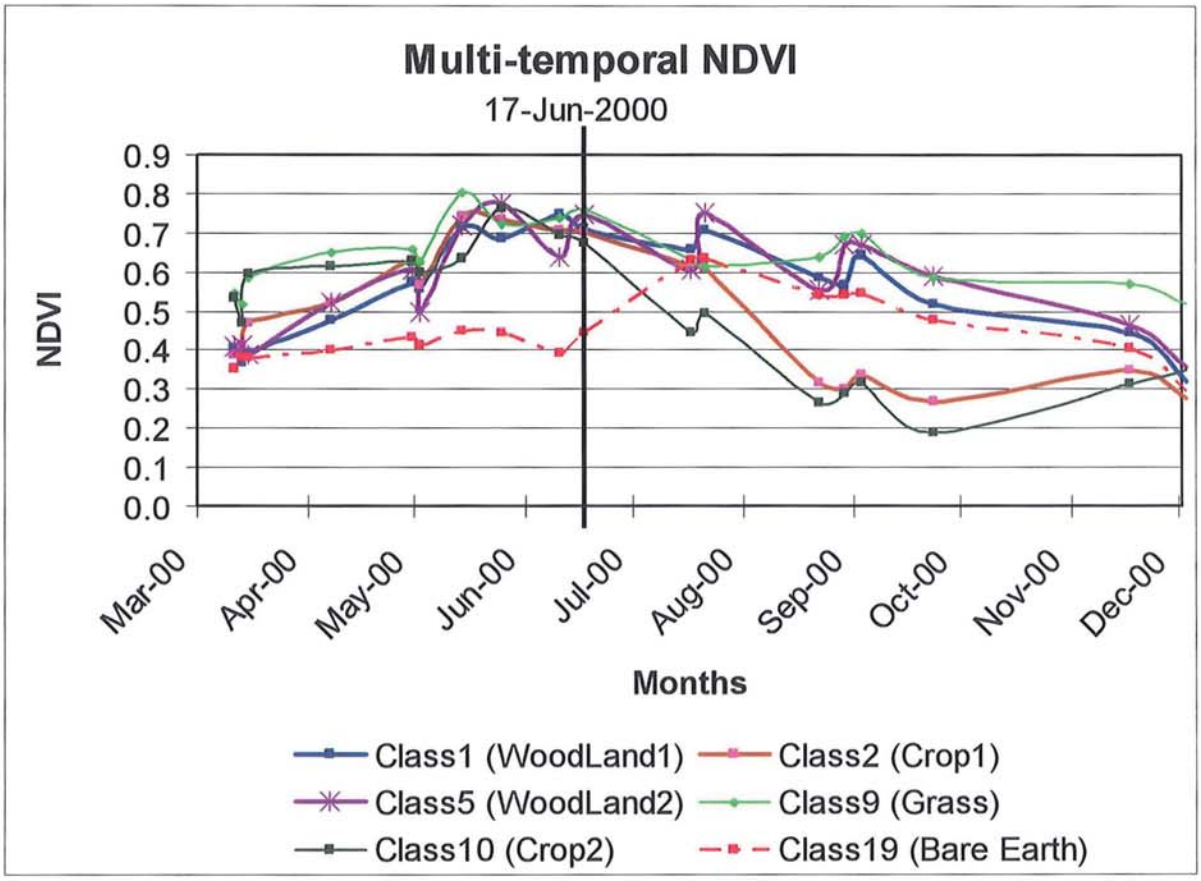

Figure 5.7: Multi-temporal NDVI (Top of the Atmosphere) for some of the classes recognized in the classified ETM+ scene

The curves fitted to the multi-temporal NDVI values were not very smooth, for two main reasons. Firstly, the NDVI value on each date was calculated from the relevant MODIS image. Each of these has a different degree of reliability due to the varied cloud cover and viewing angle. If the MODIS image was cloudy then as stated in section 5.4 the cloudy pixels were not used, thus the number of simultaneous equations was reduced.

Solving a small number of equations will increase the bias due to the uncertainty in the land cover existing in the classified ETM+ image. Similarly, different viewing angles result in different response in the MODIS images for the same land cover. This in turn affected the derived value of the land cover reflectance. Secondly, some of the sharp drops in the curves shown in figure 5.7, such as that in early May, were caused by atmospheric effects rather than real changes in chlorophyll level.

The first and most important aspect of this multi-temporal analysis discernible from figure 5.7 is to reduce the ambiguity in the classes' description. For example, class 9 was believed to be some type of crop from the FCC457 ETM+ image as certain fields had a very distinct orange coloured feature. However, from figure 5.7 it is clear how class 9 seems always to be green and thus it is most likely to be permanent grasslands. While class 9 has almost a steady NDVI value throughout the year, the NDVI for classes 2 and 10 falls dramatically during July-August indicating the die-back period of the growing season.

Another interesting feature that can be perceived from the plot, is the different length of growing season for Crop1 and Crop2. While Crop1 seems to start growing early in April and is harvested at the end of July, whereas Crop2 has an earlier emergence date (March) and is harvested at the end of June.

The noticeable variation in NDVI values can be used to distinguish cultivated areas and temporary grass lands, from the permanently green lands. In order to demonstrate the NDVI changes for each class during the period between first and last MODIS dates, the standard deviation was calculated, using all NDVI values for that class during this period

of time. For each class there is only one value for the NDVI for each MODIS image date. Figure 5.8 shows the variation in the NDVI values of each class. This figure shows that class 2, class 10, and class 17 are more likely to be agricultural crops.

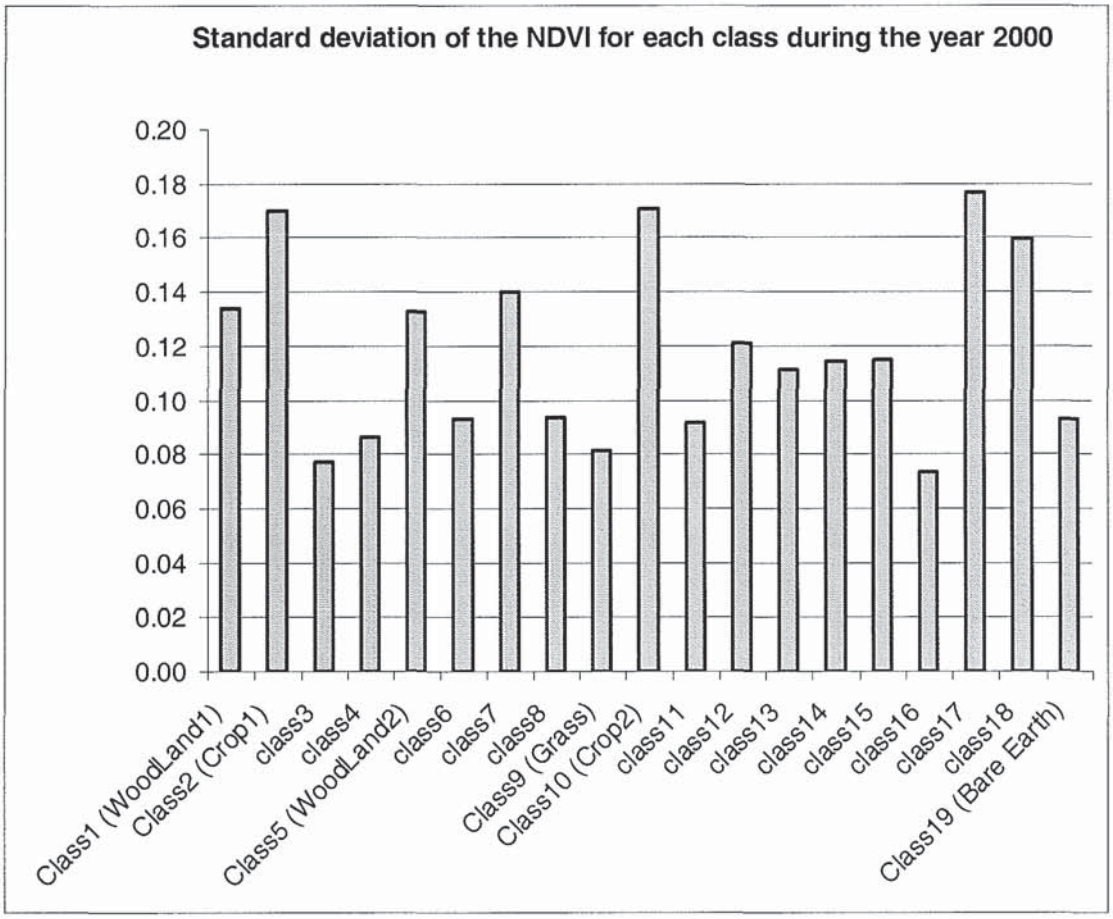

Figure 5.8: The Standard deviation of NDVI value for each class

These features of the multi-temporal analysis provide an increased likelihood of identifying the unknown vegetation classes. They also provide an opportunity to improve the classification of the ETM+ image acquired on 17-June-2000 when nearly all the vegetation classes were at peak lushness, and thus possessing less variation in the red and NIR reflectances thereby hampering the discrimination between vegetation classes.

The variation in the NDVI values may be used to indicate which of the available images would provide the greatest variation in the vegetation classes. Thus, in order to demonstrate how the NDVI varied between classes over time for each MODIS image date, the NDVI standard deviation was calculated for all vegetation classes (class ID 1-18). These standard deviations were plotted as Figure 5.9. To help in the classification process it was necessary to find the maximum variation in the vegetation classes. To reduce confusion with other classes, water and bare earth classes were omitted. This may also be useful if one is interested in finding out the date of maximum dissimilarity between two or more classes of interest.

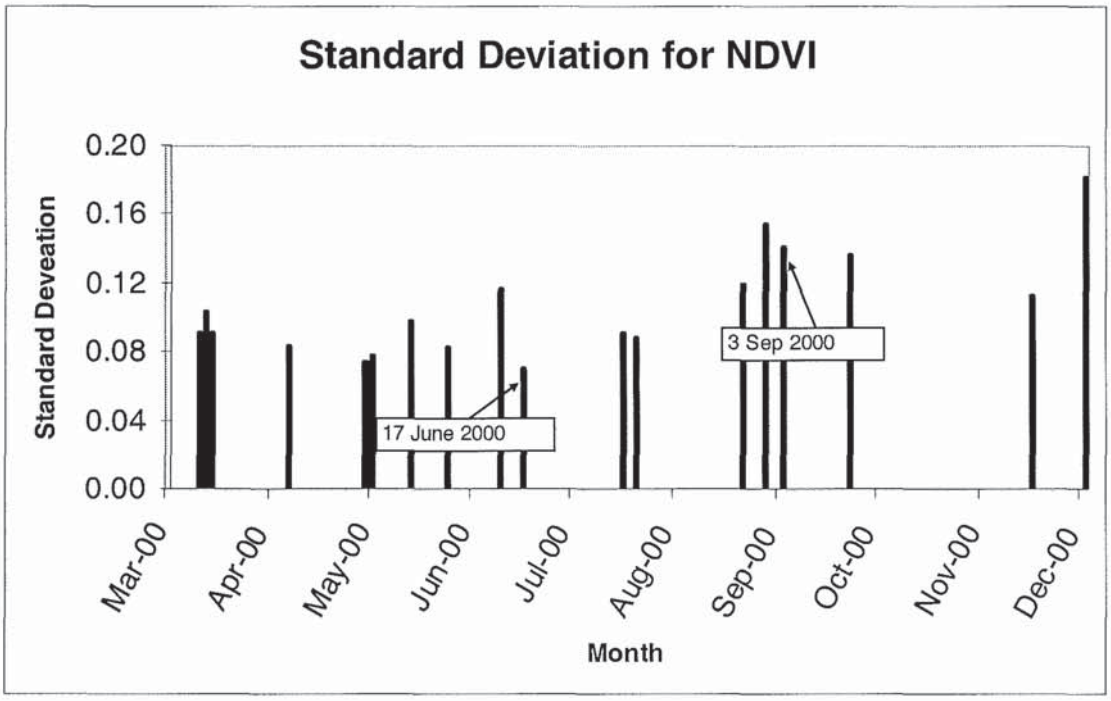

Figure 5.9: Standard deviation for NDVI between Vegetation classes in the study area

From Figure 5.9 one can see that the minimum standard deviation for the NDVI was on the 17 June 2000, which is the date of ETM+ image acquisition. This minimum NDVI variation is as expected because most of the vegetation is at its growing peak. Therefore, this date is not as useful as days where the maximum NDVI variation within vegetation classes occurs. The maximum variation seems to be either on 3rd of December or 29th of August. However, from Table 5.1 it can be seen that these two days were cloudy, thus the results could be questionable. Therefore, the MODIS image acquired on 3rd September, which is 100% cloud-free, may be identified as the most useful image for maximizing the variation between vegetation classes for the study area. If the information content in this image were exploited correctly, together with the information from the ETM+ image, then it is highly likely that some improvement in the classification would be obtained.

5.7. Summary and conclusion

In this chapter, the multi-resolution and multi-temporal analysis performed on the coarse resolution MODIS images, using the classified medium resolution ETM+ image, was described. The Linear Mixture Model was used to estimate the likely reflectance of each class from the classified ETM+ image, in each of the multi-temporal MODIS images. Figure 5.10 is a flowchart of the steps used to obtain the likely reflectance of each class from the MODIS image.

The reflectance of each class was estimated for each of the MODIS bands, rather than the ETM+ bands, to overcome the problem of different radiometric properties of these two different satellites. The results show a very good relationship between the classes' reflectance in both satellites. Furthermore, it was possible to use the multi-temporal

MODIS images to demonstrate the chronological growing stages for different vegetation types. The growing profile seems to be a very useful source of information about the type of crop and may help to improve the classification of the ETM+ image.

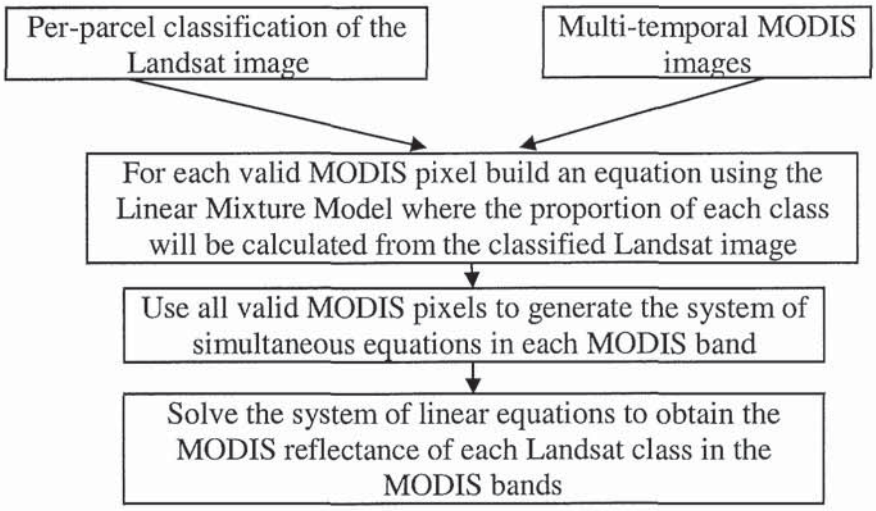

Figure 5.10: Flowchart for the process of finding the MODIS reflectance for each class in the Landsat ETM+ per-parcel classification

Improvements in the Landsat ETM+ classification are expected to be in the areas where there is confusion between crops and woodland. This can be perceived from the aerial photography, where some agricultural parcels in the classified ETM+ image get higher membership grades than the woodland classes and vice versa. The next chapter is therefore dedicated to develop a methodology to improve the ETM+ classification, especially with regard to reducing the potential confusion between crops and woodland classes, so that if a parcel is perceived as an agricultural field then it should show a higher crop class membership rather than woodland membership.

Chapter 6

The Integration of MODIS \ Terra and Landsat ETM+ Images to improve the classification results

6.1. Introduction

The results from Chapter 5 suggested some improvement might be possible using a combination of multi-temporal MODIS data and a single date Landsat ETM+ data on a per-pixel basis. Chapter 4 similarly showed that the whole parcel classifier performed better than single pixel classifiers on a single Landsat ETM+ image. This chapter combines the two approaches.

The ETM+ image was classified to twenty spectral classes using a semi-supervised classification technique (chapter 4). This technique incorporated the parcels from the OS 1:2500 digital map data in the fcm classification procedure, to assign each parcel to its most likely class. However, this might be a source of misclassification as the other likely classes were ignored even if they were almost as likely.

The multi-resolution analysis, presented in the previous chapter, enabled the identification of the likely reflectance of each class in each MODIS band. This was performed by solving a system of simultaneous equations established from the linear mixture model, modified to account for the triangular response of the MODIS sensor over the actual area sensed. The actual area of a ground pixel has one MODIS pixel width along track and up to twice MODIS pixel width along scan. The proportions of classes in each MODIS pixel were calculated from the classified ETM+ image. For this it was it was assumed that the MODIS and ETM+ images were perfectly registered with each

other. This assumption was justified since the potential misregistration is weakened due to a large MODIS instantaneous field of view. Another assumption was made regarding the hard classification of the Landsat ETM+ image. As most of the misclassified pixels were confused with their next most likely class, which had a similar reflectance, the estimated value of the reflectance was considered to be accurate given the large number of simultaneous equations used in the solution.

The objective of this chapter is to develop a strategy for integrating the information obtained from the multi-resolution and multi-temporal analysis of MODIS images with the classification process, in order to enhance the ETM+ classification. The next section discusses the problem of classification confusion, by considering other possible classes for each of the per-parcel classifications derived from the Landsat ETM+ image considered in this study.

6.2. Other likely classifications for each ETM+ parcel

The importance of this section in the context of this chapter is to give a preliminary indication of the classes that are most likely to be confused with each other in the single date Landsat ETM+ image.

Table 6.2, shows each spectral class and the other classes most likely to be confused with it. This table was created using Table 6.1, a cross tabulation of the most likely class, shown in Figure 4.28 and the second most likely class for each parcel, Figure 4.30. The other likely classes were listed in descending order along with the percentages of potential confusion. The percentage of potential confusion between the most likely class 'A' with a second most likely class 'B' is the number of pixels classified as class 'B' in

the second most likely classification divided by the total number of pixels classified as 'A' in the first most likely classification.

Table 6.2 can be read as follows: 35 % of the most likely class 1 has been labelled as class 5 in the second most likely classification. This potential confusion was regarded to be of little importance, as it was recognised from the aerial photography, that classes 1 and 5 are two types of woodlands. Similarly, the confusion between class 5 as the most likely class, and class 1 as the second most likely class is 45%. Again this will have minimal impact on the overall accuracy of the classification, if the purpose of the classification is for crop area estimation. However, of more concern is the potential confusion that may occur between woodland class 1 and crop class 2 in this study, especially regarding the quality of the classification obtained in chapter 4. Table 6.2 does not give the probability of a single pixel being a member of each class - it may be that there is a 90% probabilities of a pixel being class 1 and only 5% probability of being class 2. Class 2 is, however, still the second most likely class.

Although, a visual comparison between aerial photography and ETM+ image, shows that majority of fields of class 2 have been classified correctly as class 2, a large field in the ETM+ classification has been classified as woodland (i.e. class 1) when it was believed to be class 2. This observation was based on the logical inference, that if there is no woodland apparent in that field from aerial photography, and there is higher possible confusion between the woodland (class 1) and the crop (class 2), then it is most likely to be class 2. In other words, it is less likely to be class 4 as its degree of potential confusion with class 1 is only 17% (Table 6.1).

Table 6.1: Confusion matrix between the first and second rank classification

MAX2 Classification	MAX1 classification																				
	1	2	3	4	5	6	7	8	9	10	11	12	13	14	15	16	17	18	19	20	Total
1	0	76063	1839	34713	59147	0	2296	2	0	4220	0	17080	2666	0	3	31	89	98	0	0	198247
2	51647	0	3	52	599	0	58622	0	0	22331	0	1078	71	6	0	1	6	135	0	0	134551
3	1041	40	0	30582	40700	12540	0	49903	565	7	12038	0	72	3710	52	244	16	5	0	0	151515
4	32473	14	18507	0	1290	0	18	16204	0	196	0	197	16148	22	194	16614	2820	121	0	0	104818
5	66634	1379	40964	3506	0	332	50	132	10	24227	2	3	18	22511	0	7	6	0	0	0	159781
6	0	22	12066	99	704	0	0	63	88552	52	46986	0	0	38544	33	1	0	0	0	0	187122
7	2358	73882	0	3	0	0	0	0	0	4	0	20130	69	0	0	0	6	19169	0	0	115621
8	232	0	41548	13527	33	65	0	0	6	0	23470	0	0	4	8912	9941	34	2	0	0	97774
9	0	0	44	0	0	17475	0	4	0	0	1429	0	0	726	25	0	0	0	0	0	19703
10	1372	27845	6	27	5412	0	0	3	0	0	0	8	0	2490	1	4	1	0	0	0	37169
11	4	0	13509	14	1	52312	0	18523	7428	0	0	0	0	111	2230	18	0	0	0	0	94150
12	32072	1225	29	293	0	0	34865	20	0	15	0	0	19980	1	0	2	243	7354	0	0	96099
13	2713	126	81	25283	4	0	5	0	0	0	0	13111	0	0	0	191	14102	785	0	0	56401
14	51	0	3769	55	22993	46321	0	10	8338	6331	16	0	0	0	0	3	0	0	0	0	87887
15	0	6	9	38	5	12	0	7742	66	0	2042	0	0	0	0	6584	0	0	0	0	16504
16	18	2	137	23268	0	6	0	18577	0	28	303	0	78	0	5403	0	7034	0	0	0	54854
17	52	21	3	3851	0	0	0	75	0	0	0	126	16192	0	0	12233	0	176	0	0	32729
18	27	0	0	25	0	0	13301	0	0	0	0	5358	543	0	0	0	44	0	0	0	19298
19	0	0	0	0	0	0	0	0	0	0	0	0	0	0	0	0	0	0	328406	0	328406
20	0	0	0	0	0	0	0	0	0	0	0	0	0	0	0	0	0	0	0	780	780
Total	190694	180625	132514	135336	130888	129063	109157	111258	104965	57411	86286	57091	55837	68125	16853	45874	24401	27845	328406	780	2000000

Table 6.2: Potential Confusion with second most likely class

Class 1		Class 2		Class 3	
2nd most likely	% confusion	2nd most likely	% confusion	2nd most likely	% confusion
5	35	1	42	8	31
2	27	7	41	5	31
4	17	10	15	4	14
12	17	5	1	11	10
13	1	12	1	6	9
Class 4		Class 5		Class 6	
2nd most likely	% confusion	2nd most likely	% confusion	2nd most likely	% confusion
1	26	1	45	11	41
3	23	3	31	14	36
13	19	14	18	9	14
16	17	10	4	3	10
8	10	4	1	5	0
Class 7		Class 8		Class 9	
2nd most likely	% confusion	2nd most likely	% confusion	2nd most likely	% confusion
2	54	3	45	6	84
12	32	16	17	14	08
18	12	11	17	11	07
1	2	4	15	3	1
5	0	15	7	15	0
Class 10		Class 11		Class 12	
2nd most likely	% confusion	2nd most likely	% confusion	2nd most likely	% confusion
5	42	6	54	7	35
2	39	8	27	1	30
14	11	3	14	13	23
1	7	15	2	18	9
4	0	9	2	2	2
Class 13		Class 14		Class 15	
2nd most likely	% confusion	2nd most likely	% confusion	2nd most likely	% confusion
12	36	6	57	8	53
17	29	5	33	16	32
4	29	3	5	11	13
1	5	10	4	4	1
18	1	9	1	3	0
Class 16		Class 17		Class 18	
2nd most likely	% confusion	2nd most likely	% confusion	2nd most likely	% confusion
4	36	13	58	7	69
17	27	16	29	12	26
8	22	4	12	13	3
15	14	12	1	17	1
3	1	1	0	2	0

It would be impractical to undertake a manual analysis of this type for every parcel, in order to improve the classification quality. Therefore, there is a need to develop a mathematical model to undertake the task. This model should have the ability to increase the level of probability of a parcel belonging to a particular class, so that the correct class will get the highest probability, rather than receiving the second or third highest rank in the probability vector.

As the maximum possible information were extracted from the Landsat ETM+ image and the OS 1:2500 digital map for the classification procedure presented in chapter 4, alternative data sources were needed to develop the model for improving the classification. Potentially, the multi-resolution multi-temporal analysis of MODIS image contains valuable extra information, that if it is used appropriately may result in an improved classification.

The following section presents a discussion of the Fuzzy C-means and Linear Mixture Modelling methods that might be used to extract relevant information from the MODIS images. In order to be able to determine the degree of accuracy of each method, a simulated MODIS image was created from the ETM+ image. This was used to demonstrate whether the extracted information from the simulated image is correlated with the actual data or not. A description of how the simulated image was created will be presented first, followed by how the experiments on this image were carried out while exploring the methods employed for decomposing mixed pixels.

6.3. Simulated MODIS image using ETM+ image

This section explains how a simulated MODIS image with a nominal pixel size (250 m) was generated from ETM+ pixels.

The objective of this experiment was to explore the relationship between the observed proportions of the classes within a given MODIS pixel and the reflectance of an artificially generated mixed pixel. To achieve this, all the reflectance values from ETM+ pixels contained within a 2-MODIS-pixel wide rectangle had to be summed and the triangular weighting function applied, in order to generate a MODIS pixel. The classified ETM+ image was therefore considered as the ground truth for the simulated MODIS image, and thus the actual class proportions were known. The expected simulated MODIS reflectance was calculated from the mean reflectance of each class within the MODIS pixel range. Figure 6.1, shows the simulated MODIS image generated in this way from ETM+ band 4 (NIR).

From the real MODIS images, only two bands (Red and NIR) at the highest spatial resolution (250 m) are available. Therefore, only ETM+ bands 3 (Red) and 4 (NIR) were used to generate the MODIS bands (1 and 2). Thus the available data for this experiment are the reflectance in two bands for each mixed pixel, and the reflectance in the same two bands for each class in the study area.

Having created an image of artificial mixed pixels, the next objective was to decompose these pixels to extract the relevant information about the classes present in each mixed pixel. The extracted information could then be compared with the actual proportions used in the simulation to check the success of the method used in the decomposition. Some of

the decomposition methods and their applicability to the task in hand are briefly discussed in the sections that follow.

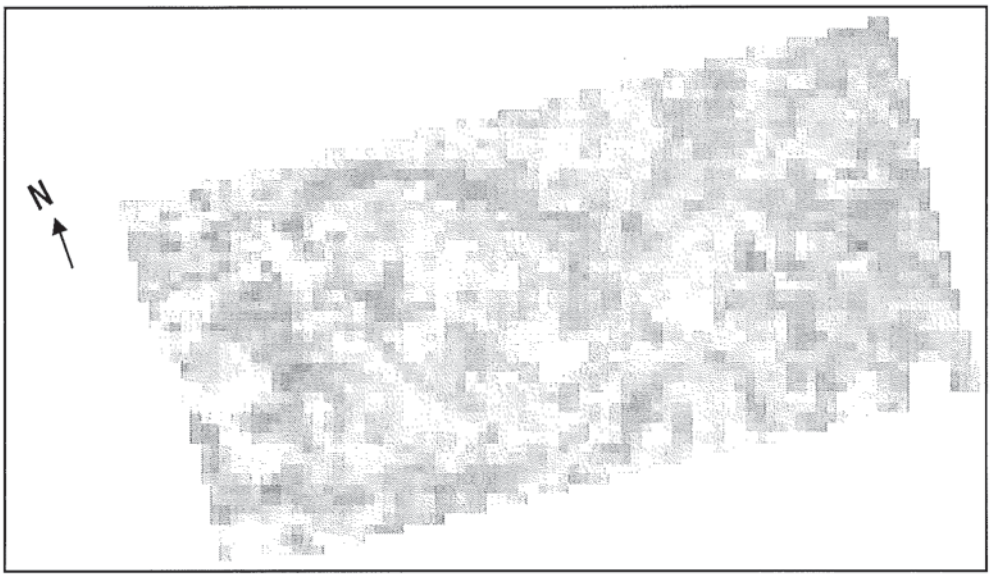

Figure 6.1: Simulated 250 m resolution MODIS image from Landsat ETM+ NIR band (date 17th June 2000)

6.4. Decomposition Methods for mixed pixels:

The decomposition of mixed pixel is a procedure for deriving the properties of the original components of the mixed pixel. However, only the proportion of the area covered by each component can be derived (Gebbinck, 1998). Although several techniques have been reported in literature to solve the unmixing problem, only two techniques will be discussed in the following subsections.

6.4.1. Fuzzy c-means

In the fuzzy c-means approach it is assumed that the membership grades are informative about the sub-pixel components and relate directly to the class proportions with good

accuracy (Maselli *et al.*, 1996). However, for coarse spatial resolution images the increasing number of possible classes that might exist in one pixel will affect the resulting mixed reflectance, and as consequences the relationship between the membership grades and the actual proportions may be weakened. Therefore, in order to determine the suitability of the fcm approach for decomposing MODIS pixels to their compositional classes the experiment described in Section 6.4.1.1 was carried out.

6.4.1.1. Decomposition of the simulated MODIS image using fcm

This experiment was performed on the simulated MODIS image (section 6.3). The output of the fcm was a matrix of membership grades, where each column was for a specific simulated MODIS pixel, and the rows showed, for each pixel, the membership grades to the classes considered.

To evaluate the degree of similarity between the fcm output and the actual proportions of the classes in the MODIS pixels, several measures were available: the cross entropy, measure of information closeness (Foody, 1995), or the correlation coefficients. The correlation coefficient between the membership and the class proportions for this data set was 0.3518, which indicated little direct relationship between the membership grades and the proportions.

The measure of information closeness can be used to measure the closeness between two data sets; the closer the values of this measure to zero the better the association between the two data sets. The histogram of the measure of information closeness between the membership grades and proportions for the experiment is shown in Figure 6.2. This figure shows that only a small part of the histogram has a measure of information

closeness close to zero. This confirms the weakness in the correlation between the membership grades and the actual proportions of classes.

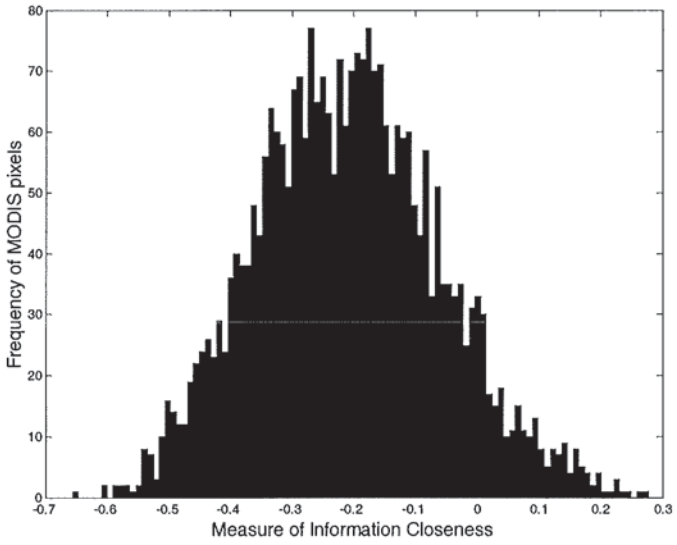

Figure 6.2: Histogram for the measure of information closeness between the membership grades from fcm and the actual proportion of classes in the simulated MODIS image

The reason behind the weak correlation between the membership grades and the actual proportions for this image may be due the relatively large MODIS pixel size, or that the hypothesis of Maselli *et al.*, (1996) as described in section 6.4.1 is not valid in this case.

To find the effect of mixing different proportions on the outputs of fcm, an experiment was conducted using the entropy of the proportions as a measure of the degree of mixing that occurs in each pixel. The entropy is used as a measure of uncertainty when there is a finite set of alternative classes (Maselli *et al.* 1994), and thus, it expresses the degree of fuzziness in the data - the higher the entropy, the higher the fuzziness in the data. The entropy is used here to measure the degree of purity in a mixed pixel, where the lower the entropy the greater the purity of the pixel. The purity in this context means the pixel

contains one major proportion for one class, and all other proportions for the remaining classes are small.

Two groups of pixels were differentiated according to their entropy values, the first group represented the pure pixels and the second group represented the highly mixed pixels. Table 6.3, shows the mean entropy value and the measure of information closeness for each of these groups. These results indicate that the fcm membership grades can be related to the actual proportions, if the pixel is composed mainly from one major class. This relation will be diminished if the pixel becomes highly mixed.

Table 6.3: Mean entropy and measure of information closeness for two groups of pixels the first group represent the highly pure pixels the second group represent the highly mixed pixels

Group	Mean entropy	Mean measure of information closeness
Group1 (pure)	0.1753	-0.0800
Group2 (mixed)	0.9988	-0.2631

Figures 6.3 and 6.4 show plots of the proportions and membership grades for two pixels, each of which is an example of one of the two groups. In figure 6.4 the mixed pixel problem caused by spectral confusion is obvious. The spectral reflectance in mixed pixel resembles the spectral reflectance of other classes. The consequence of this is that the membership grades will be reduced for the actual classes where the proportions are higher and elevated for the other classes that the reflectance of mixed pixel resembles them. Therefore, the fcm algorithm is not appropriate for deriving the class proportions, or the probabilities of classes, within the pixels of coarse resolution images where the majority of the pixels are mixed and contain more than one major class.

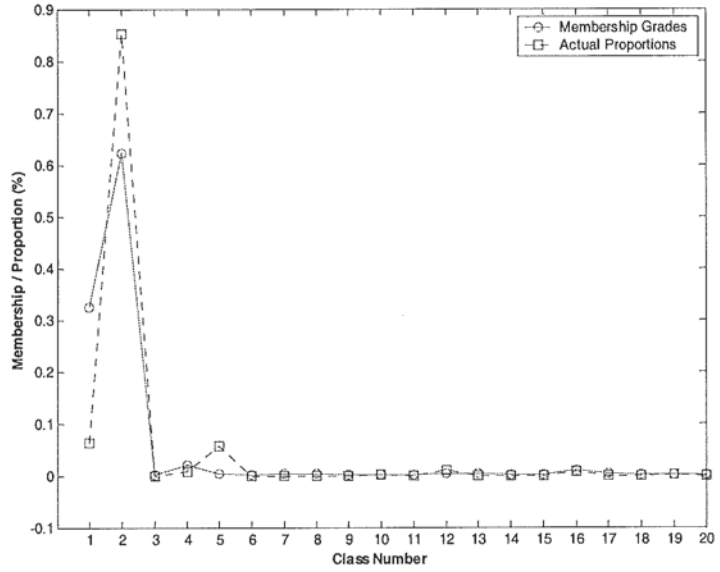

Figure 6.3: Comparison between the membership grades obtained from fcm and the actual proportions for typical pixel containing only one major class

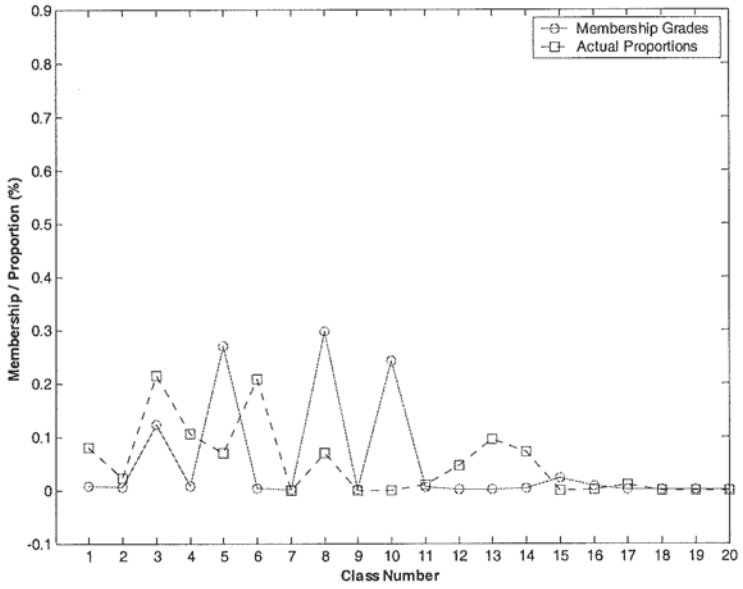

Figure 6.4: Comparison between the membership grades obtained from fcm and the actual proportions for typical pixel containing many major classes

6.4.1.2. Summary of experience using fcm to decompose mixed pixels

The experimental results obtained from decomposing the simulated coarse resolution mixed pixels using the fcm method, shows that the membership grades output does not correspond to the actual proportion of land cover. Furthermore, it does not correspond with the probability of finding the land cover in a highly mixed pixel. If a mixed pixel is composed of more than one major class, then the membership grades of other classes may increase even where classes do not even exist in that pixel. This is simply because the aggregated reflectance may resemble the reflectance of these other classes. Thus, for decomposition of coarse resolution mixed pixels the fcm is not suitable.

6.4.2. Linear Spectral Unmixing

This approach is the most widely used method for extracting the proportions of land cover in mixed pixels (Gebbinck, 1998). This model was discussed in section 2.6.1.5 and used in chapter 5 to estimate the land cover spectral signatures from MODIS bands 1 and 2 for all 20 classes identified in the ETM+ scene. This was based on the assumption that classified ETM+ image was of good quality. Thus by least square fitting, the solution of many simultaneous equations constructed from all MODIS mixed pixels may be considered as a good approximation of the signatures of the land cover classes. Due to the coarse resolution of the sensor, the variation in the reflectance within each land cover class may be considered negligible. Therefore, the error between the expected MODIS reflectance and the actual reflectance recorded by the sensor in the linear mixture model may be assumed to be due to the misclassified ETM+ pixels present in the mixed MODIS pixel.

It was therefore assumed that, by solving the linear model in reverse to achieve decomposition, the resulting estimate of the abundance of each land cover obtained within each MODIS pixel, could be used to improve the classification of land cover in these pixels. However, to be able to solve the linear equations for the unknown fractions of each endmember in a pixel, it is necessary to have many more equations than unknowns. This means that it is important to have more bands than endmember materials or land cover classes, which was not the case for the available data set, as there are 20 classes (including water and bare earth), while there are only two bands available from MODIS at 250m resolution.

The other reflected bands from MODIS images have larger pixel spacing and thus a greater number of mixed classes per pixel. This will reduce the chance of finding the correct class proportions, and hence make it more difficult to determine the spatial distribution of the classes within a very large pixel. One may argue that the number of classes originally selected from the semi-supervised classification of the ETM+ image is too large, and that some of the classes should be merged together to reduce the number of possible classes. However, merging classes will give erroneous results, because the original assumption for the classification was that each class could be described with a monomodel distribution. Furthermore, the difficulty of attempting to reduce the number of vegetation classes any further makes this option unrealistic, as was discussed in chapter 4.

Unlike complete unmixing, a partial unmixing technique has the ability to map the chosen targets by maximizing the response of the target spectrum within the data, and

suppressing the response of everything else, by considering the latter to be a composite unknown background to the target. However, the drawback of this technique is that it is possible to end up with false positive results. Furthermore, the partial unmixing technique is only good for cases of high spectral contrast between a target and its background. Therefore, it is more likely to fail when the target and its background are both vegetation.

Other methods for mixed pixels decomposition may be attempted, such as neural networks. According to Atkinson *et al.* (1997), neural networks gave the most accurate estimates in a comparison with neural networks, fuzzy c-means, and analytic mixture modelling. However, Gebbinck (1998) states that the dispersion of endmembers, relative to the within-class variation, has more impact on the accuracy with which mixed pixels can be decomposed, than on the decomposition method selected. For this reason it is not considered further for this research.

Subsequently, to solve the problem of decomposition of mixed MODIS pixels, an alternative approach was developed. This is discussed in detail in the following section.

6.5. Decomposition of MODIS pixels based on the most likely composition

The main problem of decomposition of a mixed pixel using the Linear Mixture Model was the shortage of simultaneous equations required to solve for the proportions of classes present in a mixed pixel. The traditional mixing equation can be expressed as:

$$\overline{\rho_k} = \sum_{i=1}^{N} (a_i \rho_{ik}) \qquad \textbf{Equation 6. 1}$$

where

$\overline{\rho_k}$: the measured reflectance in band k

a_i : fraction of the i^{th} class in the pixel under consideration

ρ_{ik} : the reflectance of i^{th} class in band k

N: number of classes (endmember), each with a unique and unambiguous spectral response.

If the ETM+ classification is correct then the class proportions should satisfy all the simultaneous equations. However, due to errors in the classification this will not be the case. If a single measure is given to how good the classification is, by testing all possible alternative classes, then the most likely classification will be the one that minimizes the error in the simultaneous equations. The measure of classification success can be expressed by:

$$S = \sum_k \left(\overline{\rho_k} - \sum_{i=1}^{N} (a_i \rho_{ik}) \right)^2 \qquad \textbf{Equation 6. 2}$$

In this equation a_i is no longer a variable to be determined, but it is the proportion of each class within the MODIS pixel. ρ_{ik} is now the variable that is altered. All possible permutations of classes will be considered, each of which has a different reflectance ρ_{ik}. Hence choosing a different class for any particular proportion, i, will yield a different S value. The problem can now be expressed as finding the classes, i, that minimize S. This

is not a general unmixing model, but is a method of determining which classes, obtained from the classification of the ETM+ image, best fit the observed MODIS value.

The main problem of trying all other alternative classes for each individual ETM+ pixel is that of the combinatorial explosion. Three properties can be used to reduce this explosion:

- the per-parcel classification method means that a large number of pixels are assigned the same class;
- the posterior Bayesian probabilities can be used to dismiss unlikely classifications - for example, water from a parcel displaying high NIR reflectance;
- only a limited number most likely classes need to be permuted: for example, the first and second rank of most likely classes.

To further reduce the number of possible combinations, where pixels and parcels that have been classified to a given class with high level of certainty they may be eliminated from the permutation process. For example, if the likelihood of particular pixel belonging to a specific class is 0.99, then it is pointless exploring other alternatives.

If only the first and second most likely classes are used in the permutation, then the results of minimizing the error in the simultaneous equations will yield a new classification. This new classification has the same spatial resolution of ETM+ classification, but with some pixels being reassigned the second most likely class, while the other pixels will remain as the first most likely class.

All multi-temporal MODIS images can be used in this model to obtain the classification, as it will minimise the error in all MODIS images simultaneously. However, the inconsistent size and geo-referencing problem (section 3.4.2) of MODIS pixels in the multi-temporal images, makes it necessary to process the MODIS images individually.

It is highly unlikely that one unique new classification will be obtained from all MODIS images on the days considered. In other words, on the one hand a MODIS image on a particular day may result in a classification where a pixel will be labelled as the first most likely class. On the other hand, the same pixel will be given the label of the second most likely class if it minimizes the error in MODIS image acquired on another day. Furthermore, using the MODIS images solely to decide whether or not to change the pixel label, may result in the decisions taken based on the ETM+ image being overlooked. A reasonable solution for this problem may lie in the Dempster-Shafer theory, where all lines of evidence can be aggregated according to the degree of support given to each of the hypothesis considered. The aggregation of the evidence would be based on weight-of-evidence modelling (Eastman, 2001). The uses of Dempster-Shafer theory to solve the problem of information fusion from multi-source data are discussed in the following section.

6.6. Multi-source data fusing using Dempster-Shafer theory

The main problem identified in the previous section was how to decide which class label would be most appropriate for a pixel. On the one hand, a pixel may be classified as the most likely class using the ETM+ image. On the other hand the pixel may be labelled as the first or the second most likely class, using the methodology of minimizing the error in

MODIS pixels on each of the days considered. Therefore, the problem can be stated as having two hypotheses: the first hypothesis is that the pixel belongs to the first most likely class 'A'; the second hypothesis is that the pixel belongs to the second most likely class 'B'.

The lines of evidence for each of the hypothesis 'A' or 'B' can be expressed as basic probability assignments (BPA) that give the weighting of that evidence to the support or rejection of a hypothesis under investigation. These lines of evidence can be derived from the ETM+ image and each of the multi-temporal MODIS images.

For example, the original classification obtained from ETM+ alone can be used as the first source of evidence. The probability attached to the most likely class obtained from the ETM+ classification, can be used as the basic probability assignment (BPA) from this line of evidence, to express the degree of support for the first hypothesis 'A'. The probability attached to the second most likely class can be used as the BPA from this line of evidence to express the degree of support for the second hypothesis 'B'.

The new classification obtained from each MODIS image will be used as a new line of evidence. However, minimizing the error in the expected reflectance in MODIS mixed pixels will yield a hard classification. In other words, each pixel in the resulting classification will be assigned a class that minimizes the error, without expressing the degree to which this class can be believed to be the correct class. Therefore, no direct measures of belief can be derived, which will express the degree of support for the first or second hypotheses. Another problem that may be encountered with regard to the MODIS images, is the existence of cloudy pixels. A cloudy MODIS pixel should be given BPA

that do not support either of the hypotheses, or they might be given a weighing that supports both hypotheses equally.

Therefore, to derive the BPA from MODIS images, it might be possible to consider the degree of the improvement in the classification as a measure of support for each of the hypotheses considered. In other words, if after minimizing the error in the MODIS images, the pixel is assigned the second most likely class, then from this line of evidence this pixel should give more support to the second hypothesis 'B', than the first hypothesis 'A'. This support can be expressed as a higher probability assignment for this pixel in the BPA and this value is proportional to the degree of the improvement in the error in each MODIS pixel. The greater the improvement in the root mean square error, the higher the probability that will be given to the hypothesis that the pixel belong to a specific class.

As an example, Figures 6.5 and 6.6 show the basic probability assignments (BPA) that are given to the line of evidence for pixels from the MODIS image acquired on 11-Mar-2000. In this BPA only two hypotheses were considered. The first hypothesis is that the pixels belong to the first most likely class 'A'; the second hypothesis is that the pixels belong to the second most likely class 'B'. Therefore, two BPA images are required to express the support for each of these hypotheses. The bright pixels in the first image show the areas where the pixels have more support for first hypothesis 'A' - that is the pixels belong to the first most likely class. These pixels retain their identity class, as the most likely class after the process of minimizing the error in MODIS reflectance. The second image can be seen as the complement to the first image.

The assumption considered here is that there are no other hypotheses in the decision frame except the first 'A' and second 'B' hypothesis. In other words, it is assumed that a pixel can be classified as 'A' or 'B', and thus there is no chance for a pixel to be assigned to any other label. In fact, the Dempster-Shafer theory of evidence has no such restrictions. In contrast to Bayes theory, the lack of commitment for a belief in a hypothesis does not imply commitment to the belief in its opponents. However, for the case study considered here, it was assumed that a pixel will have either the label of the first rank most likely class, or the second rank most likely class from the parcel classification performed in section 4.6. The grey colour in Figures 5.6 and 6.6, shows the pixels where the mass of support for the hypotheses considered is equal.

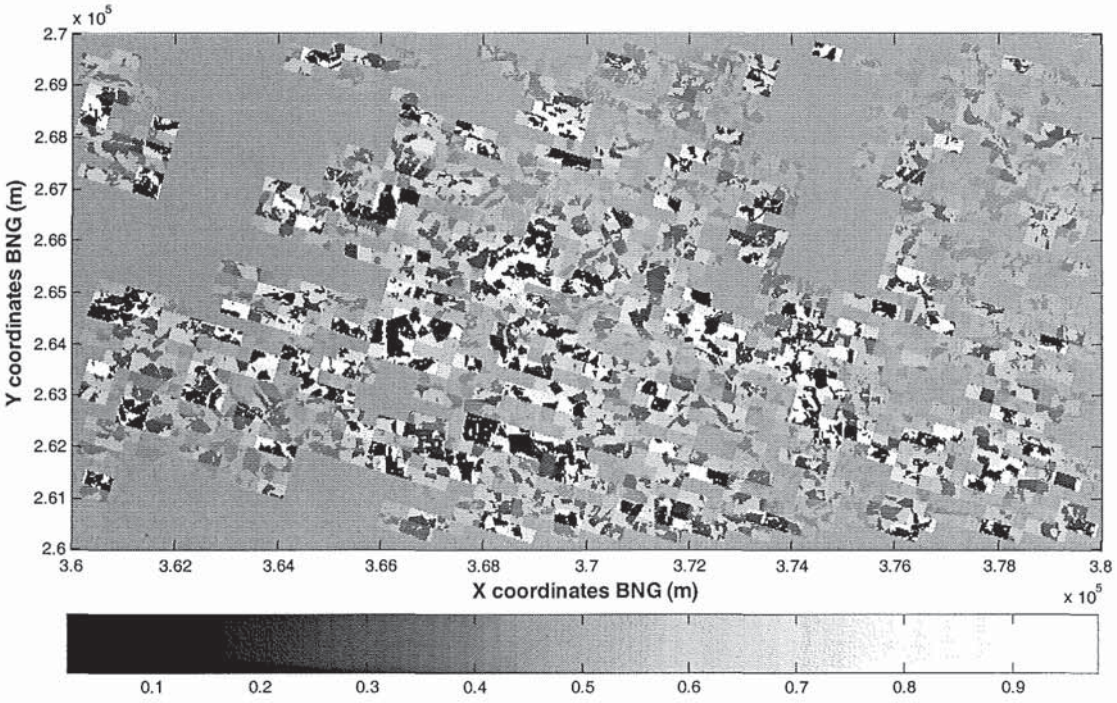

Figure 6.5: Basic probability assignment for hypothesis [A] which supports the 1st rank maximum likely class derived from MODIS (11-Mar-2000)

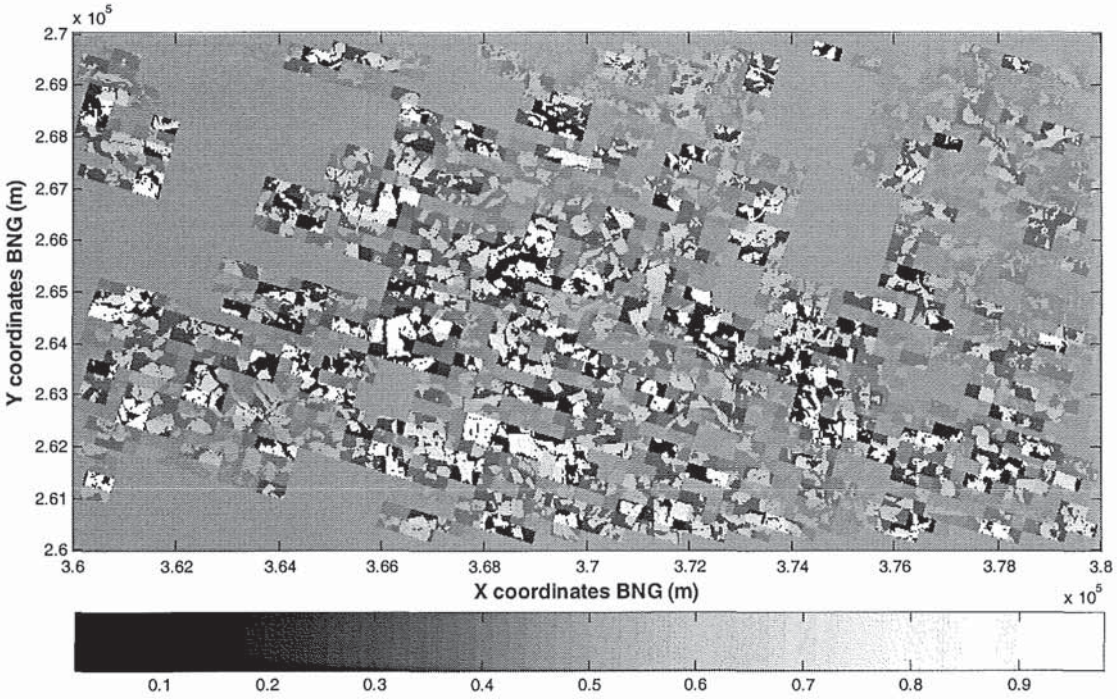

Figure 6.6: Basic probability assignment for hypothesis [B] which supports the 2nd rank maximum likely class derived from MODIS (11-Mar-2000)

The degree of support in the (BPA) images can be estimated according to the degree of the improvement in the error in the expected MODIS reflectance. If '*S1*' is the original error obtained using the original proportions of classes in a MODIS pixel, and '*S2*' is the minimum error that can be obtained, then the improvement in the error may expressed as:

$$\alpha = \frac{S1 - S2}{S1} \qquad \textbf{Equation 6. 3}$$

This equation gives the degree of improvement and not the degree of support. Therefore, to express the degree of support to each of the hypothesis, a new measure is required here. This has been taken as the basic probability assignment (BPA) for those pixels where the hypothesis 'h' is true. Following the concept of expressing the reliability for each data source shown in equation 2.34, and discussed in section 2.8.1, the BPA in this

study was assumed to be a function of both the degree of improvement and the image reliability, β. It is postulated that this may take the form of:

$$BPA_h = (\beta)^{1-\alpha} \qquad \textbf{Equation 6. 4}$$

where: h is the hypothesis that is found to be true and can be either the first or second most likely class. The exponential form for this equation was selected because of the need to combine both the image reliability and the improvement in the RMSE in MODIS pixels, so that the resulting BPA value will not exceed 1. Further research is required to verify this hypothesis.

Some MODIS images are of better quality than others, for example, of less cloud cover and the pixels are near nadir, β can be chosen to quantify the MODIS image reliability and its value is between 0 and 1. This can be selected to express the reliability of the whole MODIS image considered or, if known, the reliability of each individual MODIS pixel. For example, if a MODIS pixel contains thin clouds then its reliability will be less than a clear sky pixel. If $\beta = 1$, then the image is highly reliable and all other hypothesis will receive a zero probability. This provides a firm decision about the resulting classification - it will be the same as the set of classes which minimize the RMSE in this MODIS image. Further research is required to establish criteria for the selection of β.

For each pixel in the images the value of α will vary according to the improvement as expressed in Equation 6.3. In the case of maximum improvement ($S2$=0) then the BPA for this pixel will become equal to one, indicating total commitment to the hypothesis found to be true for this pixel.

In order to demonstrate how the value of the BPA in equation 6.4 will be changed for different values of the image reliability β and the degree of improvement α, a surface plot figure 6.7 was drawn. This figure shows that the BPA will be changed linearly with β and exponentially with α. For lower values of β, the BPA will increase exponentially according to the improvement in the RMSE. Thus, even if the image was less reliable, but a substantial improvement in RMSE was found in a MODIS pixel, then there would be good reason to believe that the new set of classes in this pixel are the correct ones.

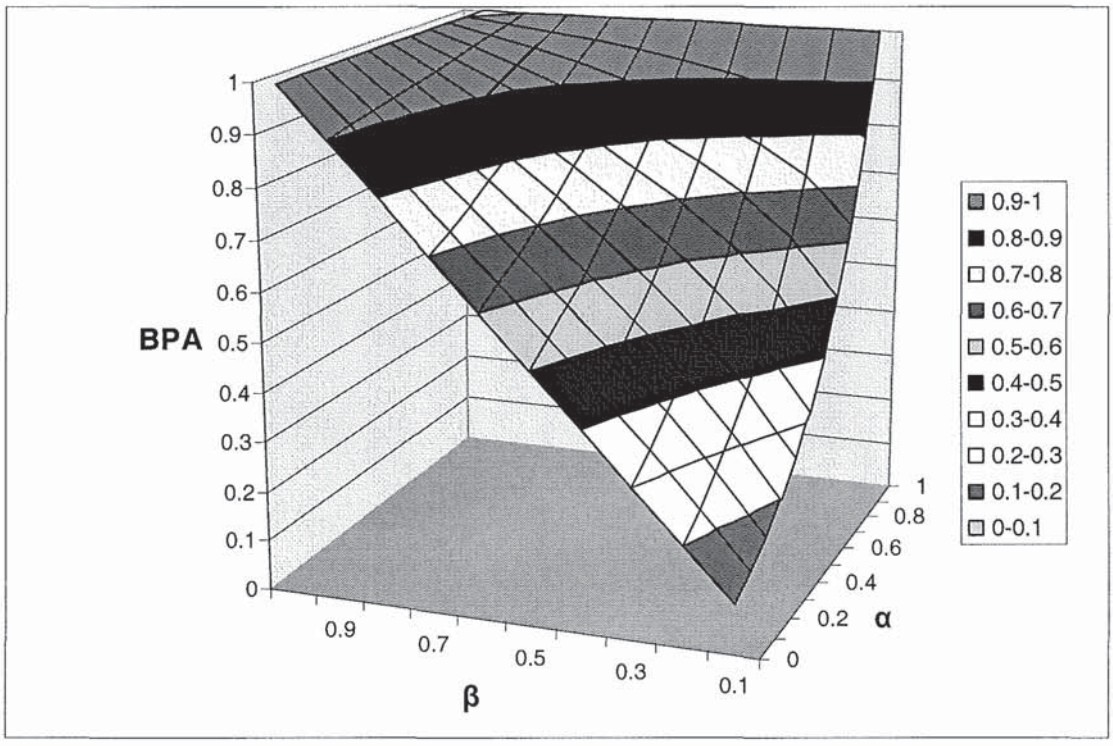

Figure 6.7: Basic Probability Assignment (BPA) for different values for the image reliability β and the degree of improvement α in the RMSE between the expected MODIS reflectance and the actual reflectance in MODIS pixel.

6.7. Model implementation

In this section the implementation of the methodology, that was developed in the previous sections 6.5 and 6.6, are described in detail. A MATLAB program was developed to perform the required calculations for this multi-resolution analysis for the MODIS and ETM+ images.

First, all information needed from each of the multi-temporal MODIS images was stored in one HDF file. The geolocations of each MODIS pixel were stored along with the corner of the footprint of each pixel assuming, it had a rectangular shape. This assumption eased the calculation of the actual IFOV and identified the ETM+ pixels that fell inside the IFOV. Even though the actual IFOV may have an elliptical shape, the increase in complexity of the analysis, may not improve the results substantially due to the expected positional error in the MODIS pixel.

The OS 1:2500 digital map was converted to raster format with the same ETM+ pixel size. A program was developed, so that nine neighbouring MODIS pixels were considered together, but only the parcels seen by the central pixel were used in the permutation of different class reflectances. This was particularly important, if a small part of a parcel was within the IFOV of the central MODIS pixel. Changing the class identity of this parcel in the central MODIS pixel will change the reflectance in the neighbouring MODIS pixels, thus affecting the total improvement. Figure 6.8 shows an example of nine neighbouring MODIS pixels with their IFOV corners and the underlying ETM+ pixels.

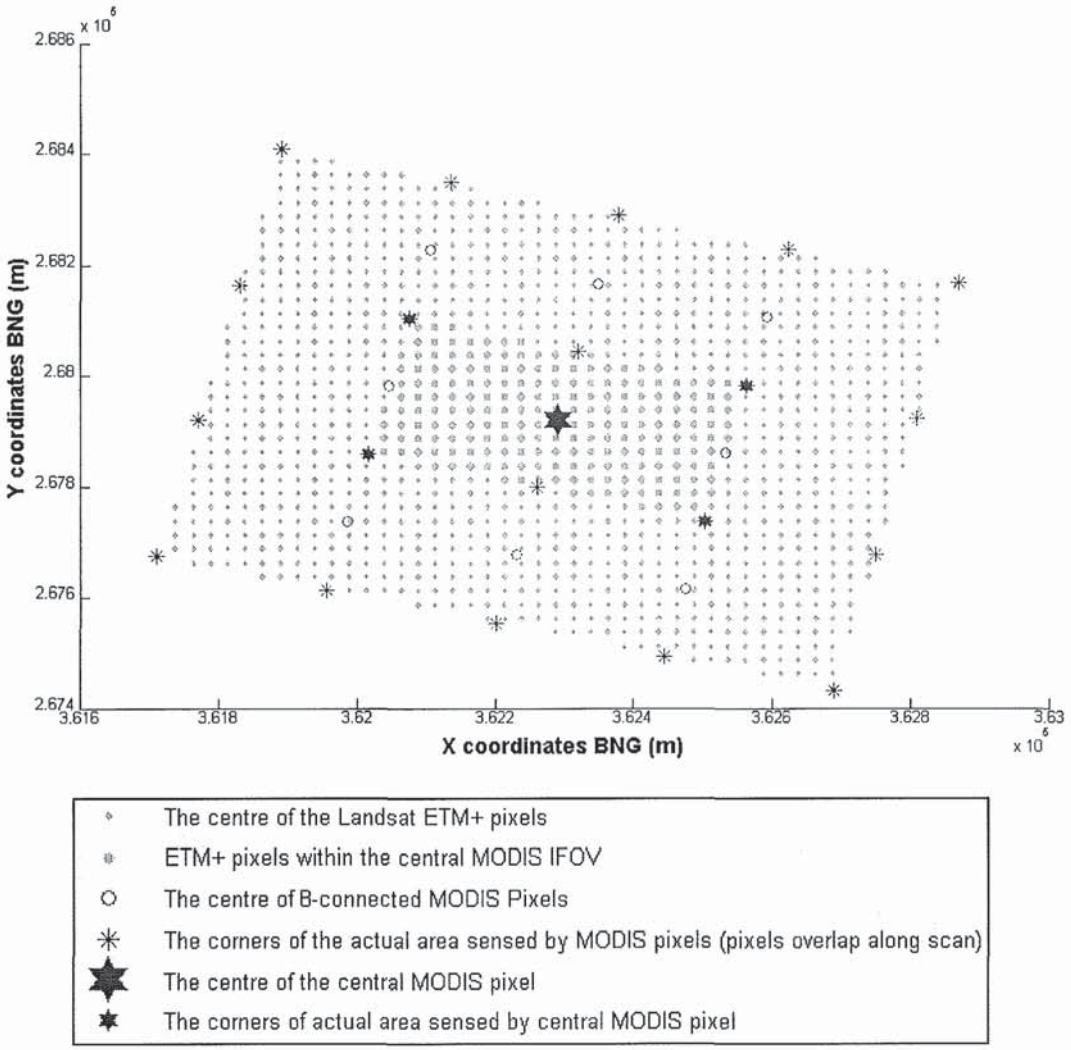

Figure 6.8: Nine (250 m) MODIS pixels with their IFOV and the underlying ETM+ pixels

The objective was now to determine the set of classes that minimize the Root Mean Square Error (RMSE) for the red and near infrared reflectance of the central MODIS pixels, by alternately changing the class identities of the ETM+ pixels falling inside the central MODIS pixel. However, instead of changing the identity of each individual ETM+ pixel, all pixels belonging to the same parcel were changed simultaneously.

The algorithm can be implemented to evaluate the most likely classes for each parcel. These can be the 1st rank and 2nd rank maximum likely class, or 1st, 2nd, and 3rd rank maximum likely class. The decision for choosing the number of the top rank maximum likely classes to be used, depends on the probability associated with these ranks. For example, if the probability is high for the 3rd rank relative to the 1st and 2nd rank, then three ranks can be tried. The following algorithm identifies the rank for each class among the three most likely classes for each parcel:

For each MODIS pixel find the eight surrounding pixels, then:

1. For each of the nine neighbouring MODIS pixels, find those parcels that are seen by this pixel and assign them to the class of the first rank most likely class.
2. Calculate the expected Red and NIR reflectance in the MODIS pixel using the triangular response function and the linear mixture model for the mixture of classes.
3. Sum the Root Mean Square Error (RMSE) for all nine MODIS pixels.
4. For the central MODIS pixel:
    4.1. Find all possible combination of the parcel taking (1, 2...n) parcels at a time, where n can be less or equal to the total number of parcels completely or partially falling in the central MODIS pixel. It is important to keep n as small as possible to avoid the combinatorial explosion. In this study, to minimize n, only those parcels of substantial coverage area within the MODIS pixel, and parcels of greatest uncertainty were selected.
    4.2. For each case of possible combination, change the class' identity of the parcel to the second rank most likely class.

4.3. Compute the expected Red and NIR reflectance of the nine MODIS pixels.

4.4. Sum the RMSE for all nine MODIS pixels. If this RMSE sum is less than the one computed in step 3, save this set of classes as (class_min_rmse).

4.5. Repeat steps 4.2 to 4.4, changing the class' identity to the third rank most likely class.

4.6. Assign each parcel in the central MODIS pixel to the final set of classes (class_min_rmse) obtained after trying all possible combination.

After completing the analysis for all MODIS pixels, a hard classification for each parcel is obtained. However, it is very likely that a parcel may be assigned to more than one class. This can happen if the parcel is viewed by more than one MODIS pixel, which is very likely due to the overlapping of the area sensed. In this case, if the first rank class is assigned from one MODIS pixel, and the second rank class is assigned from a second MODIS pixel, then the final decision will be made by comparing the improvement in the RMSE obtained from each of these two pixels. The final label for this parcel will be the label associated with the maximum improvement.

Each MODIS image may also yield different labels for each parcel. Therefore, the optimal solution may be the one that minimizes the error in all images. Another possible solution is to use the Dempster-Shafer theory of combining evidence from different sources. This was implemented for this study, as a method of combining the lines of evidence from the ETM+ image and the multi-temporal MODIS images. The hypotheses here are that the parcel belongs to the first, second or third most likely classes for a parcel. These hypotheses are singleton and the parcel can only be assigned to one of the

top three classes. The Idrisi32 program has a module called BELIEF, which can be used to combine the various lines of evidence. However, this module calculates the probability assignments for all combinations of the hypotheses, which are not required for the problem of finding only one most likely hypothesis. Thus the extra calculations make the operation of this module very slow, when combining many lines of evidence for many hypotheses. Therefore, a MATLAB program was written to restrict the calculations to singleton hypotheses only.

The main purpose for using the Dempster-shafer theory is to obtain the basic probability assignments for each hypothesis from each line of evidence. For the ETM+ image, each parcel is assigned a membership grade for each of the classes as described in chapter 4. However, these membership grades are obtained from each parcel individually and do not express the probability of belonging to each class. Therefore, the BAYCLASS module in Idrisi32 was used to obtain the likelihood of the classes occurring in each parcel. The training area for each class was obtained from the parcels with minimum uncertainty. Subsequently, the average likelihood for all pixels within the parcel was used to express the likelihood of the parcel belonging to each class.

For MODIS images the basic probability assignments were calculated as explained in section 6.6.

The result of combining the ETM+ image with the MODIS images, to improve the classification of the ETM+ image is presented in next section.

6.8. Results and discussion

For the purpose of reducing the computational costs and maximizing the information that can be obtained from multi-temporal MODIS images, only the one ETM+ image along with five MODIS images were considered here. The MODIS images were selected for the days of both minimum cloud cover, and least atmospheric effects, as discussed in relation to figure 5.7. The other MODIS images were found to be of less value, since some of them were cloudy and/or contained less variation in the classes reflectances (as discussed in chapter 5). The dates of the selected MODIS images were: 7-Apr, 14-May, 17-Jun, 21-Jul and 3-Sep-2000. The last image was obtained after some crops had been harvested, and therefore, it was important to distinguish cultivated from non-cultivated areas.

The MATLAB program written for this purpose (Section 6.7) was used to aggregate the lines of evidence from the ETM+ and the five multi-temporal MODIS images. Three hypotheses were considered for this study, in which a pixel can either be classified as: the first most likely class, the second most likely class, or the third most likely class.

It was assumed that the ETM+ pixels can only be assigned a single-class label, i.e. not mixed, and this class can only be one of the first three most likely classes. It was considered highly unlikely that the forth most likely class was correct.

From the ETM+ line of evidence, the probability images in which the parcel was classified to the 1^{st}, 2^{nd} or 3^{rd} most likely class were used as the BPA for each of the hypotheses considered.

The second line of evidence (MODIS image) gives three BPA to support each of the hypotheses. The probability was calculated for each pixel, using Equations 6.3 and 6.4, where β was considered heuristically to be equal to 0.9, since these MODIS images were considered to be highly reliable.

From the Dempster-Shafer theory, three outputs for each considered hypotheses can be obtained: belief, plausibility, and belief interval images. However, it was assumed that each parcel can be labelled with only one class which is a crisp decision. Thus, according to Shafer (1979), there are three possible choices: belief driven, plausibility driven, and mean of the interval. These three choices may generate different results. However, Tso and Mather (2001) showed that two of the decision rules (belief and plausibility) produce the same results. Therefore, the maximum belief was used to decide the final parcels crisp classifications. The resulting final classification is shown in Figure 6.9. In this figure, there is some apparent speckling in some fields. This is due small parcels created from the OS 1:2500 digital map.

The maximal belief may change if different values for the basic probability assignments are taken. For example if β, used for deriving the BPA from the MODIS images, were reduced then the belief in the first hypothesis would becomes more dominant.

In order to see whether this classification gave an improved version of the original classification obtained using the ETM+ image only, the areas confused between agricultural crop and woodlands were examined in detail. No further detailed examination was possible because there was no accurate ground truth data available for the study area. A visual comparison of the original classification derived from the ETM+

and the final classifications, together with the aerial photography, is provided in Figure 6.10. For this three sub-images are displayed and enlarged for a small area in the middle of the scene, as delineated by a box in Figure 6.9.

From Figure 6.10, one can see that some parcels, or agricultural fields, that were classified originally as woodland, have been corrected in the second classification to be agricultural field and vice versa. However, some parcels, such as the parcel numbered 7 in figure 6.10 are interpreted as agricultural field or bare soil from the aerial photography, but the enhanced classification procedure has not corrected the original woodland misclassification. On the other hand, other parcels, such as parcel number 5, which is also an agricultural field was originally classified correctly as agricultural field (class 14), but has been misclassified in the second classification as woodland (class 5).

Though, the second classification is not perfect, it may be considered as an improvement to the original classification. However, the quality of the second classification may not be judged on the basis of visual comparison only. Some quantitative measures are required to prove whether the degree of improvement is greater than the level of degradation.

To achieve a quantitative measure for evaluation, an OS 1:10000 Scale Raster map for the study area was obtained on 5th October 2004 from the Ordnance Survey through the Digmap website. All tiles of this raster map were last amended during the year 2003. Thus, this map can be considered as a ground truth for the woodland as it is unlikely to have changed significantly since 2000. Orchards were not included in this raster map of woodland extracted from the OS map. A comparison could now be performed between the woodland in this map and the woodland obtained from both classifications.

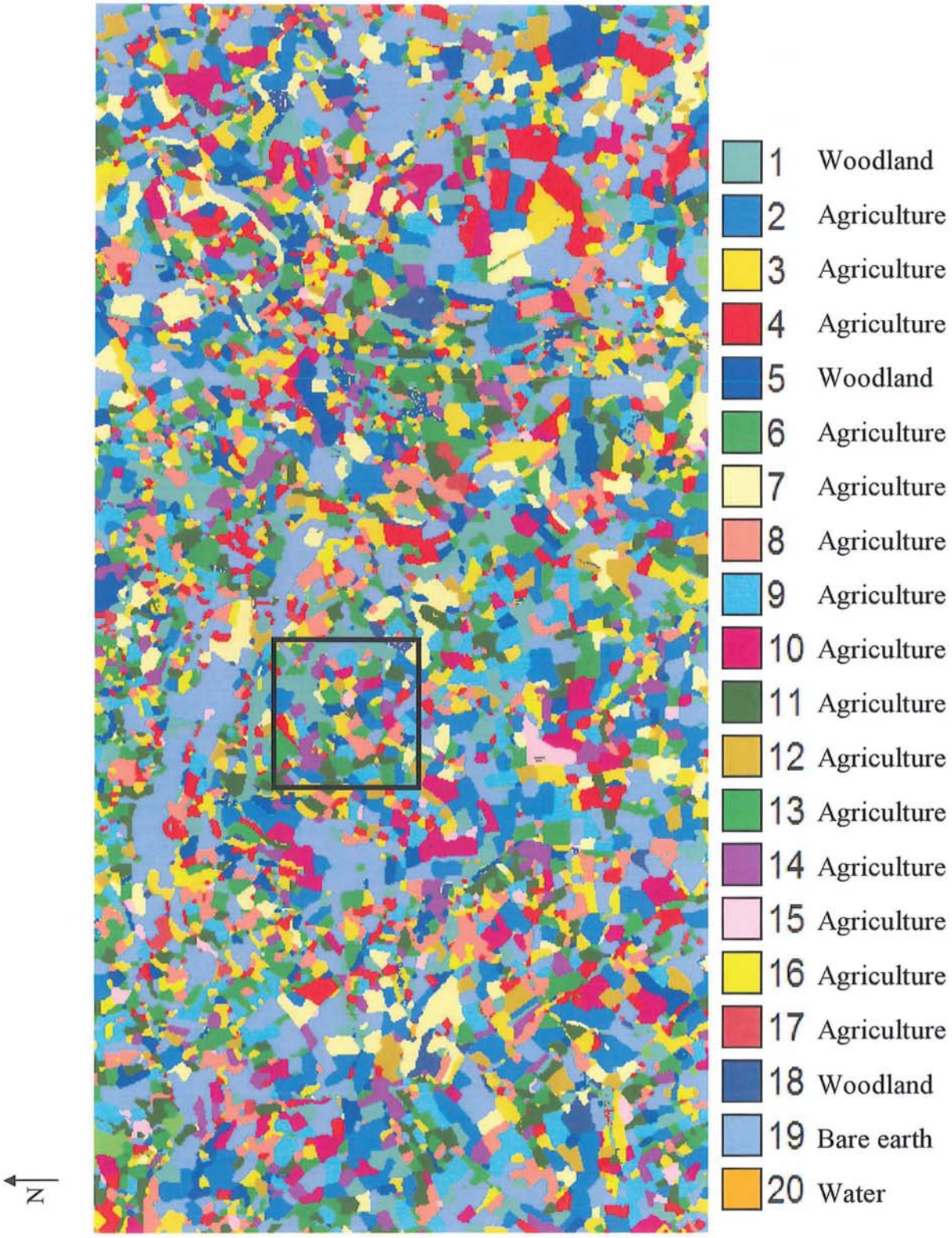

Figure 6.9: The classification results after D-S evidential reasoning

The Aerial Photography shows:

1. agricultural field
2. agricultural field
3. agricultural field
4. agricultural field
5. agricultural field
6. agricultural field
7. agricultural field
8. woodland

The original classification shows:

1. woodland (class 1)
2. agricultural field (class 2)
3. woodland (class 5)
4. woodland (class 1)
5. agricultural field (class 14)
6. woodland (class 5)
7. woodland (class 5)
8. agricultural field (class 2)

The modified classification shows:

1. agricultural field (class 2)
2. agricultural field (class 3)
3. agricultural field (class 12)
4. woodland (class 5)
5. woodland (class 5)
6. agricultural field (class 3)
7. woodland (class 5)
8. woodland (class 1)

Figure 6.10: Comparison between the original classification and the modified one for a small sub-image as delineated by a box in figure 6.9. (The legend as in Fig. 6.9)

A Boolean raster image was created for each of the maps and the two classifications. In these Boolean images all woodland pixels were assigned to 1 and all other non-woodland (including all agricultural fields, bare earth, and orchards) were assigned to 0. Figures 6.11, 6.12 and 6.13 show the woodlands extracted from the OS raster map, the woodlands from the 1st classification and the woodlands from the modified classification respectively. The cross tabulation table between the Boolean images of the map and each of the two classifications shows the number of woodland pixels that were confused between woodlands and non-woodlands for both classifications. The cross tabulation tables are shown in tables 6.4 and 6.5.

Table 6.4: Cross-tabulation for the first classification

		Ground Truth		
		Non-woodlands	Woodlands	Total
First classification	Non-woodlands	255199	14627	269826
	Woodland	30389	19785	50174
	Total	285588	34412	320000
Overall Accuracy: 0.859			Kappa: 0.39	

Table 6.5: Cross-tabulation for the second classification

		Ground Truth		
		Non-woodlands	Woodlands	Total
second classification	Non-woodlands	261670	13702	275372
	Woodland	23918	20710	44628
	Total	285588	34412	320000
Overall Accuracy: 0.882			Kappa: 0.4583	

Table 6.4 and 6.5 show that the second classification is indeed better than the first one, as the overall classification accuracy for the second is 0.882 while it is 0.859% for the first classification. The overall Kappa coefficients of agreements are 0.39 and 0.4583 for the first and the second classifications respectively. This also indicates that the second

classification has reduced the undesirable confusion between the woodlands and agricultural crops.

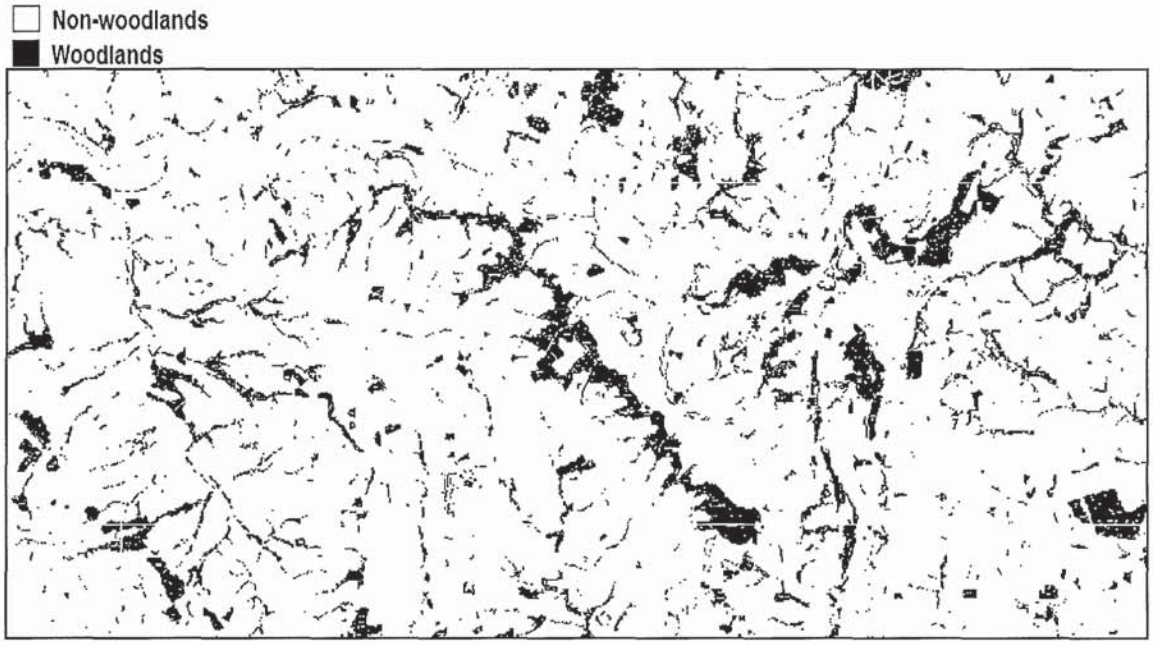

Figure 6.11: Woodlands extracted from OS raster map

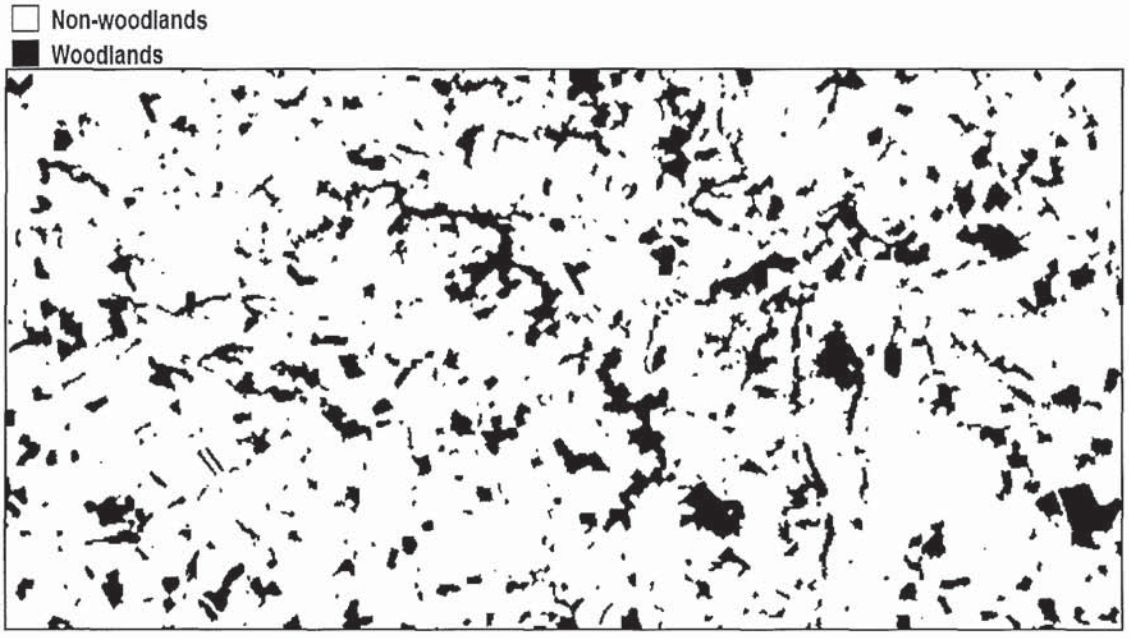

Figure 6.12: Woodlands from 1st classification using only Landsat ETM+

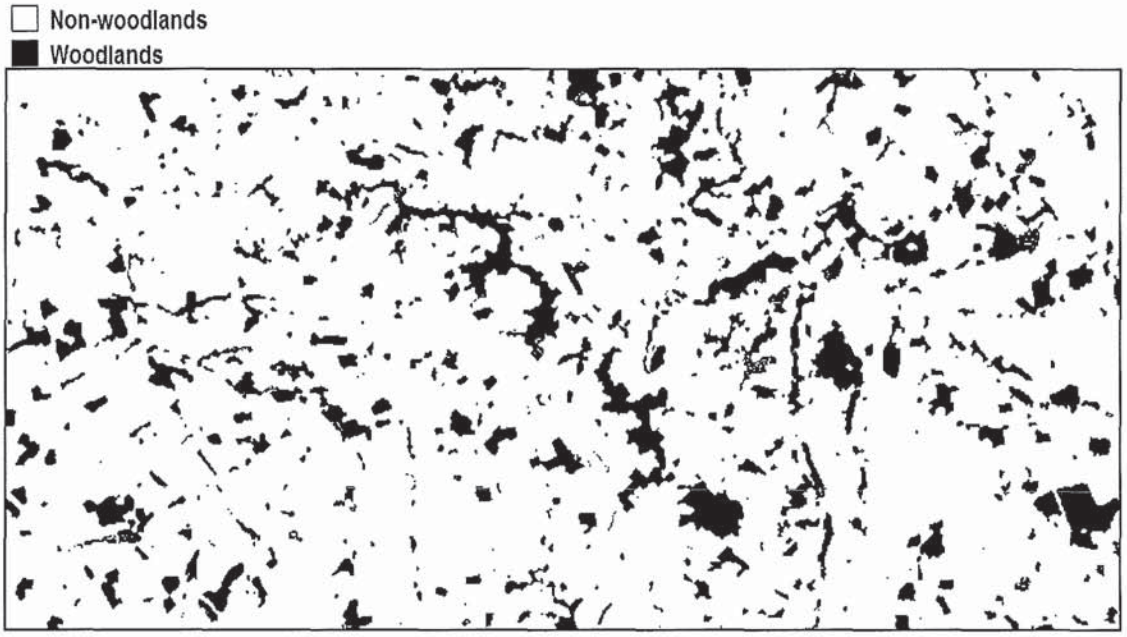

Figure 6.13: Woodlands from 2nd classification using fusion technique of Landsat ETM+ classification with multi-temporal MODIS images

The percentage of the improvement in the classification of non-woodlands is 2.54% and for the woodlands it is 4.68%, these may not be seen as a significant improvement. The original classification was visually considered to be very good, and thus there was very small chance of a large improvement using only two MODIS bands. Further, orchards may still be confused with woodlands, and they are not delineated in OS 1:10000 raster digital maps. Other reasons for the confusion may be due to the reflectance of some agricultural fields in the ETM+ image being very similar to woodlands. This means that the basic probability assignment to the woodland class is much higher than the actual agricultural class. Therefore, it is unlikely to be changed if there were no very strong evidence from the other sources to significantly reduce this assignment. The basic probability assignment, or the mass of support from the line of evidence, can greatly

influence the resulting classification. Therefore, selecting the basic probability assignments is an important step that should be handled carefully.

Additionally, the success of the classification depends more on having classes of distinctive reflectance. This feature can significantly improve the classification if it is exploited correctly. For example, the multi-temporal profile of the reflectance of the crops in an agricultural field can be utilized to accurately classify the crop.

6.9. Summary and conclusions

In this chapter a methodology was developed to integrate multi-scale multi-temporal MODIS images with a single date Landsat ETM+ image for the purpose of improving the Land cover classification. Some of the available decomposition techniques for mixed pixels were demonstrated. However, due to the large pixel size and the limited number of the MODIS image bands, the existing techniques were found to be unsuitable for extracting the appropriate information about the classes present in a MODIS pixel. Therefore, a new method, based on the concept of minimizing the error in the expected MODIS reflectance, was used to find the most likely composition of classes in each MODIS pixel. A MATLAB code was written specifically to perform a systematic permutation of the possible combination of classes using the first, second, or third most likely class of each ETM+ pixel within the IFOV of each MODIS pixel. The order of the most likely classes for each ETM+ pixel was based on the probabilities of finding each class considered in the ETM+ pixel. The result of the permutation is another classification that minimizes the error in MODIS reflectance. The new classification

assigns one label to each ETM+ pixel. This label will be the 1st, 2nd, or 3rd most likely class.

The new classification and the original classification of the ETM+ image were then merged together, using the decision rule for evidential reasoning based on the Dempster-Shafer theory of evidence. The result of the fusion is a new classification, where each pixel is assigned to one class from the set of three most likely classes based on the maximum belief that the pixel can be labelled as the 1st, 2nd, or 3rd most likely class. The classification obtained seems to be of higher quality than the original classification. Therefore, it is possible to improve the classification of a single-date satellite image by using the multi-temporal multi-resolution data from different sources. However, the degree of the improvement depends on the quality of the available data and the extractable information from these sources.

Chapter 7

Summary and Conclusions

7.1. Introduction

In this final chapter, the main conclusions of the study undertaken in this thesis are presented. Section 7.2 briefly summarises the main findings, while Section 7.3 discusses to what extent the goals set for this work have been achieved. Section 7.4, finally, suggests possible improvements to this work.

7.2. Summary

Land cover classification is made more practical with the availability of satellite imagery. However, the classification using a single date image is vulnerable to the possible confusion between vegetation classes if the image was obtained at the time of the peak of growing season or indeed during winter. Further, the variety of image classification techniques, supervised or unsupervised, have their own merits and demerits. If a method succeeds in one case for one image it may fail in another instance.

The common problem with supervised methods is the difficulties associated with finding appropriate training data or perhaps a failure to identify the land cover classes available or visible in the remote sensed image. Therefore, using the unsupervised classification may help to uncover the existing classes in the image. In this work a hybrid approach was proposed and presented in chapter 4 to classify the Landsat ETM+ image. The image was first classified using unsupervised fcm to separate the vegetation from non-vegetation classes after masking the clouds and water bodies. Then the vegetation pixels were classified using supervised fcm, where the number of classes was determined from the

indexed false colour composite image using band 4, 5 and 7 using the methodology described for classifying the vegetation area described in section 4.4.2.5. For this, the mean reflectance in each band for each class of interest was calculated. This was used as input in the supervised mode of the fcm. The result was to assign a membership grade for each vegetation pixel to each of the vegetation spectral classes identified from the indices of interest. These membership grades were then modified by using the Bayesian rule. The context of each pixel was considered as evidence to modify the a *priori* probability (membership grades) derived from the fcm in supervised mode. This process helped in reducing the overall classification uncertainty from 49.5 % to 29.6 %.

Moreover, the classification uncertainty was further reduced from 29.6 % to 20.4% through the parcel classification. The parcels were obtained by delineating fields on the OS 1:2500 digital map, with the polygons manually closed. Each parcel was then assigned a membership grade to each of the vegetation classes by combining the membership grades of each pixel in the parcel using the Bayesian multi-source rule. For this, each pixel in the parcel was considered as an independent source of information. The resulting soft classification was hardened to the maximum membership class and displayed with a colour palette similar to FCC457 colours. This version of hard parcel classification was of great quality and resembles the original ETM+ FCC457 image. It is recommended that when classifying remote sensed images for agriculture in the developed world, where mono cropping over large areas is the norm and agricultural landscapes have an inherent parcel structure, that a per-parcel classifier is used. This is consistent with the advice of Dean and Smith (2003).

Some classes (water bodies, clouds, bare earth, woodland, grass land and other crops) were visibly identifiable from either the aerial photography, or the FCC457 image, or the two used in combination. The individual crop types were not distinguishable and the agricultural census data was of no help in determining the distribution of these crops. Therefore, these crops were left as individual classes, but no labels attached to them. Some agricultural fields were misclassified as woodland classes due to their lushness and resulting spectral response.

The Moderate Resolution Imaging Spectroradiometer (MODIS) on the Terra platform provides continuous sampling of the earth surface on a daily basis. With its sweeping 2330 km wide viewing swath, MODIS covers every point on the earth every 1-2 days in 36 discrete spectral bands. However, as discussed in chapter 3, its inconsistent spatial resolution and geo-referencing make it difficult to monitor the temporal changes of the land cover.

The challenge of integrating MODIS pixels with ETM+ pixels was undertaken in chapter 5. This was performed by utilizing the parcel classification of the ETM+ image obtained in chapter 4. The linear mixture model was assumed as a good simulation for the mixing process which occurred in a mixed MODIS/Terra pixel with an IFOV equal to one MODIS pixel wide along track and up to twice that along scan. The linear mixture model was modified in chapter 5 to account for the triangular response function of MODIS/Terra sensor. Therefore, for each reflected band of MODIS/Terra image obtained on the same date of a Landsat ETM+ image, a system of linear simultaneous equations was generated from all clear sky MODIS pixels. The fraction of each class was obtained

from the underlying parcel classification of ETM+ image. The simultaneous equations were solved to obtain the reflectance of each class in each MODIS band. The spectral signature of each class in the MODIS bands exhibits a similar pattern to the signature in ETM+ bands. Similar analyses using different dates of MODIS images were performed. For each MODIS image the per parcel classification of ETM+ image was used to calculate the fraction of each class. Then the reflectance of each class on each date was computed giving, in effect, a temporal signature for each class. The NDVI values of each class on each date were then computed and plotted on a graph to display the multi-temporal profile of NDVI. The graph was relatively informative and to some extent demonstrates the chronological changes of the chlorophyll during the growing season. The dates of photosynthesis start and harvesting can also be estimated from the graph. This graph was also useful in identifying the date on which the MODIS image has a maximum variation within vegetation classes.

The temporal signature of each class was then utilized in chapter 6, to improve the parcel classification of the Landsat ETM+ image for the study area. The method was to select the combination of parcel classifications that best explained the observed MODIS images, by minimizing the error in the expected MODIS reflectance in the red and near-infrared bands. To reduce the problems of combinatorial explosion a number of heuristics were developed. These included: only considering the 3 most likely classes from the original per-parcel classification; and, only considering classes with greater uncertainty.

In order to combine the two evidence streams - the original per-parcel classification and the multi temporal MODIS imagery - the Demspter-Shafer theory of evidence was used.

The resulting hard classification was visually compared with the aerial photography and this showed an improvement over the original parcel classification. A quantitative accuracy assessment was conducted by using the OS 1:10000 raster map as a ground truth. From this map a binary image was created for the woodlands. The improvement observed in the woodlands classification was 4.7%, and for non-woodlands was 2.5%, with an overall accuracy of 88.2%. This marginal improvement is not as good as the 20% improvement reported by Tseng, *et al.* (1998). However, they used twelve multi-temporal SPOT XS images of equal spatial resolution, but in our approach we used coarse resolution multi-temporal with multi-scale MODIS images. Furthermore, in this study the multi-temporal signature was estimated and derived from the parcel classification and the multi-temporal MODIS images. Therefore, if more accurate multi-temporal signatures were obtained and more bands were used, then it is expected that better results would be obtained.

7.3. Evaluation of the work

The main aim of this work was to develop a methodology for integrating multi-temporal, multi-scale and multi-source data with the objective of improving the land cover classification derived from remotely sensed images. Two data source were selected for the study, namely: the medium resolution Landsat ETM+ image and the multi-resolution multi-temporal MODIS/Terra images.

The objective has been achieved and tested on four levels of integration as discussed in section 7.2.

Other objectives stated in each chapter were also fulfilled. For example the fourth chapter investigated the atmospheric correction of the ETM+ image and this was achieved by comparing the results of several atmospheric correction methods with the atmospherically corrected MODIS products acquired on the same dates. All methods were acceptable except the full module correction. The effect of atmospheric correction was obvious on the NDVI values which were used in the classification process.

Many activities for preparing the data sources were essential before the integration process could take place. For example, the huge file size of each MODIS product was reduced by assembling together in one file, all relevant scientific data sets for the subset image covering the study area. The problems associated with inconsistent size and geo-referencing of MODIS pixels were conquered by integrating each image individually with the ETM+ image. The spectral signature of each class in MODIS bands was derived and utilized to minimize the error in the expected reflectance in the MODIS image. Since commercial remote sensing image processing products were not available to handle these activities, suitable programs were written in MATLAB. For example most of the existing image processing software can perform grid analysis, and thus takes no account of inconsistence pixel size and the actual IFOV. This often leads to a misconception that each pixel in the remote sensed image is actually a rectangle containing the sum of all reflected radiances from within its boundaries.

With respect to the three major objectives which were set up for this work in section 1.5, each has been achieved successfully. The first objective was to develop a methodology for classifying the Landsat ETM+ image in the case of insufficient ground truth. This has

been achieved as described in section 4.4. The second major objective was to develop a methodology for integrating the OS Land-Line.Plus data with the Landsat ETM+ image to perform per-polygon classification, this also has been achieved - see section 4.6. The third major objective was to develop a methodology for integrating the classification of a single date medium resolution Landsat ETM+ image with the multi-scale multi-temporal MODIS/Terra images. The sixth chapter of the thesis explains how this has been achieved. In particular, a methodology for integrating multi-temporal, multi-resolution imagery was developed in section 6.6 based on Dempster-Shafer theory of evidence. For this it was indispensable to derive a basic probability assignment for each line of evidence, therefore, equation 6.4 was suggested and implemented in this work. This is a considerable contribution to the current trends in remotely sensed image classification discussed in section 1.3.

7.4. Recommendations and future work

From the experiments described in this thesis a number of recommendations can be made to assist in the classification of remote sensed data for agricultural land cover. Some suggestions for further research are also given to improve upon these methods.

When classifying agricultural land cover of the type seen in the UK, where crops are largely sown in homogeneous fields with discrete and often mapped boundaries, the classification is greatly improved by using the mapped polygons of fields, and utilising the classification of the polygon as a whole, as an *apriori* probability in classifying each individual pixel.

The fusion of multi resolution, multi temporal and multi platform data provides a challenge to improving land cover understanding.

Simple orthorectification of a single image using techniques such as nearest neighbour may be adequate for a single image, but when dealing with multiple images it is highly unlikely that the pixels will be exactly co-registered, and in these cases the pixels will contain a mixture of different real world land covers. Similarly the different atmospheric conditions prevailing during the different days will mean that the same emission from the ground will give rise to different sensor reception. Therefore, when integrating different remote sensed data sources, a model of the instantaneous field of view and atmospheric effects must be incorporated into the application of the data.

Multi temporal MODIS imagery can give an insight into the different growth patterns of vegetated land cover, especially the date of harvest. Dempster-Shafer weight of evidence modelling can integrate this multi temporal data with single scene ETM+ data to give an improved agricultural land cover classification. However, MODIS images have only two bands at 250m nominal spatial resolution. The remaining reflected MODIS bands are nominally at 500m or 1000m spatial resolution, but in reality these will increase with scan angle resulting in the actual area sensed being very large. Further research is required to investigate the usefulness of the remaining MODIS bands in improving the classification of land cover. Increasing the number of discriminating bands will increase the chance of finding the more likely classes in the coarse resolution image, thus improving the classification. Therefore, further improvement can be expected if more reliable hyperspectral images are used.

Alternatively, another data source may be used, for example the European satellite Medium Resolution Imaging Spectrometer MERIS (http://envisat.esa.int/instruments/meris [2005, September]). The narrow bands of MERIS will make it possible to derive more accurate global maps and more effective vegetation indices than have previously been available. Further, MERIS has 15 channels in the visible and near infrared at improved spatial resolution of 300m and still provide regional revisit every 3 days. Using this data source may improve the work carried out in this thesis. However, there is a financial cost associated with obtaining MERIS data in comparison to the free MODIS images downloadable from DAAC.

Another area of improvement may be obtained if the MODIS images were atmospherically corrected before the integration. Even though the surface reflectance MOD09 product is available, the pixel re-projection and resampling prevented the use of this product in this work. The re-projection and resampling of the pixels make it impossible to identify the actual area sensed due to the inconstant size of the pixels as described in chapter 3.

The method proposed in this work for combining multi-scale multi-temporal multi-source data to improve land cover classifications is likely to be improved if more accurate temporal signatures for land cover are available especially those acquired independent of MODIS. These might be obtained from leaf area index (LAI) publications. However, a robust radiometric calibration of the image will be required to adjust these signatures.

In Chapter 5 a methodology was presented to derive the temporal signatures using multi-temporal MODIS images with the per-parcel classification of Landsat ETM+ image. For

this, a high quality parcel classification is pre-requisite to enable a reasonable extraction of temporal signatures of the land cover. A very great amount of effort was expended and a time consuming procedure was followed in Chapter 4, to obtain such high quality parcel classification. As a consequence, in this work, the improvement that could be made to this high quality parcel classification was not significant. Therefore, a more considerable improvement can be expected were the original classification to be improved was not of a high quality. This could be very useful for scaling-up the classification of a small area of accurate classification to a regional scale where the classification overall is poor. For example the proposed integration method can improve the classification of a very large area, but first, a small representative area can be classified to a very high standard, so that a reasonable multi-temporal signature for each land cover can be identified. Subsequently, the classification of the whole area could be improved using the proposed integration method.

In section 6.6 the basic probability assignment (BPA) for the classification from MODIS images was postulated to be a function of the degree of the improvement, α, and the MODIS image reliability, β. The BPA was assumed to increase linearly with β and exponentially with α. Further research is required to verify this hypothesis and to establish criteria for the selection of the reliability values β.

The improvement of the classification was mainly based on the visual quality of the classification, though some quantitative measures were performed, there is still a need for obtaining reliable ground truth. Therefore, further quantitative accuracy assessment is required, to test the success of the methodology proposed in this work for integrating the

information from medium resolution Landsat ETM+ images and the multi-resolution multi-temporal MODIS\Terra images. For this more effort and cooperation is needed in the organisation of data collection, especially for ground truth on the date of imaging. This would enable further classification studies to be performed in the supervised mode, where quantitative accuracy measures can be derived confidently.

Finally, the concept of multi-scale integration is transferable to improve the classification of high resolution images using medium resolution with multi-spectral or hyper-spectral images. For example, the classification of a high resolution panchromatic image, such as Quickbird, can be improved using the multi-spectral medium resolution of a Landsat ETM+ image. For this, the MODIS data used in this study would be replaced by a raw Landsat ETM+ image.

References

Abkar, A. (1999), *'Likelihood-Based Segmentation and Classification of Remotely Sensed Images'*, Ph.D Thesis, Netherlands: University of Twente, ITC, Enschede.

Ahern, F.J., Goodenough, D.G., Jain, S.C., Rac, V.R., And Rochon, G. (1977), 'Use of Clear Lakes As Standard Reflectors For Atmospheric Measurements'. *Proceedings of The 11th International Symposium on Remote Sensing of Environment. Ann Arbor, MI*, 731–775.

Anderson, J.R., Hardy, E., Roach, J., and Witmer, R. (1976), 'A Land Use and Land Cover Classification System for Use with Remote Sensor Data', *Geological Survey Professional Paper,* 964, U.S. Government Printing Office, Washington, DC.

Andrews, H.C., (1972), *Introduction to Mathematical Techniques in Pattern Recognition*, New York: Wiley.

Aplin, P., and Atkinson, P.M. (2001), 'Sub-pixel land cover mapping for per-field classification', *International Journal of Remote Sensing*, **22**, 2853-2858.

Arora, M.K., Shalan, M.A., and Elgy, J. (2005), 'Crisp and Fuzzy Classification Accuracy Measures for Remotely Sensed Derived Land Cover Maps', *In:* Atkinson, P.M., Foody, G.M., Darby, S.E., and Wu, F., (eds.), *'GeoDynamics'*, London, CRC Press, 11-27, ISBN 0-8493-2837-3.

Atkinson, P.M., Cutler, M.E.J., and Lewis, H., (1997), 'Mapping Sub-Pixel Proportional Land Cover with AVHRR Imagery', *International Journal of Remote Sensing*, **18** (4), 917-935.

Azzalini, A. and Capitanio, A. (1999), 'Statistical Applications of the Multivariate Skew-Normal Distribution', *Journal of the Royal Statistical Society*: Series B, **61**, 579–602.

Ball, G.H. and Hall, D.J. (1965), 'A Novel Method of Data Analysis and Pattern Classification', *Technical Report, Stanford Research Institute*, Menlo Park, CA.

Barbieri, R. (1997), *Draft of MODIS Level 1B Algorithm Theoretical Basis Document Version 2 (ATBMOD-01),* Greenbelt MD: Goddard Space Flight Centre.

Barnsley, M.J., Moller-Jensen, L., and Barr, S.L. (2001), 'Inferring Urban Land Use Through Spatial and Structural Pattern Recognition', *In*: Donnay *et al.* (eds.) *Remote Sensing and Urban Analysis - GISDATA 9*. London: Taylor and Francis, 115-144.

Benediktsson, J.A. and Swain, P.H. (1992), 'Consensus Theoretic Classification Methods', *IEEE Transaction*, **22**(4): 688-704.

Benz, U.C., Hofmann, P., Willhauck, G., Lingenfelder, I. and Heynen, M., (2004), 'Multiresolution Object-Oriented Fuzzy Analysis of Remote Sensing Data for GIS-Ready Information', *ISPRS Journal of Photogrammetry and Remote Sensing*, **58**, 239-258.

Bezdek, J.C. (1981), *Pattern Recognition with Fuzzy Objective Function Algorithms*, Plenum, New York.

Binaghi, E. and Rampini, A. (1993), 'Fuzzy decision making in the classification of multi-source remote sensing data', Optical Engineering **6**, 1193-1203

Boardman, J.W. and Kruse, F.A. (1994), 'Automated spectral analysis: A geologic example using AVIRIS data, north Grapevine Mountains, Nevada', *In Proceedings, Tenth Thematic Conference on Geologic Remote Sensing, Environmental Research Institute of Michigan*, Ann Arbor, MI, I-407 - I-418.

Campbell, J.B. (1996), *Introduction to Remote Sensing*, London: Taylor and Francis Ltd, 2nd Edition.

Carlotto, M. J. (1999), 'Reducing the Effects of Space-Varying Wavelength-Dependent Scattering in Multispectral Imagery', *International Journal of Remote Sensing*, **20** (17), 3333-3344.

Carper, W.J., Lillesand, T.M. and Kiefer, R.W. (1990), 'The Use of Intensity-Hue-Saturation Transformation for Merging SPOT Panchromatic and Multispectral Image Data', *Photogrammetric Engineering and Remote Sensing*, **56** (4), 459-467.

Chavez, P.S. (1988), 'An Improved Dark-Object Subtraction Technique for Atmospheric Scattering Correction of Multispectral Data', *Remote Sensing of Environment*, **24**, 450 - 479.

Chavez, P.S., (1989), 'Radiometric Calibration of Landsat Thematic Mapper Multispectral Images', *Photogrammetric Engineering and Remote Sensing*, **55**, 1285–1294.

Chavez, P.S., (1996), 'Image-Based Atmospheric Corrections Revisited and Improved', *Photogrammetric Engineering and Remote Sensing*, **62**, 1025–1036.

Chavez, P.S., Berlin, G.L. and Sowers, L.B. (1982), 'Statistical Methods for Selecting Landsat-MSS Ratios', *Journal of Applied Photogrammetric Engineering*, **8**, 23-30.

Chavez, P.S., Sides S.C. and Anderson J.A. (1991), 'Comparison of Three Different Methods to Merge Multi-Resolution and Multispectral Data: Landsat TM and SPOT Panchromatic', *Photogrammetric Engineering and Remote Sensing*, **57** (3), 295-303.

Cihlar, J. and Jansen, L.J.M. (2001), 'From Land Cover to Land Use: A Methodology for Efficient Land Use Mapping Over Large Areas', *Professional Geographer*, **52**(2), 275-289.

Colwell, R.N. (1983), *Manual of Remote Sensing*, 2 edition, American Society of Photogrammetry, Falls Church, Va.

Coppin, P.R. and Bauer, M.E. (1994), 'Processing of Multitemporal Landsat TM Imagery to Optimize Extraction of Forest Cover Change Features', *IEEE Transaction on Geosciences and Remote Sensing*, **32**(4), 918–927.

Cracknell, A.P. and Hayes, L.W.B. (1993), *Introduction to Remote Sensing*, London, New York, Philadelphia, Taylor and Francis.

Crippen, R.E. (1987), 'The Regression Intersection Method of adjusting image data for band rationing', *International Journal of Remote Sensing*, **8** (2), 137-155.

Dean, A.M. and Smith G.M. (2003), 'An evaluation of per-parcel land cover mapping using maximum likelihood class probabilities', *International Journal of Remote Sensing*, **24** (14), 2905-2920.

Dekker, R.J. (2003), 'Texture Analysis and Classification of ERS SAR Images for Map Updating of Urban Areas in the Netherlands', *IEEE Transaction on Geosciences and Remote Sensing,* **41**(9), 1950-1958.

Dowman, I., (1998), 'Automated Procedures for Integration of Satellite Images and Map Data for Change Detection, GIS - Between Visions and Applications', *International Archives of Photogrammetry and Remote Sensing*, Vol. **32**, Part 4, pp. 162-168.

Eastman, J.R., (2001), *Idrisi for Windows User's Guide Version 2.* Worcester: Clark University.

EC, (1993), *CORINE Land-Cover Project - Technical Guide*, Report EUR 12585EN, Luxembourg: Office for Publications of the European Communities.

Ehlers, M. (1991), 'Multi-sensor image fusion techniques in remote sensing', *ISPRS Journal of Photogrammetry and Remote Sensing*, **46**, 19-30.

Ekstrand, S. (1994), 'Assessment of Forest Damage with Landsat TM: Correction for Varying Forest Stand Characteristics', *Remote Sensing of Environment*, **47**, 291–302.

Elgy, J., Maksimovic, C., and Prodanovic, D., (1993), 'Matching Standard GIS Packages with Urban Storm Drainage Simulation Software', *In*: 'HydroGIS 93: Application of Geographic Information Systems in Hydrology and Water Resources Management', Proceedings of the Vienna Conference, April 1993, IAHE Publication No: 211.

Esch, T., Roth, A., Strunz, G. and Dech, S., (2003), 'Object oriented classification of Landsat-7 data a for regional planning purpose', *The international archives of the photogrammetry, remote sensing and spatial information sciences*, vol. **XXXIV**-7/W9, Regenburg.

Fallah-Adl, H., Jaja, J., Liang, S., Kaufman, Y.J., Townshend, J., (1995), 'Efficient Algorithms for Atmospheric Correction of Remotely Sensed Data', *In*: *Proceedings Supercomputer 95*, IEEE Computer Society Press.

Faust, N.L. (1989), 'Image Enhancement', *In*: Kent, A., Williams, J.G., (eds.) '*Supplement 5 of Encyclopaedia of Computer Science and Technology*', Volume **20**, New York: Marcel Dekker, Inc.

Fisher, R.A. (1936), 'The Use of Multiple Measurements in Taxonomic Problems', *Annals of Eugenics*, **7**, 179-188. Available from: URL: (http://www.library.adelaide.edu.au/digitised/fisher/138.pdf [2004, March].

Fisher, P.F., Comber, A.J. and Wadsworth, R., (2005), 'Land Use and Land Cover: Contradiction or Complement', *In*: Fisher, P.F and Unwin, D.J (eds.) *Re-Presenting GIS*, Chichester: Wiley.

Foody, G.M., (1995), 'Land Cover Classification by an Artificial Neural Network with Ancillary Information', *International Journal of Remote Sensing*, **16**, 527-542.

Foody, G.M., (1996a), 'Approaches For the Production and Evaluation of Fuzzy Land Cover Classifications from Remotely Sensed Data', *International Journal of Remote Sensing,* **17**, 1317-1340.

Foody, G.M., (1996b), 'Relating The Land-Cover Composition of Mixed Pixels to Artificial Neural Network Classification Output', *Photogrammetric Engineering and Remote Sensing*, **62**: 491-499.

Foody, G.M., Campbell, N.A., Trodd, N.M. and Wood, T.F., (1992), 'Derivation and Applications of Probabilistic Measures of Class Membership from Maximum Likelihood Classification', *Photogrammetric Engineering and Remote Sensing*, **58**, 1335-1341.

Foody, G.M., Palubinska, G., Lucas, R.M, Curran, P.J., and Honzak, M., (1996), 'Identifying Terrestrial Carbon Sinks: Classification of Successional Stages in Regenerating Tropical Forest from Landsat TM Data', *Remote Sensing of Environment,* **55**, 205–216.

Forster, B.C., (1984), 'Derivation of Atmospheric Correction Procedures for Landsat MSS with Particular Reference to Urban Data', *International Journal of Remote Sensing*, **5**, 799-817.

Fraser, R.S, Bahethi, O.P. and Al-Abbas, A.H., (1977), 'The Effect of the Atmosphere on Classification of Satellite Observations to Identify Surface Features', *Remote Sensing of Environment*, **6**, 229–249.

Fraser, R.S. and Kaufman, Y.J., (1985), 'The Relative Importance of Scattering and Absorption in Remote Sensing', *IEEE Transactions on Geosciences and Remote Sensing*, **23**, 625-633.

Fukunaga, K. (1990), *Introduction to Statistical Pattern Recognition.* Second Edition, San Diego, CA: Academic Press.

García, M.C., and Álvarez, R. (1994), 'TM Digital Processing of a Tropical Forest Region in South Eastern Mexico', *International Journal of Remote Sensing*, **15**, 1611-1632.

Garguet-Duport, B., Girel, J., Chassery, J.M., and Pautou, G. (1996), 'The Use of Multiresolution Analysis and Wavelet Transform for Merging SPOT Panchromatic and Multispectral Image Data', *Photogrammetric Engineering and Remote Sensing*, **62** (9), 1057-1066.

Gebbinck, M.S.K. (1998), '*Decomposition of Mixed Pixels in Remote Sensing Images to Improve the Area Estimation of Agricultural Fields*', PhD Thesis, Veenendaal: Universal Press.

Gong, P., and Howarth, P.J. (1990), 'Land Cover to Land Use Conversion: A Knowledge-Based Approach', *Annual Conference of ASPRS*, Denver, Colorado, **4**, 447-456.

Gordon, H.R. (1978), 'Removal of Atmospheric Effects from Satellite Imagery of the Ocean', *Applied Optics*, **17**, 1631–1636.

Gordon, J. and Shortliffe, E. (1985), 'A Method for Managing Evidential Reasoning in a Hierarchical Hypothesis Space', *Artificial Intelligence*, **26**, 323-357.

Haan, J.F., Hovenier, J.W., Kokke, J.M.M. and Stokkom, H.T.C. (1991), 'Removal of Atmospheric Influences on Satellite-Borne Imagery: A Radiative Transfer Approach', *Remote Sensing of Environment*, **37**, 1–21.

Harris, J.R., Murray, R., and Hirose, T., (1990), 'IHS Transform for the Integration of Radar Imagery with other Remotely Sensed Data', *Photogrammetric Engineering and Remote Sensing*, **56**(12), 1631-1641.

Holm, R.G, Jackson, R.D., Yuan, B., Moran, M.S., Slater, P.N. and Bigger, S.F. (1989), 'Surface Reflectance Factor Retrieval from Thematic Mapper Data', *Remote Sensing of Environment*, **27**, 47–57.

Horwitz, H.M., Nalepka, R.F., Hyde, P.D. and Morgenstern, J.P. (1971), 'Estimating the proportions of objects within a single resolution element of a multispectral scanner', *Proceedings of the 7th International Symposium on Remote Sensing of Environment*, 1307-1320, Ann Arbor, Michigan.

Huguenin, R.L., Karaska, M.A., Blaricom, D.V. and Jensen, J.R. (1997), 'Sub-pixel Classification of Bald Cypress and Tu-Pelo Gum Trees in Thematic Mapper Imagery', *Photogrammetric Engineering and Remote Sensing*, **63**(6), 717–725.

Jacobsen, A., Heidebrecht, K.B. and Nielsen, A.A. (1998), 'Monitoring Grasslands Using Convex Geometry and Partial Unmixing – A Case Study', *In*: Shaepman, M., Schläpfer, and Itten, K. (eds.): *Earsel Workshop On Imaging Spectroscopy*, Remote Sensing Laboratories, Switzerland: University of Zürich, 309-316.

Jakubauskas, M.E. (1996), 'Thematic Mapper Characterization of Lodgepole Pine Seral Stages in Yellowstone National Park', USA. *Remote Sensing of Environment*, **56**:118–132.

Janssen, L.L.F., Jaarsma, M.N., and Vander Linden, E.T.M., (1990), 'Integrating Topographic Data with Remote Sensing for Land-Cover Classification', *Photogrammetric Engineering and Remote Sensing*, **56** (11), 1503-1506.

Janssen, L.L.F., Schoenmakers, R.P.H.M., and Verwaal, R.G., (1992), 'Integrated segmentation and classification of high resolution satellite images', *In*: Proceedings of the International Workshop IAPR TC7: Multisource Data Integration in Remote Sensing for Land Inventory Applications, 7-9 September, Delft, edited by M Molenaar, L. Janssen, and H. Van Leeuwen, pp. 65-84.

Kaufman, Y.J. (1985), 'The Atmospheric Effect on Separability of Field Classes Measured from Satellite', *Remote Sensing Environment*, **18**, 21-34.

Kaufman, Y.J. (1993), 'Aerosol Optical Thickness and Atmospheric Path Radiance', *Journal of Geophysical Research-Atmospheres*, **98**, 2677–2692.

Kaufman Y.J., Gitelson, A., Karnieli, A., Ganor, E., Fraser, R.S., Nakajima, T., Mattoo, S. and Holben, B.N. (1994), 'Size Distribution and Scattering Phase Function of Aerosol Particles Retrieved from Sky Brightness Measurements'. *Journal of Geophysical Research-Atmospheres*, **99**, 10341-10356.

Kaufman, Y.J. and Sendra, C. (1988), 'Algorithm for Automatic Atmospheric Corrections to Visible and Near-IR Satellite Imagery', *International Journal of Remote Sensing*, **9**, 1357-1381.

Kawata, Y., Ohtani, A., Kusaka, T. and Ueno, S. (1990), 'Classification Accuracy for the MOS-1 MESSR Data before and after the Atmospheric Correction', *IEEE Trans. Geosci. Reremote Sens.*, **28**, 755–760.

Kaufman, Y.J., Wald, A., Remer, L.A., Gao, B., Li, R. and Flynn, L. (1997), 'The MODIS 2.1 Lm Channel—Correlation With Visible Reflectance for Use in Remote Sensing of Aerosol', *IEEE Trans. Geosciences and Remote Sensing,* **35**, 1–13.

Kloer, B.R. (1994), 'Hybrid Parametric/Non-Parametric Image Classification', Paper Presented at the ACSM-ASPRS Annual Convention, April 1994, Reno, Nevada.

Kneizys, F.X., Anderson, G.P., Shettle, E.P., Abreu, L.W. and Chetwynd, J.H. (1988), *User Guide to LOWTR4AN-7*, Hanscom AFB, MA: Air Force Geophysics Lab.

Köpke, P. (1989), 'Removal of Atmospheric Effects from AVHRR Albedos', *Journal of Applied Meteorology*, **28**, 1342-1348.

Krishnapuram, R. and Keller, J.M. (1993), 'A Possibilitic Approach to Clustering', *IEEE Transactions on Fuzzy Systems*, **1**, 98-110.

Krishnapuram, R. and Keller, J.M. (1996), 'The Possibilitic C-Means Algorithm: Insights And Recommendations', *IEEE Transactions on Fuzzy Systems*, **4**, 385-93.

Latifovic, R. and Pouliot, D. (2005), 'Multitemporal land cover mapping for Canada: methodology and products', *Canadian Journal of Remote Sensing*, Vol. **31**, No. 5, 347–363.

Le Hégarat-Mascle S., Richard, D. and Ottlé, C. (2003), 'Multi-scale data fusion using Dempster-Shafer evidence theory', *Integrated Computer-Aided Engineering* **10**, 9–22, IOS Press

Lee, T., Richards, J.A. and Swain, P.H. (1987), 'Probabilistic and Evidential Approaches for Multisource Data Analysis', *IEEE Transactions on Geosciences and Remote Sensing*, GE-25 (**3**), 283-292.

Liang, S., Fallah-Adl, H., Kalluri, S., Jaja, J., Kaufman, Y.J., and Townshend, J.R.G. (1997), 'An Operational Atmospheric Correction Algorithm for Landsat Thermatic Mapper Imagery over the Land', *J. Geophys. Res.* **102**, 17173–17186.

Liang, S., Fang, H. and Chen, M. (2001), 'Atmospheric Correction of Landsat ETM+ Land Surface Imagery', *IEEE Transactions on Geosciences and Remote Sensing*, **39** (11), 2490-2498.

Lillesand, T.M. and Kiefer R.W. (2000), *Remote Sensing and Image Interpretation*, 4th Edition, New York: John Wiley and Sons.

Liou, K.N. (1980), *An Introduction to Atmospheric Radiation*. New York: Academic.

MacQueen, J.B. (1967), 'Some Methods for Classification and Analysis of Multivariate Observations', Proceedings of the Fifth Berkeley Symposium on Mathematical Statistics and Probability, **1**, 281 -297.

Markham, B.L. and Barker, J.L. (1985), 'Spectral Characterization of the Landsat Thematic Mapper Sensors', *International Journal of Remote Sensing*, **6**, 697-716.

Martínez-Casasnovas, J.A. (2000), 'A Cartographic and Database Approach for Land Cover/Use Mapping and Generalisation from Remotely Sensed Data', *International Journal of Remote Sensing*, **21** (9), 1825 - 1842.

Maselli, F., Conese, C. and Petkov, L. (1994), 'Use of probability entropy for the estimation and graphical representation of the accuracy of maximum likelihood classifications', *ISPRS Journal of Photogrammetry and Remote Sensing*, **49**, 13–20.

Maselli, F., Rodolfi, A. and Conese C. (1996), 'Fuzzy Classification of Spatially Degraded Thematic Mapper Data for the Estimation of Sub-Pixel Components', *International Journal of Remote Sensing*, **17** (3), 537-551.

Mason, D.C., Corr, D.G., Cross, A., Hogg, D.C., Lawrence, D. H., Petrou, M. and Tailor, A.M. (1988), 'The use of digital map data in the segmentation and classification of remotely-sensed images', *International Journal of Geographical Information Systems*, **2**, 195-215.

Mather, P.M. (1999), *Computer Processing of Remote Sensing Data*, Second Edition, Chichester: John Wiley.

Mcdonald, A.J., Gemmell, F.M. and Lewis, P.E. (1998), 'Investigation of the Utility of Spectral Vegetation Indices for Determining Information on Coniferous Forests', *Remote Sensing of Environment*, **66**, 250–272.

Michener, W.K. and Houhoulis, P.F. (1997), 'Detection of Vegetation Changes Associated with Extensive Flooding in a Forested Ecosystem', *Photogrammetric Engineering and. Remote Sensing,* **63**, 1363–1374.

Moran, M.S., Jackson, R.D., Slater, P.N. and Teillet, P.M. (1992), 'Evaluation of Simplified Procedures for Retrieval of Land Surface Reflectance Factors from Satellite Sensor Output', *Remote Sensing of Environment*, **41**, 169–184.

Myneni, R.B. and Asrar, G. (1994), 'Atmospheric effects and spectral vegetation indices', *Remote Sensing of Environment*, **47**, 390 – 402.

Nishihama, M., Wolfe, R., Solomon, D. and STX, H. (1997), *MODIS Level 1A Earth Location: Algorithm Theoretical Basis Document,* Version 3.0, Greenbelt MD: Goddard Space Flight Centre.

Oliver, C.J. (1991), 'Review Article: Information From SAR Images, J. Phys. D: Appl. Phys. **24**, 1493-1514. (URL: http://stacks.iop.org/0022-3727/24/1493 [2004, May].

Ouaidrari, H. and Vermote, E.F. (1999), 'Operational atmospheric correction of Landsat data', *Remote Sensing of Environment*, **70**, 4–15.

Palacio, J.L. and Luna, L. (1996), 'Improving Spectral Results in a GIS Context', *International Journal of Remote Sensing*, **17**, 2201-2209.

Pax Lenney, M., Woodcock, C.E., Collins, J.B. and Hamdi, H. (1996), 'The Status of Agricultural Lands in Egypt: The Use of Multitemporal NDVI Features Derived from Landsat TM', *Remote Sensing of Environment*, **56**, 8–20.

Pellemans, A.H.J.M., Jordans, R.W.L. and Allewijn, R. (1993), 'Merging Multispectral and Panchromatic SPOT Images with Respect to the Radiometric Properties of the Sensor', *Photogrammetric Eng. Remote Sensing*, **59**(1), 81-87.

Pohl, C. and Van Genderen, J.L. (1998), 'Multisensor Image Fusion in Remote Sensing: Concepts, Methods and Applications', *International Journal of Remote Sensing*, **19**(5), 823-854.

Potter, J. F. (1974), 'Haze and Sun Angle Effects on Automatic Classification of Satellite Data Simulation and Correction', *Proc. Soc. Photo-Opt. Instrum. Eng.*, **51**, 73–83.

Pouncey, R., Swanson, K. and Hart, K. (1999), *ERDAS Field Guide*™, Fifth Edition, Atlanta, Georgia: ERDAS®, Inc.

Price, J.C. (1989), 'Calibration Comparison for the Landsat 4 and 5 Multispectral Scanners and Thematic Mappers', *Applied Optics*, **28**, 465-471.

Ranchin, T., and Wald, L. (1993), 'The Wavelet Transform for the Analysis of Remotely Sensed Images', *International Journal of Remote Sensing*, **14**(3), 615-619.

Richards, J.A. (1993), *Remote Sensing Digital Image Analysis: An Introduction*, Second Edition. Springer-Verlag, Germany.

Richards, J.A., Landgrebe, D.A. and Swain, P.H. (1982), 'A means for utilising ancillary information in multispectral classification', *Remote Sensing of Environment*, **12**, 463-77.

Richter, R. (1990), 'A Fast Atmospheric Correction Algorithm Applied to Landsat TM Images, *International Journal of Remote Sensing*, **11**, 159-166.

Richter, R. (1996a) 'A Spatially Adaptive Fast Atmospheric Correction Algorithm', *International Journal of Remote Sensing*, **17**, 1201–1214.

Richter, R. (1996b), 'Atmospheric Correction Of Satellite Data With Haze Removal Including A Haze/Clear Transition Region', *Computers and Geosciences*, **22**(6), 675-681.

Robinove, C.J. (1981), 'The Logic of Multispectral Classification and Mapping of Land', *Remote Sensing of Environment*, **11**, 231-244.

Sader, S.A., (1987), 'Digital Image Classification Approach for Estimating Forest Clearing and Regrowth Rates and Trends', *International Geosciences and Remote Sensing Symposium*, Ann Arbor, Michigan, 18–21 May, 209–213.

Sande, C.J., Jong, S.M. and Roo, A.P.J. (2003), 'A segmentation and classification approach of IKONOS-2 imagery for land cover mapping to assist flood risk and flood damage assessment', *International Journal of Applied Earth Observation and Geoinformation*, **4**, 217-229.

Schistad Solberg, A.H., Jain, A.K. and Taxt, T. (1994), 'Multisource Classification of Remotely Sensed Data: Fusion of Landsat TM and SAR Images', *IEEE Transaction on Geosciences and Remote Sensing*, **32**(4), 768-778.

Schroeder Th. and J. Fischer (2003), *Atmospheric Correction of MERIS Imagery Above Case-2 Waters* [Online], Available: http://userpage.fu-berlin.de/~termotom/papers/TS_2003_ESA_Frascati.pdf [2005, December 21]

Sellers, P.J., Dickinson, R.E., Randall, D.A., Betts, A.K., Hall, F.G., Mooney, H.A., Nobre, C.A., Sato, N., Field, C.B. and Henderson-Sellers, A. (1997), 'Modelling the exchanges of energy, water, and carbon between continents and the atmosphere', *Science*, **275**, 502-509.

Serrano, L., Filella, I. and Penuelas, J. (2000), 'Remote Sensing of Wheat Biomass and Yield under Different N Supplies', Crop Science, 40, 723–731.

Settle, J.J. and Drake, N.A. (1993), 'Linear Mixing and the Estimation of Ground Cover Proportions', *International Journal of Remote Sensing*, **14** (6), 1159-1177.

Shafer, G. (1979), 'Allocations of Probability', *The Annals of Probability*, **7**, 827-839.

Shalan, M.A., Arora, M.K. and Ghosh, S.K. (2003), 'An Evaluation of Fuzzy Classifications from IRS 1C LISS III Data', *International Journal of Remote Sensing*, **23**(15), 3179 - 3186.

Shettigara, V.K. (1992), 'A Generalized Component Substitution Technique for Spatial Enhancement of Multispectral Images Using a Higher Resolution Data Set', *Photogrammetric Eng. Remote Sensing*, **58**(5), 561-567.

Singh, A. (1989), 'Digital Change Detection Techniques Using Remotely Sensed Data', *International Journal of Remote Sensing*, **10** (6), 989-1003.

Slater, P.N., Biggar, S.F., Holm, R.G., Jackson, R.D., Mao, Y., Moran, M.S., Palmer, J.M. and Yuan, B. (1987), 'Reflectance and Radiance-Based Methods for the In-Flight Absolute Calibration of Multispectral Sensors', *Remote Sensing of Environment*, **22**, 11-37.

Song, C., Woodcock, C.E., Seto, K.C., Lenney, M.P. and Macomber, S.A. (2001), 'Classification and Change Detection Using Landsat TM Data: When and How to Correct Atmospheric Effects?', *Remote Sensing of Environment*, **75**, 230-244.

Spanner, M.A., Pierce, L.L., Peterson, D.L. and Running, S.W. (1990), 'Remote Sensing of Temperate Coniferous Forest Leaf Area Index: The Influence of Canopy Closure, Understory Vegetation and Background Reflectance', *International Journal of Remote Sensing*, **11**(1), 95–111.

Steinnocher, K. (1999), 'Adaptive Fusion of Multisource Raster Data Applying Filter Techniques', *International Archives of Photogrammetry and Remote Sensing*, **32**, 108-115.

Takeuchi, S. and Inanaga, A. (2000), 'Scaling-up of Land Cover Information by Using Multiple Resolution Satellite Data', *Advances in Space Research*, **26** (7), 1127-1130.

Townshend, J. (1999), *MODIS Enhanced Land Cover and Land Cover Change Product Algorithm Theoretical Basis Documents (ATBD),* Version 2.0, Department of Geography University of Maryland, College Park, MD.

Tseng, Y., Hsu, P. and Chen, H. (1998), 'Automatic Detecting Rice Fields by Using Multitemporal Satellite Images,Land-parcel Data and Domain Knowledge', GISdevelopment http://www.gisdevelopment.net/aars/acrs/1998/ps3/ps3001.shtml [2004, December].

Tso, B. and Mather, P.M (2001), *Classification Methods for Remotely Sensed Data.* New York: Taylor and Francis.

Ulaby, F.T., Kouyate, F., Brisco, B. and Williams, T. H. L. (1986), 'Textural information in SAR images', *IEEE Transaction on Geosciences and Remote Sensing*, GE- **24**, 235 -245.

Vermote, E.F., Tanre´, D., Deuze, J.L., Herman, M. and Morcrette, J.J. (1997), *Second Simulation of the Satellite Signal in the Solar Spectrum (6S), 6S User's Guide* Version 2, Code 923, Greenbelt, MD: NSAS Goddard Space Flight Centre.

Verstraete, M. (1994), 'The Contribution of Remote Sensing to Monitor Vegetation and to Evaluate its Dynamic Aspects', *In*: Veroustraete, F. et al. (eds.) '*Vegetation Modelling and Climatic Change Effects'*, The Hague, The Netherlands: SPB Academic Publishing, 207–212.

Vogelman, J.E., Sohl, T. and Howard, S. M. (1998), 'Regional characterization of land cover using multiple sources of data', Photogrammetric Engineering and Remote Sensing, **64**, 45-57.

Vrabel, J. (1996), 'Multispectral Imagery Band Sharpening Study', *Photogrammetric Eng. Remote Sensing*, **62** (9), 1075-1083.

Wagtendonk, J.W. and Ralph, R. (2000), 'Hyperspectral Analysis of Multi-Temporal Landsat TM Data for Mapping Fuels in Yosemite National Park, USGS, BRD, Western Ecological Research Centre, Yosemite Field Station', Available:

http://www.werc.usgs.gov/yosemite/ma-09vanwagtendonketal.pdf [2003, February].

Wald, L., Ranchin, T. and Mangolini, M. (1997), 'Fusion of Satellite Images of Different Spatial Resolutions: Assessing the Quality of Resulting Images', *Photogrammetric Eng. Remote Sensing*, **63** (6), 691-699.

Wang, F., (1990a), 'Fuzzy Supervised Classification of Remote Sensing Images', *IEEE Transactions on Geosciences and Remote Sensing*, **28**, 194-201.

Wang, F., (1990b), 'Improving Remote Sensing Image Analysis through Fuzzy Classification Representation', *Photogrammetric Engineering and Remote Sensing*, **56**, 1163-1169.

Weisstein, E. W. (No date). *Normal Distribution* [Online], Available: http://mathworld.wolfram.com/NormalDistribution.html [2005, December 21]

Wen, G., Tsay, S., Cahalan, R.F. and Oreopoulos, L. (1999), 'Path Radiance Technique For Retrieving Aerosol Optical Thickness Over Land', *Journal of Geophysical Research*, **104**(24), 31321–31332.

Williamson, J.R. (1996), 'Gaussian ARTMAP: A Neural Network for Fast Incremental Learning of Noisy Multidimensional Maps', *Neural Networks*, **9**, 881-897.

Yocky, D.A. (1996), 'Multiresolution Wavelet Decomposition Image Merger of Landsat Thematic Mapper and SPOT Panchromatic Data', *Photogrammetric Eng. Remote Sensing*, **62** (9), 1067-1074.

Zenzo, D., Degloria, S.D., Bernstein, R. and Kolsky, H.G. (1987), 'Gaussian Maximum Likelihood and Contextual Classification Algorithms for Multicrop Classification Experiments Using Thematic Mapper and Multispectral Scanner Sensor Data', *IEEE Transaction on Geosciences and Remote Sensing*, **25**, 815-824.

Zhukov, B., Berger, M., Lanzl, F. and Kaufman, H. (1995), 'A New Technique for Merging Multispectral and Panchromatic Images Revealing SubPixel Spectral Variation', *International Conference on Geosciences and Remote Sensing Symposium* (IGARSS_95), volume **3**, 2154—2156, Florence, Italy.

Appendix 1

Charecteristic Specifications of Some Remote Sensing Sensors

In this appendix some optical sensors are listed with a summary of their characteristics. The information source and any further details on the listed sensors can be found at the URLs listed below [Last accessed 2005, December 27]:

1. http://edc.usgs.gov/guides/landsat_mss.html
2. http://landsat.gsfc.nasa.gov/
3. http://www.landinfo.com/products_satellite.htm
4. http://www.digitalglobe.com/about/quickbird.html
5. http://www.crisp.nus.edu.sg/~research/tutorial/spot.htm
6. http://www.eoc.jaxa.jp/satellite/sendata/hrvir_e.html
7. http://medias.obs-mip.fr/www/Reseau/Lettre/11/en/systemes/vegetation.html
8. http://terra.nasa.gov/
9. http://envisat.esa.int/instruments/meris/
10. http://edc.usgs.gov/products/satellite/avhrr.html
11. http://www.euromap.de/products/prod_003.html
12. http://www.euromap.de/products/prod_004.html
13. http://eo1.usgs.gov/userGuide/hyp_prod.html
14. http://terra.nasa.gov/About/ASTER/index.php
15. http://www.terrasar.de/

Table: Some optical sensor of remote sensing

Platform/Sensor	Source	Altitude (km)	Temporal Resolution (days)	Bandwidth (μm) and (spatial Resolution m)				stereo viewing
				Pan	visible	infrared	Thermal	
Landsat5 MSS	1	705	16	-	0.5 - 0.6 (82) 0.6 - 0.7 (82)	0.7 - 0.8 (82) 0.8 - 1.1 (82)	-	-
Landsat7 ETM+	2	705	16	0.5 - 0.9 (15)	0.45 - 0.52 (30) 0.52 - 0.60 (30) 0.63 - 0.69 (30)	0.76 - 0.90 (30) 1.55 - 1.75 (30) 2.08 - 2.35 (30)	10.40 - 12.50 (60)	-
Ikonos	3	681	14	0.45-0.9 (0.82)	0.45-0.52 (4) 0.52-0.60 (4) 0.63-0.69 (4)	0.76-0.90 (4)	-	Yes
QuickBird	4	450	1 - 3.5	0,45 - 0,90 (0.7)	0,45 - 0,52 (2.8) 0,52 - 0,60 (2.8) 0,63 - 0,69 (2.8)	0,76 - 0,90 (2.8)		
SPOT (HRV)	5	832	26	0.51 - 0.73 (10)	0.50 - 0.59 (20) 0.61 - 0.68 (20)	0.79 - 0.89 (20)	-	Yes
SPOT (HRVIR)	6	832	26	0.61 - 0.68 (10)	0.50 - 0.59 (20) 0.61 - 0.68 (20)	0.79 - 0.89 (20) 1.53 - 1.75 (20)	-	Yes
SPOT 4 (VEGETATION)	7	820	Daily	-	0.43 – 0.47 (1000) 0.61 – 0.68 (1000)	0.78 – 0.89 (1000) 1.58 – 1.75 (1000)		

Table (Continue): Some optical sensor of remote sensing

Sensor	Source	Altitude (km)	Temporal Resolution (days)	Bandwidth (μm) and (spatial Resolution m)				stereo viewing
				Pan	visible	infrared	Thermal	
Terra/MODIS	8	705	Daily	-	0.62 – 0.67 (250) 0.459 – 0.479 (500) 0.545 – 0.565 (500) 0.405 – 0.42 (1000) 0.438 – 0.448 (1000) 0.483 – 493 (1000) 0.526 – 536 (1000) 0.546 – 0.556 (1000) 0.662 – 0.672(1000) 0.673 – 0.683(1000)	0.841 – 0.876 (250) 1.230 – 1.250 (500) 1.628 – 1.652 (500) 2.105 – 2.155 (500) 0.743 – 0.753 (1000) 0.862 – 0.877 (1000) 0.890 – 0.920 (1000) 0.931 – 0.941 (1000) 0.915 – 0.965 (1000) 1.360 - 1.390 (1000)	3.660 - 3.840 (1000) 3.929 - 3.989 (1000) 3.929 - 3.989 (1000) 4.020 - 4.080 (1000) 4.433 - 4.498 (1000) 4.482 - 4.549 (1000) 6.535 - 6.895 (1000) 7.175 - 7.475 (1000) 8.400 - 8.700 (1000) 9.580 - 9.880 (1000) 10.780 - 11.280 (1000) 11.770 - 12.270 (1000) 13.185 - 13.485 (1000) 13.485 - 13.785 (1000) 13.785 - 14.085 (1000) 14.085 - 14.385 (1000)	-
Envisat / MERIS	9	800	3		0.4125 ± 10 (300) 0.4425 ± 10 (300) 0.490 ± 10 (300) 0.510 ± 10 (300) 0.560 ± 10 (300) 0.620± 10 (300) 0.665± 10 (300) 0.68125 ± 7.5 (300)	0.70875 ± 10 (300) 0.75375 ± 7.5 (300) 0.760625 ± 3.75 (300) 0.77875 ± 15 (300) 0.865 ± 20 (300) 0.885 ± 10 (300) 0.900 ± 10(300)		yes

Table (Continue): Some optical sensor of remote sensing

Sensor	Source	Altitude (km)	Temporal Resolution (days)	Bandwidth (μm) and (spatial Resolution m)				stereo viewing
				Pan	visible	infrared	Thermal	
AVHRR	10	850	6 hours		0.58 – 0.68 (1100)	0.72 – 1.10 (1100) 3.55 – 3.93 (1100) 10.30 – 11.30 (1100) 11.50 – 12.50 (1100)		
IRS - 1C / 1D LISSIII	11	817	24	0.5-0.75 (10)	0.52-0.59 (23.6) 0.62-0.68 (23.6)	0.77-0.86 (23.6) 1.55-1.7 (70.8)		
IRS – 1C /1D WiFS	12				0.62-0.68 (189)	0.77-0.86 (189)	-	-
Hyperion	13	705	16		220 contiguous spectral bands. VNIR (70 channels, 356 nm - 1058 nm), SWIR (172 channels, 852 nm - 2577 nm) at 10 nm bandwidth and 30 m spatial resolution			
EOS AM-1 ASTER	14	705	4-16		520-600 (15) 630-690 (15)	760-860 (15) 760-860 backward (15) 1600-1700 (30) 2145-2185 (30) 2185-2225 (30) 2235-2285 (30) 2295-2365 (30) 2360-2430 (30) 8125-8475 (90) 8475-8825 (90) 8925-9275 (90) 10250-10950 (90) 10950-11650 (90)		yes

Appendix 2

List of the modules used from Idrisi32

Source: http://www.sbg.ac.at/geo/idrisi/wwwtutor/specsa2z.htm#DISTANCE [2005, December 21]

Table for Idrisi32 modules used in this thesis

Module' Name	Brief Description
ASSIGN	Creates an image from an attribute values file by assigning the data values contained in the attribute values file to the cells belonging to defined regions. ASSIGN can also be used to reclassify integer images.
ATMOSC	ATMOSC performs the calculations necessary to correct remotely sensed images for atmospheric effects. Four models are provided: a Dark Object Subtraction (DOS) model, Chavez's Cos(t) model and a full radiative transfer equation model (FULL), and an Apparent Reflectance Model (ARM).
BAYES	Evaluates Bayes' Theorem. Prior probabilities may be input in map form. The user is also able to specify the confidence in the decision rule. BAYES is an extension to what is sometimes called a *Bayesian Weight of Evidence* approach.
BMPIDRIS	BMPIDRIS converts bitmaps from graphics packages which support the .bmp format into IDRISI for Windows images and vice versa.
COMPOSIT	Produces colour composite images.
CONCAT	Concatenates multiple images to produce a larger image.
CONTRACT	Reduces image resolution by pixel thinning or aggregation.
CONVERT	Converts between all of the image storage formats supported by IDRISI. Files may be converted to any combination of the byte, integer and real (floating point) data types and the ASCII, binary and packed (run-length encoded) file structures.
CROSSTAB	Performs image cross tabulation and cross correlation.
DISPLAY LAUNCHER	DISPLAY LAUNCHER is the module that allows you to open a new display window.
DXFIDRIS	Reads and writes DXF format vector files.
EDIT	A simple ASCII text editor for use with creating a variety of IDRISI data files. With values files, EDIT creates and maintains proper documentation files automatically.
EXPAND	Increases image resolution by pixel duplication.
EXTRACT	Creates an attribute values file from an image by extracting a summary of data values found within defined regions. The summary (minimum, maximum, range, total, mean, or standard deviation) may also be output as a table.
GRASSIDR	Converts raster files between GRASS and IDRISI.
HISTO	Produces histograms of image file values. In addition to the graphic output, numeric output includes proportional and cumulative frequencies along with simple statistics.
INITIAL	Initializes a new image with a constant value.
ISOCLUS	Performs unsupervised classification.
LINERAS	Line-to-Raster conversion.

Table for Idrisi32 modules used in this thesis (Continue)

Module' Name	Brief Description
MAKESIG	Creates signature files for each informational class for which you have created training sites.
MAXLIKE	A Maximum Likelihood classifier.
MINDIST	A Minimum Distance to Means classifier.
NDVICOMP	Composites images (eg. NDVI) using either a maximum value procedure or a quadratic mean.
OVERLAY	Undertakes pixel-wise addition, subtraction, multiplication, division and exponentiation of paired images. Maximum, minimum, -normalized ratio+ and -cover+ are also supported. On binary images, logical AND and OR operations are supported by means of the multiply and maximum operation. Other boolean operations are supported through various binary image overlay combinations.
PALETTE WORKSHOP	PALETTE WORKSHOP facilitates the creation and modification of colour palettes.
POLYRAS	Polygon-to-Raster conversion.
PROJECT	Undertakes conversions between reference systems for both vector and raster files. With raster images, a resampling is undertaken using either a nearest-neighbour or bilinear interpolation. A complete set of UTM zones based on WGS84 for the northern and southern hemispheres is included. In addition, users can construct reference system parameter files for any system based on a supported projection, thus enabled us to add the BNG (from: OS).
QUERY	Extracts pixels designated by an independent mask into a sequential file for subsequent statistical analysis.
RADIANCE	Converts raw values to calibrated radiances for LANDSAT images.
RECLASS	Reclassifies pixels by equal intervals or user-defined schemes. RECLASS is commonly used as a database query routine by reclassifying images into Boolean maps of areas meeting the specified conditions.
REGRESS	Performs regression analysis on images or attribute values files.
RESAMPLE	Determines the data values for a rectangular grid by interpolation of the values in a different (and possibly warped) grid. Linear, quadratic and cubic mappings between the grids are provided, along with nearest-neighbour and bi-linear interpolations. Vector files may also be transformed with this 'rubber sheet' procedure.
SCALAR	Adds, subtracts, multiplies, divides and exponentiates pixels by a constant value.
SSTIDRIS	Converts raster images entered with a spreadsheet to IDRISI. Can be used to read any ASCII image format with CR/LF characters at the end of each row.
STRETCH	Produces linear, linear with saturation and histogram equalization contrast stretches in preparation for image display.
SYMBOL WORKSHOP	SYMBOL WORKSHOP is used for the creation and editing of IDRISI symbol files.
TIFIDRIS	Reads and writes TIFF format files.
WINDOW	Extracts a rectangular sub-image.(in WINDOWS version direct batch processing possible)
XYZIDRIS	XYZIDRIS converts data in X, Y and Z format (e.g., spreadsheet data) to IDRISI for Windows vector point files.

Appendix 3

All codes written using MATLAB

These codes are included on a CD-ROM provided with the thesis. The MATLAB function used and their definition are listed (Source MATLAB help):

cd - Change current working directory.
dir - List directory.
delete - Delete file.
getenv - Get environment variable.
mkdir - Make directory.
union - Set union.
unique - Set unique.
intersect - Set intersection.
ismember - True for set member.
if - Conditionally execute statements.
else - IF statement condition.
elseif - IF statement condition.
end - Terminate scope of FOR, WHILE, SWITCH, TRY and IF statements.
for - Repeat statements a specific number of times.
while - Repeat statements an indefinite number of times.
break - Terminate execution of WHILE or FOR loop.
continue - Pass control to the next iteration of FOR or WHILE loop.
eval-Execute string with MATLAB expression.
function - Add new function.
nargin - Number of function input arguments.
nargout - Number of function output arguments.
input - Prompt for user input.
pause - Wait for user response.
zeros - Zeros array.
ones - Ones array.
repmat - Replicate and tile array.
rand - Uniformly distributed random numbers.
randn - Normally distributed random numbers.
size - Size of matrix.
length - Length of vector.
isempty - True for empty matrix.
isequal - True if arrays are identical.
isnumeric - True for numeric arrays.
logical - Convert numeric values to logical.
reshape - Change size.
fliplr - Flip matrix in left/right direction.
flipud - Flip matrix in up/down direction.

```
rot90      - Rotate matrix 90 degrees.
:          - Regularly spaced vector and index into matrix.
find       - Find indices of nonzero elements.
end        - Last index.
sub2ind    - Linear index from multiple subscripts.
ind2sub    - Multiple subscripts from linear index.
ans        - Most recent answer.
pi         - 3.1415926535897....
NaN        - Not-a-Number.
isnan      - True for Not-a-Number.
sin        - Sine.
cos        - Cosine.
exp        - Exponential.
log        - Natural logarithm.
log10      - Common (base 10) logarithm.
sqrt       - Square root.
abs        - Absolute value.
fix        - Round towards zero.
floor      - Round towards minus infinity.
round      - Round towards nearest integer.
mod        - Modulus (signed remainder after division).
rem        - Remainder after division.
perms      - All possible permutations.
nchoosek   - All combinations of N elements taken K at a time.
max        - Largest component.
min        - Smallest component.
mean       - Average or mean value.
median     - Median value.
std        - Standard deviation.
var        - Variance.
sort       - Sort in ascending order.
sortrows   - Sort rows in ascending order.
sum        - Sum of elements.
prod       - Product of elements.
hist       - Histogram.
histc      - Histogram count.
cumsum     - Cumulative sum of elements.
diff       - Difference and approximate derivative.
corrcoef   - Correlation coefficients.
cov        - Covariance matrix.
plot       - Linear plot.
axis       - Control axis scaling and appearance.
hold       - Hold current graph.
axes       - Create axes in arbitrary positions.
subplot    - Create axes in tiled positions.
legend     - Graph legend.
```

title - Graph title.
xlabel - X-axis label.
ylabel - Y-axis label.
texlabel - Produces TeX format from a character string
text - Text annotation.
colormap - Color look-up table.
figure - Create figure window.
gcf - Get handle to current figure.
clf - Clear current figure.
close - Close figure.
set - Set object properties.
get - Get object properties.
reset - Reset object properties.
delete - Delete object.
char - Create character array (string).
double - Convert string to numeric character codes.
cellstr - Create cell array of strings from character array.
deblank - Remove trailing blanks.
eval - Execute string with MATLAB expression.
ischar - True for character array (string).
iscellstr - True for cell array of strings.
strcat - Concatenate strings.
strvcat - Vertically concatenate strings.
strcmp - Compare strings.
strncmp - Compare first N characters of strings.
strcmpi - Compare strings ignoring case.
strncmpi - Compare first N characters of strings ignoring case.
findstr - Find one string within another.
strmatch - Find possible matches for string.
num2str - Convert number to string.
int2str - Convert integer to string.
str2double - Convert string to double precision value.
str2num - Convert string matrix to numeric array.
bin2dec - Convert binary string to decimal integer.
dec2bin - Convert decimal integer to binary string.
dlmread - Read delimited text file.
dlmwrite - Write delimited text file.
load - Load workspace from MATLAB (MAT) file.
importdata - Load workspace variables disk file.
imread - Read image from graphics file.
imwrite - Write image to graphics file.
fprintf - Write formatted data to file.
fopen - Open file.
fclose - Close file.
fileparts - Filename parts.
hdf - MEX-file interface to the HDF library.

hdfsd - MATLAB Gateway to HDF multifile scientific dataset interface.
cputime - CPU time in seconds.
double - Convert to double precision.
struct - Create or convert to structure array.
uint8 - Convert to unsigned 8-bit integer.
uint16 - Convert to unsigned 16-bit integer.
int8 - Convert to signed 8-bit integer.
int16 - Convert to signed 16-bit integer.
cat - Concatenate arrays.
permute - Permute array dimensions.
ipermute - Inverse permute array dimensions.
squeeze - Remove singleton dimensions.
struct - Create or convert to structure array.
colorbar - Display colorbar (MATLAB Toolbox).
image - Create and display image object (MATLAB Toolbox).
imagesc - Scale data and display as image (MATLAB Toolbox).
imshow - Display image.
subimage - Display multiple images in single figure.
imread - Read image file (MATLAB Toolbox).
imwrite - Write image file (MATLAB Toolbox).
imresize - Resize image.
imrotate - Rotate image.
corr2 - Compute 2-D correlation coefficient.
imhist - Display histogram of image data.
pixval - Display information about image pixels.
blkproc - Implement distinct block processing for image.
im2col - Rearrange image blocks into columns.
bwarea - Compute area of objects in binary image.
bwlabel - Label connected components in binary image.
colormap - Set or get color lookup table (MATLAB Toolbox).
gray2ind - Convert intensity image to indexed image.
im2bw - Convert image to binary image by thresholding.
im2double - Convert image array to double precision.
im2uint8 - Convert image array to 8-bit unsigned integers.
im2uint16 - Convert image array to 16-bit unsigned integers.
ind2gray - Convert indexed image to intensity image.
ind2rgb - Convert indexed image to RGB image (MATLAB Toolbox).
rgb2gray - Convert RGB image or colormap to grayscale.
rgb2ind - Convert RGB image to indexed image.
fcm - Find clusters with fuzzy c-means clustering.
combntns - Compute all combinations of a given set of values.
intrplat - Compute an interpolated latitude for a given longitude.
intrplon - Compute an interpolated longitude for a given latitude.
pdist - Pairwise distance between observations.
squareform - Square matrix formatted distance.

Appendix 4:

The mean and variance-covariance algebra

The mean vector for a particular class can be calculated using the following formula:

$$\vec{\mu} = \frac{1}{N}\sum_{j=1}^{N}\vec{S}_j \qquad \textbf{Equation A4. 1}$$

Where:

$\vec{\mu} = (\mu_1, \mu_2, \ldots, \mu_b)$ is the vector of the mean DN value of the training sample in each band.

$\vec{S}_j = (x_1, x_2, \ldots, x_b)_j$ is the vector of DN value of the j^{th} training pixel in the training sample.

N is the total number of pixels in the training sample for that particular class.

The variance-covariance matrix (*Cov*) for a particular class is a square array. The number of rows and columns are equal to the number of spectral bands under consideration. Each diagonal element in this array contains the variance of the training sample in each corresponding band. The variance can be calculated using the following formula:

$$VAR_l = \frac{N\sum_{n=1}^{N} x_n{}^2 - \left(\sum_{n=1}^{N} x_n\right)^2}{N(N-1)} \qquad \textbf{Equation A4. 2}$$

where:

VAR_l is the variance of DN value in band (l) for a particular class. This value will be placed in the (Cov) array at the diagonal element ($cov_{l,l}$)

The off-diagonal elements in the (Cov) array are the sample covariance in each two corresponding bands. For example, the covariance of the sample in two bands (l and m) can be computed using the following equation:

$$\mathrm{cov}_{l,m} = \frac{1}{N-1}\sum_{n=1}^{N}(x_n^l - \mu_m)(x_n^m - \mu_l)^T \qquad \textbf{Equation A4. 3}$$

where $x_n^{\ l}; x_n^m$ denote the DN values for the nth pixel in the training sample in band l and m respectively.

$\mu_l; \mu_m$ are the mean DN value for the training sample in both bands l and m respectively.